Asteroid Hazard Mitigation: Deflection Models and Mission Analysis

Joan Pau Sanchez Cuartielles

Submitted in fulfilment of the requirements for the Degree of Doctor of Philosophy

Department of Aerospace Engineering
Faculty of Engineering
University of Glasgow

Joan Pau Sanchez Cuartielles, January 2009

A la meva mare,

"Sooner or later, it was bound to happen. On 30 June 1908 Moscow escaped destruction by three hours and four thousand kilometres – a margin invisibly small by the standards of the universe. Again, on 12 February 1947, yet another Russian city had a still narrower escape, when the second great meteorite of the twentieth century detonated less than four hundred kilometres from Vladivostok, with an explosion rivalling that of the newly invented uranium bomb."

Arthur C. Clarke, "*Rendezvous with Rama"*.

Abstract

Small celestial bodies such as Near Earth Objects (NEOs) have become a common subject of study because of their importance in uncovering the mysteries of the composition, formation and evolution of the solar system. Among all asteroids, NEOs have stepped into prominence because of two important aspects: they are among the easiest celestial bodies to reach from Earth, in some cases with less demanding trajectories than a simple Earth-Moon trajectory and, even more meaningful, they may pose a threat to our planet. The purpose of this thesis is to provide a comprehensive insight into the asteroid hazard problem and particularly to its mitigation. Six different concepts are fully described; specifically models for nuclear interceptor, kinetic impactor, low-thrust propulsion, mass driver, solar collector and gravity tug are developed and their efficiency is assessed for a complete set of different types of hazardous celestial objects. A multi-criteria optimization is then used to construct a set of Pareto-optimal asteroid deflection missions. The Pareto-optimality is here achieved not only by maximizing the deflection of the threatening object, but also by minimizing the total mass of the deflection mission at launch and the warning time required to deflect the asteroid. A dominance criterion is also defined and used to compare all the Pareto sets for all the various mitigation strategies. The Technology Readiness Level for each strategy is also accounted for in the comparison. Finally, this thesis will also show that impulsive deflection methods may easily catastrophically disrupt an asteroid if the required energy for a deflection reaches a certain limit threshold. A statistical model is presented to approximate both the number and size of the fragments and their initial dispersion of velocity and then used to assess the potential risk to Earth posed by the fragmentation of an asteroid as a possible outcome of a hazard mitigation mission.

Acknowledgements

I would first like to acknowledge all the people who have both made this work possible and my PhD an unforgettable experience.

I want especially to thank my supervisors, Gianmarco and Max, for all their guidance, help and friendship throughout my PhD. I thank GM very much for granting me this truly fortunate *Glaswegian* experience. As an undergraduate student in Barcelona, I never dreamed of spending such a good time abroad and eventually becoming so acquainted with the English/Scottish language…especially, after having so many troubles with it in high school. I must particularly thank Max for all his advice and inspiration these last three years. In particular, I would like to recognize his countless reviews of my work. Although some times a bit exasperating, his thorough reviewing of my research have been one of the major sources of inspiration and contributed with some of the most valuable lessons of my PhD.

A big hug to my *third supervisor*, Camilla. As a friend, flatmate and colleague, she has both given to me priceless help on my work and taken care of illness, homesickness or sporadic hangovers.... I thank to Matteo and Nico, without whose friendship I would not have felt at home in Glasgow. I thank to Carles, without him, most probably, I would not have started the PhD. Also, thanks to all those friends that became my *Glaswegian* family; Janice, Christie, Giulio, Irene, DC, Daniel, Ed, Stu, Nita, Imran, Giangi, Marti, Marta, Olaya, Martina, Jim, Alan, Michael, Robbie, Chris and many others without whom this experience would have been decaffeinated.

Last but not least, I am immensely grateful for my family's steadfast support, help and patience. Ana, cari, sento que en aquest darrer any no hàgim pogut fer cap d'aquells viatges que teníem pensats. Ja saps lo molt que t'agraeixo l'esforç que has fet i la paciència que has tingut amb mi, sense tu no ho hagués pogut fer. Papa, germanetes: us estimo, la tesis la dedico a la mama, estic segur que encara li faria mes il·lusió a ella que a mi.

Contents

ABSTRACT III

ACKNOWLEDGEMENTS IV

NOMENCLATURE & DEFINITIONS XII

List of Abbreviations xii

List of Nomenclatures xii
Chapter I: Introduction to the Asteroidal and Cometary Hazard xii
Chapter II: On the Deflection of Threatening Asteroids xii
Chapter III: Hazard Deflection Missions xiv
Chapter IV: Consequences of a Fragmentation Due to a NEO Mitigation Strategy xiv
Appendices xv

INTRODUCTION TO THE ASTEROIDAL AND COMETARY IMPACT HAZARD 1

I.1. Historical Recognition of the Impact Hazard 2

I.2. Near Earth Objects 5
I.2.1. Asteroids and Near Earth Asteroids (NEAs) 5
I.2.2. Comets and Near Earth Comets 7
I.2.3. NEO Census and Impact Frequency 9
I.2.4. Consequences for the Earth 11

I.3. Asteroid Hazard Monitoring 12
I.3.1. Considerations on Warning Time 14
I.3.2. Considerations on Resonant Returns 15

I.4. Virtual Asteroids and Impacts 16
I.4.1. Apophis (99942) 16
I.4.2. Shiva (Aten) 18
I.4.3. Apollyon (Apollo) 21
I.4.4. Comet S-T (Nearly-isotropic comet) 24

I.5. Minimum Deflection Distance 25

I.6. Chapter Summary 26

ON THE DEFLECTION OF THREATENING ASTEROIDS 28

II.1. Nuclear Interceptor 29
II.1.1. Debris 30
II.1.2. Radiation 31
II.1.3. Total Achieved δv 35
II.1.4. Optimal Stand-off Distance 36
II.1.5. Model Final Remarks 38
II.1.6. Spacecraft System Definition 39
II.1.7. Nuclear Interceptor Mission Sizing 39

II.2. Kinetic Impactor 42
II.2.1. Kinetic Impactor Mission Sizing 42

II.3. Spacecraft Propulsion 44
II.3.1. Scheduled Low Thrust Model 45
II.3.2. Efficiency of the Scheduled Thrust 48
II.3.3. Analysis of Alternative Pushing Methods 50
II.3.4. Low Thrust Deflection Mission Sizing 52

II.4. Mass Driver 53
II.4.1. Mass Driver Model 54
II.4.2. Mass Driver Mission Sizing 55

II.5. Solar Collector 56
II.5.1. Spacecraft Model 57
II.5.2. Thermal Model of an Asteroid 57
II.5.3. Rate of Expelled Mass 59
II.5.4. Total Induced Acceleration 60
II.5.5. Influence of the Asteroid Spinning Rate 61
II.5.6. Solar Collector Mission Sizing 62

II.6. Gravity Tractor 65
II.1.1. System Definition & Architecture 66
II.1.2. Gravity Tractor Mission Sizing 69

II.7. Chapter Summary 70

HAZARD DEFLECTION MISSIONS 72

III.1. Asteroidal Hazard 73
III.1.1. Multi-criteria Optimization Problem Formulation 73
III.1.2. Objective Function Definition 74
III.1.3. Missions to Apophis 77
Pareto Contour Lines 80
III.1.4. Missions to Shiva 82
Pareto Contour Lines 84
III.1.5. Missions to Apollyon 85
Pareto Contour Lines 87
III.1.6. Strategy Comparison 88
III.1.7. Influence of the Technology Readiness Level 92
TRL Allocation 94

III.2. Cometary Hazard 99

III.3. Chapter Summary 105

ON THE CONSEQUENCES OF A FRAGMENTATION DUE TO A NEO MITIGATION STRATEGY 107

IV.1. Fragmentation of Asteroids 108

IV.2. NEO Deflection Requirements 111
IV.2.1. Minimum Change of Velocity 112
IV.2.2. Kinetic Impactor & Nuclear Interceptor 114

IV.3. Statistical Model of a Fragmented Asteroid 117
IV.3.1. Fragmented Asteroid Dispersion 117
Invariance of the volume element of the phase space 118
Transition Matrix 120
Probability to find a particle in a particular position 121
IV.3.2. Velocity Dispersion Model 123

IV.4. On the Nature of the Cloud of Fragments 126
IV.4.1. Time Evolution of the Cloud of Fragments 127
IV.4.2. Fragment size distribution 135
IV.4.3. Gravity Re-accumulation 138

IV.5. Consequences of a Fragmentation 142
IV.5.1. Average Predicted Fragments and Impacts: SKE=500 J/kg 145
IV.5.2. Expected Damage 150
IV.5.3. Other Scenarios Analysed 157
Barely catastrophic fragmentation with 100 J/kg 159
Catastrophic fragmentations with 1000 J/kg 161
Highly catastrophic fragmentations with 5000 J/kg 163

IV.6. Chapter Summary 165

CONCLUSIONS 167

V.1. Summary of the Research Results 167
V.1.1. Conclusions 170

V.2. Further Research 171

APPENDICES 173

A.1. Deflection Formulas 173
A.1.1. Gauss' Variational Equations 173
A.1.2. Proximal Motion Equations 175
A.1.3. Accuracy of the Proximal Motion 176
A.1.4. State Transition Matrix 179
A.1.5. Optimal Deflection Direction 180

A.2. Nuclear Interceptor Appendices 181
A.2.1. Further derivations 181
A.2.2. Model Uncertainties in Composition and Radiative Energy 183
A.2.3. Model Uncertainties with asteroid shape 185

A.3. Solar Collector Appendices 186
A.3.1. Expelled Mass Integration 186

A.4. Appendices on the Consequences of Asteroid Fragmentation 188
A.4.1. Expelled Mass Integration 188

A.5. Bibliography 192

List of Figures

Introduction to the asteroidal and cometary impact hazard

FIG. I-1 IMAGES TAKEN BY GALILEO SPACECRAFT 4
FIG. I-2 NEAR EARTH ASTEROID FAMILIES 7
FIG. I-3 ACCUMULATIVE SIZE DISTRIBUTION OF NEAR EARTH OBJECTS 10
FIG. I-4 DIAGRAM OF TORINO SCALE RISK CATEGORIES 13
FIG. I-5 HISTOGRAMS OF THE 100 ATEN 19
FIG. I-6 HISTOGRAMS OF THE 100 APOLLO. 22
FIG. I-7 DENSITY DISTRIBUTION OF THE OBJECTS IN THE APOLLO LIST 23

On the Deflection of Threatening Asteroids

FIG. II-1 GEOMETRIC DIAGRAM OF THE SPACECRAFT DETONATION AND ASTEROID. 34
FIG. II-2 INTEGRATION OVER THE SPHERICAL CAP. 34
FIG. II-3 CHANGE IN VELOCITY OF ASTEROID *APOPHIS*. 35
FIG. II-4 RADIATION ANALYSIS 36
FIG. II-5 OPTIMAL ALTITUDE OF DETONATION. 37
FIG. II-6 TOTAL DELTA-V AND CONTRIBUTIONS OF THE NI ATTEMPTING TO DEFLECT *COMET S-T*. 38
FIG. II-7 NUCLEAR INTERCEPTOR DRY MASS REQUIRED FOR MINIMUM DEFLECTION 41
FIG. II-8 IMPACTOR MASS REQUIRED TO ACHIEVE THE MINIMUM DEFLECTION. 43
FIG. II-9 TOTAL IMPULSE AND DEVIATION ACHIEVED FOR A VARYING α 47
FIG. II-10 ASTEROID ORBITAL FRAMES 48
FIG. II-11 AVERAGED SCATTERING FACTOR 50
FIG. II-12 COMPARISON AMONG THREE POSSIBLE LOW-THRUST STRATEGIES 51
FIG. II-13 MASS REQUIRED FOR A LOW THRUST DEFLECTION MISSION 53
FIG. II-14 MULTI-MASS DRIVER CONCEPT FROM *J. OLDS ET AL* 54
FIG. II-15 MASS DRIVER SIZE REQUIRED TO DEFLECT EACH ONE OF THE STUDIED CASES 56
FIG. II-16 ENERGY LOSS AND THRUST FOR A 100-METER DIAMETER MIRROR. 61
FIG. II-17 DEVIATION AS A FUNCTION OF THE ROTATIONAL SPEED 62
FIG. II-18 MINIMUM DIAMETER OF THE SC ABLE TO DEFLECT A THREATENING ASTEROID. 64
FIG. II-19 MINIMUM MASS OF THE SC ABLE TO DEFLECT A THREATENING ASTEROID 65
FIG. II-20 GEOMETRIC DIAGRAM OF THE GRAVITY TUG AND ASTEROID CONFIGURATION . 66
FIG. II-21 COMPARISON BETWEEN LOW THRUST MITIGATION MISSION AND GRAVITY TUG 69
FIG. II-22 MASS REQUIRED FOR A GRAVITY TUG DEFLECTION MISSION 70

Hazard Deflection Missions

FIG. III-1 PARETO SETS FOR THE SIX DEVIATION METHODS APPLIED TO *APOPHIS*. 79
FIG. III-2 CONTOUR LINES FOR A 13,720 KM DEFLECTION OF *APOPHIS* 81
FIG. III-3 PARETO SETS FOR THE SIX DEVIATION METHODS APPLIED TO $SHIVA_3$ 83
FIG. III-4 CONTOUR LINES FOR A 9,690 KM DEFLECTION OF *SHIVA* ASTEROIDS 84
FIG. III-5 PARETO SETS FOR THE SIX DEVIATION METHODS APPLIED TO $APOLLYON_3$ 86
FIG. III-6 CONTOUR LINES FOR AN 8,202 KM DEFLECTION OF *APOLLYON* ASTEROIDS 88
FIG. III-7 *TRL* MAPPING INTO REQUIRED DEVELOPMENT EFFORT 94
FIG. III-8 HISTOGRAMS OF THE NEAR EARTH COMETS 100
FIG. III-9 MINIMUM REQUIRED ΔV FOR A $\varepsilon \cdot R_{\oplus}$ DEFLECTION 101
FIG. III-10 INTERCEPTION MASS OF THE DEFLECTION MISSION TO MITIGATE *COMET S-T*. ... 102
FIG. III-11 INTERCEPTION TRAJECTORY ΔV 103
FIG. III-12 MINIMUM TRAJECTORY ΔV AND MASS IN SPACE FOR A NI 104
FIG. III-13 PARETO SETS FOR THE NI APPLIED TO ASTEROID *COMET S-T* 105

FIG. IV-1 ESTIMATES OF THE CRITICAL SPECIFIC ENERGY Q^* 109
FIG. IV-2 CRITICAL SPECIFIC ENERGY Q^* FROM 40M TO 1KM IN DIAMETER 110
FIG. IV-3 MINIMUM REQUIRED ΔV FOR A $\varepsilon \cdot R_{\oplus}$ DEFLECTION 113
FIG. IV-4 MINIMUM SKE REQUIRED FOR A DEFLECTION MISSION WITH 5,000KG 115
FIG. IV-5 SNE PROVIDED BY ATTEMPTING TO DEFLECT A THREATENING ASTEROID 116
FIG. IV-6 VOLUME ENCLOSING 97% PROBABILITY TO FIND A FRAGMENT 128
FIG. IV-7 VOLUME ENCLOSING 97% PROBABILITY TO FIND A FRAGMENT 129
FIG. IV-8 VOLUME ENCLOSING 97% PROBABILITY TO FIND A FRAGMENT 130
FIG. IV-9 SCHEMATIC OF THE 4 FEATURES OF AN ELLIPSOIDAL CLOUD 131
FIG. IV-10 EVOLUTION OF THE FEATURES DEFINING THE ELLIPSOIDAL CLOUD 132
FIG. IV-11 RELATIVE MOTION TRAJECTORIES 133
FIG. IV-12 EVOLUTION OF THE PROBABILITY DENSITY $P(\mathbf{x};t)$ 135
FIG. IV-13 NUMBER OF PIECES EXPECTED TO BE FOUND IN A FRAGMENTATION 137
FIG. IV-14 PERCENTAGE OF FRAGMENTS ESCAPING THE GRAVITATIONAL FIELD OF THE LARGEST FRAGMENT (*APOPHIS*) 141
FIG. IV-15 PERCENTAGE OF FRAGMENTS ESCAPING THE GRAVITATIONAL FIELD OF THE LARGEST FRAGMENT (*SHIVA*$_3$ AND *APOLLYON*$_3$) 142
FIG. IV-16 IMPACT LIKELIHOOD FOR ALL THE TEST CASES 143
FIG. IV-17 IMPACT LIKELIHOOD MAPPING INTO MINIMUM REQUIRED δv 145
FIG. IV-18 EVOLUTION OF THE IMPACT LIKELIHOOD FOR DIFFERENT FRAGMENT SIZES 148
FIG. IV-19 AVERAGE NUMBER OF IMPACTS 149
FIG. IV-20 DAMAGE EVOLUTION OF A FRAGMENTATION OF *APOPHIS* 154
FIG. IV-21 DAMAGE RATIOS OF *APOPHIS* 155
FIG. IV-22 DAMAGE RATIOS OF *SHIVA*$_3$ AND *APOLLYON*$_3$ 156
FIG. IV-23 DAMAGE RATIOS OF *APOPHIS*, *SHIVA* AND *APOLLYON* FOR 100J/KG 160
FIG. IV-24 DAMAGE RATIOS OF *APOPHIS*, *SHIVA* AND *APOLLYON* FOR 1000J/KG 162
FIG. IV-25 DAMAGE RATIOS OF *APOPHIS*, *SHIVA* AND *APOLLYON* FOR 5000J/KG 164

Appendices

FIG. A-1 DEFLECTION ERROR APPLIED TO *SHIVA* 176
FIG. A-2 DEFLECTION RELATIVE ERROR APPLIED TO *SHIVA*. 177
FIG. A-3 DEFLECTION ERROR APPLIED TO *APOLLYON*. 177
FIG. A-4 DEFLECTION RELATIVE ERROR APPLIED TO *APOLLYON*. 178
FIG. A-5 DEFLECTION RELATIVE ERROR APPLIED TO *COMET S-T* 178
FIG. A-6 DEVIATION ACHIEVED ON *SHIVA* WITH $||\Delta V||$=0.01 M/S. 180
FIG. A-7 SCHEMATIC OF THE GEOMETRY BEHIND THE INTEGRATION IN EQ.(2.13) 181
FIG. A-8 SURFACE INTEGRATION USING THE SPHERICAL CAP SURFACE 182
FIG. A-9 TOTAL ACHIEVED CHANGE OF VELOCITY OF ASTEROID *APOPHIS* 185
FIG. A-10 EFFICIENCY OF THE NUCLEAR DEFLECTION FOR AN ELONGATED BODY 186
FIG. A-11 CALCULATED "AVERAGE" K 191
FIG. A-12 HISTOGRAM OF CONSTANT *K* 192

List of Tables

Introduction to the asteroidal and cometary impact hazard

TABLE I-1 SUMMARY OF THE MOST COMMON CLASSES OF ASTEROID FROM THOLEN'S TAXONOMY 6
TABLE I-2 TOTAL NUMBER OF NEO KNOWN AT 16TH DECEMBER 2008. 11
TABLE I-3 KEPLERIAN ELEMENTS USED IN THIS STUDY FOR (99942) *APOPHIS* 17
TABLE I-4 PHYSICAL CHARACTERISTICS USED IN THIS STUDY FOR (99942) *APOPHIS* 17
TABLE I-5 KEPLERIAN ELEMENTS USED FOR *SHIVA*. 20
TABLE I-6 *SHIVA* GROUP OF IMPACTORS AND THEIR PHYSICAL CHARACTERISTICS 20
TABLE I-7 KEPLERIAN ELEMENTS USED FOR *APOLLYON* 23
TABLE I-8 *APOLLYON* GROUP OF IMPACTORS AND THEIR PHYSICAL CHARACTERISTICS 24
TABLE I-9 KEPLERIAN ELEMENTS USED FOR *COMET S-T*. 25
TABLE I-10 *COMET S-T* AND ITS PHYSICAL CHARACTERISTICS 25
TABLE I-11 HYPERBOLIC FACTOR AND MINIMUM DEFLECTION DISTANCE. 26

On the Deflection of Threatening Asteroids

TABLE II-1 ENERGY DISTRIBUTION 30
TABLE II-2 VALUES FOR OPACITY AND ABSORPTION CALCULATED FOR FORSTERITE. 32
TABLE II-3 ITOKAWA(25143) INFORMATION 46

Hazard Deflection Missions

TABLE III-1 DESIGN MARGINS FOR THE SPACECRAFT MASS 76
TABLE III-2 SEARCH DOMAIN FOR THE MULTI-OBJECTIVE ANALYSIS 77
TABLE III-3 STRATEGY DOMINANCE FOR *APOPHIS* 90
TABLE III-4 STRATEGY DOMINANCE FOR $SHIVA_1$ 90
TABLE III-5 STRATEGY DOMINANCE FOR $SHIVA_2$ 90
TABLE III-6 STRATEGY DOMINANCE FOR $SHIVA_3$ 90
TABLE III-7 STRATEGY DOMINANCE FOR $SHIVA_4$ 90
TABLE III-8 STRATEGY DOMINANCE FOR $APOLLYON_1$ 91
TABLE III-9 STRATEGY DOMINANCE FOR $APOLLYON_2$ 91
TABLE III-10 STRATEGY DOMINANCE FOR $APOLLYON_3$ 91
TABLE III-11 STRATEGY DOMINANCE FOR $APOLLYON_4$ 91
TABLE III-12 TECHNOLOGY READINESS LEVELS. 93
TABLE III-13 TRL AND ΔT_{DEV} FOR ALL THE DEVIATION METHODS 98
TABLE III-14 STRATEGY DOMINANCE FOR *APOPHIS* 99
TABLE III-15 STRATEGY DOMINANCE FOR $SHIVA_3$ 99
TABLE III-16 STRATEGY DOMINANCE FOR $APOLLYON_3$ 99

On the Consequences of a Fragmentation due to a NEO Mitigation Strategy

TABLE IV-1 SUMMARY OF THE ORBITAL CHARACTERISTICS OF THE FOUR CASES 112
TABLE IV-2 FRAGMENT GROUPS FOR THE COMPUTATION OF IMPACT LIKELIHOOD AND AVERAGE NUMBER OF IMPACTS WITH F_R EQUAL TO 0.5, 0.25 AND 0.1 146
TABLE IV-3 EXPECTED DAMAGED AREA FOR *APOPHIS*. 151
TABLE IV-4 EXPECTED DAMAGED AREA FOR *SHIVA*. 151
TABLE IV-5 EXPECTED DAMAGED AREA FOR *APOLLYON*. 152
TABLE IV-6 SUMMARY OF ALL THE SIMULATED FRAGMENTATION SCENARIOS 158
TABLE IV-7 APPROXIMATE FRAGMENT CENSUS FOR A FRAGMENTATION WITH 100 J/KG. . 159
TABLE IV-8 APPROXIMATE FRAGMENT CENSUS FOR FRAGMENTATIONS WITH 1000 J/KG.. 161
TABLE IV-9 APPROXIMATE FRAGMENT CENSUS FOR FRAGMENTATIONS WITH 5000 J/KG.. 163

Appendices

TABLE A-1 APPROXIMATE MAXIMUM ERROR COMMITTED BY THE ASSUMPTIONS IN COMPOSITION AND RADIATION WAVELENGTH 184
TABLE A-2 30 EXPERIMENTS FROM *DAVIS & RYAN*. 188
TABLE A-3 30 EXPERIMENTS FROM *DAVIS & RYAN* 189

Nomenclature & Definitions

List of Abbreviations

NEO/A	=	Near Earth Object/Asteroids
K-T	=	Cretaceous-Tertiary
MOID	=	Minimal Orbital Intersection Distance
IEO	=	Interior Earth Orbit
NEC	=	Near Earth Comet
PHO/A	=	Potentially Hazardous Objects/Asteroids
JPL	=	Jet Propulsion Laboratory
MJD2000	=	Modified Julian Days counted since 1st January 2000 at 12:00 p.m.
TRL	=	Technology Readiness Level

List of Nomenclatures

Chapter I: Introduction to the Asteroidal and Cometary Hazard

a	=	semi-major axis of an orbit, km or AU
r_p	=	periapsis of an orbit, km or AU
r_a	=	apoapsis of an orbit, km or AU
N	=	number of objects
D	=	diameter, km or m
H	=	absolute magnitude
p_v	=	albedo
f	=	impact frequency, yr^{-1}
P	=	Palermo index
IP	=	impact probability
$R_\oplus$	=	Earth' radii (6,378.1 km)
e	=	eccentricity of an orbit
i	=	inclination of an orbit, deg
Ω	=	argument of the ascending node of an orbit, deg
ω	=	argument of the perigee of an orbit, deg
M	=	mean anomaly of an orbit, deg
t_{MOID}	=	time at the Minimum Orbit Interception Distance point, also referred as virtual impact time, MJD2000
ε	=	hyperbolic correcting factor
μ_e	=	gravitational constant of the Earth (398,600.441 km^3/s^2)
v_∞	=	the hyperbolic excess velocity, km/s

Chapter II: On the Deflection of Threatening Asteroids

m_{debris}	=	mass of the nuclear interceptor's debris that impacts the asteroid, kg
S	=	fraction of area of the shock wave that intersects the asteroid
m_i	=	mass of the spacecraft at the Near Earth Object arrival, kg
λ	=	asteroid central angle, deg
R_a	=	mean radius of the Near Earth Object, m

H	=	altitude of detonation of the nuclear interceptor, m
v_{debris}	=	velocity of the debris from the nuclear Interceptor, m/s
f_{xxx}	=	fraction of delivered energy in the form indicated by the subscript
$\delta \mathbf{v}_{xxx}$	=	impulsive change of velocity produced as indicated by the subscript, m/s
β	=	momentum enhancement factor
S_{sc}	=	scattering factor
M_a	=	mass of the asteroid, kg
E_A	=	received energy per unit area, J/m^2
m_A	=	mass per unit area, kg/m^2
z	=	asteroid depth, m
ρ_a	=	mean density of the asteroid, g/cm^3
μ_o	=	opacity of a material to a certain radiation, m^2/kg
μ_en	=	mass-absorption coefficient of a material to a certain radiation, m^2/kg
K	=	*kerma* or Kinetic Energy Released in the Material, J/kg
E_v	=	energy of sublimation, J/g
v_e	=	excess velocity of the expelled or sublimated material, m/s
p_A	=	linear momentum per unit area, kg/s/m
Z_max	=	maximum radiation depth, m
ε	=	elevation angle, deg
m_exp	=	mass of sublimated asteroid's material, kg
E_t	=	total energy released by the nuclear interceptor, J
h	=	distance from the nuclear explosion to a specific point on the surface of the asteroid, m
m_d	=	dry mass of the spacecraft, kg
m_wh	=	mass of the nuclear warhead, kg
YTW	=	yield-to-weight ratio of the nuclear device, kTons/ kg
t_w	=	warning time defined as $t_{MOID} - t_\text{int}$, d
t_int	=	NEO interception time, d
$\Delta \mathbf{v}_{S/C}$	=	impact relative velocity of the spacecraft with respect to the asteroid, m/s or km/s
T_n	=	thrust, N
m_power	=	mass of the power subsystem, kg
τ	=	mass-to–power ratio, kg/W
ξ	=	specific thrust, N/W
t	=	time, d or s
I_t	=	total impulse produced by a propulsion system, Ns
F	=	force, N
t_push	=	total duration of the deflection (pushing) manoeuvre, d or s
I_sp	=	specific impulse of a propulsion system, s
g_0	=	standard free fall constant, 9.81 m/s^2
$\hat{v}$	=	unit vector along the asteroid orbital velocity
ϖ	=	asteroid complementary latitude, deg
ϕ	=	asteroid obliquity angle, deg
P_K	=	kinetic power provided by the mass driver, W
m_launch	=	mass expelled per shot by the mass driver method, kg
$\Delta t_{shooting}$	=	time available to shoot the dug material, s
P_solar	=	radiation power density on the illuminated surface of the asteroid, W/m^2
A_m	=	cross section area of the mirror, m^2
A_s	=	area of the illuminated spot, m^2
η_eff	=	efficiency of the mirror assembly
S_flux	=	solar flux at 1 AU, 1367 W/m^2
r_fi	=	distance from spacecraft to the Sun, km

T	=	temperature, K
T_{subl}	=	sublimation temperature, K
c	=	heat capacity, J/kg/K
k	=	thermal conductivity, W/m/K
$erfc(f(x))$	=	complementary error function of f(x)
Q_{cond}	=	heat flux loss by conduction, W/m^2
Q_{rad}	=	heat flux loss by radiation, W/m^2
σ	=	Stefan-Boltzmann constant, 5.67051×10^{-8} $W/m^2/K^4$
ε_{bb}	=	black body emissivity
v_{rot}	=	rotational velocity of the asteroid equatorial surface, m/s
$\bar{V}$	=	average velocity of evaporated particles, m/s
M_m	=	molecular mass, kg
a_{solar}	=	acceleration achieved by the asteroid due to material ablation, m/s^2
F_g	=	gravity attraction between the spacecraft and the asteroid, N
F_{hover}	=	effective vertical thrust, N
d	=	hovering distance, m
ϕ_{ex}	=	exhaust cone half-angle, deg
G	=	universal gravitational constant, 6.67259×10^{-11} $m^3/kg/s^2$

Subscripts

$()_0$	=	initial
$()_f$	=	final

Chapter III: Hazard Deflection Missions

t_l	=	launch date, MJD2000
t_w	=	warning time defined as $t_{MOID} - t_l$, d
m_0	=	mass launched into space, kg
$\Delta\mathbf{r}$	=	vector distance at the Minimum Orbit Interception Distance, km
$\delta\mathbf{r}$	=	deviation vector in the Hill coordinate frame, km
t_{dev}	=	time required to upgrade the TRL of a given method, man-years
ToF	=	time of flight, d

Chapter IV: On the Consequences of a Fragmentation Due to a NEO Mitigation Strategy

Q^*	=	barely catastrophic disruption critical specific energy, J/kg
f_r	=	fragmentation ratio
m_{max}	=	mass of the largest fragment, kg
v_{impact}	=	asteroid impact velocity, km/s
SKE	=	specific kinetic energy of a kinetic impact mitigation, J/kg
SNE	=	specific nuclear energy of a nuclear interception mitigation, J/kg
$\mathbf{X}(t)$	=	state vector of positions $\mathbf{x}$ and velocities $\mathbf{v}$ at time t, km and km/s
$\rho(\mathbf{X})$	=	probability density
$\phi^{\Delta t}(\mathbf{X}(t))$	=	dynamical *flux* of the system that propagates $\mathbf{X}(t)$ a given Δt
$d\Xi(t)$	=	differential of volume of phase space at time t
$\mathbf{J}$	=	jacobian matrix
$\mathbf{q}$	=	vector of generalized coordinates
$\mathbf{p}$	=	vector of generalized momenta
$H(\mathbf{q},\mathbf{p})$	=	Hamiltonian
$\mathbf{A}$	=	asymmetric square matrix for a 6-D state vector $\mathbf{Q}(t) = (\mathbf{q}(t), \mathbf{p}(t))$

$\mathbf{\Phi}(t,t_0)$	=	state transition matrix
$P(\mathbf{x};t)$	=	probability to find a fragment in a relative position $\mathbf{x}$ at a time t
$\delta(\mathbf{x}-\mathbf{r_0})$	=	probability of a particular fragment to have position $\mathbf{x}-\mathbf{r_0}$
$\mathbf{r}_0$	=	initial position of the centre of mass of the unfragmented asteroid, km
$G(\mathbf{v}(0))$	=	probability that a given fragment has velocity $\mathbf{v}(0)$
$\hat{t}$	=	orbit's tangential direction
$\hat{n}$	=	orbit's normal direction
$\hat{h}$	=	orbit's out-of-plane direction
$\boldsymbol{\mu}$	=	mean velocity vector of a fragment, m/s
$\boldsymbol{\sigma}$	=	standard deviation vector of a fragment, m/s
k	=	efficiency of transmission of the collisional energy constant
b	=	exponent of the power law distribution
v_{esc}	=	escape velocity of a fragment, km/s
r_i	=	minimum distance between the centres of the fragment i and the largest fragment, km

Subscripts

$()_t$	=	vector component tangent to the orbit
$()_n$	=	vector component normal to the orbit in the orbit plane
$()_h$	=	vector component normal to the orbit plane

Appendices

μ	=	gravitational constant $G \cdot m$, km^3/s^2
b	=	semi-minor axis of an orbit, km
p	=	semilatus rectum of an orbit, km
n	=	angular velocity of an orbit, s^{-1}
v	=	orbital velocity, km/s

Chapter I

Introduction to the Asteroidal and Cometary Impact Hazard

Asteroidal and cometary impact hazard is very easily taken either too earnestly or too jestingly, especially among people who are not acquainted with the problem. Hence, among all possible life threatening hazards, this prospect, more than any other, requires facts and numbers to lean on to avoid a subjective perspective. The so-called "giggle factor[1]", for example, is the name that scientists in this field gave to the recurrent hilarity generated when discussing impact hazard mitigation. The same reaction would have been unthinkable if discussing epidemic mitigation. The other end of the reaction scale is, as well, common, especially after the discovery of asteroid Apophis(99942) and its large diffusion in the popular media. On a general chat about impact hazard, one can realize that people generally feel more afraid of asteroidal impact than of other more earthly risks such as electrocution, even when statistically there are more than 4 times more chances of being victims of electrocution than of an asteroid impact[2]. Obviously impact hazard causes irrational fear. Cometary and asteroidal impacts have been playing a very active role in the Earth's geological and biological history and at least one mass extinction is thought to have been caused by a celestial collision[3]. This, of course, happens in a time scale that is measured in tens of millions of years, but, as humans, we seem to have a better capability to grasp a global effect collision than understanding 100,000,000 years of time. This first chapter will aim to present the facts that will allow the reader to have a better perspective and understanding of the problem.

I.1. Historical Recognition of the Impact Hazard

The first recognition of the threat posed by extraterrestrial bodies dates back to the last decade of the 17th century, when Edmund Halley suggested that cometary impacts may have caused global catastrophes on Earth. He conjectured about this cosmic threat not long after predicting the 76-years return of a comet known today as Comet Halley. Nevertheless, the notion of asteroid did not yet exist and it would take another 200 years before it would enter the domain of astronomy.

Astronomers started finding celestial bodies with orbits between Jupiter and Mars at the beginning of 19th century, following the hint given by the *Titus-Bode Law*[1], which predicted the "gap" between these two planets as an allowable position to discover new planets in the solar system. This series of newly discovered 'planets', such as Ceres, Vesta and Pallas, remained points of light even under the highest telescope magnifications, instead of resolving into discs as other planets did. William Herschel, discoverer of Uranus, was the first in suggesting a new category for these new celestial bodies. He called them asteroids, after the Greek asteroeides, meaning "star-like".

The first Mars-crossing asteroid was discovered in 1898 and named Eros, following the tradition of naming asteroidal objects after Roman or Greek deities. It took another 34 years to catch sight of the first Earth-crossing asteroid, named 1862 Apollo. This occurred in 1932, only a few years after the Odessa Crater in Texas became the first proven impact crater on Earth[4].

The first efforts on estimating asteroidal and cometary impact rates came from Fletcher Watson[5] during the 40s and Ernst Julius Öpik[6] during the 50s. It was the latter together with Ralph Baldwin[7], a leading figure in the history of lunar geology, who first envisaged the damage that an asteroid impact could cause to the Earth.

At the dawn of the space era, the first interplanetary missions confirmed E.J. Öpik's visions of moon-like cratered surfaces on other planets of the solar system. In July 1965, Mariner-4 flew over Mars, sending back pictures showing an uninhabited cratered surface, a very disappointing view for most of the science-fiction readers of the time. Two decades later Mariner 10 would show similar features on the Mercurian surface and the Voyager probes showed that the same features extended to the satellites orbiting the giant planets in the outer solar system.

[1] A rough rule, formulated by Titus in 1766 and Bode in 1778, that predicts the spacing of the planets in the solar system.

In 1968, asteroid (1566) Icarus, 1.3km in diameter, performed a close Earth approach of 6 million km distance (more than 16 times the Earth-Moon distance or 0.04 A.U.). The same year, MIT Press published Project Icarus[8], becoming the first ever asteroid hazard mitigation proposal, as a result of an assignment set to a group of students at the Massachusetts Institute of Technology. The report hypothesised on an attempt to deflect or destroy asteroid Icarus using six 100-Megaton hydrogen bombs launched in sequence from the Kennedy Space Center by six Saturn V rockets. This project inspired the movie "Meteor", premiered in 1979 and starring Sean Connery.

Rendezvous with Rama, the acclaimed novel by Arthur C. Clark, was published in 1972. The novel described an early asteroid warning program called "Project Spaceguard", which is set up after a fictional asteroid strikes Italy on September 11, 2077, destroying Padova and Verona and sinking Venezia. The term "Project Spaceguard" was later adopted for several international efforts in NEO detection and study.

Despite the aforementioned examples, the modern awareness of the hazard began to materialize with the publication of Alvarez *et al.*'s famous work, which presented their hypotheses for the dinosaur extinction[3]. The "*Extraterrestrial Cause for the Cretaceus-Terciary Extinction*" was published in 1980, advocating that an asteroid of 10 $\pm$ 4 km in diameter could have been the cause of the K-T extinction, 65 million years ago. This hypothesis was further strengthened after being linked with the Chicxulub crater in Mexico's Yucatan peninsula.

In 1992, NASA produced the "*Spaceguard Survey Report*" after a request from U.S. Congress. The document described an international survey network of ground-based telescopes with the goal of locating 90% of the large Near-Earth Objects (i.e., >1 km in diameter) within 25 years, instead of the two centuries that it would have taken at the discovery rate of the time.

The dramatic impact on Jupiter of comet Shoemaker-Levy 9, on July of 1994, received substantial coverage from popular media all around the world. The comet was discovered by Carolyn S. Shoemaker, her husband, Eugene Merle Shoemaker, and David H. Levy a year before the impact. At least 21 cometary fragments, with diameters up to 2 kilometres, caused massive explosions that were easily seen by the Galileo spacecraft (Fig. I-1) and left visible scars on Jupiter for many months. One of the consequences of this striking event was the redefinition of the Spaceguard survey with the so-called Shoemaker

Report, which recommended a 10-years program to complete the previous proposed survey. NASA publicly supported this program in 1998.

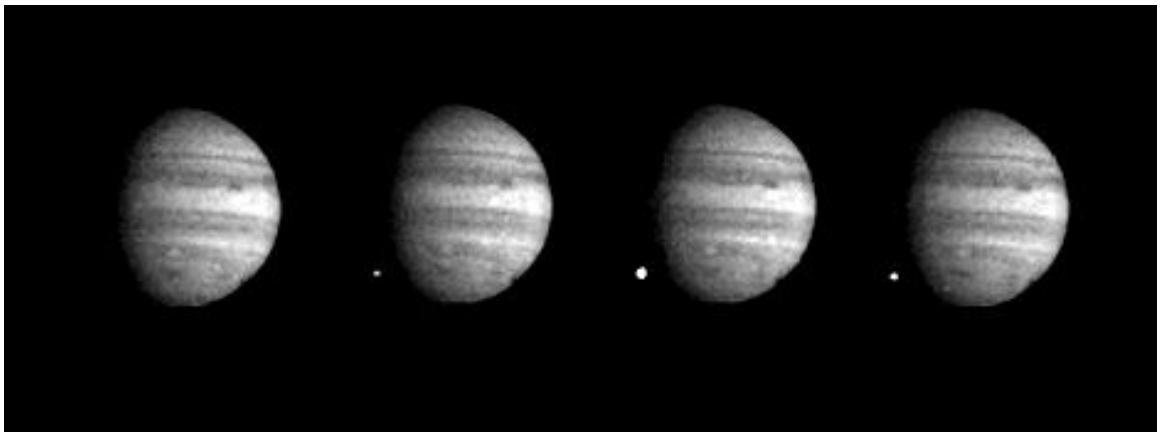

Fig. I-1 Sequence of images taken by Galileo spacecraft showing the fireball caused by the impact of 1 of the 21 fragments of comet Shoemaker-Levy 9 that fell into Jupiter on July 1994.

In 1995, the Vulcano Workshop, organized by the International Astronomical Union, set up the basis for the Spaceguard Foundation, the first organization whose only objective is to promote the international efforts in NEO discovery, follow-up and study. At present, the organization is based in Rome, and coordinates more than 70 observatories.

In 2000, the UK Government set up a Task Force on Potentially Hazardous NEOs, whose goal is to make proposals to the UK government on how the United Kingdom should best contribute to international effort on Near Earth Objects. The Task Force presented a report[9] in September 2000. The UK Government provided an initial response in February 2001, creating the NEO information centre, the first governmental organization solely dedicated to the impact hazard.

The release in 1998 of two Hollywood blockbusters, Armageddon and Deep Impact, featuring asteroid impacts and the possibility of extinction for human civilization, fertilized the terrain for the immense following in the popular media of the discovery of (99942) Apophis. Asteroid Apophis was discovered in December 2004 and caused a brief period of concern due to the unprecedented high risk that this object involved. Initially, a possible impact with the Earth was calculated for 2029, with a probability of 2.5%. Following further orbit determination the impact on 2029 was ruled out, but currently there is still a possibility of a resonant return with an impact on 2036, having less than 1 in 45,000 chances.

I.2. Near Earth Objects

By convention, a celestial body is considered a Near Earth Object (NEO) if its perihelion is smaller than 1.3 A.U and its aphelion is bigger than 0.983 A.U. This is a very broad definition that can be further divided in different sub-groups depending on the object's orbital parameters. The most obvious subdivision is between asteroids and comets, which not only have very different orbital attributes, but also differ in physical characteristics and astrodynamical history.

I.2.1. Asteroids and Near Earth Asteroids (NEAs)

Asteroids are small celestial bodies, ranging from dust-sized fragments to ten-kilometre objects, remnants of the formation of the solar system, prevented from aggregating into a planet-size body by the gravitational influence of the giant planets. Most asteroids are in fairly stable orbits between Mars and Jupiter, the so-called Asteroid Belt, containing about a million objects with a combined mass of only 1/1000 the mass of the Earth.

The dynamics of these bodies are strongly influenced by a combination of close encounters with other planets, resonant dynamics and Yarkovsky effect. A common storyline for many Earth-crossing asteroids began in the main asteroid belt, slowly drifting away from a quasi-stable orbit due to the Yarkovsky thermal force. At some point the drifting asteroid entered into a region of powerful dynamic resonances (e.g., ν_6 secular resonance or 3:1 mean motion resonance with Jupiter), rapidly changing its eccentricity enough to reach planet-crossing orbits (i.e., taking between 0.5 million to 1 million years[10]).

The large majority of Earth-crossing and Mars-crossing asteroids, the latter being roughly 4 times more numerous than the former, will end their wandering around the solar system either colliding with the Sun or in an escape hyperbolic orbit. Only a small fraction will strike a planet or a moon.

The taxonomy of asteroids, other than by orbital characteristics, is based on optical properties. It began with a simple color classification and evolved together with the optical sensing to a more complex taxonomy. The most common classification is Tholen's[11] and is based on albedo and spectral characteristics, from which the surface mineralogy is estimated. Table I-1 summarises the most common asteroid categories; among those in the

table, C-type or dark carbonaceous asteroids and S-type or stony silicaceous account for 90% of all the asteroids (i.e., 45% approximately for each class[12]).

Table I-1 Summary of the most common classes of asteroid from Tholen's taxonomy.

Class	Albedo	Surface Mineralogy
C	Low (<0.04)	Hydrated silicates + carbon, organics
D	Low(<0.05)	Carbon and probably organic rich silicates
P	Low	Carbon and probably organic rich silicates
M	Moderate(0.10-0.18)	Metal, possible trace silicates
S	Moderate(~0.14)	Metal + olivine+ pyroxene

Near Earth Asteroids are commonly subdivided in three further groupings depending on their orbital characteristics: the Apollo asteroids ($a \geq 1.0 A.U$; $r_p \leq 1.0167 A.U$), the Atens ($a < 1.0 A.U$; $r_a \geq 0.983 A.U$) and the Amors ($1.0167 A.U < r_p \leq 1.3 A.U$) (see Fig. I-2). A fourth group, the IEO or Interior-to-Earth Orbit, although not "formally" considered part of the NEO group, comprises all the asteroids with trajectories inside the orbit of the Earth ($r_a \leq 0.983 A.U$).

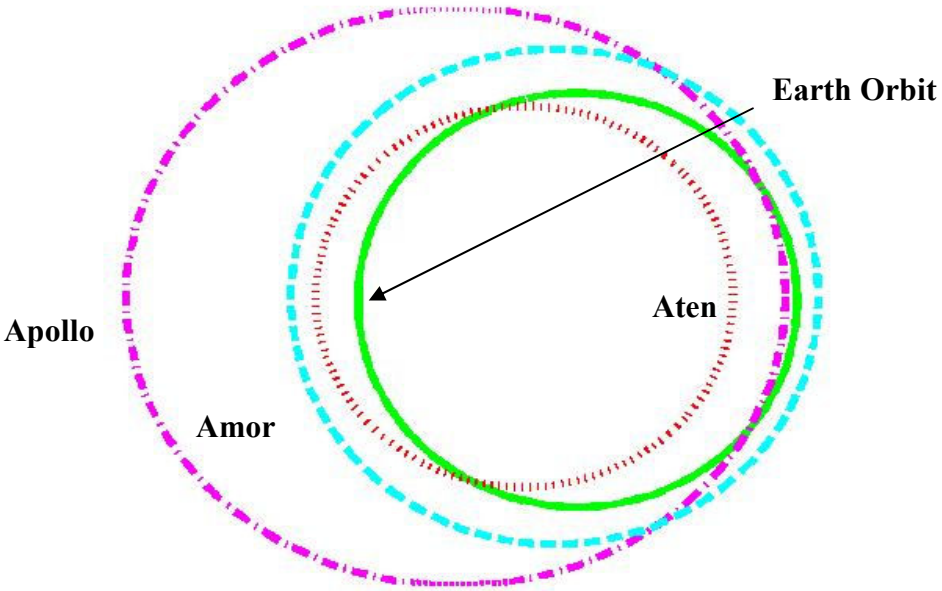

Fig. I-2 Near Earth Asteroid families

The understanding of the NEA population is a challenging undertaking since NEO surveys have been traditionally biased against some kind of orbits that are more easily observed than others and the dynamical evolution of the objects originating from different sources is not fully understood. Debiased models indicate that 32±1% of the NEA population belongs to the Amor group, 62±1% of the NEA are Apollos and 6±1% are Atens[10]. The same models suggest, assuming random values for the argument of the perihelion and the longitude of nodes, that 21% of NEA have a Minimal Orbital Intersection Distance (MOID), i.e., minimum possible closest approach between two objects, smaller than 0.05 A.U.

A Near Earth Object with a MOID smaller than 0.05 A.U. and absolute magnitude (H) smaller than 22 (or in other words an asteroid larger than 150 meters assuming 13% albedo) is considered to be a Potentially Hazardous Object or a PHO. This kind of object deserves special attention and its orbital determination and tracking are considered top priority.

I.2.2. Comets and Near Earth Comets

"Comets are like cats; they have tails, and they do precisely what they want."
-David H. Levy

The Near Earth Object list is not only formed by asteroids, but also by comets. In the past, these objects were distinguished from other celestial objects because of their "tail". Indeed, the word "comet" evolves from the Greek *komē*, meaning "hair of the head",

which makes reference to the hairy look of the comet's tail. Nowadays, knowledge about these objects has changed a good deal from the Aristotelian idea of a meteorological phenomenon, although there is still an intense debate about cometary diversity, formation and evolution[13],[14].

Two distinct cometary groups can be distinguished: the *Nearly-isotropic comets* and the *Ecliptic comets*. The main characteristic of the *Nearly-isotropic comets* is its arbitrary inclination (i.e., typically more than 20^o) and they include two further groups: the *Long-period comets* (T>200 years) and *Halley-type comets* (T< 200 years). The *Ecliptic comets*, on the other hand, have a relatively low inclination (i<20^o) and a short orbital period ($T \leq 20 years$).

The most widely accepted cometary theory alleges that the two main sources of comets are the remote Oort cloud and the trans-neptunian scattered disk[10],[13]. The Oort cloud is a spherical cloud of matter believed to be located approximately at 50,000 A.U from the Sun, which is a quarter of a distance to the closest star. Numerical simulations of the evolution of the early solar system seem to show that the matter orbiting in the Oort cloud was originally formed in the Jupiter-Uranus region and scattered out by gravitational effects. Some of this matter originally scattered from the Jupiter-Uranus region constitutes now the nearly-isotropic cometary family. Besides the Oort cloud, two more orbital regions can be identified outside the orbit of Neptune: the Kuiper Belt, a dynamically stable region ranging from 30 A.U to 50 A.U, where Pluto, the down-graded planet, is found, and a more erratic milieu called the scattered disk that extends approximately from 50 A.U to 100 A.U. This is believed to be the source of the *Ecliptic comets*.

Comets seem to have a large range of physico-chemical properties and their connections with the different dynamical classes or origins are poorly understood. Cometary bodies contain many different volatile materials, e.g. H_2O, HCN, CH_3CN, CO, H_2CO, etc, and the concentration ratio of these materials varies enormously. The most common volatile detected within the comet's out-gassing is water, although there is still an intense debate about how much water is contained in a comet. The two comets explored in situ, comet Tempel 1 and Comet Wild 2, seem to indicate that there is little water on the surface, which resembles an asteroid's surface, both in appearance and composition[15]; thus the main sources of out-gassing water are thought to be sub-surface[16].

The arrival of most comets at the Earth vicinity, in particular for long-period comets, is unpredictable. They are discovered when they are inside the orbit of Jupiter, which

means that the closest Earth approach can occur in less than 9 months after the comet has been discovered and, unlike with asteroids, a realistic comet threat scenario would be driven by a very short warning time. Estimates of the impact flux of long-period comets have been attempted by many authors and through many different techniques and, although different techniques entail different outcomes, a recurrent solution estimates the relative threat of long-period comets as ~1% the threat posed by Near Earth Asteroids[10].

It is interesting to notice that from the beginning of cometary detection, back in 18th century, until nowadays the rate of cometary Earth close approaches discovered has remained almost constant, despite the enormous improvement in telescopes and search technology. This seems to suggest a scarcity of small active comets, since they would have been detected with technological improvements. It is also remarkable that the size distribution of comets larger than 2 km in diameter seems to decrease not as steeply as for asteroids of the same size. It seems therefore possible that most of the large craters on the Moon and the extinction level large impacts on Earth may have in fact been caused by comets[17].

I.2.3. NEO Census and Impact Frequency

Population estimates computed by different authors[10] are shown in Fig. I-3. These estimates have been calculated by extrapolation either from lunar and planetary cratering records or from real survey data. *Stokes et al.* [10] adjusted a constant power law to the population estimates from Fig. I-3, working out an approximated accumulative population equation such as:

$$N(> D[km]) = 942 D^{-2.354} \qquad (1.1)$$

where N is the number of objects with diameter larger than a given diameter D.

From Eq.(1.1), the total population of Near Earth Objects capable of a Tunguska-size atmospheric explosion (~80m diameter) or more destructive consequences is close to 350,000 objects. The current NEO survey programs focus their attention on cataloguing objects larger than 140m diameter, which have a population estimate of around 100,000 objects. This survey of objects with approximately 140m in diameter is expected to be 90% completed by 2020.

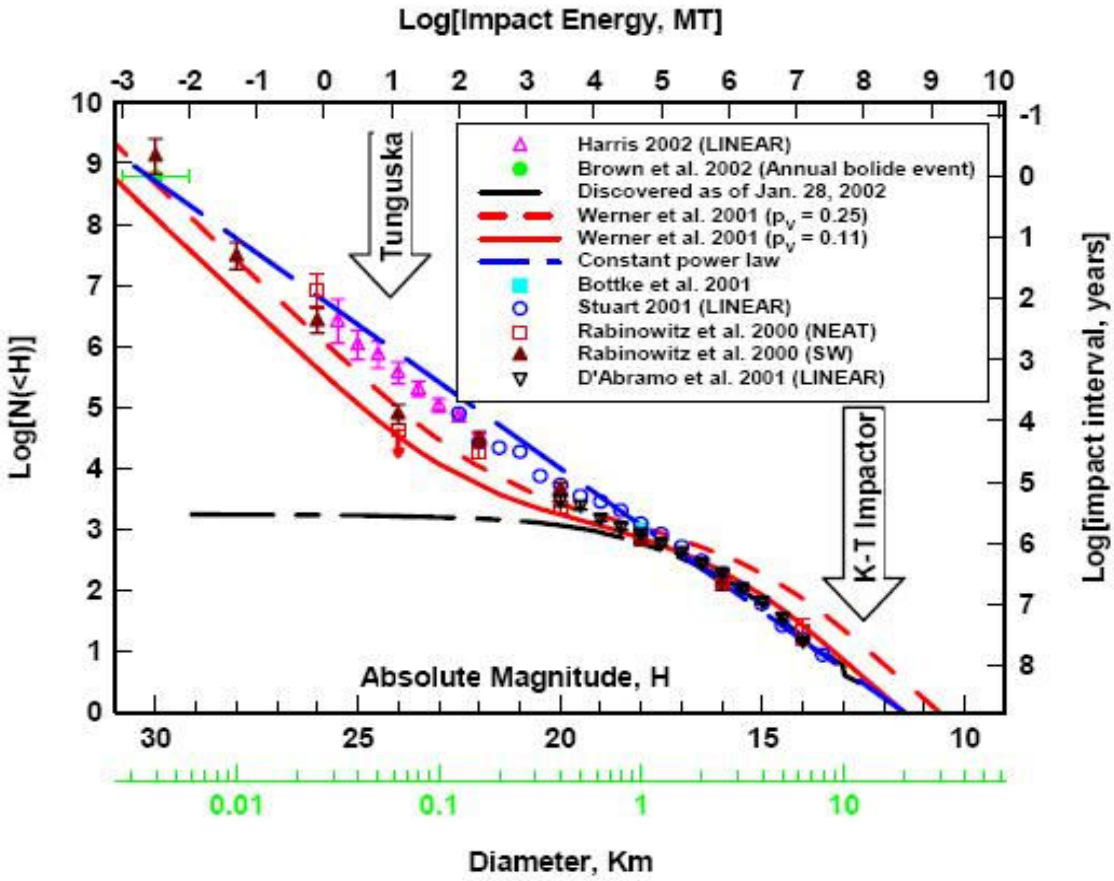

Fig. I-3 Accumulative size distribution of Near Earth Objects, from *Stokes et al*[10]. *Werner et al.* related the Near Earth Asteroids population with the Moon cratering record (two lines for different albedos, p_v=0.11 for the estimation in the range of H<17 and p_v=0.25 in the H>17 range), *Harris*, *Bottke et al.*, *Stuart & Rabinowitz et al.* adjusted the population depending on the actual discoveries against the expected through simulation, *D'Abramo et al.* used the re-detection statistics to estimate the NEA population, finally *Brown et al.* studied the annual bolide entries into the atmosphere. The black dash-dot line plots completed NEA survey by January 2002.

Table I-2 summarises the total number of Near Earth Objects discovered by the end of 2008. The census of objects larger than 1 kilometer is close to completion, as proves the steady annual decrease of discoveries since 2000. The number of detections of any object size has however been increasing and by the end of 2008 has not yet reached a maximum; 648 objects were added to the survey during 2007, while 808 were added in 2008.

Table I-2 Total number of Near Earth Objects known at 1st January 2009. Data courtesy NASA's NEO program.

NEC	Aten	Apollo	Amor	PHA	NEA	NEO
82	481	3130	2242	1000	5863	5945

Considering a single PHO impact frequency of 8.4×10^{-9} yr^{-1} and a population estimate of 198 objects larger than 1km diameter, from *Stokes et al.*[10], the accumulative impact frequency can be easily estimated using the following power law:

$$f(>D[km]) = 1.7x10^{-6} D^{-2.354}[yr^{-1}] \quad (1.2)$$

I.2.4. Consequences for the Earth

As is well known, the Earth's atmosphere presents a very effective protective layer against hypervelocity impacts from extraterrestrial bodies. When a small asteroid travels through the Earth's atmosphere it generates a shock wave, causing a strong drag force, which dissipates the object's kinetic energy as thermal energy, which in turn consumes the object. Although this dissipation protects the Earth surface from direct damage, that is, cratering, the consequent blast wave can still cause considerable harm. A well known example of this kind of event is the famous Tunguska impact[18], which on 30th June 1908 devastated 2000 km^2 of Siberian forest. Such an event is expected to occur once every 2000 to 6000 years, and taking into account that only 1/3rd of the surface is covered by land, it is thought-provoking that Tunguska impact took place only a century ago.

According to *Hills & Goda*[19], the range of object diameter that could deliver an air blast capable of producing surface damage without cratering goes from 50m to 150m. This is considering only stony asteroids, which are approximately 95% of the Near Earth Object population. Metallic asteroids do not dissipate their energy in the atmosphere as efficiently as the less dense stony asteroids and even a few meters metallic bolide could be able to reach the Earth's surface. *Bland & Artemieva*[20] also discussed that the Earth's atmosphere was more effective at dissipating kinetic energy than previously modelled and argued that the upper limit for an air blast is in fact 220m for stony objects.

An asteroid that does not deliver enough energy at the surface is unlikely to produce deep water waves if the impact occurs at sea. Since most of the Earth's surface is covered by water and shorelines are among the most populated areas of the planet, it is widely believed that sea impacts of objects between 200m to 1km diameter could be more harmful

than an equivalent land impact. An impact of this range of objects occurs approximately once every 15,000 years, although this frequency is basically driven by the lower limit of the range, for example an impact on the range 500m to 1km would occur only once every 150,000 years.

An impact of an object larger than 1km diameter can potentially trigger a global environmental catastrophe. The threshold between regional and global effects of an impact appears to be between 10^5 and 10^6 Mt energy range[21], which, depending on impact velocity and density, should be equivalent to an object with at least 1km diameter. A collision of an object of that size would generate an immense amount of suspended particles, such as dust, soot from fires ignited by the impact and water vapour, within the atmosphere. This would reduce solar irradiation at the surface and, depending on the magnitude of this reduction, could induce a global temperature drop, the so-called nuclear-winter, or even a global cessation of the photosynthesis. Moreover, the ejecta plume of the asteroid and the shock wave may burn the atmospheric nitrogen, generating enough nitrogen oxides that, in turn, could destroy the ozone layer.

At the top of the environmental global effects, we find the K-T impact, or Cretaceous-Tertiary-like impact[3], considered to be the cause of the dinosaur extinction, 65 million years ago. Apart from the aforementioned effects, this sort of catastrophic impact resulted in changes in atmospheric and oceanic composition, which, added to other global effects, caused the last global extinction event (without considering the debated human-triggered Holocene extinction event, currently happening).

I.3. Asteroid Hazard Monitoring

After a new object is discovered, by wide-angle telescopes such as US LINEAR or the Catalina-Schmidt telescope, follow-up observations are carried out by more conventional systems (i.e., smaller observatories and/or in lower altitudes) in order to accurately determine its orbit. These observations carried out during the remaining days of the observational opportunity may not be enough to properly discard any impact risk of a newly discovered object and may therefore require more observations at future opportunities, which may however occur years later. Furthermore, the already existing and catalogued asteroids and comets may require monitoring, particularly the Potentially Hazardous Objects (or PHOs), in order to refine their always-changing orbital elements.

Currently, there are two systems scanning for potential impacts and monitoring Near Earth Objects Orbits. These two independent systems, NEODyS at the University of Pisa[22] and Sentry at JPL[23], have also proved successful in reporting the asteroid and comet hazard to the NEO community and general public. For this purpose two impact hazard scales have been created: Torino Impact Hazard Scale[24] and Palermo Technical Scale[12]. The *Torino* scale is intended as a tool to communicate the impact risk to the general public with a 0 to 10 hazard integer scale (see Fig. I-4), where both the collision probability and the kinetic energy of the object are taken into account. The *Palermo* scale was developed, instead, as a tool to help astronomers to discern about the computational and observational resources that should be given to a particular object for further orbital determination.

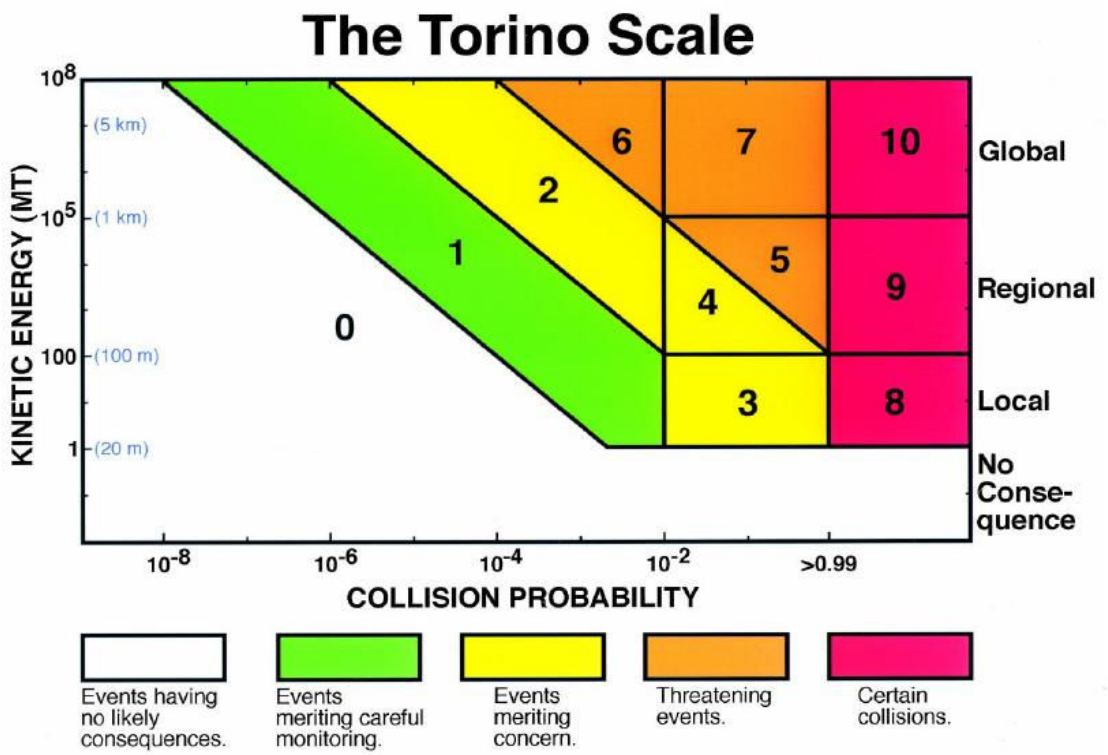

Fig. I-4 Diagram of Torino Scale risk categories[24].

The *Palermo* index of an asteroid can be calculated using the following formula:

$$P = \log_{10} \frac{P_I}{f_B \cdot \Delta T\left[yr\right]}$$
$$f_B = \frac{3}{100} E\left[MT\right]^{-4/5} \left[yr^{-1}\right] \qquad (1.3)$$

where P_I is the probability of impact of the asteroid, f_B is the "background" frequency or annual frequency of impacts of an energy E or greater and ΔT is the years remaining until the impact with probability P_I. Hence, the *Palermo* scale relates the probability of the

impact of a particular object with the statistical risk, which is largely based on lunar cratering records.

As of 1st January 2009, there are no objects among the 1000 Potentially Hazardous Asteroids with positive Palermo index, which means that there is no object threatening the Earth with an impact probability higher than the statistical risk. The highest Palermo index today is -1.82, which is almost two orders of magnitude lower than the statistical risk. The highest ever score was achieved by 99942 Apophis, which reached a +1.1 score in December 2004. The Palermo index for this object dropped to -2.41, after its orbit was computed with increased precision and the ellipsoid of uncertainty of the object position was consequently reduced. By the time that the new generation of surveys begins with the new LSST[25] and Pan-STARRS[26], scheduled for the first half of the 2010 decade, several objects are expected to be found in the Palermo scale region between 0 and 1 and maybe one additional object with P higher than 1.

I.3.1. Considerations on Warning Time

When a new threatening asteroid is spotted, its impact probability is always very low, since the ellipsoid of uncertainty of its position, at the encounter time, is much larger than the Earth's volume. The impact probability will then increase with each new improvement of its orbit determination and will keep growing as long as the Earth capture region remains inside the collapsing uncertain region. If the threatening asteroid is not a real impactor, the impact probability will drop suddenly at a certain point during the process of refining its orbital parameters; this happens when the collapsing uncertain region moves outside the Earth capture region. The probability of impact may however not reach zero; this would happen if the uncertain region still encompasses keyholes allowing the asteroid a resonant return (see example of Apophis in section I.4.1).

Chesley & Spahr[27] simulated the capability of the survey systems, such as the LINEAR system (brightness limiting magnitude of 20) or the future Pan-STARRS project (brightness limiting magnitude of 24), to discover threatening asteroids, using populations of thousands of virtual impactors based on realistic NEA populations. Among the conclusions, it is interesting to see that an asteroid survey such as LINEAR should detect about 70% of the possible impactors of 360 m diameter within 10 years, but would still miss 5% of the impactors even with 100 years survey. A survey like Pan-STARRS will be able to detect 70-m diameter asteroids with the same ease as 360-m diameter asteroids for the LINEAR system.

The detection lead time, or time before impact when an asteroid is detected, is definitively important in order to determine the warning time, which is defined here as the time available to react to an already detected and confirmed threat, but is surely not the only factor before an asteroid is considered a threat and a mitigation plan is put forward. *Chodas & Giorgini*[28] studied the time needed for a newly discovered impactor to have its orbital accuracy determined so that its impact probability is at least 50%. They concluded that in most of the cases the 50% impact likelihood is reached at the second observational period, although the time-span between the first and the second observational period varies with the object's size and orbit, observatory brightness magnitude limit and intervening planetary close approaches. The majority of the 700-m diameter objects, 73%, reach the 50% impact likelihood within 5 years of their discovery for a survey with limiting brightness magnitude of 20 and follow-up observation continuing down to 22, only 27% of the 140-m size object reach the same point within 5 years and 17% for objects of 70 meters diameter. Including radar observation in the follow-up improved greatly those percentages[28], as it would certainly happen with a higher limiting magnitude survey (e.g. Pan-STARRS) .

I.3.2. Considerations on Resonant Returns

If an asteroid has a very close planetary approach, its orbit will be modified in exactly the same way that a spacecraft orbit uses a planetary flyby to modify its own orbit. If the close approach is such that the asteroid's orbital period becomes commensurable with the orbital period of the planet, both objects, planet and asteroid, will meet again after an integer number of orbits, when this happens a resonant return is said to occur[29]. A good example of resonant return is Apophis' possible impact in 2036, when after 6 orbital revolutions it will meet again the Earth, 7 years after the 2029 flyby.

For a resonant return like the Apophis possible impact in 2036 to occur, the asteroid must pass through a very small area in the planetary target plane or the b-plane of the encounter. This small area is called a *keyhole*, a term coined by *Paul Chodas*[30]. One can use the analytical theory described in *Valsecchi et al*.[29] to characterize the set of keyholes of a particular close approach. The results may show several very small areas, sub-kilometer diameter, for a particular close encounter. If a resonant return impact is bound to happen, a mitigation scenario could take advantage of the pre-resonant dynamics and simply move the asteroid away from the dangerous keyhole, which would require only a few kilometers deviation. The main problem with this kind of mitigation scenario is again

due to the small size of the keyhole, which entails the extreme challenge of verifying that the asteroid is indeed heading the keyhole.

I.4. Virtual Asteroids and Impacts

In order to improve the understanding of the mitigation strategies and the models described in Chapter II, this thesis will make use of a group of virtual impactors. As will be shown, this set of virtual asteroids and comets represents a meaningful set of realistic impact scenarios. Since, obviously and luckily, there are no real impactors to choose from, the virtual group needed to be generated by other means. Four objects are used: Apophis, the most threatening asteroid currently known, an Aten asteroid, an Apollo asteroid and a long-period comet. The last three objects were generated by statistical analysis of orbital data from NASA's NEO program database. The following sections describe each one of virtual objects and the methodology used to generate them.

I.4.1. Apophis (99942)

Asteroid Apophis has been one of the most cited celestial objects over the last few years and not only in scientific literature[31]. The reason for such popularity is the unprecedented record in impact probability (IP) that this object initially reached shortly after its re-discovery in December 2004 (it was first spotted in June 2004). Apophis attained a ~2.7% of probability to impact the Earth on 13th April 2029 and a +1.1 on the Palermo scale. Such impact threat is still today the highest value ever reached for an asteroid or comet threat. The observations continued until early July 2005, time at which Apophis moved to the daytime sky. By that time, the 2.7% IP (impact probability) had already dropped substantially, since the ellipsoid of uncertainty had shrank considerably due to the improved accuracy in the knowledge of Apophis' orbital elements and had left the Earth capture region outside the feasible positions on 13th April 2029. Yet, even if the 2029 impact has been completely ruled out, the predicted orbit is expected to have a very close Earth encounter with a minimum distance of $5.89 \pm 0.35 R_{\oplus}$ [31]. Within this small uncertain area there are several possible keyholes for resonant return, leaving an accumulative impact threat of 1 in 43,000 chances[23].

The orbit of Apophis is currently extremely well characterized, with less than 2000 km uncertainty in its position during the 2029 encounter. Near-term ground-based optical astrometry can only weakly affect that estimation, but in 2013 Apophis will perform an

Earth approach that should allow radar measurements (e.g., Arecibo) to enable direct size measurements, 3D shape reconstruction and spin-state estimation. This accurate physical data will probably allow a better estimation of orbital perturbations and, likely, eliminate any probability of Apophis passing through a keyhole[32].

Due to the concern that the not-negligible Apophis' IP currently spawns, this asteroid is an obvious candidate for this study. Table I-3 and Table I-4 summarize the orbital and physical data used to represent Apophis in this work.

Table I-3 Keplerian elements used in this study for (99942) Apophis. Ephemeris are updated from JPL solar system dynamics[23] as of July 2008.

	a (AU)	e	i (deg)	Ω (deg)	ω (deg)	M (deg)	*Epoch* (MJD)	t_{MOID} (MJD)
Apophis	0.922	0.191	3.331	204.5	126.4	222.3	53800.5	62240.3

Table I-4 Physical characteristics used in this study for (99942) Apophis. Mass is calculated assuming spherical shape, impact velocity is calculated with the ephemeris in Table I-3.

	Diameter (m)	Density (g/cm^3)	Mass (kg)	Rotational Period (h)	Albedo	V impact (km/s)	Energy (MT)	Impact Frequency (years)
Apophis	270±60[33]	2.6[12]	$2.7x10^{10}$	30.62[34]	0.33±0.08[33]	12.62	~500	~25,000

Our Apophis impact scenario is foreseen to have a very close encounter on 14th April 2029, with a MOID distance of $4.75R_{Earth}$. Notice the small difference between the predicted real flyby (i.e., $5.89 \pm 0.35R_{\oplus}$) and that forecasted by our ephemeris. The difference is in fact very small if we take into account for example that the model to propagate Apophis, used by NEODyS and JPL, also accounts for perturbations from all planets of the Solar system, the Moon, Ceres, Pallas and Vesta. Our virtual Apophis will have a 5.85 km/s relative velocity at encounter, which, due to the hyperbolic orbit followed after entering into the sphere of influence of the Earth, will translate into a hypothetical impact velocity of 12.62 km/s. Eq.(1.2) can then be used to estimate the frequency of impacts of objects of the size of Apophis, which is ~ 25,000 years.

I.4.2. Shiva (Aten)

A list of the 100 Atens with the lowest MOID was taken from the most dangerous ECA (Earth Crossing Asteroid) from NASA's *NEO program* database. Fig. I-5 shows the histograms of 5 keplerian elements (a, e, i, Ω, ω) together with the histogram of the diameter of the 100 objects. As can be seen in the table, the three first keplerian elements (a, e, i) roughly resemble a Gaussian distribution (with symmetry at 1 A.U. or 0 degrees for the semimajor axis a and inclination i respectively), while ascending node Ω and the argument of the periapsis ω have a more stochastic behaviour. Therefore, the semimajor axis, eccentricity and inclination of our virtual Aten were generated using the mean of the aforesaid variables, while the orientation of the orbit (i.e., the angular Keplerian elements Ω and ω) was modified such that the MOID was minimal. Finally, the mean anomaly M_0 is chosen to generate a virtual encounter or collision on a fixed date.

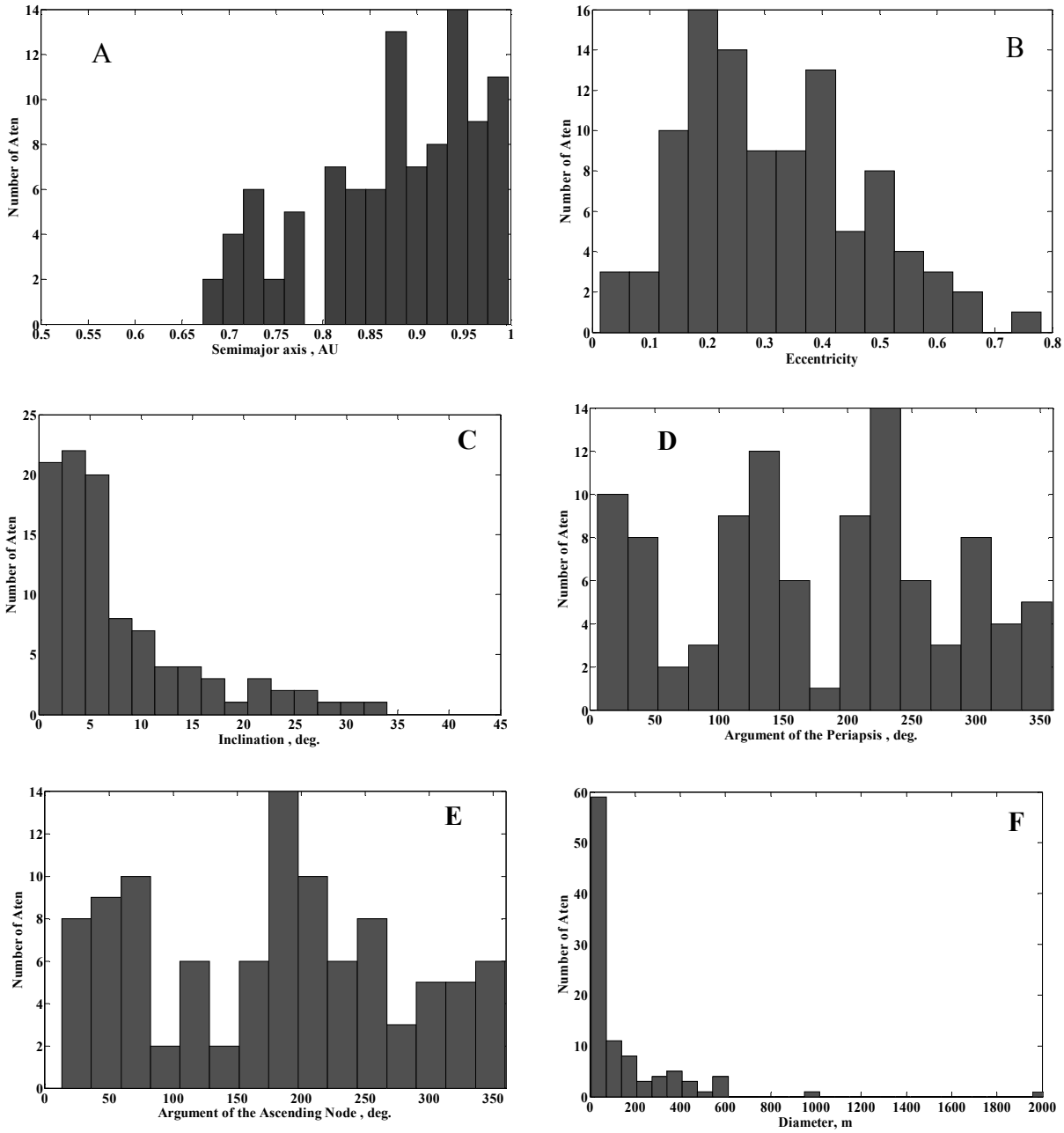

Fig. I-5 Histograms of the 100 Aten list: A) Semimajor Axis B) Eccentricity C) Inclination D) Argument of Periapsis D) Argument of the Ascending Node F) Diameter. The size of the objects was calculated using the standard absolute magnitude H-diameter relation[12] using an average albedo of Pv=0.13[10].

To simplify the identification of the Aten virtual impactor, we will name it *Shiva*, which continues with the custom of naming asteroids from ancient gods and, in particular, impact threatening asteroids with horrific god names (e.g., *Apophis*, which was the Egyptian devil demon). *Shiva* refers to the Hindu god of destruction and renewal. This name has already been used to name both a 400-km wide crater in the Indian Ocean and

the hypothesis in which, not only the K-T extinction, but most of the mass extinctions of life on Earth have been in fact caused by asteroidal and cometary impacts[35].

Table I-5 Keplerian elements used for *Shiva*.

	a (AU)	*e*	*i* (deg)	Ω (deg)	ω (deg)	*M* (deg)	*Epoch* (MJD)	t_{MOID} (MJD)
Shiva	0.875	0.313	7.828	259.9	50.65	97.21	62481.0	62182.1

Table I-5 shows the keplerian elements used to describe *Shiva*'s orbit. The impact scenario for this asteroid has a hypothetical impact on 15th February 2029, where the MOID distance is only $0.5xR_{Earth}$, well inside the Earth surface. The relative velocity at encounter is 9.77 km/s, which translates to a 14.85 km/s impact after the hyperbolic final approach. In this case, we will also consider a range of different masses, thus our models will also be applied to a range of different asteroid sizes. The different *Shiva* asteroids, their masses, impact energy and approximated impact frequency are displayed in Table I-6.

Table I-6 *Shiva* group of impactors and their physical characteristics. Diameter is calculated assuming spherical shape and constant density, impact velocity is calculated with the ephemeris in Table I-5.

	Diameter (m)	Density (g/cm^3)	Mass (kg)	Rotational Period (h)	Albedo	V impact (km/s)	Energy (MT)	Estimated Impact Frequency (years)
$Shiva_1$	72	2.6[12]	$5x10^8$	4.33[36]	0.20	14.85	~13	~1,000
$Shiva_2$	154	2.6[12]	$5x10^9$	4.33[36]	0.20	14.85	~130	~10,000
$Shiva_3$	332	2.6[12]	$5x10^{10}$	4.33[36]	0.20	14.85	~1,300	~50,000
$Shiva_4$	716	2.6[12]	$5x10^{11}$	4.33[36]	0.20	14.85	~13,000	~250,000

An important feature of our virtual asteroids is the surface albedo, which is a crucial characteristic for the efficiency of the deflection models that depend on solar energy. Since S-class and C-Class asteroids account for, approximately, 90% of the total population and a high albedo will downgrade the efficiency of the solar-based strategies, an albedo slightly higher than the average will be used. From *Alan W. Harris*[37], the S-class average albedo is 0.184, with a standard deviation of 0.059, while the C-Class asteroid mean albedo is 0.058 with a standard deviation of 0.024, therefore the use of an albedo of 0.20 will include more than 54% of the whole NEO population.

I.4.3. Apollyon (Apollo)

The last remaining Earth-crossing near-Earth objects belong to the Apollo group. A list of 100 Apollos is retrieved from NASA's *NEO program* database. Fig. I-6 shows the histograms of this set of 100 Apollos with the lowest MOID for 5 keplerian elements (a, e, i, Ω, ω) and size distribution. Like in the Aten case, the semimajor axis a, the eccentricity e and the inclination i roughly resemble a Gaussian distribution, but this time we can notice that the histogram of the argument of the periapsis is clearly not stochastic. In fact, we can distinguish two bell curves, one around 90 degrees and the other around 270 degrees. This is mainly a consequence on the distribution of the semimajor axis and eccentricity of our set, which, as can be seen in Fig. I-7, is filled with asteroids having distances to the Sun similar to that of the Earth (thus 1 AU and susceptible of low MOID) at true anomalies close to ±90 degrees. As done previously, the semimajor axis, eccentricity and inclination are generated using the means of the set and the angular keplerian elements, while Ω, ω and M_0, are modified such that the encounter distance for a fixed collision date is minimum.

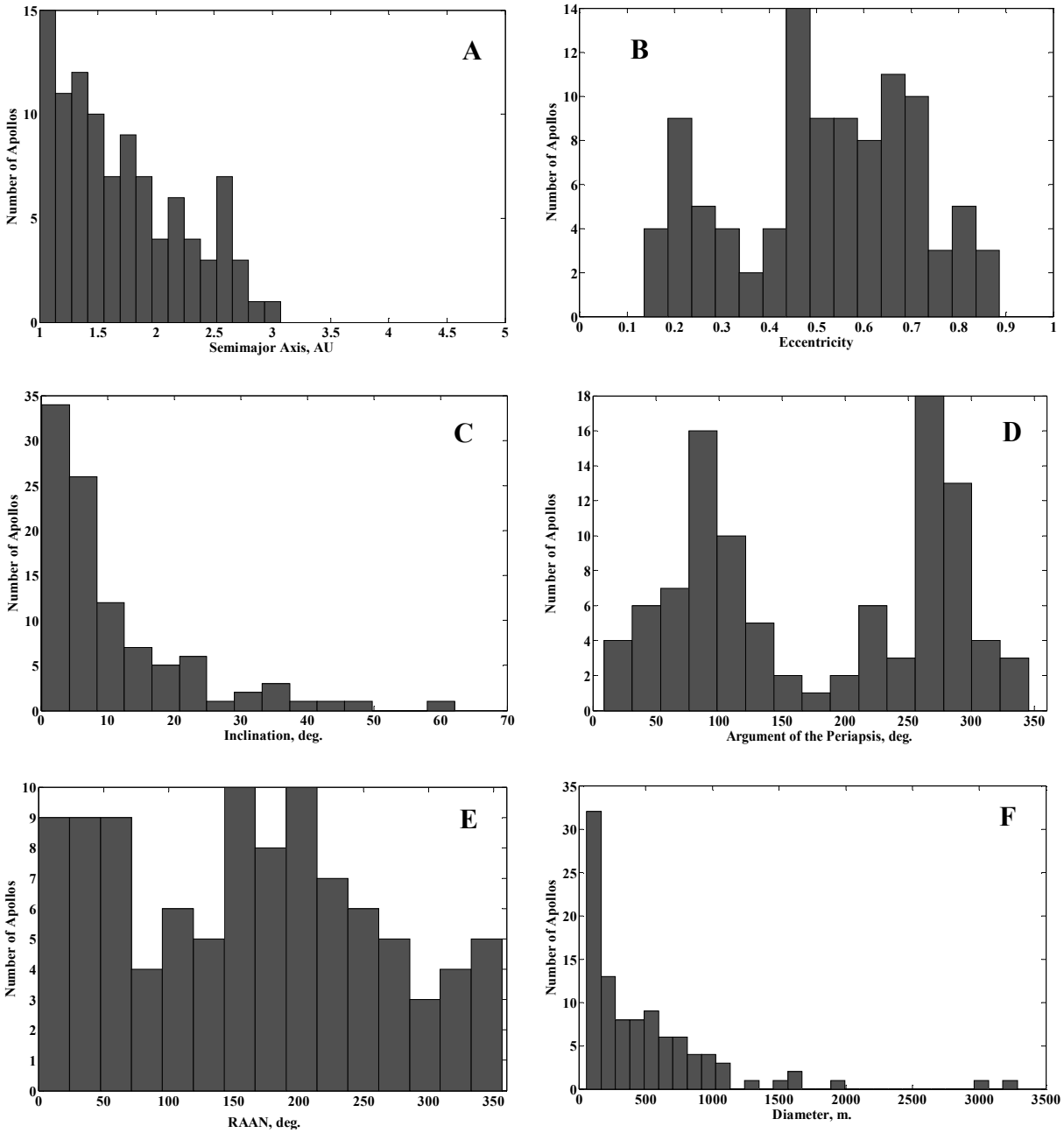

Fig. I-6 Histograms of the 100 Apollo List: A) Semimajor Axis B) Eccentricity C) Inclination D) Argument of Periapsis D) Argument of the Ascending Node F) Diameter. The size of the objects was calculated using the standard absolute magnitude H-diameter relation.

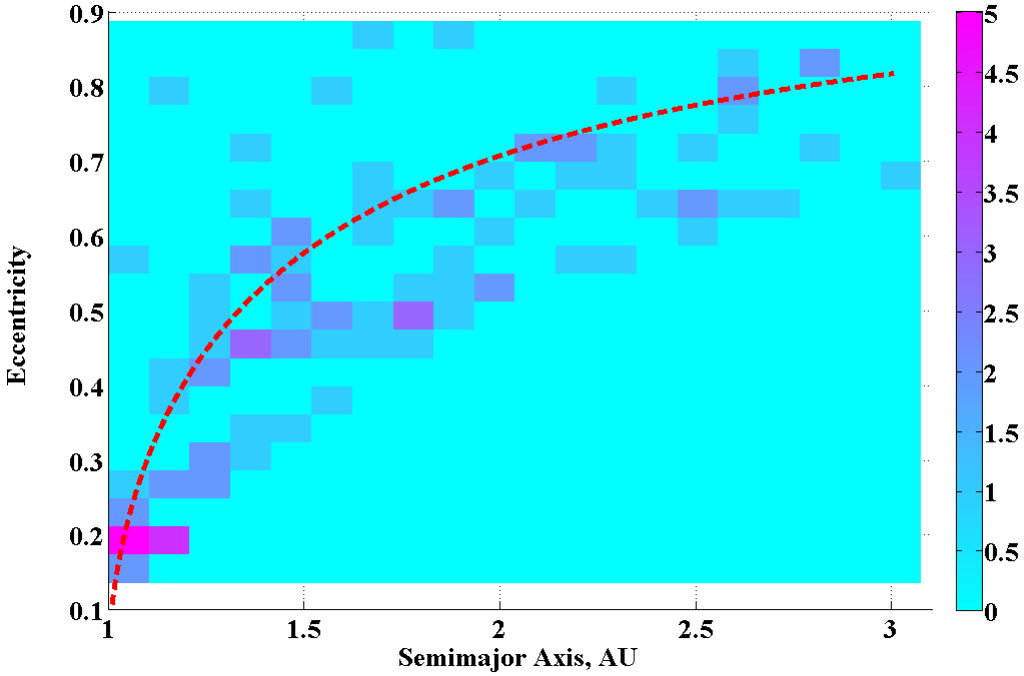

Fig. I-7 Density distribution of the objects in the Apollo list function of the semimajor axis and eccentricity. The superposed red line shows the combinations of eccentricity and semimajor axis whose distance equal to 1 AU occurs at a true anomaly of ±90 degrees, thus all the solutions that fall close of that line will have arguments of the perigee either close to 90 or to 270.

As in the *Shiva* case and to facilitate the use of the virtual asteroids, the Apollo virtual impactor will be refereed as *Apollyon*. This name echoes both the Greek god of the Sun Apollo and the subgroup of asteroids from which we generated our virtual impactor. *Apollyon* is however the greek for "the destroyer", which fits our criteria. Table I-7 summarize the keplerian elements of this impactor.

Table I-7 Keplerian elements used for *Apollyon*.

	a (AU)	e	i (deg)	Ω (deg)	ω (deg)	M (deg)	*Epoch* (MJD)	t_{MOID} (MJD)
Apollyon	1.706	0.518	10.70	266.8	121.2	18.09	62488.0	62488.0

Four different mass sizes are also studied in this case: $5x10^8$kg, $5x10^9$kg, $5x10^{10}$kg and $5x10^{11}$kg (see Table I-8). The important physical characteristics are assumed using the same argumentation for the *Shiva* case. The orbit generated delivers an impact on 17th December 2029, with a relative velocity of 13.82 km/s at Earth encounter, which translates to an impact velocity of 17.78 km/s. The *Apollyon* has therefore higher impact energy than the *Shiva* impact. This is to be expected since *Apollyon* has a higher eccentricity and a larger semimajor axis than *Shiva*.

Table I-8 *Apollyon* group of impactors and their physical characteristics. Diameter is calculated assuming spherical shape and constant density, impact velocity is calculated with the ephemeris in Table I-7.

	Diameter (m)	Density (g/cm^3)	Mass (kg)	Rotational Period (h)	Albedo	V impact (km/s)	Energy (MT)	Estimated Impact Frequency (years)
$Apollyon_1$	72	2.6[12]	$5x10^8$	4.33[36]	0.20	17.78	~19	~1,000
$Apollyon_2$	154	2.6[12]	$5x10^9$	4.33[36]	0.20	17.78	~190	~10,000
$Apollyon_3$	332	2.6[12]	$5x10^{10}$	4.33[36]	0.20	17.78	~1,900	~50,000
$Apollyon_4$	716	2.6[12]	$5x10^{11}$	4.33[36]	0.20	17.78	~19,000	~250,000

I.4.4. Comet S-T (Nearly-isotropic comet)

A preliminary analysis of the main differences between asteroidal and cometary deflection is carried out in Chapter III and a nearly-isotropic comet is also generated with this purpose. Currently there are only 82 Near Earth Comets, from which only 2 are nearly-isotropic comets with MOID smaller than 0.05 AU. We cannot therefore generate a comet based on statistical analysis of potentially dangerous comets. On top of that, the range of possible values for some of the keplerian elements, such as inclination, is extremely large and with homogenous distribution. The goal of our virtual comet is therefore only to help us to comprehend the principal differences between an Asteroid Hazard Mitigation and a Comet Mitigation. Even if a full study of the Comet Hazard Mitigation is out of the scope of this thesis, work on Hazard Mitigation should include at least enough discussion to understand the possible risk of cometary objects.

Among the two potentially dangerous comets identified, *comet Swift-Tuttle* has the lowest MOID (i.e., 0.000892 A.U or approximately $1/3^{rd}$ the Earth-Moon distance). The semimajor axis, eccentricity and inclination of this object are used to generate our cometary impactor, and as done previously, the orientation of the orbit (i.e., Ω, ω and M_0) is modified such that a virtual Earth collision occurs during 2029. Table I-9 shows the resultant keplerian elements of this comet, which will be referred from now on as *Comet S-T*.

Table I-9 Keplerian elements used for *Comet S-T*.

	a (AU)	*e*	*i* (deg)	Ω (deg)	ω (deg)	*M* (deg)	*Epoch* (MJD)	t_{MOID} (MJD)
Comet S-T	26.092	0.963	113.45	70.77	152.94	0.141	13742.2	62421.4

Comet S-T has a virtual encounter on 12th October 2029 with a relative velocity of 59.3 km/s. This is a huge relative velocity, due to both the almost parabolic orbit and the retrograde trajectory of the comet. Cometary objects seems to be depleted of small bodies and present a peak of the size-frequency distribution located at 1.4km diameter[10]. Therefore, a cometary impact would most certainly have global effects on Earth. Luckily, impacts of objects such as the one described in Table I-10 (i.e., *Comet S-T*) or smaller only occur every 100 million years.

Table I-10 *Comet S-T* and its physical characteristics. Diameter is calculated assuming spherical shape and constant density, impact velocity is calculated with the ephemeris in Table I-9.

	Diameter (m)	Density (g/cm^3)	Mass (kg)	Rotational Period (h)	Albedo	V impact (km/s)	Energy (MT)	Impact Frequency (years)
Comet S-T	1500	1.1[12]	$2x10^{12}$	4.33[36]	0.04[12]	60.34	~900,000	~100,000,000

I.5. Minimum Deflection Distance

In the following chapters, the efficiency of the different deflection methods will be evaluated by considering the spacecraft mass required to apply a given deflection method and achieve a fixed deviation distance at the asteroid-Earth encounter. Fixing the deviation distance as the minimum distance that an asteroid needs to be shifted in order to miss the Earth will provide us with the minimum size, in terms of on-orbit mass, of the deflection mission required to deflect the threatening asteroid. If the Earth atmosphere is neglected, the minimum distance necessary to avoid a collision of the asteroid with the Earth should clearly be one Earth radius $R_{\oplus}$.

After a deflection manoeuvre is applied, the achieved miss distance will be computed by means of proximal motion equations expressed as a function of the variations of the orbital elements, determined using Gauss' planetary equations (see Appendix A.1). This method computes the relative distance between two objects orbiting the Sun, assuming no gravity interaction between them. When an asteroid or a comet is in proximity of the Earth,

its orbit is essentially hyperbolic with the Earth at the focus of the hyperbola. Hence, during the final Earth approach, the threatening object will suddenly relocate the gravitational focus of its orbit from the Sun to the Earth, and this phenomenon is perceived as a sudden curvature of the object's trajectory towards the Earth. In order to account for this gravitational pull of the Earth during the asteroid's final approach, the minimum distance of one Earth radius $R_\oplus$ will need to be corrected accordingly. The correcting factor is:

$$\varepsilon = \frac{r_a}{r_p} = \sqrt{1 + \frac{2\mu_e}{r_p v_\infty^2}} \tag{1.4}$$

and defined as the ratio between r_a, which is the minimum distance between the hyperbola asymptote and the Earth, i.e., focus[2] of the hyperbola, and the perigee distance of the hyperbolic orbit r_p, which was fixed to $R_\oplus$ (minimum distance to avoid collision without considering the atmosphere altitude), μ_e is the gravitational constant of the Earth and v_∞ the hyperbolic excess velocity. Note that the correcting factor only depends on the hyperbolic excess velocity of the threatening object. Table I-11 summarizes the minimum deflection distance for the four virtual threatening objects.

Table I-11 Hyperbolic factor and minimum deflection distance.

	v_∞ (km/s)	ε	r_a (km)
Apophis	5.85	2.16	13,764
Shiva	9.78	1.52	9,690
Apollyon	13.83	1.29	8,202
Comet S-T	59.30	1.02	6,491

I.6. Chapter Summary

The seriousness of the extraterrestrial impact hazard has been well understood for more than 20 years, although, when confronting the problem of designing and studying possible space mission to mitigate this hazard, one faces a huge number of variables and uncertainties that would make the problem completely unmanageable unless some

[2] The minimum distance between the focus and the asymptote of a hyperbolic orbit is equal to minus the semiminor axis b of the hyperbola, $r_a = -b$.

assumptions are made. This Chapter summarizes the different possible variables and uncertainties that play an important role on the hazard and assumptions take the form of four possible virtual impactors that the following chapters will study in depth.

Table I-3, Table I-5, Table I-7 and Table I-9 describe the orbital elements of the different virtual impactors. The set of impactors includes 2 Atens, 1 Apollo and 1 Comet. The latter will be used only as an example to highlight the differences between asteroid and cometary mitigation. Table I-4, Table I-6, Table I-8 and Table I-12 describe some of the physical properties of the virtual bodies as well as the kinetic energy at the encounter and the accumulative impact frequency (i.e., impact frequency of bodies with diameter equal or bigger). We shall notice that the impact frequency is only a statistical approximation that does not takes into account orbital distribution. In fact bodies with lower relative velocity will have generally higher impact probability since they spend more time within the Earth-capture cross section of the Earth's orbit, hence for example an asteroid of the Aten group has statistically more chances of being an impactor than an asteroid of the Apollo group. Finally, Table I-11 provides an estimate of the minimum distance that an asteroid needs to be deflected in order to avoid a collision with the Earth.

Chapter II

On the Deflection of Threatening Asteroids

Even before the scientific community reached a general agreement about the potential threat posed by the asteroidal and cometary population, the analysis and design of possible deflection techniques was already spurring the imagination of many. This is evident by the amount of movies, novels and student projects that had already conjectured on different deflection scenarios even before the publication of the famous work by *Alvarez et al.*[3]. The latter, together with the organization of the first workshop on the consequences of a cometary or asteroidal impact[38] in 1981, a year after the publication of *Alvarez*'s work, is believed to have marked an inflection point in the recognition of the impact threat by the scientific community.

An undergraduate student project from the *Massachusetts Institute of Technology* in 1968 is believed to be the first analysis and design of an impact hazard mitigation mission[8]. Perhaps influenced by the Cold War culture of the time, this first mitigation report suggested the use of several large 100-megaton nuclear warheads launched by Saturn V rockets with the sole purpose of completely destroying the threatening object. More than 4 decades have passed since the publication of that first work on asteroid deflection and many others have followed, among them numerous interesting alternatives that do not contemplate the use of nuclear weapons.

All the deflection methods suggested to date can be grouped into two broad groups: impulsive deflection methods which provide a quasi-instantaneous change of the velocity vector of the threatening object and slow push deflections which act on the asteroid or comet over extended periods of time. This chapter will examine kinetic impactor and nuclear interceptor methods as techniques providing an impulsive change in the linear momentum of the asteroid. The slow push or low thrust methods can be further divided into; techniques actively producing a controlled continuous low-thrust, such as attached propulsion devices[39] (e.g., electric/chemical engines, solar sails) or gravitational tugs[40];

techniques producing a passive low-thrust by an induced change of the thermo-optical properties of the asteroid surface, such as enhanced Yarkovsky effect[41] or enhanced emissivity through white paint; techniques producing a controlled thrust by the ablation of the asteroid surface[42] (e.g., through laser beams or solar collectors); or, finally, techniques producing a multi-impulsive change of the asteroid linear momentum by the ejection of surface material, such as the mass driver[43].

The number of methods proposed by researchers in the field is enormous and analysing all of them would be an unmanageable task. This chapter will therefore focus on six different techniques; nuclear interceptor, kinetic impactor, low-thrust propulsion, mass driver, solar collector and gravity tug, which, in the author's opinion, comprise a good overview of all possible methods. Most of the techniques that will not be presented can be considered to be variations of the models developed in this chapter, e.g., laser ablation could be thought as a variation of the ablation model developed for the solar collector method. Other techniques, such as enhanced Yarkovsky effect or white paint, require acting upon the asteroid for centuries before they achieve a reasonable deflection and thus will not be considered in this thesis either.

This Chapter will present a number of models; one for each deflection method. Though, a few of them were initially taken from literature, the contribution in redefining and adapting the models to the analysis carried out in Chapter II and Chapter III is not marginal.

II.1. Nuclear Interceptor

Nuclear devices carry the highest energy density among all the deviation methods currently available. Not surprisingly the first deviation strategy ever proposed[8] suggested the use of nuclear bombs to change the collision course of an asteroid. On the other hand, it is worthwhile to remark that this technology could represent a significant risk. As pointed out by Carl Sagan in the *Pale Blue Dot*[44], all mitigation technologies can be a double-edge sword if misused. For obvious reasons delivering nuclear warheads in space could represent a higher menace than other deflection methods. This fearsome risk, intrinsic to this technology, would most probably raise political and security issues, which would certainly make the development of a deflection strategies based on nuclear weapons not only a technological problem. The work described here however has not considered these additional issues.

The model used in this study is based on a stand-off configuration over a spherical asteroid. This type of configuration requires detonating the nuclear charge at distance H from the asteroid surface. The method is less sensitive to possible uncertainties in the asteroid composition and surface morphology[45], unlike other nuclear-based configurations, such as buried and surface explosions.

The energy released during a nuclear explosion is carried mainly by X-rays, neutrons, gamma radiation and debris and its distribution depends mostly on the type of nuclear reaction.

Table II-1 shows the distribution of energy used in this work, which is taken from Hammerling[45] and based on the information in Glasstone[46]. As can be seen in the table, an important part of the total energy is carried in the form of kinetic energy by the debris resulting from the explosion. Although its momentum coupling, or efficiency in producing linear momentum change, is much smaller than that of radioactive processes (as will be seen later), this effect cannot however be neglected. In the following, a model for the computation of the change in the velocity of the asteroid due to debris and radiation is presented.

Table II-1 Energy Distribution

Source	X-ray	Neutrons	Gamma-rays	Debris	Others
Fission	70%	1%	2%	20%	7%
Fusion	55%	20%	1%	20%	4%

II.1.1. Debris

After detonation of the nuclear device, part of the debris, from the spacecraft structure and components, will impact the surface of the asteroid. Assuming that the explosion produces a spherical shock wave and the debris is homogeneously distributed on the surface of this shock wave, the total amount of debris impacting the asteroid m_{debris} is given by the mass of the spacecraft at the Near Earth Object arrival m_i, multiplied by the ratio S between the total area of the shock wave and the portion of it that intersects the asteroid:

$$m_{debris} = Sm_i , \tag{2.1}$$

where S can be readily calculated using the maximum asteroid central angle $\lambda_{\max}$ (Fig. II-1) as:

$$S = \frac{1}{2}(1 - \sin\lambda_{\max}),$$

which can be written as a function of the radius of the asteroid R_a and the altitude of detonation H:

$$S = \frac{1}{2} - \frac{\sqrt{H}}{2}\frac{\sqrt{H + 2R_a}}{R_a + H}. \tag{2.2}$$

Here, and in the following, m_i is the mass of the spacecraft without the propellant to perform the transfer from the Earth to the NEO. The impacting velocity of the debris v_{debris} is then given by:

$$v_{debris} = \sqrt{\frac{2 f_{debris} E_t}{m_i}}, \tag{2.3}$$

where E_t is the total yield released by the nuclear interceptor and f_{debris} is the fraction of delivered energy in kinetic form (see Table II-1). The final increment in the asteroid velocity δv_{debris} is calculated by using the conservation of linear momentum:

$$\delta v_{debris} \approx \beta S_{Sc} \frac{m_{debris} v_{debris}}{M_a} \tag{2.4}$$

where $S_{Sc} = 2/\pi$ and accounts for a conservative estimation of 180-degrees scattering of the debris, β is the momentum enhancement factor[47], which is conservatively chosen to be 2 (see Section II.2 for further discussion), and M_a is the mass of the asteroid.

II.1.2. Radiation

Assuming that the attenuation of energy penetrating into the asteroid follows the *Beer-Lambert law*, the radiant energy attenuated per unit area dE_A by a layer of material of thickness dz and mass per unit area $dm_A = \rho_a dz$ is:

$$dE_A = -\mu_o E_A dm_A, \tag{2.5}$$

where μ_o is the opacity of the material, E_A is the received energy per unit area and ρ_a is the mean density of the asteroid. The opacity μ_o, or mass-attenuation coefficient, describes how the energy is attenuated as it passes through the asteroid, a small attenuation indicates that the material in question is relatively transparent to a particular radiation, while a large attenuation indicates a high degree of opacity. Thus its value depends on the radiation type, the associated energy and the material considered.

In accordance to Eq.(2.5) the energy per unit area varies with the depth *z* as:

$$\frac{dE_A}{dz} = -\mu_o \rho_a E_A , \tag{2.6}$$

which, when integrated over *z*, gives the amount of energy per unit area remaining at a given depth:

$$E_A(z) = E_A(0) e^{-\rho_a \mu_o z} , \tag{2.7}$$

where $E_A(0)$ is the energy on the external surface, and depends on the distance from the explosion.

The absorbed energy *K* at a specific depth *z* per unit area and unit mass is:

$$K = \mu_{en} E_A(z) , \tag{2.8}$$

which is also known as *kerma*, an acronym standing for Kinetic Energy Released in the Material. The mass-absorption coefficient μ_{en} differs from the mass-attenuation μ_o on the fact that the latter accounts for both the absorption and the scattering of energy, while the former estimates only the statistical energy that is absorbed by a sample of matter. In order to be able to assess the values of the absorption and attenuation we will assume that the asteroid's surface is mainly made of forsterite (i.e., Mg_2SiO_4) and that the energy of the impacting radiation is 10 kev for X-ray, 2 Mev for gamma-ray and 14 Mev for neutron radiation[45]. With these hypotheses the opacity and absorption for the different radiations were calculated using tables of radiation attenuation from the *National Institute of Standard and Technology*[48], and shown in Table II-2. Surprisingly, values in Table II-2 are more sensitive to wavelength (i.e., the energy) than to the material composition as can also be seen in Hammerling[45] calculations. Further information about calculation and validity of opacity and absorption can be found in the appendices (Appendix A.2.2).

Table II-2 Values for opacity and absorption are calculated for forsterite (i.e., Mg_2SiO_4) by summing over its constituents weighted according to their atomic percent.

	X-ray	Neutron	Gamma-ray
μ_0	1.426 m^2/kg	0.00496 m^2/kg	0.00445 m^2/kg
μ_{en}	1.370 m^2/kg	0.00496 m^2/kg	0.00234 m^2/kg

A portion E_v of the absorbed energy K goes into the sublimation process (sublimation enthalpy), while the remaining energy is converted into kinetic energy and accelerates the sublimated material to a velocity v_e given by:

$$v_e = \sqrt{2\left(K - E_v\right)}\,. \tag{2.9}$$

If we consider forsterite as the main component of the asteroid, then the sublimation enthalpy is $E_v = 5.03$ kJ/g (Wang[49]). This assumption is likely to represent a worst case scenario since the surface of the asteroid might have more volatile materials, and the regolith may even help to increase the thrust/energy efficiency. The variation of the linear momentum per unit area dp_A gained by the asteroid due to the evaporated mass is:

$$dp_A = \rho_a v_e dz\,, \tag{2.10}$$

which integrated from the surface of the asteroid to the maximum depth at which the evaporation takes place, $Z_{\max}$, gives the total linear momentum per unit area:

$$P_A = \int_0^{Z_{\max}} dp_A dz\,. \tag{2.11}$$

The maximum depth $Z_{\max}$ can be computed by solving $K - E_v = 0$, which results in:

$$Z_{\max} = \frac{1}{\rho_a \mu_o} \ln\left(\frac{\mu_{en} E_A(0)}{E_v}\right). \tag{2.12}$$

Taking into account the elevation angle ε of the incoming radiation (see Fig. II-1), the linear momentum per unit area p_A becomes:

$$P_A = \int_0^{Z_{\max}\cdot\sin\varepsilon} \rho_a \sqrt{2\left(\mu_{en} E_A(0) e^{-\rho_a \mu_0 \frac{z}{\sin\varepsilon}} - E_v\right)}\, dz \tag{2.13}$$

Similar to the integration Eq.(2.13), but without considering the velocity v_e, provides the mass ablated and expelled from the asteroid surface:

$$m_{\exp} = \int_0^{Z_{\max}\cdot\sin\varepsilon} \rho_a dz \tag{2.14}$$

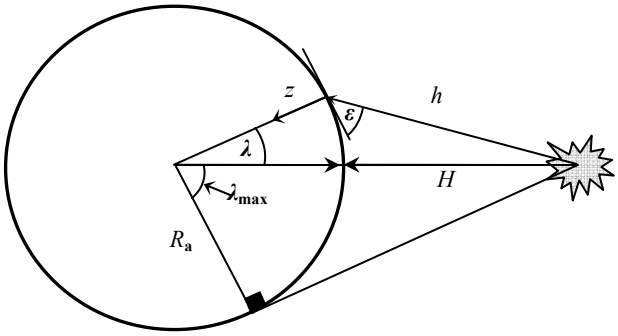

Fig. II-1 Geometric diagram of the spacecraft detonation and asteroid.

Eq.(2.13) can now be integrated over the entire radiated surface. Using the equation of the surface of a spherical cap (see Fig. II-2):

$$S_{\text{cap}} = 2\pi R_{\text{a}}^2(1-\cos\lambda), \tag{2.15}$$

we obtain an integration dependant only on the asteroid central angle λ, which leads to the following double integration:

$$P = \sqrt{8}\pi R_a^2 \rho_a \int_0^{\lambda_{\max}} \left(\int_0^{Z_{\max}\cdot\sin\varepsilon(\lambda)} \left(\mu_{en} \frac{f_{radiation} E_t}{4\pi\left[h(\lambda)\right]^2} e^{-\frac{\rho_a \mu_o z}{\sin\varepsilon(\lambda)}} - E_v \right)^{1/2} dz \right) \sin\lambda d\lambda, \tag{2.16}$$

where E_t is the total energy released by the explosion, $f_{radiation}$ is the fraction of energy corresponding to each one of the three radiation contributions shown in Table II-1, and h is the distance from the explosion to the surface of the asteroid. The distance h and the elevation angle ε are expressed as a function of the central angle $\lambda \in [0 \quad \lambda_{max}]$ (see Fig. II-1), where $\lambda_{\max}$ corresponds to the distance to the horizon of the asteroid as seen from the spacecraft. Finally, the $\delta v_{radiation}$ experienced by the asteroid is calculated by integrating Eq.(2.16) and dividing it by the total mass of the asteroid.

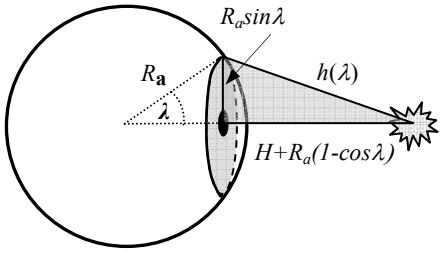

Fig. II-2 Integration over the spherical cap.

II.1.3. Total Achieved δv

Finally, the total δv provided by the nuclear interceptor is therefore the sum of the three radiative components plus the contribution of the debris:

$$\delta v = \delta v_{gamma} + \delta v_{X\text{-}rays} + \delta v_{debris} + \delta v_{neutrons} \tag{2.17}$$

Fig. II-3 shows the total δv given by the combination of all four components (i.e. X-ray, neutron radiation, gamma radiation and debris) as well as the individual contribution of each as a function of H. In this example, the spacecraft carries a nuclear fusion device with a mass of 600 kg in the proximity of asteroid *Apophis*. Fig. II-3 shows that the neutron radiation gives the highest contribution to the total δv; note that the same conclusion is also valid for a nuclear fission device. For this example, the optimal stand-off distance, or altitude at which the maximum total increment of velocity occurs, is at an altitude H equal to $0.20R_a$.

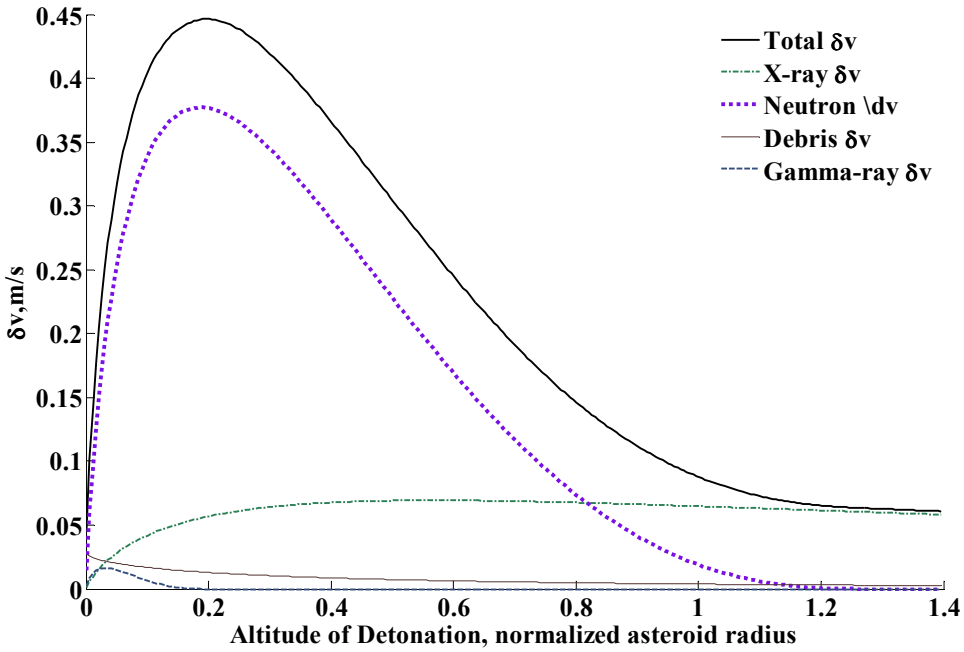

Fig. II-3 Change in velocity of asteroid *Apophis* achieved with a Nuclear Interceptor carrying a fusion device of 600 kg, as a function of altitude of detonation *H*. The distance is normalized using the asteroid average radius.

The ablated mass m_{exp} and the average velocity of the sublimated material produced by each one of the types of radiation are plotted in Fig. II-4. It can be observed that X-rays produce very high excess velocities but ablate a very thin layer of material from the surface of the asteroid. On the other hand, neutron radiation produces more evaporation, since this

radiation penetrates deeper into the asteroid and this is a more efficient way of providing impulse to the asteroid.

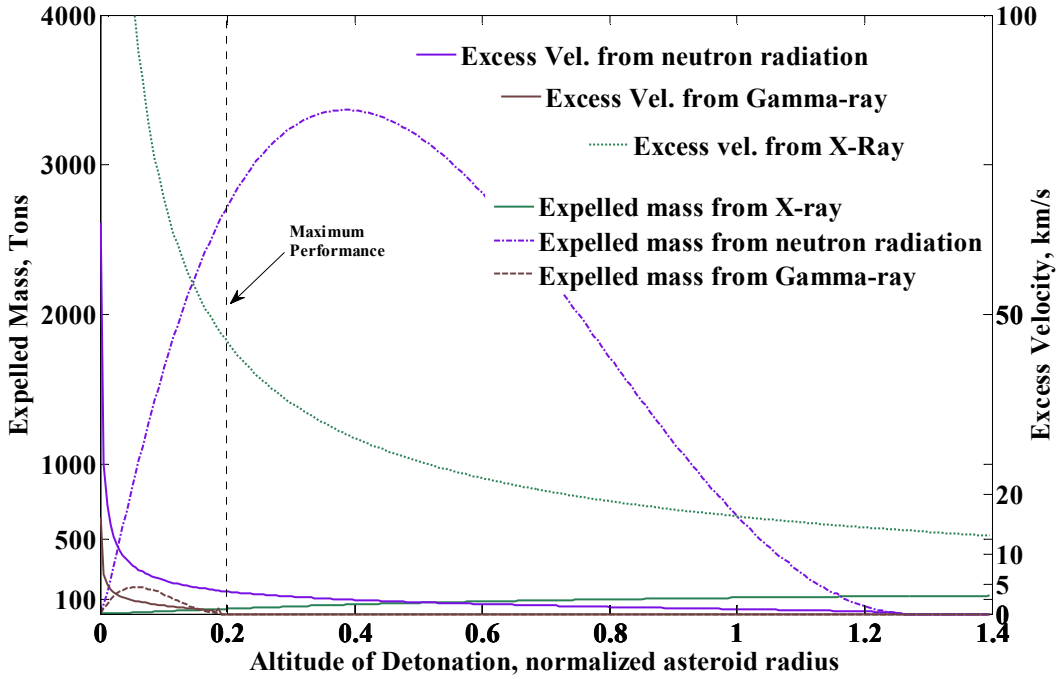

Fig. II-4 Radiation analysis. *Y* axis on the left shows the mass evaporated by the three main radiation components of the nuclear explosion, *Y* axis on the right shows the excess velocity of the material that have been evaporated, X axis is the asteroid radius normalized altitude of detonation.

II.1.4. Optimal Stand-off Distance

As can be inferred from the previous results (Fig. II-3), the altitude of the detonation is a key parameter for the performance of this approach. It is therefore paramount for a nuclear interceptor mission to detonate the nuclear device at the point where Eq.(2.17) is maximum. In Fig. II-3, we determined that the optimal stand-off distance was $H = 0.20R_a$, but, unfortunately, this distance is neither constant nor straightforward. A combination of energy transferred and area of surface radiated will provide the maximum change in the velocity of the asteroid, but the way that these two elements combine changes depending on the density of the target asteroid ρ_a, the mass of the spacecraft at the Near Earth Object arrival m_i and the radius of the Near Earth Object R_a.

One of the main contributors to the radiation opacity of the asteroid material is the density of the target asteroid ρ_a, hence this parameter will have an important impact to determine the proportion of energy that is effectively used to sublimate material or to accelerate the already sublimated mass. Since twice a given amount of energy applied to

accelerate the sublimated mass only produces a $\sqrt{2}$ increment of velocity, the radiative energy will have a higher effect in providing change of velocity if used to sublimate instead of accelerating. On the other hand, the mass of the spacecraft at the Near Earth Object arrival m_i and the radius of the Near Earth Object R_a have a direct effect on the energy density at the surface, which again affects the share between excess velocities and amount of mass ablated. Fig. II-5 shows the aforementioned dependence of the optimal stand-off point.

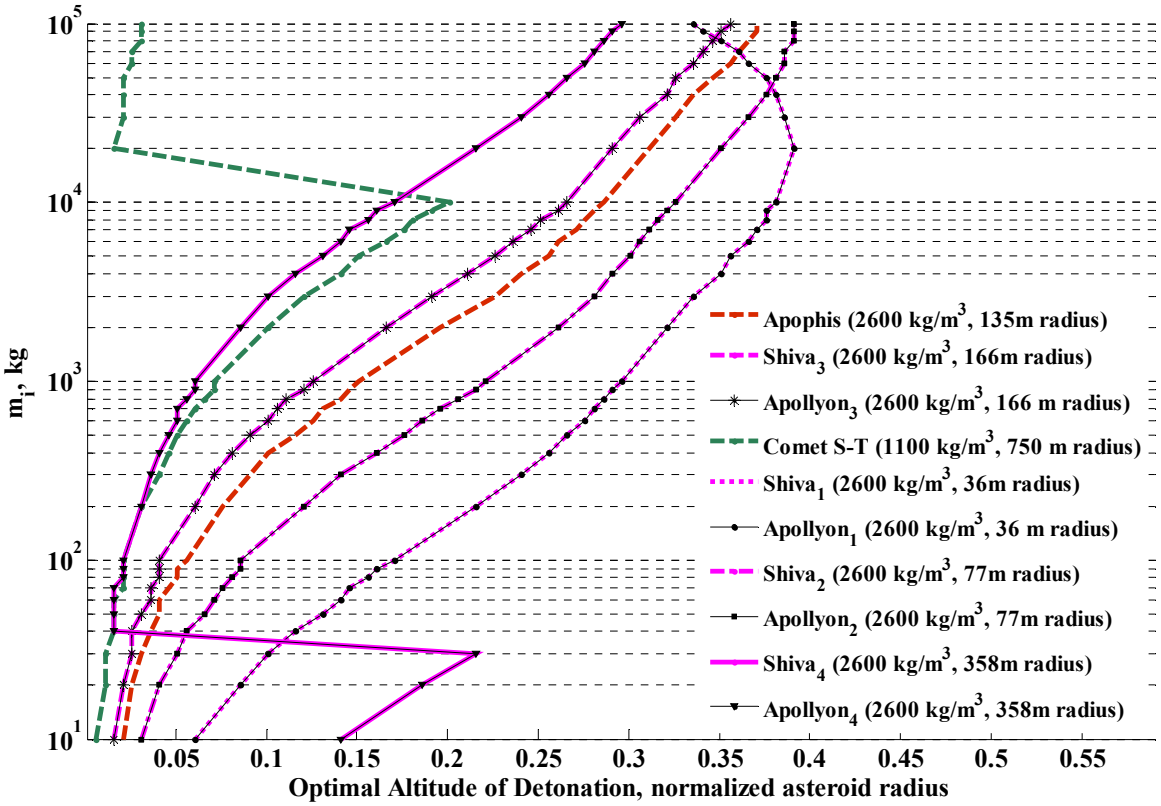

Fig. II-5 Optimal Altitude of Detonation as a function of the mass of the spacecraft at the Near Earth Object arrival m_i. Notice that each pair of same size *Shiva* and *Apollyon* is superposed in the figure since they have both the same radius and density.

Note that the optimal stand-off point is usually driven by one type of radiation; in Fig. II-3, for example, neutron radiation is the dominant contribution. Although for most of the studied scenarios the dominant contribution comes from neutron radiation, for some cases however the x-ray radiation can become dominant. A sharp change in the optimal altitude of detonation in Fig. II-5 is indicative of a sudden change of dominance among the contribution of these two main radiations. For example, as shown in Fig. II-5, the *Comet S-T* has a sudden change from an optimal altitude at $0.20R_a$ when m_i is 10,000kg to an altitude of $0.016R_a$ when m_i reaches 20,000kg. Fig. II-6 shows how this sudden change in

the optimal distance between m_i at 10,000kg and at 20,000kg occurs at the point when the contribution of the nuclear radiation is larger than the X-ray radiation, which, contrarily to what happens with *Apophis*, is the dominant radiation in the δv contribution for *Comet S-T* from 100 kg to 10,000kg of initial mass m_i.

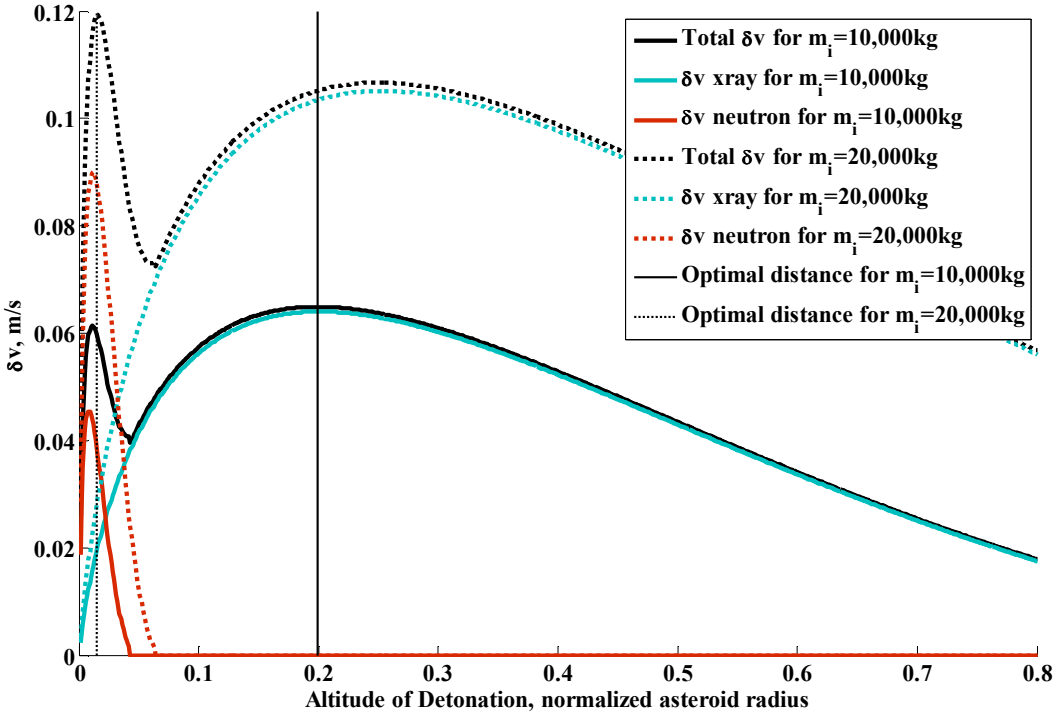

Fig. II-6 Total delta-v and delta-v contributions of nuclear and x-ray radiation for two nuclear deflections with m_i 10,000kg and 20,000kg attempting to deflect *Comet S-T*.

II.1.5. Model Final Remarks

Although the core of the model developed here is initially based on the radiation coupling model found in the work of Hammerling[45], the numerical integration of Eq.(2.16) allows a more general analysis of the nuclear option. An important result of this model compared with previous existing models is the optimal stand-off distance: Harmmerling *et al.* found an optimal distance $H=\left(\sqrt{2}-1\right)R_a$ and the same result was previously found by Ahrens[50]. These works computed the optimal stand-off distance by maximizing the sum of two fractions, the energy disposed over the asteroid against the total energy $S=0.5\cdot(1-\sin\lambda_{\max})$ and the radiated surface against the total asteroid surface $S_a=0.5\cdot(1-\cos\lambda_{\max})$. The model developed here shows that the optimal distance is driven by both excess velocity and mass expelled. This ensues a distance which is smaller (in

some cases even one order of magnitude smaller) than what previously predicted. This indicates that the previous methods were probably an oversimplification of the problem.

The model has been developed assuming a spherical asteroid, yet it is very unlikely that a Near Earth Object would have a spherical shape. This assumption however does not seem to represent a substantial source of error. As can be seen in Appendix A.2.3, even in the worst possible configuration (i.e., detonation over the smallest cross section area) on a very elongated body (i.e., asteroid Geographos[3]) corresponds only to a 18% reduction in the magnitude of the applied δv.

II.1.6. Spacecraft System Definition

We assume that a spacecraft carries a nuclear device with a mass $m_{wh} = 0.3m_d$, where m_d is the dry mass of the spacecraft and the 30% fraction accounts for the portion of dry mass allocated to payload[51]. In this model, the dry mass m_d is equivalent to the m_i or mass at NEO interception since we do not require propellant after intercepting the asteroid. Fig. II-3 shows the importance of maximizing the neutron radiation for *Apophis* and the same happens for all the other cases apart from few exceptions; very large objects (i.e., $Shiva_4$, $Apollyon_4$ and *Comet S_T*) and low spacecraft mass at the asteroid arrival m_i (i.e., less than 20kg m_i for $Shiva_4$ and $Apollyon_4$ and 10,000kg m_i for *Comet S_T*). A fusion device is therefore chosen as primary payload, since its fraction of nuclear radiation is considerably higher (see Table II-1). The energy delivered by the explosion E_t can be computed as:

$$E_t = YTW \cdot m_{wh} \tag{2.18}$$

where *YTW* is the yield-to-weight ratio of a thermonuclear device. This parameter strongly depends on the mass of the nuclear device: the larger the mass, the higher the *YTW* ratio. We chose a *YTW* ratio of 0.75 kTons/kg in order to be consistent with the work of P.L.Smith *et al.*[52] and J.L.Remo[53]. This seems to be a conservative option since the *YTW* may range from 0.6 kTons/kg for a 165 kg warhead to 2.25 kTons/kg for a 4000kg warhead[54].

The two engineering parameters described in this section, the YWT and the payload allocation fraction (i.e., 30% in this case), provides the connection between physics of the model and the spacecraft system design. As a consequence of the uncertainty related with these two engineering parameters, the change of velocity δv provided by the nuclear model also has an inherent engineering uncertainty. The values of these parameters were

[3]http://echo.jpl.nasa.gov/~lance/nea_elongations.html

chosen so that the nuclear deflection model yields a feasible lower boundary for the asteroid change of velocity achieved by a given a dry mass. Since the payload fraction is not expected to suffer large variation from the chosen nominal value, the upper boundary would occur if the *YTW* ratio is 2.25 kTons/kg (three times the chosen value for the model), for which the achieved delta velocity would be twofold the lower bound.

II.1.7. Nuclear Interceptor Mission Sizing

Concluding the description of the nuclear interceptor model, this last section presents the minimum required mass m_i (i.e., mass of the spacecraft at asteroid arrival) necessary to deflect each one of the threatening virtual asteroids introduced in Chapter I. The deflection was set equal to the minimum distance required to miss the Earth, which, as seen in Chapter I (Section I.5), is equal to 1 Earth radius $R_\oplus$ multiplied by a hyperbolic factor ε, unique to each threatening asteroid. The Earth-asteroid transfer is not yet considered (see Chapter III for a complete analysis and comparison), thus the warning time t_w is, here, defined as the time-span covered from the moment when the nuclear interceptor reaches the asteroid and detonates its charge t_{int}, to the time of the virtual impact t_{MOID}.

Given the mass m_i of the spacecraft and the mass and size of the targeted asteroid, the model described through the previous sections yields us the magnitude of the change of velocity sustained by the targeted asteroid $\delta v(m_i)$. The final deflection is then calculated using the direct mapping between the initial change of velocity $\delta\mathbf{v}$ and the deflection $\delta\mathbf{r}$ provided by the transition matrix $[\partial\delta\mathbf{r}(t_{MOID})/\partial\delta\mathbf{v}(t_{int})]$ (see Appendix A.1 for further description of this methodology).

$$\delta\mathbf{r}(t_{MOID}) = \left[\frac{\partial\delta\mathbf{r}(t_{MOID})}{\partial\delta\mathbf{v}(t_{int})}\right]\delta\mathbf{v}(t_{int}) \tag{2.19}$$

The modulus of the vector $\delta\mathbf{v}(t_{int})$ is $\delta v(m_i)$, while the direction of the same vector, in the analysis carried out in this section, is such that maximises the modulus of deflection $\delta\mathbf{r}(t_{MOID})$. The calculation of the optimal direction is described in Section A.1.5. At this point, a root-finding algorithm can search for the mass m_i necessary to provide a deflection $|\delta\mathbf{r}(t_{MOID})|$ equal to $\varepsilon \cdot R_\oplus$ at a given time t_{int}. The results of this root-search for a range of t_{int} within 20 years of warning time are shown in Fig. II-7.

The required mass m_i shown in Fig. II-7 includes a very wide range of spacecraft sizes, which goes from 10 kg to 1,000,000kg. For long warning times t_w, the required

change of velocity δv, to obtain a safe deflection, may be very small and the nuclear model may also output a very small spacecraft mass m_i. This model does not consider technological limitation related with the size of the spacecraft and therefore scales to any mass m_i. Although both the upper end (e.g.,>250,000kg) and lower end (e.g., <100kg) on the Y axis from Fig. II-7 may be a bit unrealistic in terms of technology readiness to build such large or small spacecraft, the forecasted spacecraft mass m_i can still be taken as a measure of the difficulty of such an endeavour. Fig. II-7 then displays a very good efficiency of the nuclear method for all the virtual asteroids.

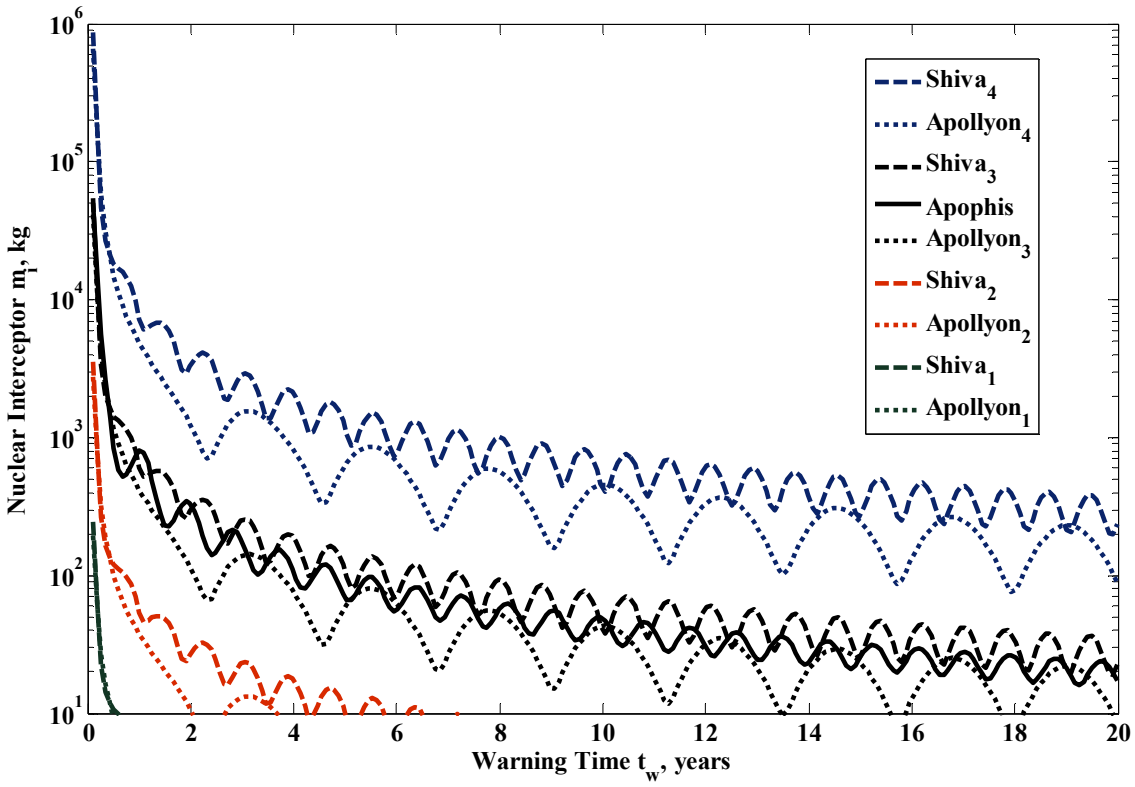

Fig. II-7 Nuclear Interceptor dry mass m_d required to deflect the asteroid at the time of the virtual impact by a distance of 1 Earth radius $R_\oplus$ multiplied by the hyperbolic factor of the threatening asteroid.

One of the remarkable features of Fig. II-7, the oscillatory behaviour of the nuclear interceptor mass m_i with respect to the warning time t_w, is a distinct characteristic of the impulsive deflection methods. These oscillations are also related to the variation of the asteroid velocity over a complete orbital period. An optimum approach to deflect an asteroid involves changing the asteroid's orbital period[4], which can then be achieved by increasing/decreasing the magnitude of the asteroid's orbital velocity. The most efficient

[4] Except for very short warning times (see appendix A.2.5).

time along an orbit to perform an impulsive manoeuvre to increasing/decreasing the orbital velocity is therefore when the asteroid is moving at its highest speed, and this, of course, occurs at the asteroid's perihelion. Each one of the minimums in Fig. II-7 corresponds then to a mitigation scenario where the nuclear interceptor reaches the asteroid at the perihelion.

II.2. Kinetic Impactor

The Kinetic Impactor is the simplest concept for asteroid hazard mitigation: the asteroid's linear momentum is modified by ramming a mass into it. The impact is modelled as a simple inelastic collision resulting into a change in the velocity vector of the asteroid multiplied by a momentum enhancement factor[47]. The enhancement is due to the blast of material expelled during the impact.

The value of the enhancement factor is extrapolated from cratering analysis, such as the one performed by *K. A.* Holsapple[55], and hypervelocity experiments, such as *Tedeschi et al*[47]. Both studies are Earth-based experiments on a small scale and their applicability to realistic asteroid size and conditions is difficult to quantify. A conservative value of 2 was chosen for all the analysis in this chapter and in Chapter III. At the light of the results in *Tedeschi et al*[47], most of the asteroids would be expected to obtain higher values of the enhancement factor; the maximum value is *Tedeschi*'s experiments is almost fivefold the value chosen for this model, which occurred for a compacted snow target. Only monolithic-like asteroids (e.g. metallic objects) capable to absorb the collision through deformation, producing very little amount of debris, would obtain an enhancement factor smaller than 2. The variation of the velocity of the asteroid due to the impact is then given by:

$$\delta \mathbf{v} = \beta \frac{m_i}{\left(M_a + m_i\right)} \Delta \mathbf{v}_{S/C} \tag{2.20}$$

where β is the momentum enhancement factor, $\Delta \mathbf{v}_{S/C}$ is the relative velocity of a impactor of mass m_i with respect to the asteroid at the deviation point and M_a is the mass of the asteroid.

II.2.1. Kinetic Impactor Mission Sizing

Once the minimum deflection distance is defined (see Section I.5 in Chapter I), one can compute the minimum $\delta \mathbf{v}$ required to achieve the demanded deflection by using the transition matrix defined in Appendix A.1.4, which is defined through the proximal motion

equations (i.e., through a root-finding search such that Eq.(2.19) is equal to the minimum deflection distance). Following this calculation of the minimum change of velocity required to deflect the threatening asteroid, the required impact mass m_i can also be estimated for a given relative impact velocity $\Delta \mathbf{v}_{S/C}$ (Eq.(2.20)). Fig. II-8 shows the minimum impact mass m_i to achieve the minimum deflection distance from Earth as a function of warning time t_w. The resultant impact mass m_i obviously depends upon the chosen impact velocity $\Delta \mathbf{v}_{S/C}$ but it can be seen that the shape of the curve does not vary. In Fig. II-8, the left Y axis scales the results for an impact velocity $\Delta \mathbf{v}_{S/C}$ of 15 km/s, while the right Y axis scales for a 50 km/s impact.

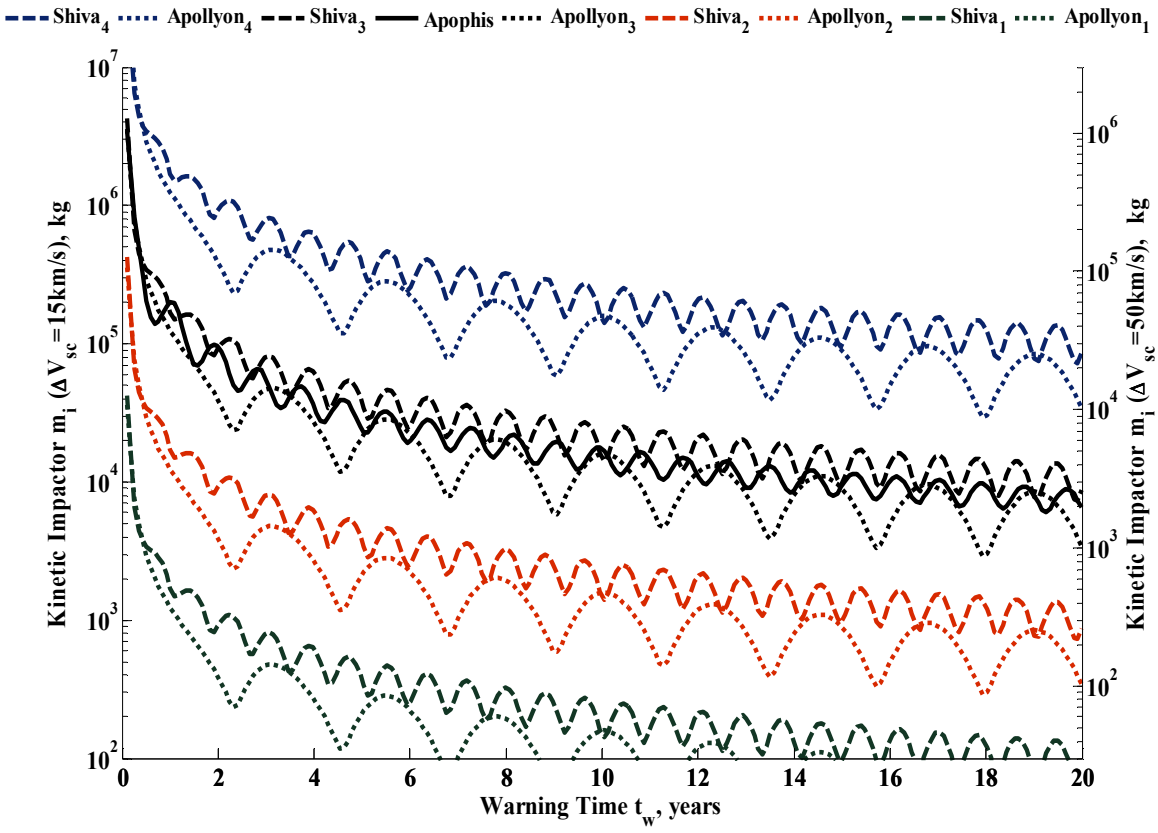

Fig. II-8 Impactor mass required to achieve the minimum deflection distance from Earth as a function of warning time t_w. Left Y axis shows results for a 15 km/s impact, while right Y axis presents a 50 km/s calculation.

It is interesting to note from Fig. II-8 how threatening asteroids of the size of *Apophis* could be easily deflected by impacts with only a few thousand kilograms of mass and velocities of around 50km/s if enough warning time is available. This makes this simple deflection method an interesting alternative to other technologically more demanding methods. Retrograde impacting trajectories could provide this deflection method with impact velocities in the order of 60 km/s[56] and, as demonstrated by the results of the first

Global Trajectory Optimization Contest[57], this kind of trajectories are possible even without using advance propulsion systems.

II.3. Spacecraft Propulsion

A straightforward mitigation strategy could consist of a spacecraft landing on the asteroid and using its propulsion system to push the asteroid off the impact trajectory. Either traditional chemical propulsion or low thrust propulsion systems could be used. Chemical propulsion provides very high thrust, but the excess velocity of the exhaust gasses is about ten times lower than that of the ionized plasma of low thrust propulsion systems and thus requires much more propellant to deliver the same change in the linear momentum of the asteroid. For this reason a strategy based on a high thrust chemical engine was considered less efficient than a strategy with a low-thrust engine.

On the other hand, for electric propulsion (or low thrust approaches in general) the rotation of the asteroid becomes an issue. On a rotating asteroid the thrust vector of the system will not maintain a constant pointing. The propulsion system will have to be switched on and off when the correct thrusting direction occurs or the asteroid rotation will have to be modified so that the propulsion system can be continuously active[39]. Another issue for such a mitigation approach is the definition of an appropriate attachment system between the propelling spacecraft and the asteroid. Finally, a problem pointed out by *Scheeres et al.*[58] is the possible formation of a transient atmosphere due to the surface operations: the combination of loose regolith and low gravity could result in a transient atmosphere of dust that could potentially affect the spacecraft mechanics and operations leading to contingencies.

Depending on how the thrust is applied and controlled we can divide the class of propulsion-based deflection methods into three subclasses: scheduled low-thrust, de-spin and push or precession and push.

In the following sections the scheduled low thrust model will be described in detail. The other possible low thrust techniques will be briefly outlined and then compared to the scheduled thrust option. For a detailed discussion of these alternative techniques the interested reader can refer to the work of *Scheeres et al*[39].

II.3.1. Scheduled Low Thrust Model

The scheduled thrust model assumes a mission in which two spacecraft land on opposite sides along the equator and thrust through the centre of mass of the asteroid. By properly scheduling the periods when the engines are switched on and off, we can obtain a quasi-constant thrust and a limited scattering factor. The scattering factor takes into account the misalignment from the optimal thrusting direction, so that when multiplied by the thrust of the engine we obtain the effective force applied in the optimal thrusting direction.

The total thrust of the system, i.e. the thrust of both engines together, is calculated using the following linear relationship:

$$T_n = m_{power}\frac{\xi}{\tau} \tag{2.21}$$

where m_{power} is the mass of the power subsystem, τ is the mass-to-power ratio and ξ is the specific thrust. The specific thrust ξ is set equal to 34 mN/kW which represents an average value for the most common ion thrusters[51]. It is also assumed that the available power is generated by a subsystem with a mass which is 50% of the dry mass of the spacecraft, $m_{\text{power}}=m_{\text{d}}/2$, and capable of delivering 40 watts per kilogram (τ = 25 kg/kW[51]).

The mass of the system at the arrival at the asteroid m_i includes the propellant mass for the manoeuvre and the dry mass m_d of the spacecraft. Since the thrust of the propulsion system is fixed by the dry mass m_d and will remain constant for the whole mission, the total impulse I_t produced by the propulsion system on the asteroid can be computed as follows:

$$I_t = \int_{t_0}^{t_f} F dt = T_n\left(\frac{t_f - t_0}{2}\right) \tag{2.22}$$

where $F = T_n/2$ is the net force applied to the asteroid. Now, the total impulse can also be computed using the variation in linear momentum produced by the ionized gas expelled from the propulsion system:

$$I_t = -\int_{t_0}^{t_f}\frac{dm}{dt}v_e dt = (m_i - m_d)v_e \tag{2.23}$$

By combining Eqs.(2.21)–(2.23), we can obtain the dry mass m_{d} as a function of the initial mass m_{i} and of the duration of the pushing action $t_{push} = t_f - t_0$:

$$m_d = \frac{m_i}{\left[1+\frac{\xi}{2\tau I_{sp} g_0}\frac{t_{push}}{2}\right]} \tag{2.24}$$

The manoeuvre could be as long as the time left before the asteroid impacts the Earth, although pushing for so long is not necessarily the best strategy. Since the dry mass depends not only on the initial mass, but also on the duration of the deviation manoeuvre, see Eq.(2.24), a better option may be to reduce the duration of the pushing maneuver to achieve a higher dry mass for a fixed initial mass, which then translates into a better level of thrust (see Eq.(2.21)).

An analysis of the achievable deviation as a function of the manoeuvre duration was performed for several different asteroids chosen from the three groups of NEOs, i.e., Apollo, Aten and Amor[5]. Given an initial spacecraft mass m_i and a warning time $t_{w,}$ the achieved deviation was computed by numerically integrating Gauss' planetary equations over a variable pushing time. This procedure was applied to the set of different asteroids, analysing the total achieved deviation as a function of the proportion α of the total time available for applying the deviating action, $\alpha = t_{push}/t_w$, and varying the latter from 7 days to 20 years of warning time. Fig. II-9 is an example of the aforementioned analysis applied to the Apollo asteroid Itokawa(25143), Table I-3 describes the main characteristics of this object.

Table II-3 Itokawa(25143). Information is updated from JPL solar system dynamics[23] as of November 2008.

a (AU)	*e*	*i* (deg)	Ω (deg)	ω (deg)	*M* (deg)	*Epoch* (MJD)	Diameter (m)	Density (g/cm^3)	Mass (kg)
1.324	0.280	1.622	69.1	162.8	350.8	54800	333	1.9	3.5x10^{10}

Fig. II-9 shows the total achieved deviation (right axis) and the total impulse (left axis) for a low-thrust deviation mission at asteroid Itokawa as a function of the pushing time proportion α. For this example, the mass of the spacecraft at the beginning of the pushing action was fixed to be m_i = 10,000 kg and the maximum available pushing time was fixed to 10 years. The results show how the maximum deviation is not achieved when the spacecraft is pushing for the whole available time before the collision. It is, instead, more convenient to use a higher thrust for a shorter time.

[5] A total of eight different objects were used for the analysis: Itokawa, Castalia and Apollyon as Apollo asteroids, Apophis, 1999KW4 and Shiva as Atens asteroids and Nyx and Quetzalcoalt as Amor asteroids.

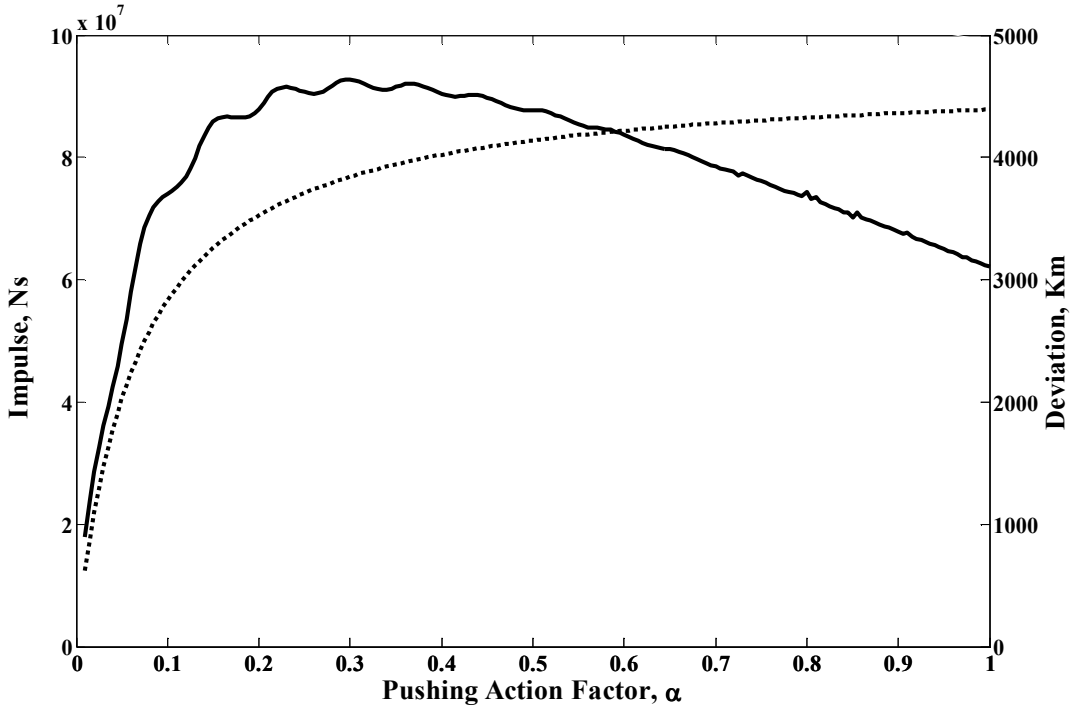

Fig. II-9 Total impulse and deviation achieved for a varying α. The impulse is represented by the dotted line, while the deviation is the solid line.

Thus, for each different scenario, the length of the pushing manoeuvre can be optimized to achieve the maximum deflection. Nevertheless, a numerical search of the optimal duration of the low thrust manoeuvre is computationally expensive. The analysis carried out in chapter III would have required several months in order to perform a single multi-objective optimization of the low thrust method if the optimal duration of the pushing manoeuvre would have been computed at each single run of the model. Therefore a quick estimation of the thrust duration was required. The result in Fig. II-9 suggests stopping the pushing manoeuvre after the last perigee passage before 50% of the time between the arrival at the asteroid t_0 and the impact date, which is also satisfied for any warning time larger than several complete asteroid's orbits (i.e., 2-3, approximately). For mission scenarios with very short warning times (less than 3 years) the low thrust method would push the asteroid all the available time.

The aforementioned prediction of the duration of the pushing action matches the maximum deviation for all the asteroids considered here and for any warning time with an average error of less than 2% and a maximum error of 8%. Taking into account that thrusting throughout the entire available warning time results in deflections, which are on average, 17% smaller than those achieved after optimizing the duration of the thrusting manoeuvre, together with the fact that the aforementioned prediction reduces the

computational time by a factor of 40, we can conclude that the approximate prediction is a good compromise between improving the efficiency of the low thrust method and reducing the computational time. At this point, given the duration of the thrusting manoeuvre, the mass of propellant and the thrust can be calculated with Eq.(2.24).

II.3.2. Efficiency of the Scheduled Thrust

In order to measure the efficiency of the scheduled thrust, compared to a continuous thrust directed along the optimal direction, we can define the *scattering factor* S_{sc} as:

$$S_{sc} = \frac{\int_0^{l_{rotation}} (\vec{F} \cdot \hat{v}) dt}{\int_0^{l_{rotation}} \vec{F}_{optim} dt} \tag{2.25}$$

where the integrations are along one complete asteroid rotation l_{rotation}, $\hat{v}$ is the unit vector along the optimal thrusting direction, $\vec{F}$ is the force vector delivered by the propulsion system attached to the asteroid and $\vec{F}_{optim}$ is a force vector with equal magnitude but always directed along the optimal direction $\hat{v}$.

If we assume that the asteroid is spinning much faster than it is orbiting around the Sun, we can define an asteroid orbit inertial reference frame and an asteroid equatorial inertial frame as shown in Fig. II-10.

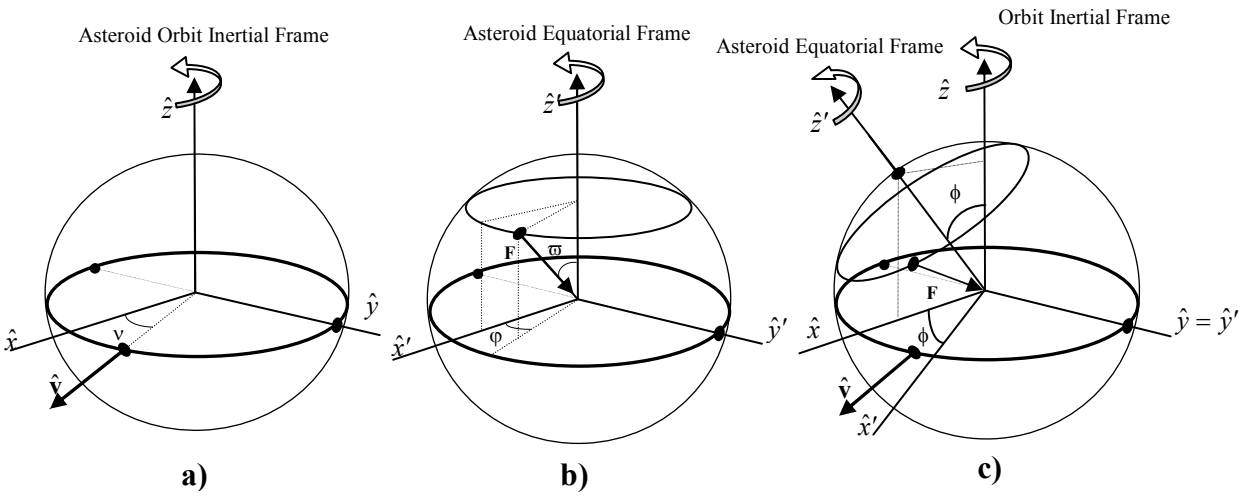

Fig. II-10 *a*) Asteroid inertial orbital frame, *b*) asteroid equatorial inertial frame, *c*) a composition of both frames together.

In the asteroid orbit frame, Fig. II-10a, the angle ν is the angle between the orbital velocity and the $\hat{x}$ axis, this angle will perform a 360-deg rotation at every orbit. In the asteroid equatorial frame, Fig. II-10b, the angle φ is the angle between the projection of the force vector on the $\hat{x}'\hat{y}'$ plane and the $\hat{x}'$ axis. The angle φ will perform a full revolution at every rotation of the asteroid. The obliquity of the asteroid's equator ϕ is the rotation angle necessary to align the asteroid's orbital inertial coordinates with the asteroid equatorial inertial coordinates. Eq.(2.25) can now be re-written as follows:

$$S_{sc}(\nu,\phi,\varpi) = \frac{\int_{\varphi_0}^{\varphi_f} (|F|\hat{F}(\varphi,\varpi,\phi)\cdot\hat{v}(\nu))d\varphi}{\int_0^{2\pi} |F|\hat{v}(\nu)d\varphi} \tag{2.26}$$

where the integration limits φ_0 and φ_f are chosen so that the scalar product $\hat{F}\cdot\hat{v}$ is positive in order to have a constant increase in the asteroid linear momentum.

Integrating Eq.(2.26) along a complete orbit, i.e., ν from 0 to 2π, and dividing by 2π, we obtain an average *scattering factor* that depends only on the obliquity of the asteroid and the complementary latitude ϖ of the landing site. Fig. II-11 shows the *scattering factor* as a function of the obliquity angle ϕ and of the complementary latitude ϖ. The figure shows that for every obliquity it is always possible to choose a landing site that guarantees a *scattering factor* not lower than 0.25. Therefore, it is always possible to have at least 25% of efficiency of thrust without changing the rotational state of the asteroid. Note that this analysis does not depend on the asteroid shape but only on the obliquity of the asteroid's equator, thus the efficiency of the scheduled thrust is not affected by the asteroid shape.

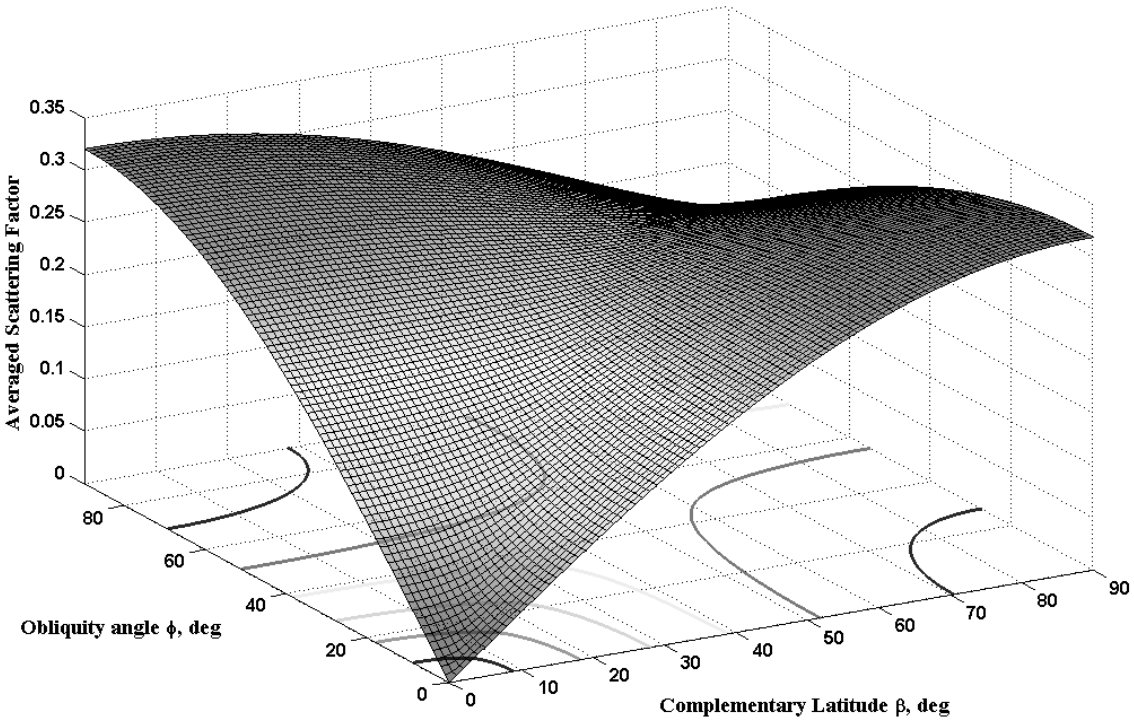

Fig. II-11 Averaged scattering factor

II.3.3. Analysis of Alternative Pushing Methods

Two alternatives have been suggested in order to solve the problem caused by the asteroid's rotation: asteroid de-spinning and simultaneous precession and push. Both techniques require a modification of the spinning rate of the asteroid. The de-spin method is a three phase method; during the first phase the low thrust propulsion is used to stop the rotation of the asteroid, next, a new rotational state is imposed in order to match the asteroid's orbital period, then the propulsion system is used to push the asteroid out of the collision trajectory. The second alternative requires one to re-orient the asteroid rotational pole and, as demonstrated by *Scheeres et al.*[39], there is always an axial tilt that allows a continuous thrust while maintaining a constant relative orientation between the rotational axis and the optimal thrusting direction.

Fig. II-12 shows the effective total impulse produced by each one of the aforementioned techniques for a wide range of thrust levels. The effective total impulse for the scheduled thrust is the product of the thrust, scattering factor and pushing time. The effective total impulse for the de-spin method instead is the product of thrust and available pushing time once despin has been achieved. Finally, the effective total impulse for the

precession-push method is the product of the thrust component in the direction of the asteroid velocity and the pushing time.

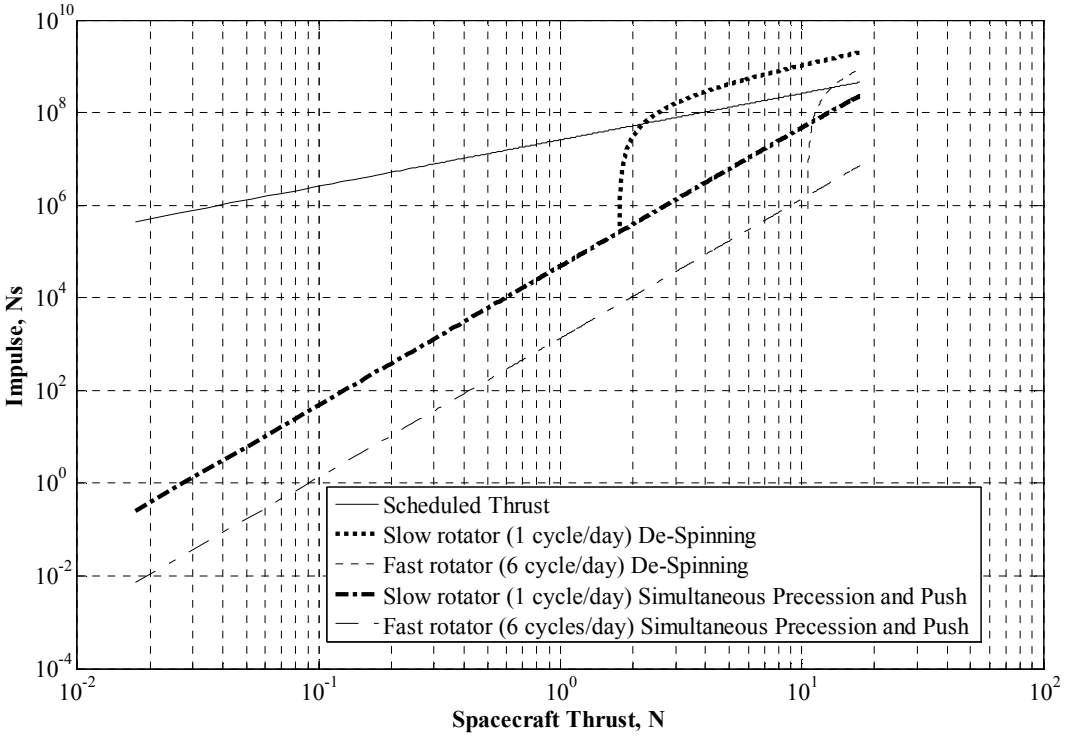

Fig. II-12 Comparison among three possible low-thrust strategies for a wide range of thrust levels and 20 years of pushing time.

As can be seen in Fig. II-12, the de-spinning technique requires a minimum level of thrust in order to stop the rotation of the asteroid before impact with the Earth. This minimum thrust level depends on the angular velocity of the asteroid's rotation and the time available for despinning and deviating the asteroid. On the other hand, for the simultaneous precession and push, considering that the asteroid already has the correct configuration to start the deviating manoeuvre as soon as the spacecraft arrives, the faster the rotation is, the higher the fraction of thrust that goes into controlling the precession, hence less variation of the linear momentum for the same propellant consumption. For the analysis in Fig. II-12, the maximum available time was set to 4 years for all the low-thrust methods.

In the remainder of this thesis, all analyses on the low-thrust propulsion method will consider only the scheduled approach, since, as Fig. II-12 shows, the scheduled thrust method performs well for all thrust levels, spinning rates and available pushing time considered. Besides, the scheduled thrust method is the simplest concept among the three options and thus the most technologically feasible option. Both the de-spin method and the simultaneous precession and push would require a gimballing attachment which would

allow pushing in directions other than the perpendicular to the asteroid surface. On top of these technological issues, the scheduled thrust represents the most robust option in terms of asteroid uncertainties, since the other two options are affected by the asteroid shape and rotation.

II.3.4. Low Thrust Deflection Mission Sizing

Again, we will use the low thrust model to deflect the virtual asteroids outlined in Chapter I by a minimum Earth-asteroid deflection distance (see Section I.5 in Chapter I). As done previously, the Earth-asteroid transfer is not considered and the initial mass m_i refers to all the mass remaining after the Earth-asteroid transfer. This includes the dry mass of the spacecraft and the propellant to be used during the pushing operations. Fig. II-13 shows the minimum initial mass m_i required to achieve the minimum asteroid deflection to avoid the collision of each test case asteroid as a function of warning time t_w. Unlike in the impulsive deflection models (see Section II.1.7), in the low thrust methods the calculation of the deflection distance $\delta\mathbf{r}$ is not achieved by means of the transition matrix Eq.(6.7), but by integrating instead the Gauss's planetary Equations (Eq.(6.2)). The results of a root-finding algorithm searching for the mass m_i that provides the required minimum deflection at different warning times t_w are shown in Fig. II-13. The direction of the thrust used in this analysis is that that achieves maximum deflection (see Section A.1.5).

Considering that 50,000kg was the maximum payload capability for Earth-Moon transfer insertion of the legendary Saturn V rocket, used by NASA during the Apollo and Skylab programs or that 10,500kg is the GTO-payload mass capability of the modern Ariane 5, we can grasp the technological difficulties that a low thrust mission to deviate the largest asteroids considered in this thesis would pose. This technology may however be very suitable for the lower range of the masses considered here (i.e., $\leq 5x10^9$ kg).

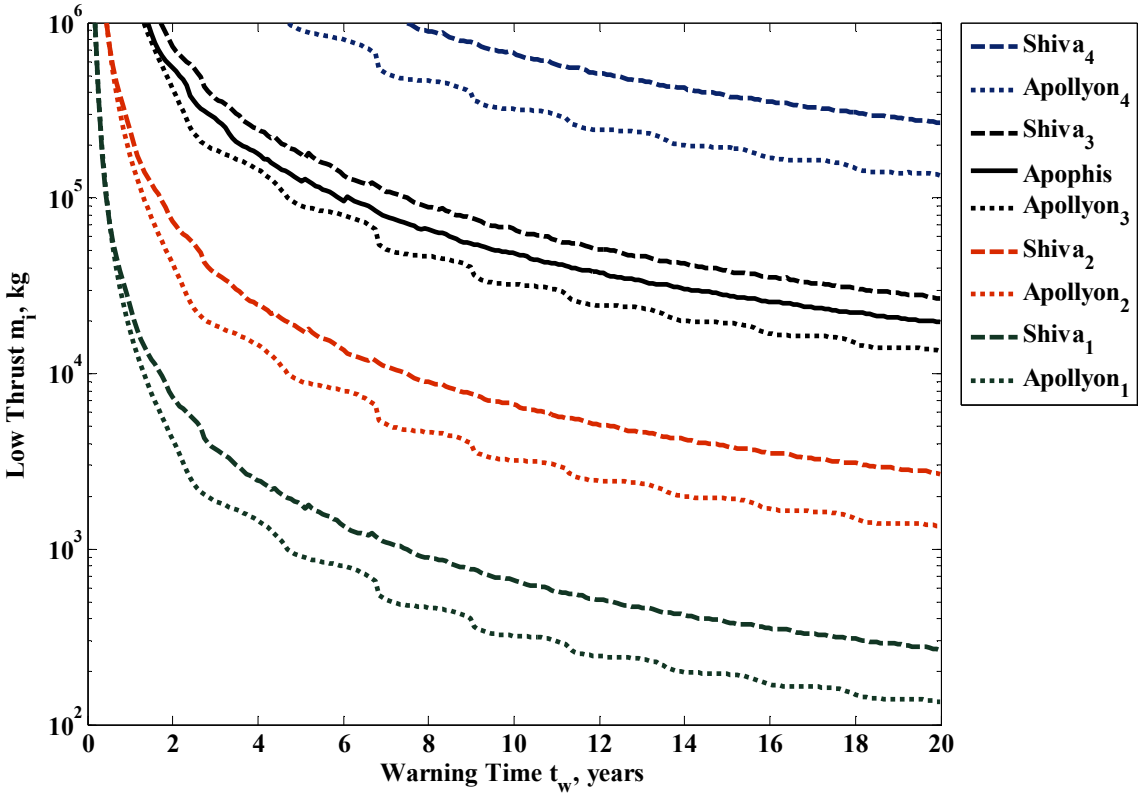

Fig. II-13 Mass required for a low thrust deflection mission capable to deflect each one of the studied test case by distance equal to the minimum Earth-asteroid distance. The list of test cases in the legend is ordered following the results of the required m_i.

If one of the most remarkable features of Fig. II-7 and Fig. II-8, both impulsive mitigation methods, was the oscillatory behaviour of the interception mass m_i, an outstanding feature of all low thrust methods is the almost absence of it. If the low thrust method entails pushing or pulling the asteroid during several orbital periods, the oscillatory behavior will become smoother, although may not disappear completely, like in this case for all the *Apollyon* asteroids.

II.4. Mass Driver

The mass driver system generates a change in the velocity vector of the asteroid by shooting into space pieces of the asteroid outer crust. Surface material is dug by a drilling device and accelerated into space through an electromagnetic railgun. The advantage of this strategy is that the material used to change the linear momentum of the asteroid is obtained in situ and not carried from Earth.

Fig. II-14 Multi-mass driver concept from *J.Olds et al*[43].

II.4.1. Mass Driver Model

The model for the mass driver was developed assuming that a spacecraft with mass m_d lands along the equator of the asteroid and directing the railgun along a line perpendicular to the rotation axis, which is assumed to be perpendicular to the velocity vector of the asteroid. Furthermore, it was assumed that when the railgun is not pointing in an optimal direction, the mass driver is collecting material. The dug material is shot once per rotation when optimal pointing conditions within a given tolerance are met.

The mass of the power subsystem was assumed to account for 30% of the dry mass m_{d}, which is in agreement with the results obtained by J. Olds[43]. The mass-to-power ratio τ was set to 25 kg/kW[51], which is an averaged value for the power sources most commonly used in space. The energy efficiency of the railgun was set to 30%[59], hence approximately one third of the electrical energy generated by the power source is transformed into kinetic energy:

$$P_K = 0.3\frac{m_{power}}{\tau} \tag{2.27}$$

where $m_{power} = 0.3 \cdot m_d$ is the mass of the power system and P_K is the total power converted into kinetic energy.

In literature, a value of 100-300 m/s is considered as a realistic excess velocity for the expelled mass[43],[50]. In this work, an excess velocity of 200 m/s, which is within current

technological capabilities[59], has thus been chosen for all the analysis. Given the excess velocity, the mass expelled per shot can be calculated with the following equation:

$$m_{launch} = \frac{2P_K \Delta t_{shooting}}{v_e^2} \tag{2.28}$$

where $\Delta t_{\text{shooting}}$ is time available to shoot the dug material into space, which was set equal to the time required by the pointing vector of the railgun to span a 10 degrees arc around the rotation axis of the asteroid, i.e., $\Delta t_{shooting} = \left(1/36\right) T_{rot}$, where T_{rot} is the rotational period of the asteroid. The power generated when the mass driver is not shooting (97% of the time) is sufficient for the mining system, e.g. a coring drill, to prepare the next projectile[60],[61].

The change in the velocity of the asteroid is determined by using the conservation of linear momentum and taking into account the change in the asteroid mass consequent to every shot:

$$\delta v = \frac{m_{launch}}{M_a(t)} v_e \tag{2.29}$$

At each impulsive δv there is a corresponding finite variation of the orbital elements of the asteroid and the new set of orbital parameters has to be calculated before the subsequent impulsive action.

Note that, similarly to the low-thrust method, the mass driver generates a δv only when the railgun points in the correct direction. The performance of this method, therefore, is not affected by the shape of the asteroid but only by its rotational state.

II.4.2. Mass Driver Mission Sizing

Again, as in previous sections, the mass diver interception mass m_{i} required to achieve a given deflection δr_0 with a warning time t_w can be calculated through the root search of $\delta r_0 - \left|\delta \mathbf{r}(m_i, t_w)\right|$, where $\delta \mathbf{r}(m_i, t_w)$ is yielded by the combination of the mass driver model and the deflection formulas described in the Appendices (see Section A.1). Fig. II-15 shows the mass m_{i} required to deflect each one of the test cases from Chapter I a distance equal to the minimum deflection distance (see Section I.5). As expected, the multi-impulsive manoeuvre of the mass driver provides an interception mass m_{i} showing the same features as the low thrust method, although, when compared with Fig. II-13, the good performance of the mass driver concept is noteworthy.

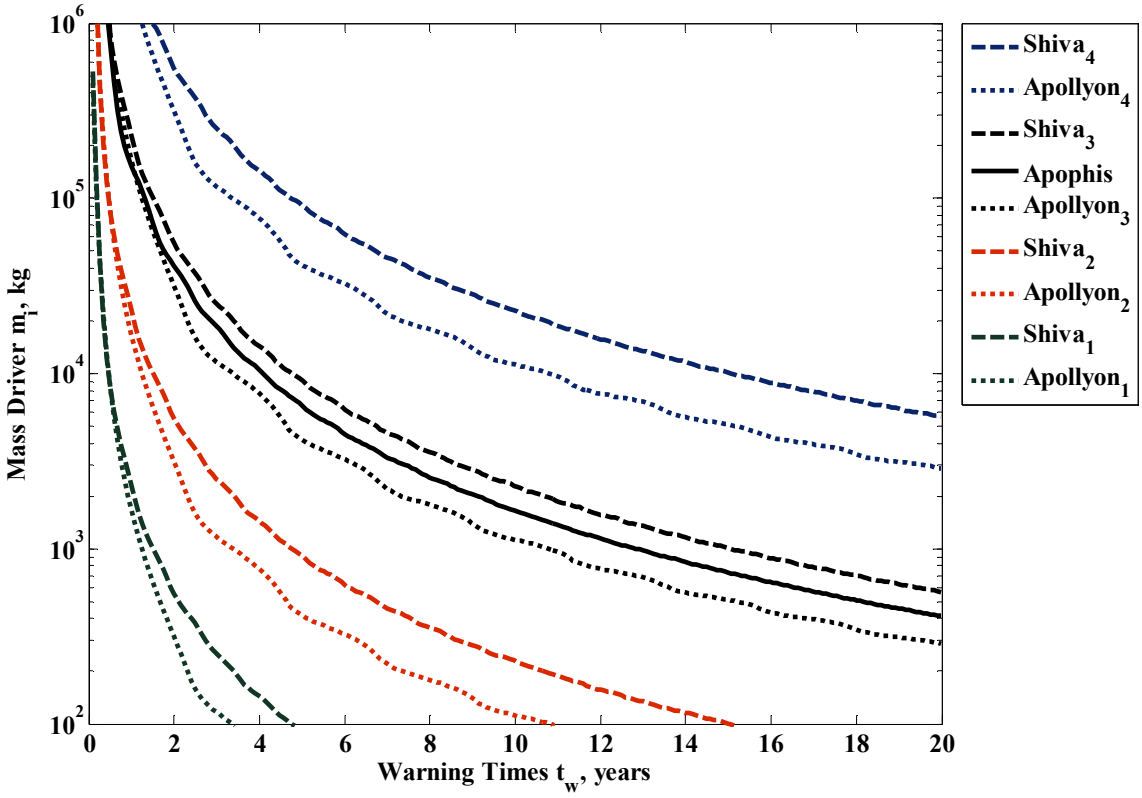

Fig. II-15 Mass Driver size required to deflect each one of the studied test case by distance equal to the minimum Earth-asteroid distance. The list of test cases in the legend is ordered following the results of the required m_i.

II.5. Solar Collector

In 1994, *Melosh et al.*[42] proposed the use of a mirror to focus the solar energy onto a small portion of the surface of the asteroid. The resulting heat sublimates the surface material creating a jet of gas and dust that produces a continuous thrust. This thrust ultimately alters the orbit of the asteroid in a similar fashion to how a comet's orbit is altered by the expulsion of material from surface jets. A conceptually similar idea is to use a laser beam, either powered by a nuclear reactor or solar arrays, to induce the required sublimation of the surface material. In the following, a model is proposed to compute the deviating acceleration due to the flow of gases derived from the sublimation of the asteroid's surface. Although applicable to both the solar collector and laser beam concepts, the spacecraft model that will be described in the following analyses will be based on the use of a solar concentrator. This choice was motivated by the expected mass of the laser together with the power unit required to operate it: after a first estimation, the mass of a deployable mirror resulted to be smaller than the equivalent mass of the laser plus power unit. However, this does not intend to rule out the laser option; on the contrary, although, a

more detailed spacecraft system analysis might demonstrate that the laser option is more advantageous than the solar collector, the sublimation model presented in this section maintains validity and the resulting conclusions are applicable to either approach.

II.5.1. Spacecraft Model

It is assumed that the solar concentrator is made of a layer of reflecting material mounted on an inflatable supporting structure[62]. The inflatable structure, together with the deployment system, attachments and related harnessing are assumed to account for 30% of the total dry mass of the spacecraft, thus allocating to the solar collector itself the 30% of dry mass representing payload of the spacecraft[51]. From the work of *John M. Hedgepeth*[62],[63] the mass-to-area ratio of the inflatable solar concentrator is estimated to be 0.1 kg/m^2. This is a conservative estimate when compared with the size and mass of space experiments such as Znamya and Echo balloons. The size of the spacecraft is related to the amount of energy focused on the surface of the asteroid through the concentration ratio. This is defined as the area of the reflective surface over the area of the illuminated spot. Concentration ratios between 2000 and 3000 are possible for space solar concentrators[63]. In the following, a concentration ratio of 2500 will be used, which is equivalent to a diameter for the illuminated spot 50 times smaller than the diameter of the mirror.

II.5.2. Thermal Model of an Asteroid

If a beam of light is focused onto the surface of the asteroid, the received power density can be calculated by using:

$$P_{solar} = \eta_{eff} \frac{S_{flux}}{r_{fi}^{\,2}} \frac{A_m}{A_s} \left(1 - p_v\right) \tag{2.30}$$

where A_m is the cross-section area of the reflective surface of the mirror, perpendicular to the direction of the solar radiation, A_s is the area of the illuminated surface on the asteroid, $\eta_{eff} = 90\%$ is the efficiency of the mirror assembly, $S_{flux} = 1367$ W/m^2 is the solar flux at 1 AU, r_{fi} is the distance from the spacecraft to the Sun, which scales the solar flux, and the albedo p_v was chosen as 0.2. This value approximates the albedo of a S-type asteroid, the surface of which is mostly composed of olivine. For the specific deviation method under investigation an albedo of 0.2 would correspond to a worst case scenario.

The time a portion of the surface spends under the spot beam is a function of the angular rotation of the asteroid and of the size of the spot. This last parameter is also function of the size of the mirror and the concentration ratio. The thermal model assumes the system (i.e., asteroid) to be an infinitely long rod, with the illuminated spot on one side of it. The illuminated surface is at a temperature of 1800 K, which is the sublimation temperature of forsterites[49]. The long rod model represents a good approximation of the real system. In fact it can be proved that the conduction loss through the perimeter of this rod is much smaller than the energy loss due to the movement of the surface (i.e. asteroid rotation with a fixed beam).

Sublimation is due to the total absorbed energy. The net absorbed energy is the total energy focused on the surface minus the radiation and conduction losses. Energy loss due to conduction can be computed by first solving the differential equation for the surface temperature T,

$$\frac{\partial^2 T}{\partial x^2} = \frac{c\rho_a}{\kappa}\frac{\partial T}{\partial t} \tag{2.31}$$

where c is the heat capacity (750 J/kg/K), ρ_a is the asteroid density, and κ is the thermal conductivity (2 W/m/K in this case). The thermal conductivity and heat capacity were calculated using average values from different silicate materials on Earth, which are likely found on asteroids, and proved consistent with the values predicted by *J.L.Remo*[64]. Using the following initial and boundary conditions[6],

$$\begin{aligned} &T(x,0) = T_0 = 278\,K \\ &T(0,t) = T_{subl} = 1800\,K \\ &\lim_{x\to\infty} T(x,t) = T_0 \end{aligned}$$

and applying a Laplace transformation, the above differential equation can be solved to give:

$$T(x,t) = T_0 + \left(T_{subl} - T_0\right)\cdot erfc\left(\frac{x}{2\sqrt{\frac{\kappa t}{c\rho_a}}}\right) \tag{2.32}$$

Finally, to calculate the conduction loss $Q_{\text{cond}} = k\cdot\partial T/\partial x$, the derivative of the temperature profile is calculated through a series expansion of the complementary error

[6] T_0=278K is computed assuming a blackbody radiating isothermal sphere at 1 AU with equal emissivity and absorptivity.

function, $erfc(f(x))$. Therefore, with this model, the heat flux loss by conduction Q_{cond} on the surface of the asteroid ($x = 0$) can be computed using the following expression:

$$Q_{cond} = \frac{T_{subl} - T_0}{\sqrt{\frac{\pi t}{c\kappa\rho_a}}} \tag{2.33}$$

II.5.3. Rate of Expelled Mass

The heat generated by sunlight will produce a flow of sublimated mass m_{exp}. Part of the energy goes into the sublimation process and part into the acceleration of the expelled mass m_{exp} . The mass flow rate can be computed as:

$$E_v \frac{dm_{exp}(t)}{dt} = \Delta Q = P_{solar} - Q_{out} \tag{2.34}$$

where E_v is the sublimation enthalpy, $dm_{exp}(t)/dt$ is the flow of sublimated mass and Q_{out} is the sum of the conduction heat loss Q_{cond} and the radiation heat loss Q_{rad} . The radiation heat loss Q_{rad} is defined according to the black body radiation formula as:

$$Q_{rad} = \sigma\varepsilon_{bb}T^4 \tag{2.35}$$

where σ is Stefan-Boltzmann constant, and ε_{bb} is the black body emissivity. Expanding the terms in Eq.(2.34) and solving for the mass flow, gives:

$$\frac{dm_{exp}}{dt} = \frac{1}{E_v}\left(P_{in} - Q_{rad} - Q_{cond}\right) \tag{2.36}$$

In order to calculate the total sublimated mass, Eq.(2.36) is integrated over the surface area under the illuminated spot. Note that, if the mass flow rate dm_{exp}/dt is negative, then there is not enough energy to sublimate the asteroid surface. Consequently, the limits of the integration have to be adjusted to avoid negative results. The horizontal surface position, *x,* and the illumination (or exposure) time can be related through the rotational velocity, v_{rot}, such that $x = v_{rot} \cdot t$ and $dx = v_{rot} \cdot dt$. Therefore, the integral can be rewritten in terms of the exposure time *t*, where the limits of the integration t_{in} and t_{out} are the times at which the asteroid surface moves inside and outside of the illuminated spot. Thus, the total mass flow is:

$$(\dot{m}_{exp})_{total} = 2v_{rot}\int_0^{y_{max}}\int_{t_{in}}^{t_{out}} \frac{1}{E_v}\left(\left(P_{in} - Q_{rad}\right) - \left(\sqrt{\frac{c\kappa\rho}{\pi}}\left(T_{subl} - T_0\right)\right)\sqrt{\frac{1}{t}}\right) dt\, dy \tag{2.37}$$

which is solved in detail in the Appendix A.3.

II.5.4. Total Induced Acceleration

Once the flow rate of evaporated material is computed, the average velocity of the particles is determined by using the Maxwell distribution for particles of an ideal gas:

$$\bar{V} = \sqrt{\frac{8kT_{subl}}{\pi M_m}} \tag{2.38}$$

where M_m is the mass of a single molecule of forsterite (Mg_2SiO_4) and k the Boltzman constant.

The acceleration a_{solar} achieved by the asteroid due to the sublimation process, can be calculated by dividing the thrust produced by the evaporation of the surface material and the remaining mass of the asteroid[7], corrected through a scattering factor S_{sc} which accounts for the plume dispersion:

$$\left\| \mathbf{a}_{solar} \right\| = \frac{\left(S_{sc} \cdot \bar{V} \cdot (\dot{m}_{\text{exp}})_{total} \right)}{M_a(t)} \tag{2.39}$$

The scattering factor was computed assuming that the particles of debris and gas are accelerated uniformly over a semi-sphere, which corresponds to a 180 degrees plume cone. By integrating over the semi-sphere the effective components of the acceleration we get a value $S_{sc} = \frac{2}{\pi}$.

Fig. II-16 shows the effects of the radiation and conduction heat losses, as well as the thrust delivered by a 100 meter diameter mirror. In this simulation, the asteroid is assumed to have zero rotational velocity, but the exposure time varies between 0 and 30 seconds. As can be seen, below 5 seconds of exposure time the thrust level drops significantly.

[7] The asteroid mass M_a decreases due to the evaporation and, although for most of the cases the loss of mass is insignificant, for some cases it has in fact important effect, e.g. for a 100-meter diameter mirror the mass flow rate is of the order of 1 kg/s, which for small asteroids and given enough time can have a very significant effect.

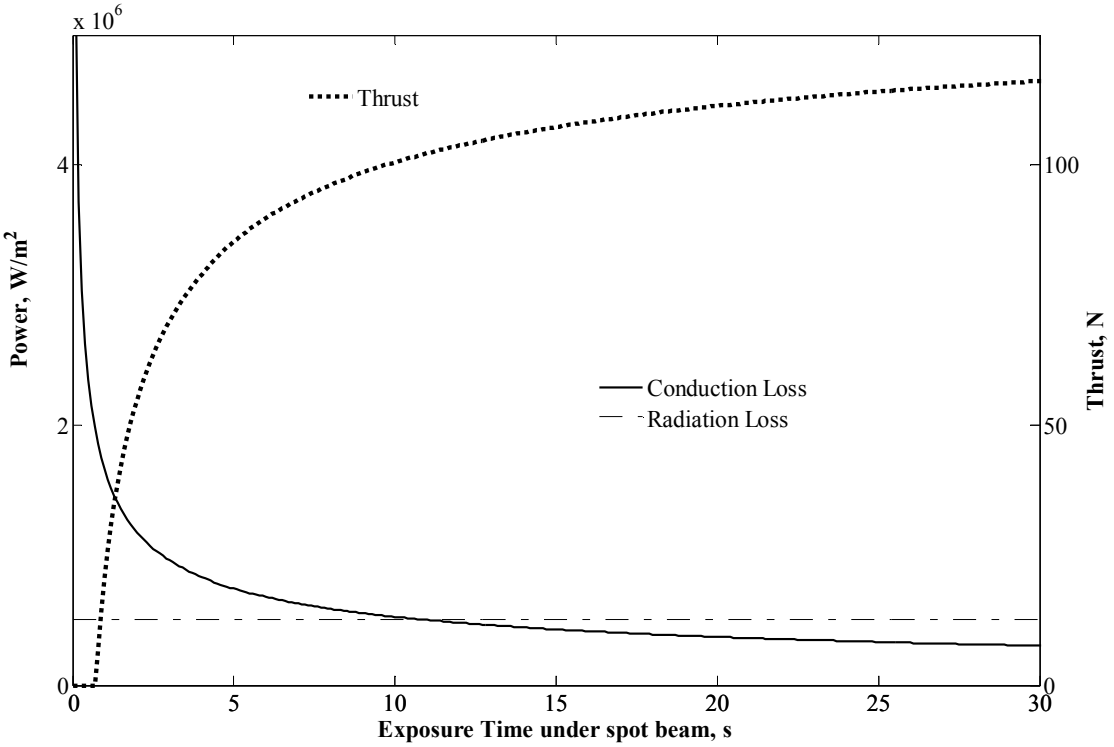

Fig. II-16 Energy loss (left axis) and thrust (right axis) for a 100-meter diameter mirror.

II.5.5. Influence of the Asteroid Spinning Rate

As mentioned above, the exposure time, i.e., the time that the surface spends under the focused solar beam, depends strongly on the rotational speed of the asteroid. Fig. II-17 shows the deviation achieved with a 60 meter mirror imparting a deflection action on asteroid *Apophis*. The deviation was computed by propagating Gauss' planetary equations for a period of two years with the deviating action aligned with the instantaneous velocity vector of the asteroid. As can be seen in the figure, as the rotation speed increases, the achievable deflection decreases monotonically.

In light of the work of *A. W. Harris*[36], the most probable rotation state seems to be about 5.5 cycles/day. For this angular velocity, a mission with a 60 meter in diameter mirror would achieve a deviation of 14,000 km after two years of operations. Since the upper physical limit on the rotational speed is expected to be between 8 to 12 cycles/day[36], Fig. II-17 shows that the deviation achieved with a solar collector, for any possible rotational state, would be at least 70% of the deviation achieved for a 5.5 cycles/day rotator. The upper limit on the rotational speed is assumed to be due to the rotational upper limit for asteroids without cohesive or tensile strength (i.e. rubble piles).

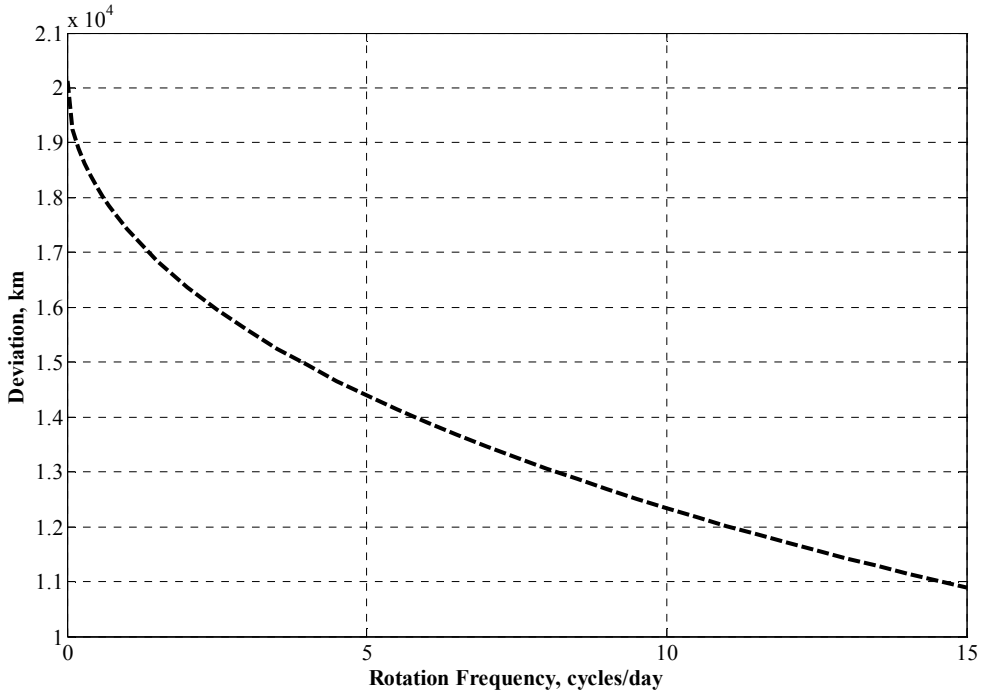

Fig. II-17 Deviation as a function of the rotational speed produced by a 60 m diameter mirror acting on an Apophis-like asteroid during 2 years.

Finally, the elongation of the asteroid combined with its rotational state can affect the performance of this deflection method because the distance of the target spot on the surface of the asteroid from the mirror can vary with time. However, we can assume that the focal point of the mirror can be adjusted to cope with this variation. Adapting the focal point is a technological problem that does not affect the model presented in this section but will be considered later in Chapter III when the Technology Readiness Level of each method is examined. A first analysis of the problem related to focusing and pointing the light of the Sun, can be found in other works by *Maddock et al.*[65] and *Vasile*[66]. In the same works, there is a preliminary analysis of the control of the mirror in proximity of the asteroid.

II.5.6. Solar Collector Mission Sizing

The model described above will be used to deflect some of the virtual asteroids outlined in Chapter I (the procedure explained in Section II.3.4 is also used here). Like in previous mission sizing subsections, the Earth-asteroid transfer is not considered, thus the solar collector interception mass m_i refers to the dry mass of the solar collector system. In Chapter III, where a full comparison among the different deflection methods is carried out, mass margins will be allocated to each deflection methods following technological motivations. These margins will try to account for several issues that have not been addressed explicitly in the models sections from this chapter, as, for example, the station

keeping mass budget. Even if a preliminary analysis[65],[66] can show that the station keeping mass budget will not modify to a great extent the results of the solar collector model, the operational cost of very long deflection manoeuvres (e.g. lasting several years) will substantially increase the cost not only of a solar collector deflection, but of any deflection requiring many years of highly accurate manoeuvring and control. Hence, a six-month limit of operations was set for the results in this section, minimizing, then, possible operational cost.

Fig. II-18 plots the diameter of the solar collector required to deflect the virtual asteroids a distance equal to the minimum Earth's deflection distance (see section I.5.). While for short warning times, the size of the mirror structure inferred from Fig. II-18 may be beyond current technological capabilities, it is interesting to see how for long warning times (> 10 years) it is possible to deflect the three medium size asteroids (~$5x10^{10}$kg) with less than 30 m-diameter mirrors. A minimum size of 15.5 meters is still necessary to deflect *Apophis* with 20 years of warning time. Note that some currently flying spacecraft and others that have already flown have similar sizes, e.g. Rosetta wing span of 32 meters. One of the most outstanding features in Fig. II-18 is the very large oscillation in the results for $Apollyon_3$, which escape from the range of diameters considered in the plot. The diameter of the solar collector necessary to deflect $Apollyon_3$ achieves values similar to those for *Apophis* and $Shiva_3$ only for a very short period of its orbit. It is worth remembering that $Apollyon_3$, as all the Apollo asteroids, has a larger semimajor axis than the two Aten asteroids, i.e., *Apophis* and $Shiva_3$, therefore it spends most of its time at much further distances from the Sun than the other two objects. It is only when $Apollyon_3$ is moving close to its perihelion that the solar flux is at its maximum and receives as much solar radiation intensity as *Apophis* or $Shiva_3$ receive during their entire orbits. On the other hand, when the asteroid reaches a distance from the Sun of 2.5 AU, the solar collector method becomes incapable of sublimating any material from the asteroid surface, thus producing no impulse to the asteroid, since the power density is not high enough to render Eq.(2.34) positive. This implies that the energy collected by the mirror is not enough to heat up the surface to the sublimation point.

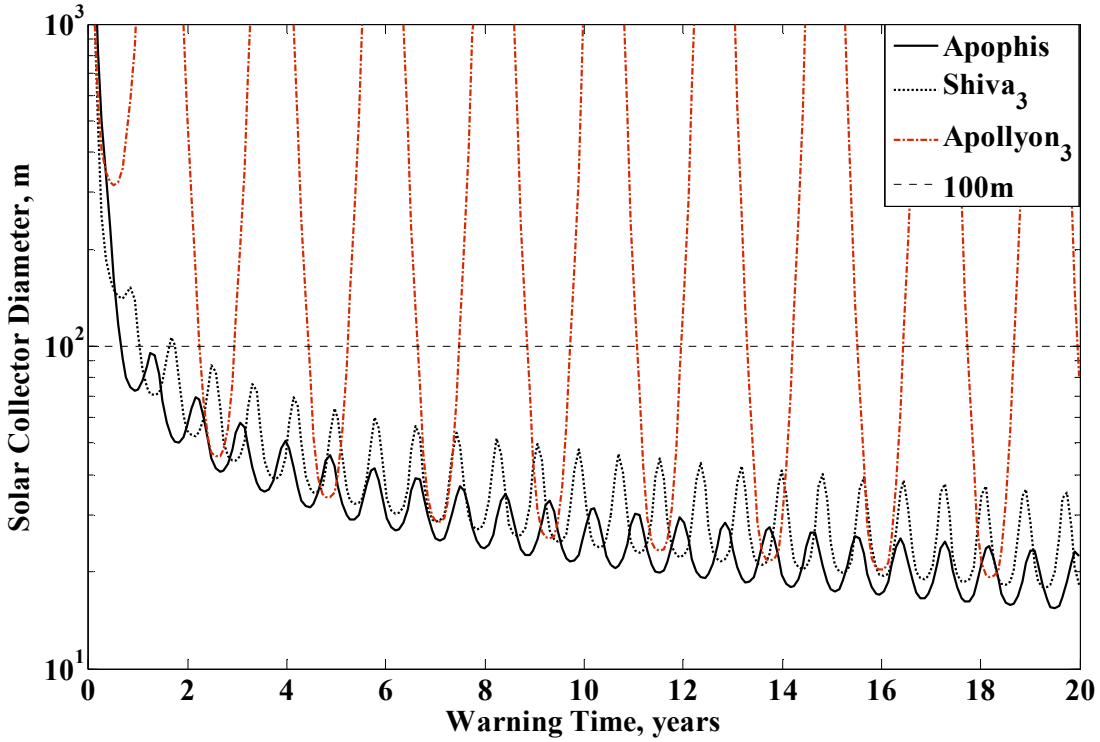

Fig. II-18 Minimum diameter of the Solar Collector able to deflect the threatening asteroid by a minimum deflection distance.

Fig. II-19 presents the solar collector mass m_i as a function of warning time t_w for the complete set of virtual asteroids. As in the nuclear interceptor case, the m_i range goes from 10 kg to 1,000,000 kg. The lower limit should be considered only as an indication of the ease to endeavour the deflection of a small threatening asteroid using the solar collector strategy, since scaling spacecraft to very small sizes can be technologically even more challenging than scaling to very large sizes.

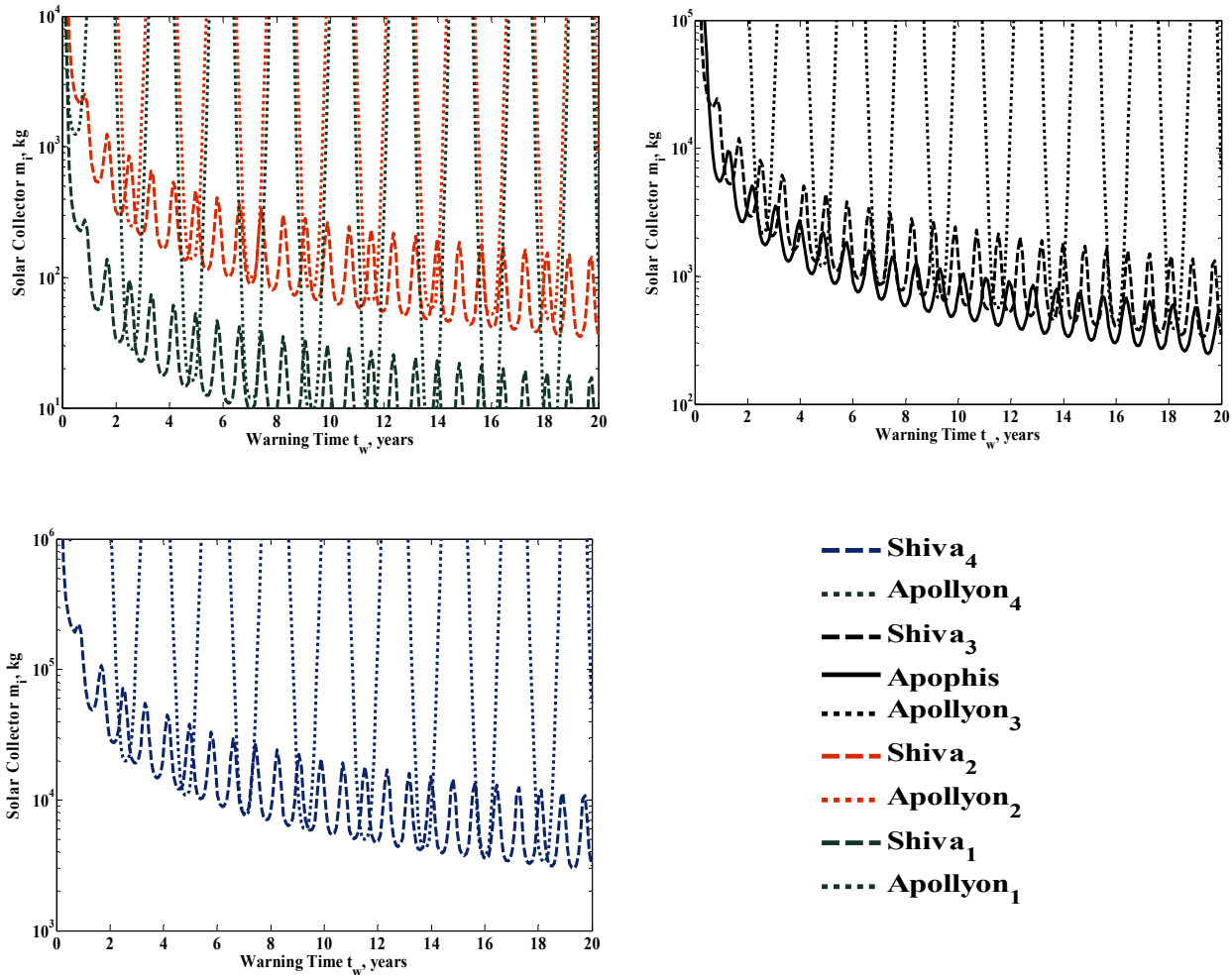

Fig. II-19 Minimum mass of the Solar Collector able to deflect all the virtual asteroids by a distance equal to the minimum deflection distance.

II.6. Gravity Tractor

The gravity tractor exploits the mutual gravitational attraction between an asteroid and a spacecraft to pull the asteroid off its collision course with the Earth. In order to perturb the asteroid in the desired way, the spacecraft should maintain a constant hovering position during the pulling period. This concept was proposed by *Lu & Love*[40] as a means of modifying the orbit of an asteroid, overcoming the uncertainties inherent to the asteroid surface composition, morphology and spinning rate.

II.6.1. System Definition & Architecture

The following hypotheses are used to develop the mathematical model of the gravity tractor:

1. The power subsystem accounts for 50% of the dry mass m_d.
2. The power subsystem is capable of delivering 40 watts per kilogram (τ = 25 kg/kW).
3. The propulsion subsystem generates 0.034 N/kW.

The total thrust T_n of the spacecraft is then computed by using Eq.(2.21). The closer the spacecraft hovers above the asteroid surface the bigger the gravity pull is. However, the exhaust gasses must not impinge on the asteroid surface, otherwise the centre of mass of the NEO-spacecraft system will remain unperturbed: in fact, it is the stream of mass escaping the system which generates a change in the linear momentum of the NEO[67]. Note that, according to the action-reaction principle, using a specific amount of thrust to push the asteroid or using the same thrust to hover above it would lead to the same variation of the linear momentum, hence the same deviation. On the other hand, the thrusters must be properly pointed such that the cone of the exhaust gasses does not intersect the asteroid surface (see Fig. II-20). As a consequence, the effective vertical thrust F_{hover} is always smaller than the total thrust $T_{n,}$.

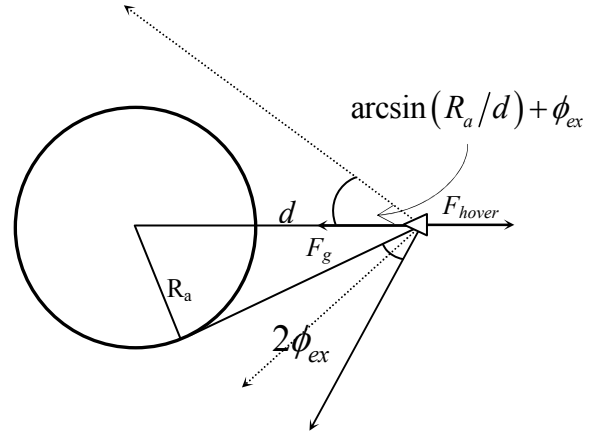

Fig. II-20 Geometric diagram of the Gravity Tug and asteroid configuration.

As mentioned above, the thrusters have to be slanted laterally by an angle $\phi_{ex} + \arcsin(R_a/d)$, where ϕ_{ex} is equal to half the angle of the exhaust cone, in order to avoid the impingement of the propulsion gasses. With this configuration, the hovering distance can be calculated by solving the following system of equations:

$$\begin{aligned} F_{hover} &= T_n \cdot \cos\left(\arcsin\left(\frac{R_a}{d}\right) + \phi_{ex}\right) \\ F_g &= \frac{GM_a m_i}{d^2} \\ F_{hover} &= F_g \end{aligned} \tag{2.40}$$

where F_g is the gravity attraction between spacecraft and asteroid, F_{hover} is the thrust force in the direction of the asteroid, ϕ_{ex} is chosen to be 20 degrees (in agreement with *Lu & Love*[40]), R_a is the mean radius of the asteroid, G is the universal gravity constant, M_a is mass of the asteroid, m_i is the mass of the spacecraft at the beginning of the pulling manoeuvre and d is the hovering distance.

Since the spacecraft is consuming propellant to hold its hovering position, its mass will slowly decrease over time. The reduction in mass would allow the spacecraft either to hover closer to the surface or to reduce its thrust level while hovering at the same altitude. The latter option (i.e., keeping the hovering distance constant) is more advantageous since a reduction in thrust leads to a lower propellant consumption, which in turn translates into a higher mass of the power subsystem for a fixed initial mass into space, which translates into a higher initial thrust and a lower hovering distance. By iterating this process, an optimal hovering point can be found that makes the constant altitude option more efficient than the variable altitude one.

If the constant altitude option is adopted, the mass of the spacecraft at any time t during the pulling manoeuvre can be computed assuming a mass consumption linearly proportional to the pulling action F_{hover} :

$$m(t) = m_i e^{-\left(\frac{GM_a(t-t_0)}{d^2 \cos\left(\arcsin\left(\frac{R_a}{d}\right)+\phi_{ex}\right) I_{sp} g_0}\right)} \tag{2.41}$$

with the acceleration imparted to the asteroid simply given by:

$$a_{gtug}(t) = \frac{Gm(t)}{d^2} \tag{2.42}$$

Therefore, the remaining mass m_d, at the end of a pulling manoeuvre with duration Δt_{tug} is:

$$m_d = m_i e^{-\left(\frac{GM_a \Delta t_{gtug}}{d^2 \cdot \cos\left(\arcsin\left(\frac{R_a}{d}\right)+\phi_{ex}\right) \cdot I_{sp} g_0}\right)} \tag{2.43}$$

and by using Eq.(2.43) in the system of equations (2.40), we obtain:

$$\frac{m_i e^{-\left(\frac{GM_a \Delta t_{tug}}{d^2 I_{sp} g_0 \cos\left(\arcsin\left(\frac{R_a}{d}\right)+\phi_{ex}\right)}\right)}}{2} \frac{\xi}{\tau} \cos\left(\arcsin\left(\frac{R_a}{d}\right)+\phi_{ex}\right) - \frac{GM_a m_i}{d^2} = 0 \tag{2.44}$$

which has to be solved to determine the hovering distance d.

Fig. II-21 shows the total impulse provided by both, the low thrust and the gravity tug methods. It also shows the force produced by these two deviation methods on the asteroid. For a specific low thrust mitigation mission, the force is constant during the whole deviation manoeuvre (note that the monotonic decrease of the low thrust force in Fig. II-21 is due to the fact that the X axis refers to missions with a given duration of the pushing action, the X axis is not the time line of a particular mission), while for a gravity tug mission the force decreases as a function of the mass of the spacecraft. It is interesting to note that, for pulling manoeuvres longer than 13 years the force initially exerted by the gravity tug is higher than the force exerted by a low-thrust spacecraft with equal initial mass m_i. On the contrary, the total impulse is higher for the low-thrust method for deviation actions shorter than 135 years, the moment at which the total impulse provided by the gravity tug becomes higher than the one achieved by the low thrust.

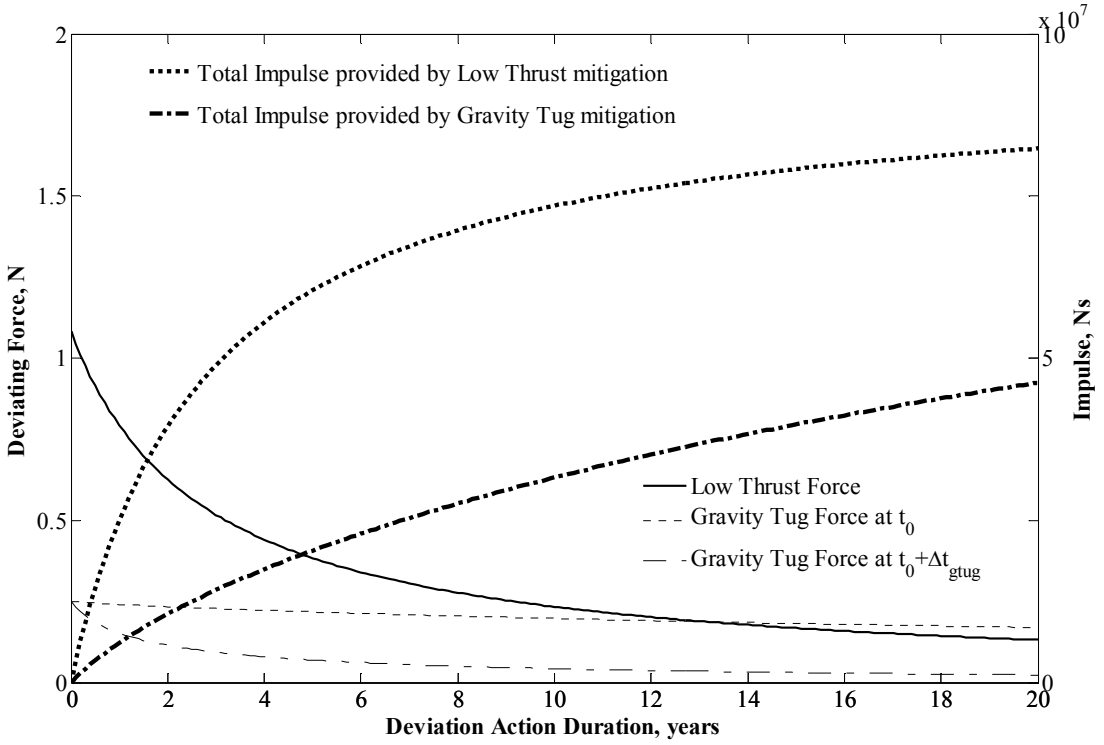

Fig. II-21 Comparison between a Low Thrust mitigation mission and a Gravity Tug for a possible deviation of *Apophis*. Initial mass at asteroid arrival is 5000 kg for both methods.

Before concluding this section it is worth noting that the spacecraft has to hover at a relatively close distance from the asteroid and accurately maintain its position and velocity. Since the shape and composition of the asteroid have an impact on its gravity field, the gravity tractor is not totally immune from the problems related to the unknown composition and morphology. Therefore, hovering control in an inhomogeneous gravity field generated by a non-spherical asteroid is an issue that has to be taken into account. However, a complete analysis of the effect of a non-spherical asteroid on the control of the gravity tug is out of the scope of the work presented here and has already been performed by other authors. The interested reader can refer to the work of *Broschart & Scheeres* and *Kawaguchi et al.* for more details[68],[69].

II.6.2. Gravity Tractor Mission Sizing

Once again, using the method described above, the minimum mass m_i required to deflect by a minimum mitigation distance each one of the test case asteroids using a gravity tractor can be calculated for a varying warning time t_w (see Section II.3.4). The results are shown in Fig. II-22. Clearly, the mass m_i required for a gravity tractor mitigation is large and, on top of that, this kind of method requires very long operational times, which may have a strong influence on the total cost of the mission.

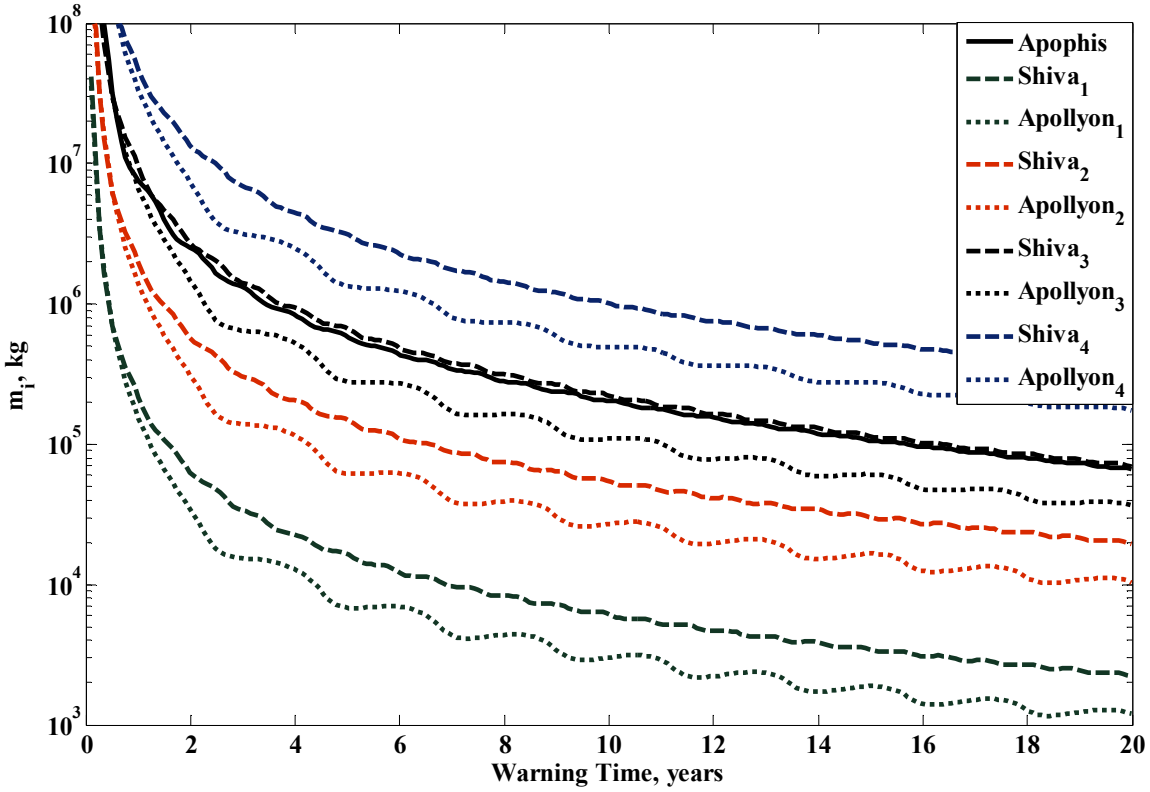

Fig. II-22 Mass required for a gravity tug deflection mission able to deviate each one of the test case studied by the minimum Earth-asteroid distance.

II.7. Chapter Summary

Over the last few years, the possible scenario of an asteroid threatening to impact the Earth has stimulated an intense debate, among the scientific community, about possible deviation methods. As a consequence, a large number of mitigation scenarios have been proposed in the scientific literature, although comprehensive quantitative comparison was still lacking[70]. This chapter set the basis of the multi-criteria criteria comparison carried out in Chapter III by introducing six different mitigation strategies modelled; nuclear interceptor, kinetic impactor, low thrust tug, mass driver, solar collector and gravity tractor.

Each one of the models developed yields the total impulse or acceleration imparted to the asteroid, given the orbital and physical characteristics of the threatening object and the spacecraft mass at encounter. Once the induced impulse (or acceleration) is known, Gauss' planetary equations can be integrated to compute the final deviation at the Earth-asteroid encounter. As shown by Fig. II-7, Fig. II-8, Fig. II-13, Fig. II-15, Fig. II-19 and Fig. II-22, some of the methods perform better than others, although, clearly, in order to bring forth a

complete assessment on their efficiency a few issues still need to be included into the discussion: technology readiness, the Earth-asteroid trajectory, the operational costs, etc.

The chapter did not intend to rule out other possible methods, although many can be considered as combinations and/or variations of the models developed here; for example a targeted deflection of a small asteroid could be used for a subsequent impact and deflection of a threatening object[71], but this can be considered as a combination of two deflections; a first very accurate deflection of a small asteroid with any one of the described methods together with a kinetic impact. Its efficiency can therefore be already extrapolated from the analysis carried out here. The chapter also did not considered methods requiring warning times in the order of centuries (e.g. enhanced Yarkovsky), but only those that could possibly deflect a threatening object with a maximum warning time of 20 years.

Chapter III

Hazard Deflection Missions

The efficiency of six possible deflection techniques (namely nuclear interceptor, kinetic impactor, low-thrust propulsion, mass driver, solar collector and gravity tug) was addressed in Chapter II. We now discuss the feasibility of a *real* deflection scenario with the current space technology and knowledge. We will therefore take into account additional criteria, such as launcher capability, interception or rendezvous trajectories and technology readiness, in order to improve our understanding of the problem and we will also compare the efficiency of the different deflection strategies from a wider standpoint offered by the preliminary design of complete deflection missions.

The following two sections deal with asteroidal and cometary hazard respectively. In order to analyse the asteroidal threat, we make use of the three different virtual asteroids presented in Chapter I; *Apophis*, *Shiva* and *Apollyon*. Preliminary missions were designed that, starting from Earth, intercept or rendezvous with the threatening objects and then apply the maximum correction of the impacting trajectory given the remaining mass of the spacecraft at the asteroid. Thousands of these missions were computed for each one of the six models presented in Chapter II. A summary of the results is given here, and then the different methods are compared using an original procedure based on the concept of dominance of each set of computed preliminary mission. Although in this chapter we use only three different criteria to define the concept of dominance, the same procedure could be used for a more extensive analysis including other figures of merit that were not modelled in this work, such as for example the mission cost or mission success reliability.

The impact hazard posed by nearly isotropic comets is instead characterized through the study of the *Comet S-T*. The analysis includes both the study of the efficiency of each one of the deflection models applied to a cometary object such as *Comet S-T* (i.e., much larger in size and lower density) and the cost analysis of the interception trajectories as a function of warning time. The aim of this secondary study is to underline the main difference between the asteroidal and cometary hazard.

III.1. Asteroidal Hazard

In the following sections a complete comparative assessment of the effectiveness of complete hazard mitigation missions aiming to deflect near-Earth asteroids is presented. Each one of the deflection methods presented in Chapter II is now subjected to a multi-criteria optimization method in order to construct a set of Pareto optimal missions for each deflection method. These Pareto optimal solutions were found by maximizing the deviation, while at the same time minimizing the mass of the spacecraft at departure from the Earth and the warning time, which in this chapter denotes the time from launch to the foreseen impact of the asteroid with the Earth. A dominance criterion is defined and used to compare all the Pareto sets for all the various mitigation strategies. Finally, a Technology Readiness Level is associated to each strategy in order to estimate the required technological development.

III.1.1. Multi-criteria Optimization Problem Formulation

The optimality of each strategy is here defined through a number of criteria or objectives that have to be attained. Unlike single objective problems, multiple objective problems look for a set of optimal values rather than a single optimal one. The general problem is to find a set X of feasible solutions $\mathbf{x}$ such that the property $P(\mathbf{x})$ is true for all $\mathbf{x} \in X \subseteq D$:

$$X = \{\mathbf{x} \in D \mid P(\mathbf{x})\} \tag{3.1}$$

where the domain D is a hyper-rectangle defined by the upper bound b_i^u and lower bound b_i^l on the components of the vector $\mathbf{x}$:

$$D = \left\{x_i \mid x_i \in [b_i^l, b_i^u] \subseteq \Re, i = 1,...,n\right\} \tag{3.2}$$

All the solutions $\mathbf{x}$ satisfying property P are here defined to be optimal with respect to P or P-optimal and X can be said to be a P-optimal set. In the case of multi-objective optimization, if P is a dominance condition or Pareto optimality condition for the solution $\mathbf{x}$, then the solution is Pareto-optimal if $P(\mathbf{x})$ is true.

Each function vector j is associated to a scalar dominance index I_d such that:

$$I_d(\mathbf{x}_j) = \left|\left\{i \mid i \in N_p \wedge \mathbf{x}_i \succ \mathbf{x}_j\right\}\right| \tag{3.3}$$

where the symbol $|\ |$ is used to denote the cardinality of a set, $\succ$ represents the dominance of the $\mathbf{x}_i$ solution over the $\mathbf{x}_j$ solution and N_p is the set of the indices of all the available feasible solutions. A solution vector $\mathbf{x}_i$ dominates a solution vector $\mathbf{x}_j$ when all the components of the criteria, or objectives, vector $\mathbf{f}(\mathbf{x}_i)$ associated to $\mathbf{x}_i$ are better (higher or lower) than all the components of the criteria vector $\mathbf{f}(\mathbf{x}_j)$ associated to $\mathbf{x}_j$. The property *P(***x***)* in this case simply defines non-dominated solutions:

$$X = \left\{ \mathbf{x} \in D \mid I_d(\mathbf{x}) = 0 \right\} \tag{3.4}$$

The search for the *P*-optimal sets *X*, for each strategy, was performed through an agent-based search approach hybridized with a domain decomposition technique[72],[73], the Evolutionary Predictive Interval Computation tool, or EPIC.

III.1.2. Objective Function Definition

The following three criteria or figures of merit were selected to define the optimality of each strategy:

- The warning time $t_w = t_{MOID} - t_l$, which, unlike in Chapter II, now is the interval between the launch date and the time at the point of Earth closest approach (i.e., virtual impact)[8]; this figure of merit defines how far in advance we need to know that an impact is going to occur, and gives a measure of our capability of reacting quickly to an incoming danger.
- The mass into space m_0 at departure, which is the mass of the spacecraft at the Earth, after launch; this figure of merit gives a measure of how difficult implementing a given strategy could be, if m_0 is not within current launch capabilities the difficulty of a given strategy increases.
- The total deviation Δr_{tot} at encounter calculated as $\Delta r_{tot} = \|\Delta\mathbf{r} + \delta\mathbf{r}\|$ where $\Delta\mathbf{r}$ is the vector distance of the asteroid from the Earth at the MOID point and $\delta\mathbf{r}$ is the variation given by the integration of Gauss' planetary equations (see Appendix A.1); this figure of merit, together with the mass into space, gives a measure of how easy deflecting an asteroid with a given method is. Note that we use the total deviation as figure of merit and not the ability of a particular deflection method to avoid the passage of the asteroid through dangerous key-

[8] In Chapter II, since we did not consider the Earth-asteroid trajectory, warning time was not including it. Now we start our deflection endeavour at the Earth, instead of at the asteroid.

holes[74]. In this case even a small $\delta\mathbf{r}$ would produce significant results, greatly enhancing the effectiveness of a given deflection method, and other criteria should be considered, such as the controllability and manoeuvrability of a given deflection strategy.

These three criteria represent perhaps the minimum set of figures of merit required to efficiently measure the capability of a deflection strategy to mitigate a possible impact hazard. By itself, the magnitude of the total deflection Δr_{tot} has little information, but with the ancillary information provided by the warning time t_w and the mass into space m_0 the efficiency of a given deflection method can be studied. The mitigation of the impact hazard is always going to be a time constrained problem, since the defection is clearly needed before the impact occurs and after the hazard has been discovered, thus the warning time is a necessary feature to judge the feasibility of a certain method. On the other hand, the combination of Δr_{tot} and mass into space m_0 gives us a good idea of how efficient a method is at deflecting asteroids. Finally, these three criteria may also give us a first estimate on other important characteristics of a space mission, such as mission cost (since the cost should be related with both mass launched into space and operational time) and the mission reliability (since a deflection Δr_{tot} largely above a certain distance-threshold should also indicate a high reliability to achieve that distance-threshold).

The t_{MOID} is the date at which the asteroid reaches the point of Minimum Orbit Interception Distance from the Earth. Note that the Earth does not need to be at that physical point in the orbit; the aim of this analysis is to measure the effectiveness and efficiency of each deviation method and not to reproduce a real impact scenario. In the following analyses, the t_{MOID} for each asteroid is the same for all the deflection strategies, and is kept fixed for all the simulations. See the summary table of each test case, in Chapter I, for the t_{MOID} values.

Even though the strategies have been modelled with a very conservative approach, an additional margin in the mass into space m_0 was added in order to take into account the corrective manoeuvres required during both the transfer leg and the deflecting arc (for low thrust approaches). These margins, that can be found in Table III-1, are also related, to some extent, to the maturity level of a given technology.

Table III-1. Design Margins for the Spacecraft Mass.

Strategies	m_0 margin
Solar Collector	25%
Electric Propulsion	25%
Mass Driver	25%
Gravity Tug	25%
Nuclear Interceptor	10%
Kinetic Impactor	5%

The criteria vector for a given method A is then defined as:

$$\mathbf{f}^A = \left[t_w{}^A, m_0{}^A, -\left\| \Delta r + \delta r \right\|^A \right]^T \tag{3.5}$$

where m_0 is augmented according to the design margin for method A. The problem is to find the set X of feasible solutions that are not dominated with respect to the criteria vector $\mathbf{f}^A$. Each solution corresponds to a mission leaving the Earth at a departure time t_0, performing a transfer to the asteroid either along a Lambert's arc or a low-thrust spiral for a transfer time T and then applying the deviation action for a time t_{push}.

Deviation strategies whose action is impulsive, such as kinetic impactor and nuclear interceptor, are considered to use chemical propulsion systems and thus the transfer was modelled as a simple Lambert's arc. The velocity change required to transfer the spacecraft from the Earth to the asteroid was used to compute the propellant mass by means of Tsiolkovsky's rocket equation. For all the other deviation strategies, the transfer was modelled as a low-thrust spiral through a shape-based approach[75], assuming a departure from the Earth with zero relative velocity. Shape-based approaches represent the trajectory connecting two points in space with a particular parameterized analytical curve (or shape), then the spacecraft's control thrust required to reproduce the curve can be derived. By tuning the shaping parameters of the low-thrust curve a trajectory requiring minimum propellant mass can be found.

The operational time at the asteroid t_{push} was set equal to the difference between the time of the virtual impact, or time at the point of closest approach, and the time at interception, except said otherwise or for those strategies for which the model provides an optimal value for t_{push}, for example the low thrust method. All celestial bodies that the spacecraft may encounter during its trajectory are considered to be point masses with no gravity and analytical ephemerides are used for the Earth and the asteroids.

The general solution vector is defined as:

$$\mathbf{x} = [m_0, t_0, T, n_R, \lambda_{s1}, \lambda_{s2}]^T \tag{3.6}$$

where n_R is the number of revolutions of the Lambert's arc or of the low-thrust spiral and λ_{s1} and λ_{s2} are two shaping parameters for the low-thrust arcs (exponential shape[75] was used), if they apply. The search domain D is defined by the values in Table III-2. For each deflection method, all the mission opportunities with a launch in the interval [t_{MOID}-1000 t_{MOID}-7300] MJD2000 (i.e., Modified Julian Days counted since 1st January 2000 at 12:00 p.m.) and a transfer time in the interval [25 1000] days were considered. Note that the range of masses into space is pretty wide, varying from as low as 100 kg to as high as 100 tons, to account for a large variety of spacecraft designs, from mini-satellites to massive spacecraft. Note also that the propellant mass required for the transfer is subtracted from m_0 when the spacecraft is at the asteroid. The residual mass, either m_i (interception mass) or m_d (dry mass), depending on the model, is then used to compute the deviation. All the missions that had a residual mass so low to produce a deviation smaller than one kilometre were discarded and not included in the Pareto sets.

Table III-2. Search domain for the multi-objective analysis.

m_0 (kg)	t_0 (MJD2000)	T (days)	n_R	λ_{s1}	λ_{s2}
100	t_{MOID}-7300	25	0	-1	-1
100000	t_{MOID}-1000	1000	3	1	1

III.1.3. Missions to Apophis

Fig. III-1 shows the Pareto optimal solutions found by the agent-based[72],[73] search for each deviation method aimed at deflecting an Apophis-like asteroid with an impact date on 14th April 2029. Each solution shown in Fig. III-1, so each black dot, represents Pareto-optimal deflection mission to the asteroid *Apophis*, i.e., no other mission can be designed by changing the parameters in the solution vector in Eq.(3.6) that is able to improve all the three criteria at the same time. It is important to remark that each black dot from Fig. III-1 contains more information than the represented by the 3-D figures below, such as the departure and arrival dates, the propellant consumption, the dry mass of the spacecraft, the deflection operational time-span and the deflection direction, thus they are complete preliminary mission designs.

Note that the range of warning times and mass into space are almost the same for all the six methods, while the range of the achieved deviation is substantially different. For

example for the same mass into space and for the same warning time, the solar collector and nuclear interceptor achieve a deviation which is two orders of magnitude higher than that of the kinetic impactor. Furthermore, all strategies that employ a single impulse transfer present a characteristic striped distribution of the solutions mainly due to the periodicity of the optimal launch date. Note that for the two impulsive methods, i.e., nuclear interceptor and kinetic impactor, the direction along which the deviating action is applied depends solely on the transfer and therefore an optimal launch date corresponds to a Pareto optimal solution.

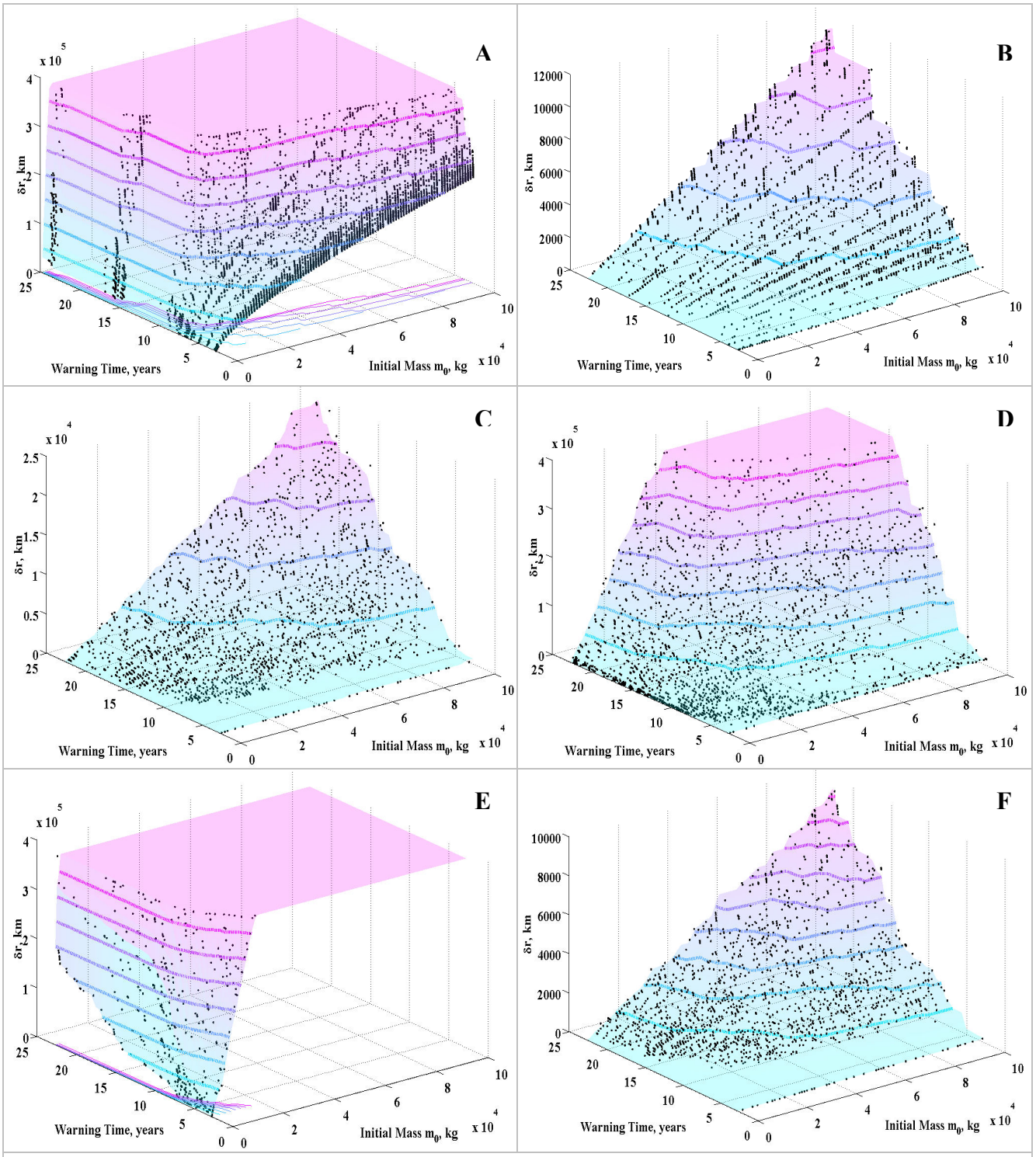

Fig. III-1 Pareto sets for the six deviation methods applied to asteroid *Apophis*. A) Nuclear Interceptor. B) Kinetic Impactor. C) Low Thrust Propulsion. D) Mass Driver. E) Solar Collector. F) Gravity Tug.

The surfaces plotted in Fig. III-1: A, E and D have a plateau at a deviation value of about 400,000 km. The plateau is due to the fact that the integration was stopped once the deviation reached one Earth-Moon distance. In order for the hypotheses behind the proximal motion equations to hold true, the variation of the orbit radius δr must be small compared to the unperturbed one. Therefore the Earth-Moon distance, was taken as the upper threshold limit since this is considered to be sufficient to remove the threat of an impact. The size of the plateau regions suggests that both solar collector and nuclear interceptor provide similar performance. Note that the two approaches are utterly different, as the deviation is achieved through a continuous thrusting arc in the former case and through an impulsive change of the linear momentum in the latter.

Pareto Contour Lines

A simple way to compare the 3D Pareto fronts of the different strategies and asteroids is by plotting deviation isolines, thus a line or curve along which the value of the deflection δr is constant. Fig. III-2 shows the isolines for a deflection of 13,724 km for each deviation strategy targeting to deflect *Apophis*. Note that this is the minimum deviation necessary to deflect *Apophis*, which is computed by taking into account, not only the volume of the Earth, but also the deflection of the trajectory of *Apophis* due to the Earth's gravity attraction as described in section I.5.

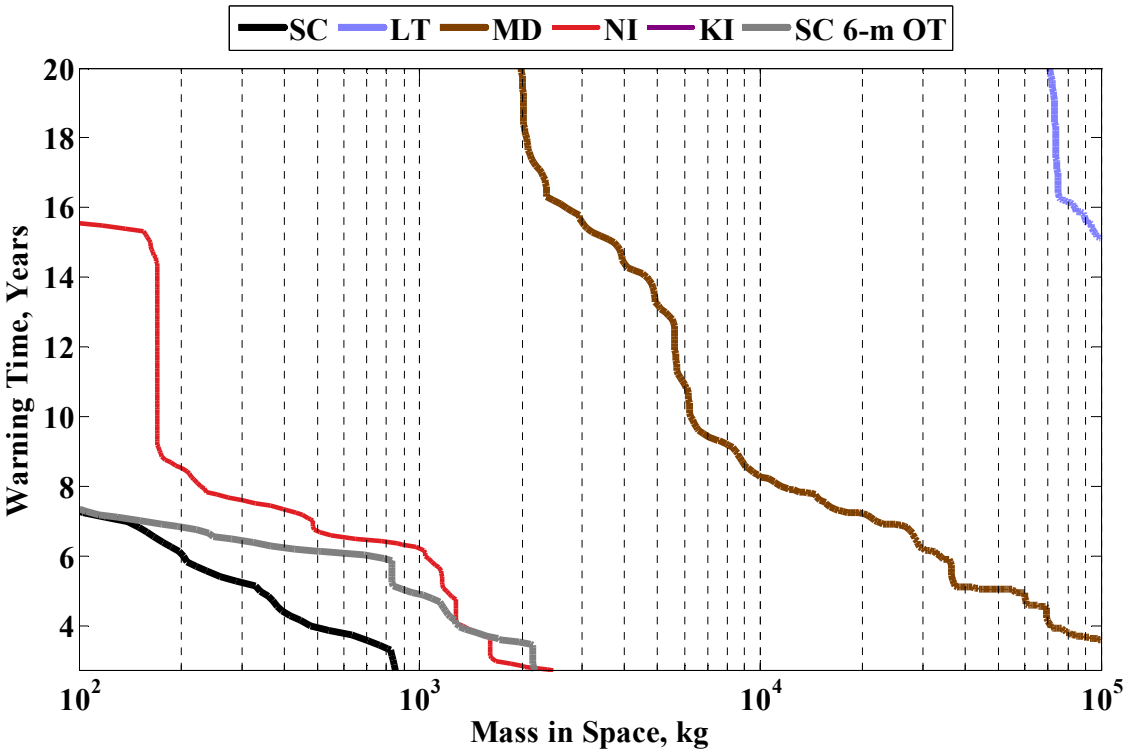

Fig. III-2 Pareto front contour lines for a 13,720 km deflection of *Apophis* for all the analyzed deviation methods. The legend of the figures stands as follows: SC-solar collector, LT-low thrust, MD-mass driver, NI-nuclear interceptor, KI-kinetic impactor and SC 6-m is the solar collector model with a constraint in the operational pushing time of six months.

Fig. III-2 shows how only four strategies out of the six analysed are able to deflect *Apophis* by 13,720 km, namely solar collector (SC and SC 6-m), low thrust (LT), mass driver (MD) and nuclear interceptor (NI). In fact, only three strategies, the mass driver, the nuclear interceptor and the two solar collector approaches, yield the desired deviation with a mass in space smaller than 100,000 kg and a warning time shorter than 10 years. The low thrust method is also able to provide the minimum necessary deflection, although requiring a mass into space very close to 100,000kg and almost 20 years of warning time. The only difference between the two solar collector approaches presented in Fig. III-2 is the time of the pushing manoeuvre, or in other words, the operational time at the asteroid. The SC approach uses as pushing manoeuvre time all the available warning time, i.e., time left for the impact after reaching the asteroid, while the second scenario, SC 6-m, uses only the first six months after arrival as pushing time.

III.1.4. Missions to Shiva

This section summarizes the results of the multi-criteria optimization of deflection missions aiming to mitigate the threat posed by a Shiva-like asteroid. The virtual *Shiva* asteroids range from $5x10^8$kg to $5x10^{11}$kg, which in terms of impact frequency translates to one impact each 1,000 to 250,000 years respectively (see Table 7 in Chapter I). Fig. III-3 shows the Pareto optimal solutions found by the agent-based search targeting to deflect $Shiva_3$. The Pareto optimal solutions for the three remaining sizes of *Shiva* are similar in shape and distribution of the solutions, as should be expected, since the only difference between the four test cases is the mass of the asteroid. Since the small differences are difficult to spot in the general 3D view of the Pareto fronts, they were not reproduced in this Chapter, although an analysis of the complete data is performed by means of the deflection isolines.

The Pareto-optimal sets in Fig. III-3 show similar features to the previous results in Fig. III-1. Again, only three deflection methods reach the deviation plateau at 400,000 km (nuclear interceptor, mass driver and solar collector) and similar striped configuration is clearly seen in impulsive methods. We can also observe that the synodic period between the Earth and *Shiva* is playing a more significant role in the optimality of the launch date, and thus in the distribution of the optimal solutions, since a 4-years wide stripe configuration can be also observed in low trust methods.

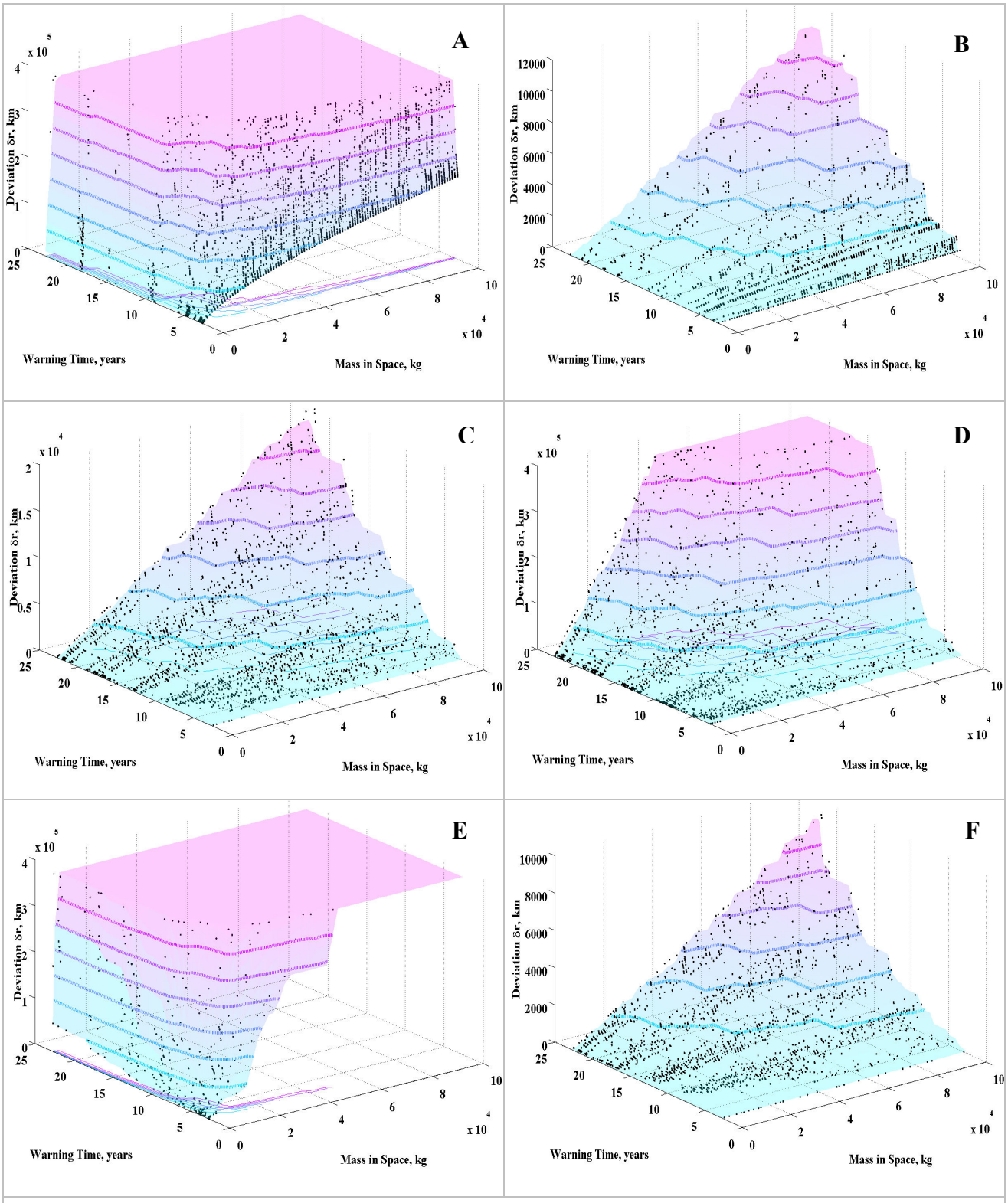

Fig. III-3 Pareto sets for the six deviation methods applied to asteroid *Shiva*$_3$. A) Nuclear Interceptor. B) Kinetic Impactor. C) Low Thrust Propulsion. D) Mass Driver. E) Solar Collector. F) Gravity Tug.

Pareto Contour Lines

Fig. III-4 shows the isolines for a 9,690-km deflection on the four *Shiva* cases for different deflection methods. *Shiva*'s orbit has a higher relative velocity at Earth encounter than the *Apophis* case, therefore its orbit is less affected by the Earth's gravity during the asteroid's final approach, and, as a consequence, the minimum deflection required to mitigate *Shiva*'s threat is 4,000 km shorter than for *Apophis*.

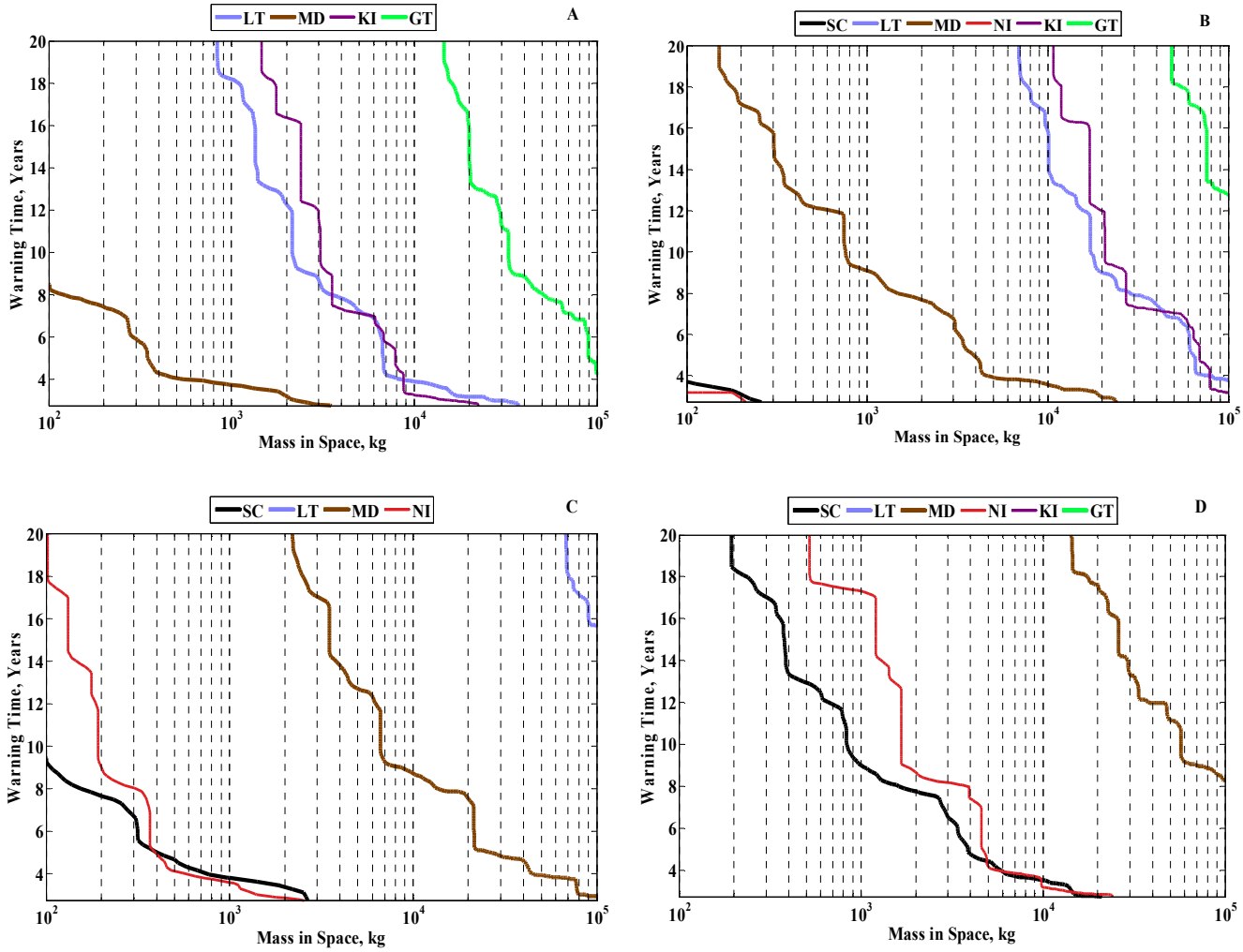

Fig. III-4 Pareto front contour lines for a 9,690 km deflection of all four *Shiva* asteroids (see Table I-6) and for all the analyzed deviation methods. A) $Shiva_1$ B) $Shiva_2$ C) $Shiva_3$ D) $Shiva_4$. The legend of the figures stands as follows: SC-solar collector, LT-low thrust, MD-mass driver, NI-nuclear interceptor, KI-kinetic impactor, GT-gravity tug.

It is remarkable to see how all the strategies are, in principle, possible candidates for the deflection of Shiva-like asteroids with mass smaller than 5×10^9kg. Notice that if the solar collector and the nuclear interceptor do not appear in Fig. III-4A is because the corresponding isoline is outside the range of mass in space and warning time studied. This, unlike for the low thrust, kinetic impactor and gravity tug methods in Fig. III-4D, implies

that all the solutions in the studied domain are above the required deflection distance. As discussed in Chapter II, this may appear to be an excessive scaling of the model, and unfeasible from a technological point of view, but it is nevertheless indicative of a very good performance of these two strategies. It is also remarkable to note the good performance of the kinetic impactor method, which, although the simplest of the studied concept, performs as well as the low thrust method, especially for short warning times. As expected, for the largest *Shiva* case, only the three most efficient methods are able to provide the required deviation within the range of mass into space and warning time.

III.1.5. Missions to Apollyon

This section describes the results of the multi-criteria optimization on the deflection of the *Apollyon* series. As previously mentioned, the Pareto surfaces of the different elements of each series are similar in shape, thus only one, $Apollyon_3$, is shown in Fig. III-5. Again, the 3D images of the $Apollyon_3$'s Pareto solutions are similar in shape to the previously shown for *Apophis* and $Shiva_3$. We can however notice that the striped configuration is now slightly more evident than in previous results, this feature is magnified here by the larger semimajor axis and eccentricity of *Apollyon* with respect the Aten examples.

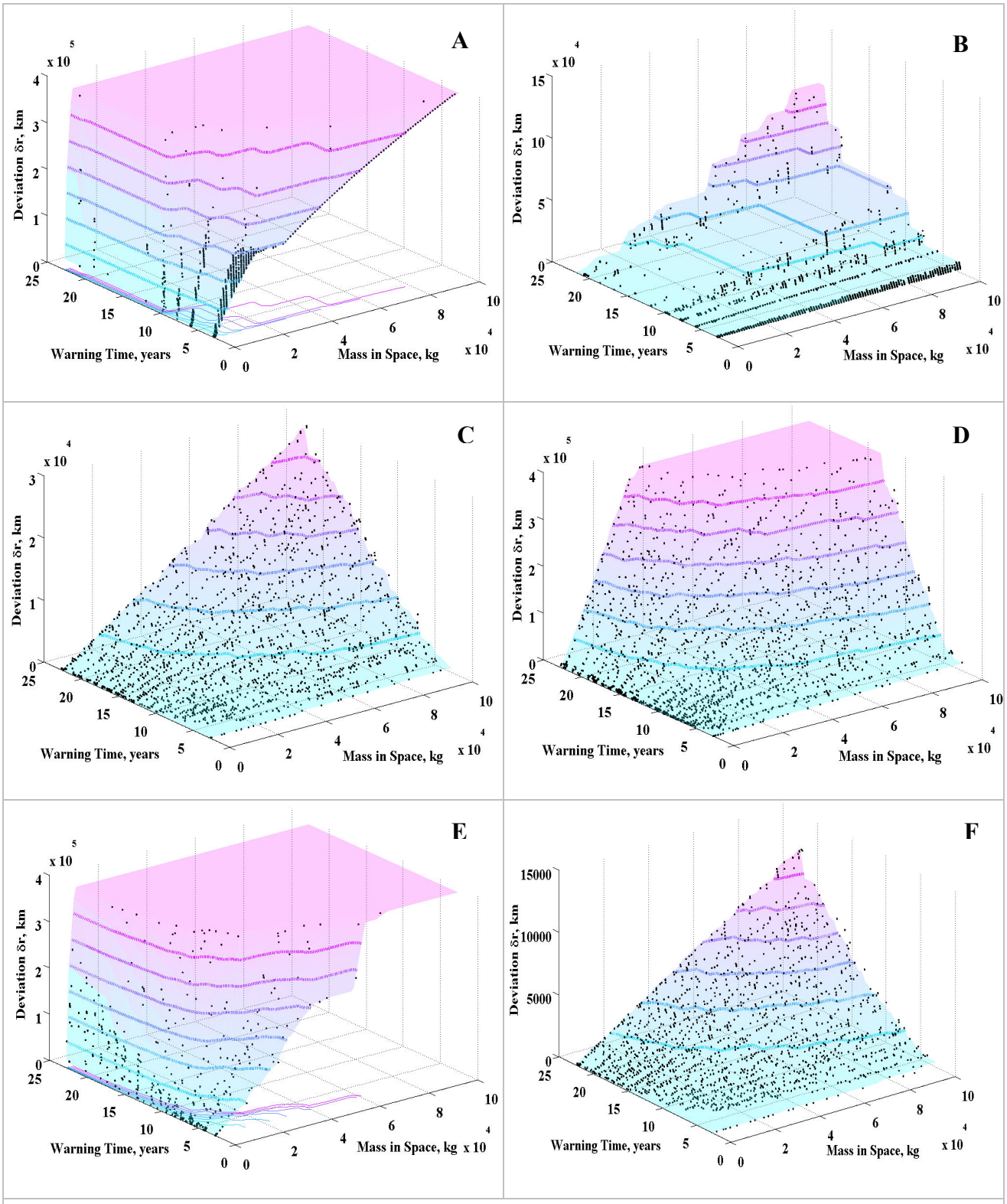

Fig. III-5 Pareto sets for the six deviation methods applied to asteroid *Apollyon*$_3$. A) Nuclear Interceptor. B) Kinetic Impactor. C) Low Thrust Propulsion. D) Mass Driver. E) Solar Collector. F) Gravity Tug.

Pareto Contour Lines

The following figure, Fig. III-6, shows now the isolines for an 8,202-km deflection on the four *Apollyon* cases. One of the most outstanding differences between the *Apollyon* results and those for the two Aten objects (*Apophis* and *Shiva*) is the very good performance of the kinetic impactor. As commented previously, we already noticed from Fig. III-4 that the deflection efficiency of the kinetic impactor was very similar to that of the low thrust deflection. The isolines for the *Apollyon* cases (Fig. III-6) show, not only how the kinetic impactor clearly outperforms the low thrust method, but how the kinetic impactor's efficiency increases almost tenfold when compared with the Aten cases. The main reason for the high efficiency of the kinetic impactor in the *Apollyon* cases is due to the fact that Apollo asteroids have higher eccentricity and inclination and therefore a higher relative velocity with respect to the orbit of the Earth. A high-speed and optimal impact trajectory is therefore less expensive, in terms of propellant mass, than in the two Aten cases and more mass-efficient than a rendezvous. We should remember that both the velocity of the impact and its direction are the result of simple Lambert arc calculation.

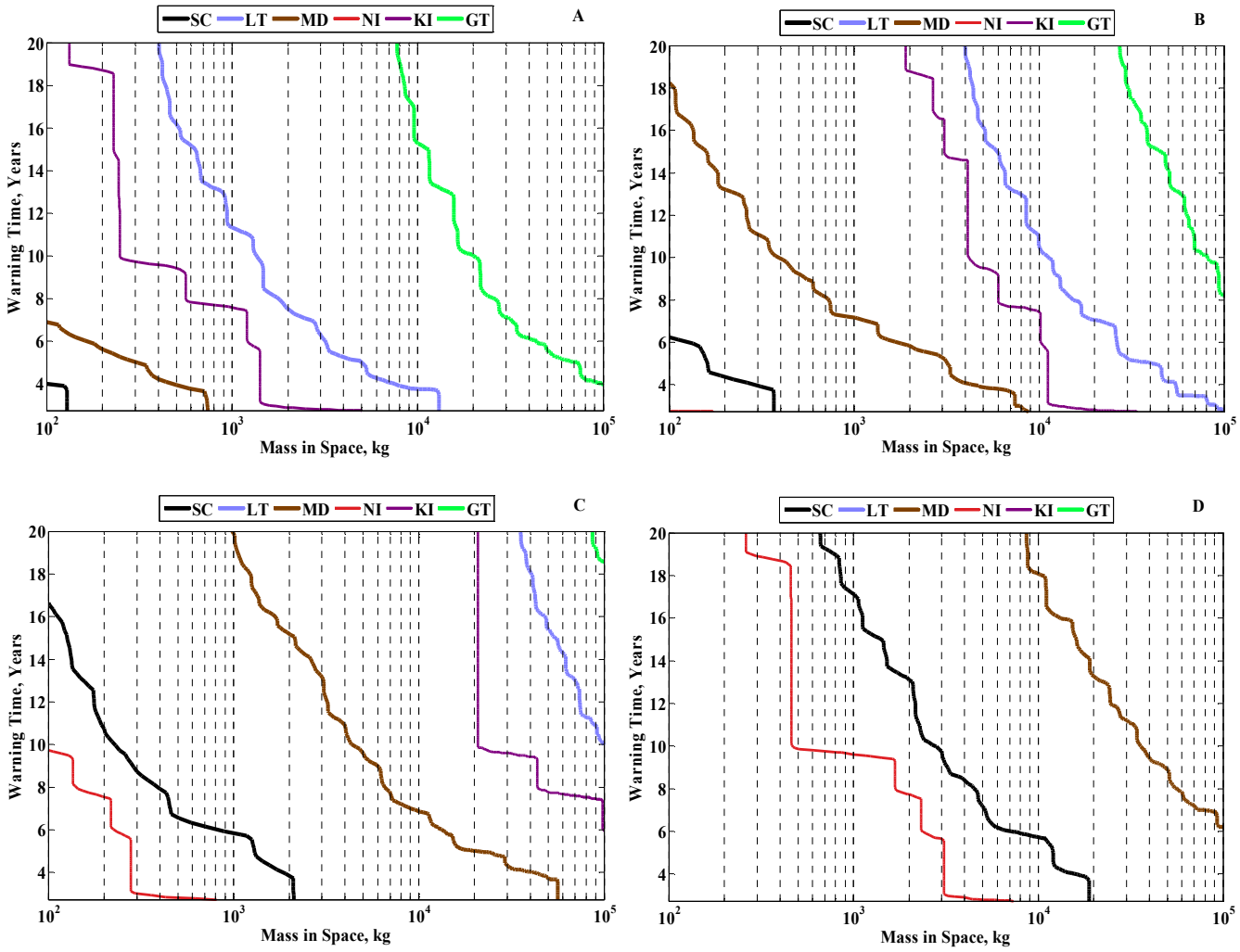

Fig. III-6 Pareto front contour lines for an 8,202 km deflection of all four *Apollyon* asteroids for all the analyzed deviation methods. A) *Apollyon*$_1$ B) *Apollyon*$_2$ C) *Apollyon*$_3$ D) *Apollyon*$_4$. The legend of the figures stands as follows: SC-solar collector, LT-low thrust, MD-mass driver, NI-nuclear interceptor, KI-kinetic impactor, GT-gravity tug.

III.1.6. Strategy Comparison

The effectiveness and efficiency of each strategy are expressed, in this Chapter, through a set of Pareto optimal points (e.g., Fig. III-1, Fig. III-3 and Fig. III-5). In order to compare one strategy against the others it is possible to use the concept of dominance of one Pareto set over another: an element (or solution belonging to the Pareto set) i of strategy A is said to be dominated by element j of strategy B if all the components of the vector objective function $\mathbf{f}_j^B$ are better (i.e., t_w and m_0 smaller and $\|\Delta r + \delta r\|$ bigger) than all the components of the vector objective function $\mathbf{f}_i^A$. Then, the dominance index $I_i(m_A)$

of an element *i* of strategy *A* with respect to strategy *B* is the cardinality of the set of elements of the Pareto-optimal set of strategy *B* that dominate element *i*:

$$I_i(m_A) = \left| \left\{ j \,|\, \mathbf{f}_i^A \prec \mathbf{f}_j^B \right\} \right| \tag{3.7}$$

where the dominance symbol $\prec$ in Eq.(3.7) means that $\mathbf{f}_j^B$ dominates $\mathbf{f}_i^A$, i.e. all the components of $\mathbf{f}_j^B$ are better than all the components of $\mathbf{f}_i^A$. Thus if the value of the dominance index of the element *i* is 0, it means that there are no solutions in the Pareto-optimal set of strategy *B* that have all the three criteria that are better than the three criteria associated to element *i*. We can now say that strategy *A* dominates strategy *B* if the percentage of the elements of *A* that are dominated by *B*, i.e. the percentage of elements of *A* with dominance index $I(m_A)$ different from 0, is less than that of the elements of *B* that are dominated by *A*:

$$\begin{aligned} d_i(m_A) &= \begin{cases} 1 \text{ if } I_i(m_A) > 0 \\ 0 \text{ if } I_i(m_A) = 0 \end{cases} \\ m_A \succ m_B &\Rightarrow \frac{1}{N_A}\sum_{i=1}^{N_A} d_i(m_A) < \frac{1}{N_B}\sum_{j=1}^{N_B} d_j(m_B) \end{aligned} \tag{3.8}$$

where N_A is the total number of the solutions in the Pareto set of method (or strategy) m_A and N_B is the total number of solutions in the Pareto set of method (or strategy) m_B.

The following nine tables (Table III-3 to Table III-11) show the dominance of the six different strategies applied to all nine test cases. The numbers in the tables are the percentage of elements of the method in the corresponding row that "dominate" over the elements of the method in the corresponding column, or in other words, the percentage of elements of the method in the corresponding row that obtained zero in Eq.(3.7). For example, if we look at the yellow-shaded box in Table III-3, we see that 100% of the solutions in the Pareto set of the Mass Driver dominate (i.e. all the three criteria are equal or better) the solutions in the Pareto set of the Low Thrust. Note that the numbers in every column do not necessarily add up to 100 with the corresponding numbers in every row. For example, for *Apophis* (see green-shaded boxes in Table III-3) 16% of the Kinetic Impactor solutions are dominant over Low-thrust solutions while 98% of Low-Thrust solutions are dominant over Kinetic Impactor solutions. The reasons for this are twofold; firstly, because we compute the percentage of elements being equal or better, so that two equal elements will dominate over each other; secondly, because we compute the percentage of points

within each Pareto set, therefore it could well be that 100% of the points of a set are dominating only a small fraction of the points of another set.

Table III-3 Strategy Dominance for *Apophis*.

	NI	**KI**	**LT**	**MD**	**SC**	**SC** *6m*	**GT**
Nuclear Interceptor (**NI**)		*100*	*100*	*100*	*1*	*5*	*100*
Kinetic Impactor (**KI**)	*0*		*16*	*0*	*0*	*0*	*100*
Low Thrust (**LT**)	*0*	*98*		*0*	*0*	*0*	*100*
Mass Driver (**MD**)	*0*	*100*	*100*		*0*	*0*	*100*
Solar Collector (**SC**)	*100*	*100*	*100*	*100*		*100*	*100*
Solar Collector *6-m OT*	*99*	*100*	*100*	*100*	*18*		*100*
Gravity Tug (**GT**)	*0*	*1*	*0*	*0*	*0*	*0*	

Table III-4 Strategy Dominance for *Shiva$_1$*.

	NI	**KI**	**LT**	**MD**	**SC**	**GT**
Nuclear Interceptor (**NI**)		*100*	*100*	*100*	*43*	*100*
Kinetic Impactor (**KI**)	*0*		*44*	*0*	*0*	*100*
Low Thrust (**LT**)	*0*	*78*		*0*	*0*	*100*
Mass Driver (**MD**)	*0*	*100*	*100*		*0*	*100*
Solar Collector (**SC**)	*71*	*100*	*100*	*100*		*100*
Gravity Tug (**GT**)	*0*	*0*	*0*	*0*	*0*	

Table III-5 Strategy Dominance for *Shiva$_2$*.

	NI	**KI**	**LT**	**MD**	**SC**	**GT**
Nuclear Interceptor (**NI**)		*100*	*100*	*100*	*20*	*100*
Kinetic Impactor (**KI**)	*0*		*31*	*0*	*0*	*100*
Low Thrust (**LT**)	*0*	*88*		*0*	*0*	*100*
Mass Driver (**MD**)	*0*	*100*	*100*		*0*	*100*
Solar Collector (**SC**)	*92*	*100*	*100*	*100*		*100*
Gravity Tug (**GT**)	*0*	*0*	*0*	*0*	*0*	

Table III-6 Strategy Dominance for *Shiva$_3$*.

	NI	**KI**	**LT**	**MD**	**SC**	**GT**
Nuclear Interceptor (**NI**)		*100*	*100*	*100*	*10*	*100*
Kinetic Impactor (**KI**)	*0*		*42*	*0*	*0*	*100*
Low Thrust (**LT**)	*0*	*88*		*0*	*0*	*100*
Mass Driver (**MD**)	*0*	*100*	*100*		*0*	*100*
Solar Collector (**SC**)	*90*	*100*	*100*	*100*		*100*
Gravity Tug (**GT**)	*0*	*1*	*0*	*0*	*0*	

Table III-7 Strategy Dominance for *Shiva$_4$*.

	NI	**KI**	**LT**	**MD**	**SC**	**GT**
Nuclear Interceptor (**NI**)		*100*	*100*	*100*	*7*	*100*
Kinetic Impactor (**KI**)	*0*		*61*	*0*	*0*	*76*
Low Thrust (**LT**)	*0*	*95*		*0*	*0*	*100*
Mass Driver (**MD**)	*0*	*100*	*100*		*0*	*100*
Solar Collector (**SC**)	*94*	*100*	*100*	*100*		*100*
Gravity Tug (**GT**)	*0*	*68*	*1*	*0*	*0*	

Table III-8 Strategy Dominance for *Apollyon*$_1$.

	NI	**KI**	**LT**	**MD**	**SC**	**GT**
Nuclear Interceptor (**NI**)		*100*	*100*	*100*	*100*	*100*
Kinetic Impactor (**KI**)	*0*		*100*	*1*	*0*	*100*
Low Thrust (**LT**)	*0*	*0*		*0*	*0*	*100*
Mass Driver (**MD**)	*0*	*100*	*100*		*1*	*100*
Solar Collector (**SC**)	*0*	*100*	*100*	*95*		*100*
Gravity Tug (**GT**)	*0*	*0*	*0*	*0*	*0*	

Table III-9 Strategy Dominance for *Apollyon*$_2$.

	NI	**KI**	**LT**	**MD**	**SC**	**GT**
Nuclear Interceptor (**NI**)		*100*	*100*	*100*	*100*	*100*
Kinetic Impactor (**KI**)	*0*		*100*	*1*	*1*	*100*
Low Thrust (**LT**)	*0*	*0*		*0*	*0*	*100*
Mass Driver (**MD**)	*0*	*100*	*100*		*0*	*100*
Solar Collector (**SC**)	*1*	*100*	*100*	*100*		*100*
Gravity Tug (**GT**)	*0*	*0*	*0*	*0*	*0*	

Table III-10 Strategy Dominance for *Apollyon*$_3$.

	NI	**KI**	**LT**	**MD**	**SC**	**GT**
Nuclear Interceptor (**NI**)		*100*	*100*	*100*	*99*	*100*
Kinetic Impactor (**KI**)	*0*		*100*	*4*	*0*	*100*
Low Thrust (**LT**)	*0*	*0*		*0*	*0*	*100*
Mass Driver (**MD**)	*0*	*100*	*100*		*0*	*100*
Solar Collector (**SC**)	*2*	*100*	*100*	*100*		*100*
Gravity Tug (**GT**)	*0*	*0*	*0*	*0*	*0*	

Table III-11 Strategy Dominance for *Apollyon*$_4$.

	NI	**KI**	**LT**	**MD**	**SC**	**GT**
Nuclear Interceptor (**NI**)		*100*	*100*	*100*	*99*	*100*
Kinetic Impactor (**KI**)	*0*		*100*	*12*	*1*	*100*
Low Thrust (**LT**)	*0*	*0*		*0*	*0*	*99*
Mass Driver (**MD**)	*0*	*100*	*100*		*0*	*100*
Solar Collector (**SC**)	*8*	*100*	*100*	*100*		*100*
Gravity Tug (**GT**)	*0*	*0*	*0*	*0*	*0*	

From the dominance comparison, the solar collector and nuclear interceptor result to be the dominant methods in the domain under consideration. Solar collector achieves better performance than nuclear interceptor for the Aten class, but not for the Apollo class. This is due mainly to the fact that the smaller semimajor axis of the Aten group means better solar radiation and therefore higher efficiency of the solar collector. It is interesting to underline that the Kinetic Impactor dominates the Low Thrust option for the Apollo case. The same result can be seen in Fig. III-6, though limited to one particular value of deflection δr.

Despite the fact that, as shown in the isolines Fig. III-4 and Fig. III-6, for small size asteroids, techniques such as kinetic impactor, low thrust and gravity tug become effective, the relative performance between two deflection strategies shows only slight changes. For example, we can notice in Table III-7 the improvement of the gravity tug performance relative to the kinetic impactor. This change is due to fact that if an asteroid is 10 times heavier, for a fixed kinetic impact (i.e., fixed m_i, $\Delta \mathbf{v}_{S/C}$) the $\delta \mathbf{v}$ applied to the asteroid would be 10 times smaller. On the other hand, the same gravity tug would apply an acceleration on average only 5 times smaller for a 10 times heavier asteroid. Yet, we do not observe the same improvement of the gravity tug Pareto front in Table III-11 since the kinetic impactor Pareto front is substantially better for *Apollyon*, and the dominance does not change despite the relative performance improvement.

Furthermore, it should be noted, that due to the stochastic nature of the search for Pareto optimal solutions performed by the optimizer, the 3-D surfaces in Fig. III-1, Fig. III-3 and Fig. III-5 can locally change if the optimizer is run multiple times. As a consequence, the dominance evaluation is subject to minor changes; an increase or decrease of a few percentage points.

III.1.7. Influence of the Technology Readiness Level

As an additional criterion, we considered the technology readiness level (*TRL*) of each method as a measure of its expected viability in the near future. We assumed that in the case of an impact the required time to implement a given deviation method had to take into account the necessary development effort and that the development effort was driven by the component of the technology composing the deviation method having the lowest *TRL*. The development effort is here measured in man years (amount of work performed by an average worker in one year). Although this is not an exact measure of the time required to implement a given technology, it provides a good estimation of the increased difficulty to bring a given technology to full operational capability. The actual development time depends on the amount of available resources and on political considerations that are however out of the scope of this analysis. Therefore, we assume that the development effort is a measure of the required delay in the implementation of a given deflection method. To be more precise, the warning time is redefined to be the time between the point when a given technology starts to be developed and the predicted impact time. For example, given a technology that needs a man-time Δt_{dev} to bring it to a sufficient level of development to be launched, the warning time becomes $t_w = t_{MOID} - t_l + \Delta t_{dev}$,

where t_1 is the launch date. We use a standard definition of *TRL*[76],[77], as summarized in Table III-12, assume no limitations due to economic or political issues, and no developments driven by other applications or breakthrough discoveries. We assign the current *TRL* to each of the deviation methods and assume that it will remain constant until t_{MOID}-t_w. These assumptions correspond to a situation in which cost is not an issue should a global threat be faced, but, on the other hand, both economic and political issues prevent any development not motivated by a confirmed catastrophic impact.

Table III-12 Technology Readiness Levels.

TRL	Technology Readiness
1	Basic principles observed and reported
2	Technology concept and/or application formulated
3	Analytical & experimental critical function and/or characteristic proof-of-concept
4	Component and/or breadboard validation in laboratory environment
5	Component and/or breadboard validation in relevant environment
6	System/subsystem model or prototype demonstration in a relevant environment (ground or space)
7	System prototype demonstration in a space environment
8	Actual system completed and "Flight qualified" through test and demonstration (ground or space)
9	Actual system "Flight proven" through successful mission operations

The *TRL* of each deviation methodology is determined by taking into account past missions and state of the art scientific research. The *TRL* for each method is then mapped into the number of man-years Δt_{dev} needed to increase a given technology from its current *TRL* to *TRL* 9, through the logistic function[78]:

$$t_{dev} = \frac{a}{1+e^{-\frac{\Lambda - t_c}{\tau}}} + b \tag{3.9}$$

where t_{dev} is the required development effort (measured in man years) to bring a technology from *TRL* 1 to *TRL* Λ. The parameter t_c represents a turning point for the development of a technology when the critical function characteristics have been already demonstrated experimentally and analytically but the components have not yet been tested in a relevant environment. Around that point, we expect a maximum increase in the investments to turn a conceptual design into a first hardware prototype. In the following and according to the TRL standard definitions[76],[77],[78], we set t_c to *5*, which is the value corresponding to *TRL5*. The coefficients *a*, *b*, and τ were chosen so that:

$$
\begin{aligned}
&t_{dev}(\Lambda = 2) = 0; \\
&t_{dev}(\Lambda = 9) = 15; \\
&t_{dev}(\Lambda = 7) - t_{dev}(\Lambda = 4) = 10
\end{aligned}
\tag{3.10}
$$

The set of boundary conditions in Eq.(3.10) corresponds to a maximum development effort of 15 man-years from *TRL 2* to *TRL 9* and a development effort from breadboard to first prototype system demonstration into space of 10 man-years. The resulting Δt_{dev} is simply the difference between the t_{dev} at *TRL 9* and the t_{dev} at a given *TRL* Λ (see Fig. III-7).

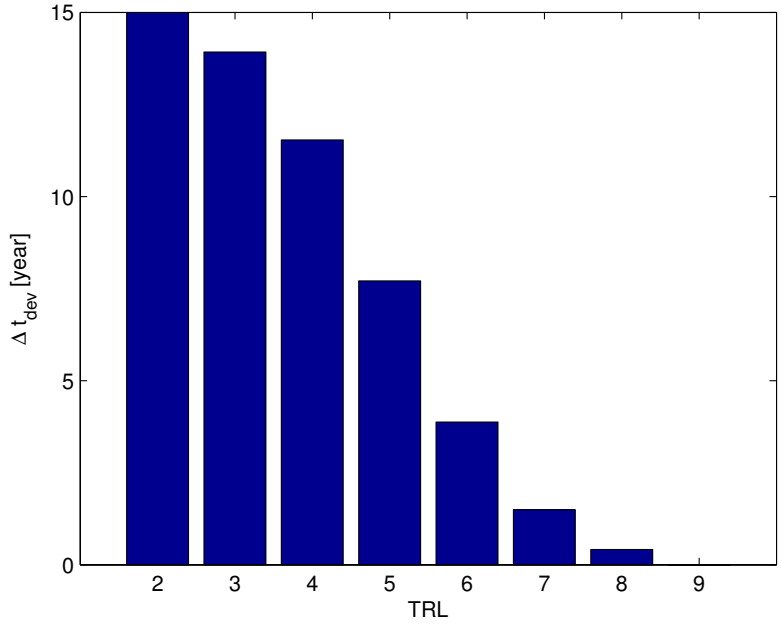

Fig. III-7 *TRL* mapping into required development effort to reach full operational capabilities.

Note that we start with a minimum *TRL* of 2 since the basic concept and application have already been formulated for all the deflection methods under consideration. Then, when allocating the *TRL* to each deflection method we will distinguish between innovative technologies pre or during mission assessment phase (*TRL* 1 to 4) and existing technologies during mission definition phase (*TRL* 5 to 9).

TRL Allocation

In the following discussion we will assign a *TRL* to each one of the deflection methods. Each deviation method is characterized by a number of critical technologies that need to be developed in order make the method actually feasible. The technologies considered in this analysis are only strictly related to each deflection method model presented in Chapter II and do not include the development of new launch capabilities and

the required increase in the knowledge of the physical and orbital characteristics of the asteroids. Once the critical technologies for a given deflection method are identified, a *TRL* is assigned to each technology. We then allocate to the whole deflection method the *TRL* of the least developed critical technology. Since the *TRL* for some methods and technologies is uncertain, due to several concurrent factors, we assign to each deflection method an interval of *TRLs*. These intervals represent our level of confidence in the present level of development of a given technology. The assignment is based on Table III-12 and on the assumption that a technology at *TRL* 9 that is reused in a new application with new requirements will be downgraded to *TRL* 4. Note also that we consider a technology at TRL 9 only when it has successfully flown on not only one, but multiple missions.

Kinetic Impactor: although the kinetic impactor strategy has not been completely proven yet, a mission with similar characteristics, Deep Impact, has already flown successfully. Furthermore, although the impact velocity is a critical issue for this strategy, the average impact velocity of all solutions found in this study was in the region of 10 km/s, which is indeed very similar to the Deep Impact crash velocity (~ 10.2 km/s). For this deflection method, we consider two critical issues: high precision targeting and enhancement factor. The former issue would require a better knowledge of the motion of the centre of mass and rotational state of the asteroid in order to correctly hit the asteroid and transfer the required Δv, the latter issue would require a better knowledge of the composition and morphology of the asteroid. Thus, both cases are related to an increased knowledge of the characteristics of the asteroid. The former issue would also require the development of accurate navigation and orbit determination capabilities for fast close encounters. However, we can assume that this technology is already available and at *TRL 9* given all the past and present missions using gravity assist manoeuvres. Since only one example of high velocity impact exists, we assign a *TRL* ranging between 7 and 8 to the kinetic impactor.

Nuclear Interceptor: nuclear weapons have not been tested in space since the *Limited Test Ban Treaty* forbids all nuclear use in both space and atmosphere. Furthermore, although the effects of a nuclear explosion can be considered to be well known, there has not been any Nuclear Interceptor prototype or any equivalent prototype in space, therefore the *TRL*

should be no higher than 6. On the other hand the launch of nuclear warhead is fully developed (e.g., ICBM), thus we assign a *TRL* ranging from 6 to 8.

Low Thrust: Low Thrust requires the following main critical technologies; low-thrust propulsion, nuclear power generation, autonomous rendezvous and landing, anchoring system. Low-thrust engines delivering the required level of thrust have been used as main propulsion systems since 1998, with Deep Space 1. They could therefore be considered at *TRL 9* already. On the other hand, some missions in the Pareto set require a thrusting time of more than 1000 days, which exceeds the operational lifetime of current electric engines. For those missions either a complete redesign of the propulsion system or multiple engines would be required, in the former case the *TRL* would be not higher than 4. Rendezvous and landing operations for small spacecraft can be considered at *TRL 7* due to previous (e.g., NEAR[79]) and ongoing missions to comets and asteroids (such as Rosetta[80] and Hayabusa[69]). Nuclear reactors delivering between 1 to 10 kW have already flown since 1965 (e.g., the US SNAP-10A) and higher power reactors can be derived from terrestrial ones with limited new developments, thus this technology can be considered at least to be between *TRL* 6 and 7. An anchoring system has already been designed for the lander of Rosetta though for more massive spacecraft the anchoring and landing system would require further development therefore their *TRL* cannot be considered higher than 6. Therefore, overall, the *TRL* for the Low Thrust method can be considered ranging from 4 to 6.

Gravity Tug: Gravity Tug requires the following main critical technologies; autonomous proximal motion control in an inhomogeneous gravity field, nuclear power generation, low-thrust propulsion. A hovering approach to asteroid Itokawa was used by the mission Hayabusa[69]. The same technique is proposed for the gravitational tug, but to a completely different level of accuracy and autonomy and therefore its *TRL* should be between 3 (no test in relevant environment) and 5 (if Hayabusa is considered to be an example of hovering in relevant environment). Low-thrust propulsion has the same *TRL* as for Low-Thrust deviation methods and shares the same issues, in particular the operational lifetime since the number of missions with a pushing time higher than 1000 days is higher than for the Low-Thrust. Nuclear power generation for this method has the same *TRL* as for the Low-Thrust technique therefore the overall *TRL* for the Gravity Tug ranges from 3 to 5.

Mass Driver: Mass Driver requires the following main critical technologies; autonomous rendezvous and landing, autonomous mining in microgravity, high power railgun system, nuclear power generation, anchoring system. Magnetic railgun systems have already been developed and used on Earth for other applications[59], we can thus assume a *TRL 5* for this technology. Rendezvous and landing is at *TRL 7*, as discussed previously for the low thrust technique. Nuclear power generation is between *TRL 6* and *TRL 7*, also as discussed in the low thrust method. The anchoring system and the mining system in microgravity instead require a substantial development [60],[61],[81],[82], thus their *TRL* should not be higher than 4. Though drilling systems have been already tested in space (e.g., Apollo program[83]), the level of power involved for a successful implementation of the Mass Driver would require a substantial redesign of the mining and anchoring system to cope with the microgravity conditions. Since a conceptual design for this technology already exists[84] (*TRL* 2) we can assign a *TRL* ranging between 2 and 4 to the Mass Driver.

Solar Collector: Solar Collector requires the following main critical technologies; adaptive optics, deployment and control of ultra-light mirrors, autonomous orbit control, accurate autonomous pointing. The mirrors have to focus the light of the Sun in every operational condition and therefore the curvature has to be actively controlled, furthermore it is expected that the light is collimated by a series of lenses. The collimation of the beams is of primary importance to maintain the required power density, especially for rotating asteroids with high elongation, for which the closest and farthest distance from the spacecraft could be considerable (i.e., larger than 100 meters). Adaptive optics for terrestrial[85] and space applications have been developed and used in space on telescopes and therefore their *TRL* could be considered to be at 7, on the other hand, for this particular application it would require an autonomous control of the pointing and focusing dependent on the power density of the illuminated spot. This would require a substantial redesign and a new development, therefore the *TRL* should be between 2 and 3. The deployment of ultra-light structures of small to medium dimensions has already been tested in space and would be between *TRL 6* and *7*[86] and ultra-light adaptive mirrors for space have already been developed and prototyped and would be between *TRL* 4 and 5 [87],[88], on the other hand the deployment and control of large focusing mirrors is still at a conceptual stage and therefore at *TRL 2*. Accurate autonomous orbit control is at the same level of the Gravity

Tug and therefore is at *TRL* 4. The overall *TRL* for the Solar Collector is thus considered to be between 2 and 3.

The *TRL* intervals for each deviation methods are summarized in Table III-13. These are then converted into a Δt_{dev} according to Fig. III-7, which shows the man-years Δt_{dev} needed to increase a given technology from its current *TRL* to *TRL* 9.

Table III-13 TRL and Δt_{dev} for all the deviation methods.

Deviation Method	TRL intervals	Δt_{dev} [man-years]
Kinetic Impactor	7-8	1.5-0.4
Nuclear Interceptor	6-8	3.9-0.4
Low-Thrust	4-6	11.5-3.9
Gravity Tug	3-5	13.9-7.7
Mass Driver	2-4	15-11.5
Solar Concentrator	2-3	15-13.9

The development time Δt_{dev} due to the technology readiness level is now applied to the Pareto optimal sets by adding it to the warning time t_w:

$$\mathbf{f} = \left[t_w + \Delta t_{dev}, m_0, -\left\| \Delta r + \delta r \right\| \right]^T \tag{3.11}$$

Since the impact date is kept fixed for all the strategies, all the Pareto optimal solutions that, by adding the new Δt_{dev}, would require an updated warning time $t_w + \Delta t_{dev}$ such that the arrival date at the asteroid exceeds the t_{MOID} are removed from the comparison. As a consequence, a strategy with a low technology readiness requires a longer warning time for the same deviation or a lower deviation for the same warning time. The following three tables (Table III-14 to Table III-16) show the intervals of dominance of all the strategies for a simulated deviation of *Apophis*, *Shiva₃* and *Apollyon₃* after applying the range of *TRL* from Table III-13. Note that, when two numbers are shown in the tables, numbers on the left correspond to the results using the lower TRL boundary (numbers on the left in Table III-13) for all the technologies, while numbers on the right correspond to the results using the upper TRL boundary (numbers on the right in Table III-13). When only one result is shown in Table III-14 to Table III-16, it means that the results remained constant for both lower and upper TRL cases.

Table III-14 Strategy Dominance for *Apophis*.

	NI	**KI**	**LT**	**MD**	**SC**	**SC** *6m*	**GT**
Nuclear Interceptor (**NI**)		*100*	*100*	*100*	*100-98*	*100-99*	*100*
Kinetic Impactor (**KI**)	*7-0*		*99-39*	*61-54*	*59*	*59*	*100*
Low Thrust (**LT**)	*0*	*1-87*		*7-36*	*7-48*	*7-48*	*100*
Mass Driver (**MD**)	*0*	*99-100*	*100*		*0-18*	*0-18*	*100*
Solar Collector (**SC**)	*33-36*	*100*	*100*	*100*		*100*	*100*
Solar Collector *6-m OT*	*20*	*100*	*100*	*100*	*24*		*100*
Gravity Tug (**GT**)	*0*	*0*	*1-0*	*11-4*	*11-15*	*11-15*	

Table III-15 Strategy Dominance for *Shiva*$_3$.

	NI	**KI**	**LT**	**MD**	**SC**	**GT**
Nuclear Interceptor (**NI**)		*100*	*100*	*100*	*100*	*100*
Kinetic Impactor (**KI**)	*26-0*		*100-92*	*94-90*	*91*	*100*
Low Thrust (**LT**)	*0*	*0-50*		*34-51*	*34-59*	*100*
Mass Driver (**MD**)	*0*	*97-99*	*100-99*		*0-43*	*100*
Solar Collector (**SC**)	*0-2*	*100*	*100*	*100*		*100*
Gravity Tug (**GT**)	*0*	*0*	*0*	*0*	*0*	

Table III-16 Strategy Dominance for *Apollyon*$_3$.

	NI	**KI**	**LT**	**MD**	**SC**	**GT**
Nuclear Interceptor (**NI**)		*100*	*100*	*100*	*100*	*100*
Kinetic Impactor (**KI**)	*75-0*		*100*	*98-97*	*97*	*100*
Low Thrust (**LT**)	*0*	*0*		*34-46*	*34-57*	*100*
Mass Driver (**MD**)	*0*	*63-86*	*100*		*0-15*	*100*
Solar Collector (**SC**)	*0*	*100*	*100*	*100*		*100*
Gravity Tug (**GT**)	*0*	*0*	*0*	*0*	*0*	

By comparing Table III-14, Table III-15 and Table III-16 with Table III-3, Table III-6 and Table III-10 some preliminary considerations can be drawn. The first is that when the Technology Readiness Level is considered, the kinetic impactor becomes competitive since its Pareto front encloses parts of the criteria space that the other strategies are not able to cover. On the other hand, even after the technology readiness shifting is applied, the solar collector strategy remains particularly competitive, despite the fact that the nuclear interceptor has better comparative performance in the three tables.

III.2. Cometary Hazard

We will now briefly discuss the issue of the cometary hazard, its mitigation and the main difference with its asteroidal counterpart. When looking at the 149 surveyed Near Earth Comets (NEC)[9] (see Fig. III-8), one may notice how most of the cometary objects

[9] Note that in Chapter I, Section I.4.4., it is said that there are 82 NEC, this is because the list used in the histograms in Fig. III-8 contains not only the comets but also fragments from their disruption.

have Apollo-like orbits, which points out that most of the NEC are in fact *Ecliptic comets* (see Section I.2.2). All other objects in Fig. III-8 with seemingly random distribution of the inclination are *Nearly-isotropic short-period* (<200 years) *comets* (see also Section I.2.2). There are no *Nearly-isotropic long-period* (>200 years) *comets* among the surveyed NECs. This lack of long period objects is due to the fact that comets are very faint objects when far from the Sun, due to both their small size and low albedo (~0.04), and thus are practically undetectable until they are well inside the orbit of Jupiter[10].

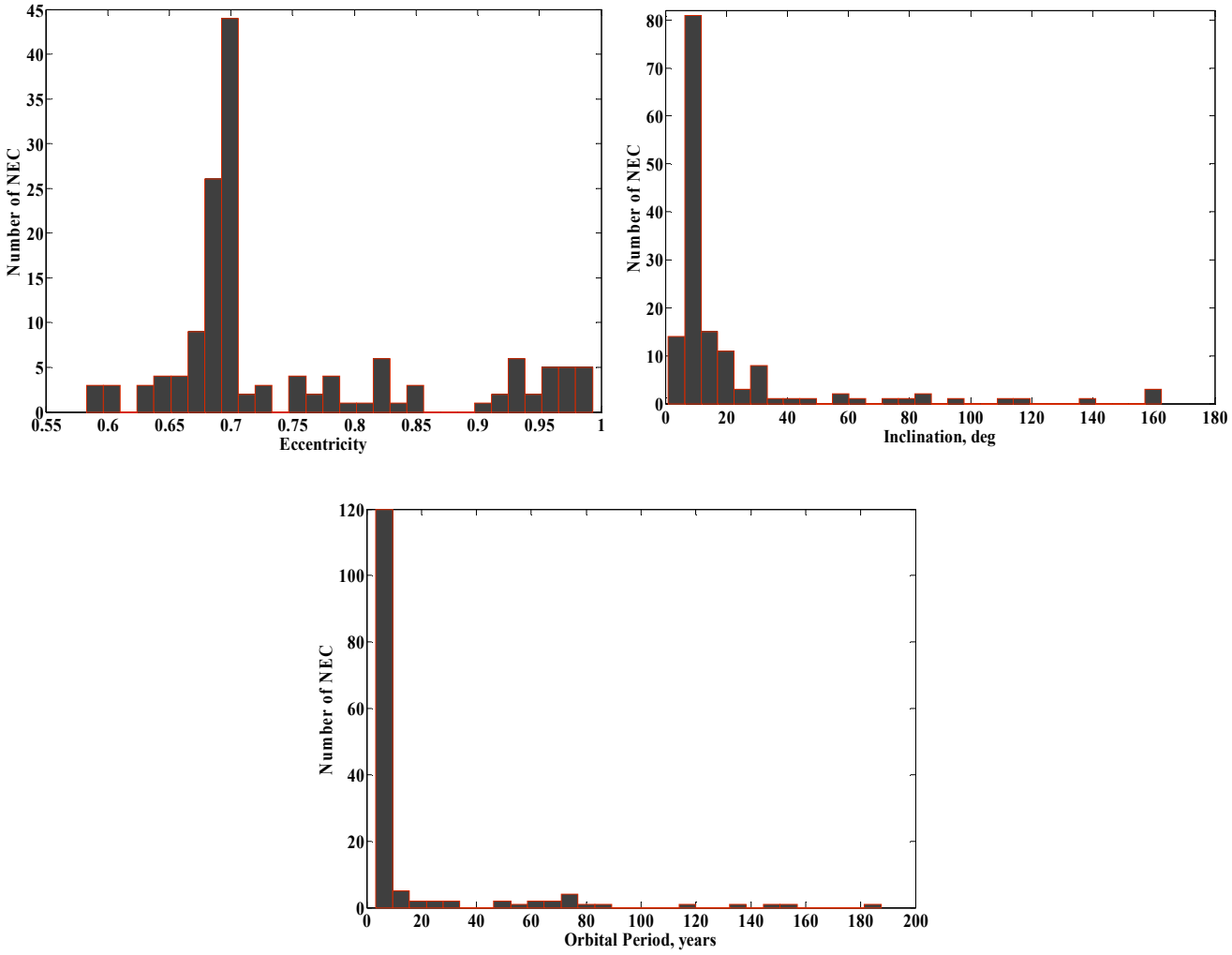

Fig. III-8 Eccentricity, inclination and orbital period histograms of the 149 Near Earth Comets retrieved from NASA's NEO program at 14th November 2008.[23]

Most probably, a NEC would be then detected only when approaching its perihelion and so the arrival of long period and parabolic objects from the Oort cloud cannot be foreseen. A cometary impact scenario should therefore feature either very similar characteristics to the Apollo threats, through a short-period ecliptic comet, or a very short warning time, most probably measured only in months, if through a nearly-isotropic comet.

Since we have already studied *Apollyon* as an example of objects with high eccentricity and low inclination orbit, we will now focus the analysis on nearly-isotropic comets.

The virtual threatening comet presented in Chapter I, *Comet S-T*, is a 133-years nearly-isotropic comet, see Table I-9 and Table I-10. Fig. III-9 shows the change of velocity required to deflect *Comet S-T* the minimum distance necessary to miss the Earth (see Section I.5). For comparison purposes, the figure also shows the velocity required to deflect *Apophis* from an impact trajectory. As shown in the figure, the delta-velocity needed to deflect a highly eccentric long period object such as *Comet S-T* is even less demanding than that required to deflect an Aten-like asteroid. This is mainly due to two reasons; firstly, because, the comet moves at a much higher speed than the asteroid, hence a given delta-velocity produces a larger increment of orbital period in the comet case, secondly, because the comet's orbit is barely altered by the Earth's gravity (due to, again, its large orbital velocity). *Comet S-T* therefore needs only half of the deflection distance needed by *Apophis* in order to miss the Earth (see Table I-11 for hyperbolic factors).

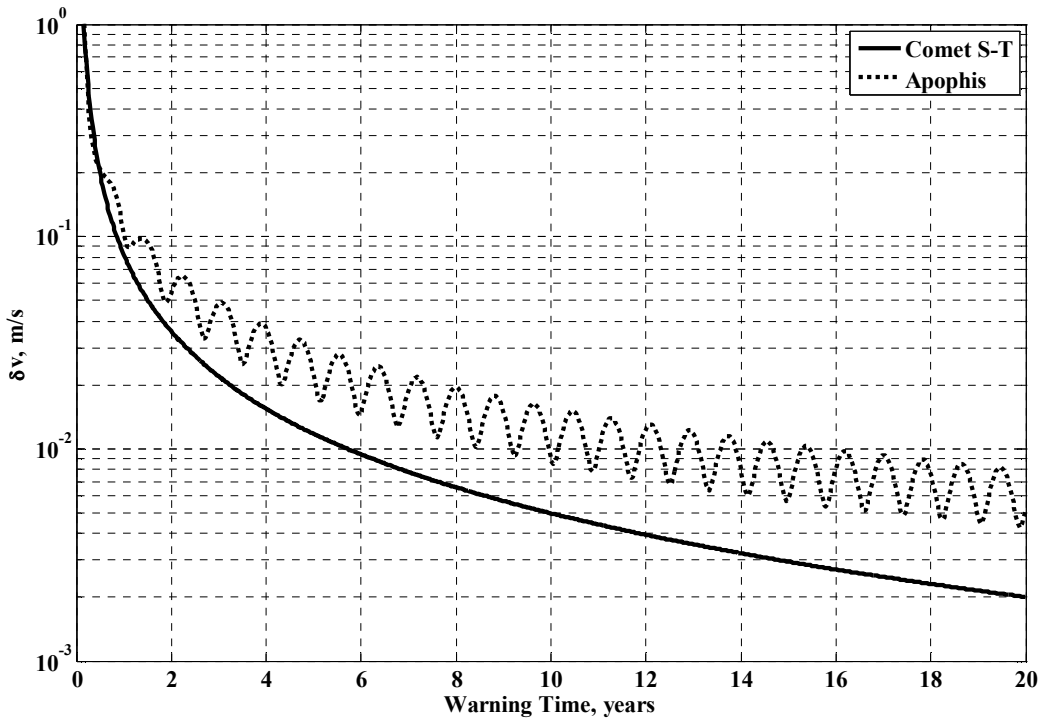

Fig. III-9 Minimum required Δv for a $\varepsilon \cdot R_{\oplus}$ deflection, where $R_{\oplus}$ is the Earth radius and ε is the hyperbolic factor of each particular case.

Fig. III-10 shows the spacecraft mass m_i required at the comet encounter in order to deflect the comet's impact trajectory using the six deflection methods presented in Chapter II. The nuclear interceptor performs very well for the entire range of warning time, and is

clearly the most effective deflection technique among the six analysed. If the solar collector strategy was performing stunningly well for Aten-like asteroids, the opposite happens in the comet case. *Comet S-T* performs only one periapsis approach during the 20 years time prior to the virtual impact and it is only within the year prior to the final impact that the comet reaches a distance from the Sun at which the solar collector generates enough radiation energy to start the sublimation of surface material needed to produce thrust. The efficiency of the solar collector method is therefore greatly reduced by the shape of the comet's orbit. It is also remarkable to note the loss of efficiency of the gravity tractor. This is due to the fact that the comet has a lower density than the asteroids, and has therefore a bigger size than asteroids with similar mass, which implies larger slanting angle for the gravity tug's thrusters, and this, as explained in Section II.12., results into a lower efficiency.

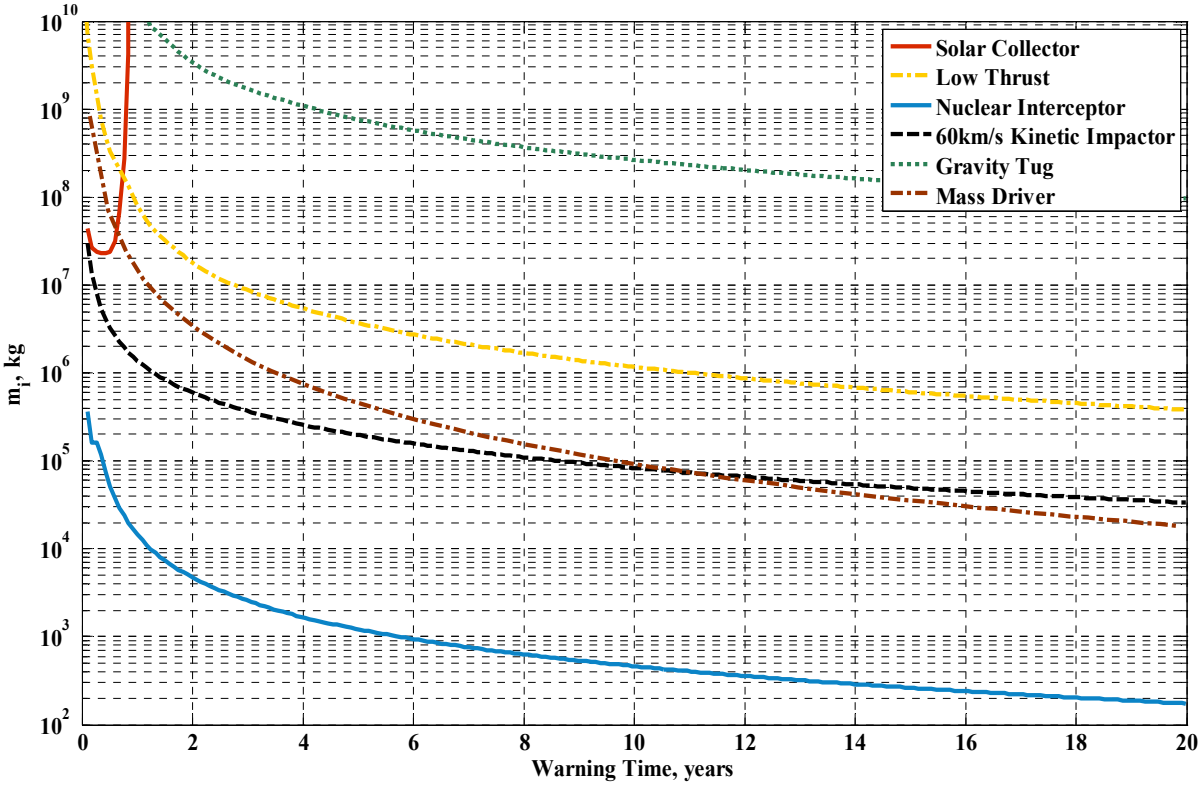

Fig. III-10 Interception mass m_i of the deflection mission required to mitigate the hazard posed by *comet S-T*.

In general, we see from Fig. III-10 that impulsive methods are more effective than low thrust methods for a comet-like threat. We should also notice that the reason why the kinetic impactor performs so efficiently, and even out-performs the mass driver for warning times shorter than 12 years, is due to the fact that the impact velocity chosen is very high (i.e., 60 km/s), which seems perfectly possible when dealing with a retrograde

comet like *Comet S-T*. Moreover, even if methods like the mass driver could perform better than a simple kinetic impactor for long warning times, we still need to account for the propellant mass required to rendezvous with the comet. Screening all possible launch dates and time of flight *ToF* with a Lambert arc, we can derive an approximate delta-velocity requirement for both intercept and rendezvous the comet as a function of the time available until the impact, thus warning time minus the time of flight of the trajectory $t_i = t_w - ToF$. As we see in Fig. III-11, for both cases the delta-velocity required is extremely high, although, at any given time, the rendezvous option is at least twice as expensive as the interception option.

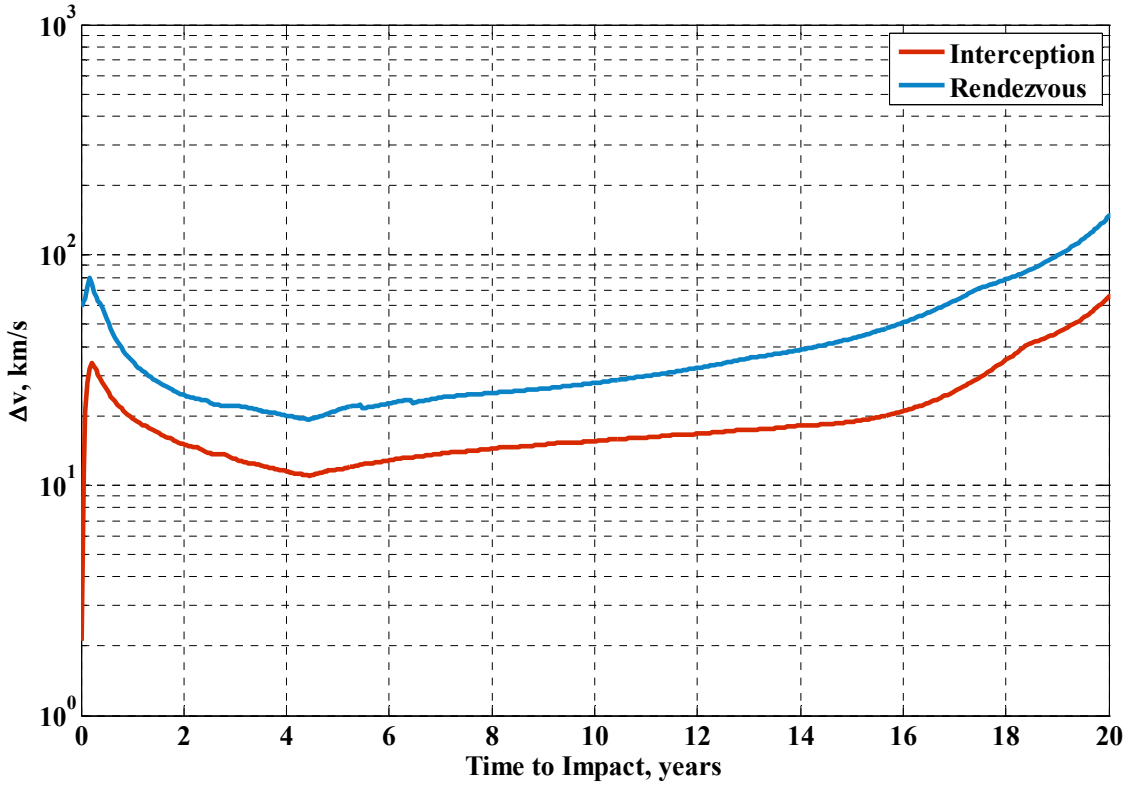

Fig. III-11 Interception trajectory delta-velocity requirements as a function of the time remaining from interception to impact.

Now, if we consider the fact that this sort of celestial threat may not be detected before the comet has crossed the orbit of Jupiter, we should be considering warning times shorter than a year. Fig. III-12 presents the approximate required minimum delta-velocity to reach the comet, departing from Earth within the last year of the comet's trajectory and allowing us the time to impact specified along the X axis of the figure. In other words, the

black curve in Fig. III-12 shows the minimum delta-velocity of a *pork-chop*[10] screening through all possible values of departure times and time of flights that allow us to act onto the comet within that last year. Using Tsiolkovsky's rocket equation, the minimum mass launched into space m_0 needed to deflect the comet within the last year of its trajectory can also be extrapolated by taking into account both the delta-velocity to reach the comet, shown in Fig. III-12, and the minimum interception mass m_i of the nuclear interceptor, shown in Fig. III-10. It is then clear from the figure that such a deflection would be utterly impossible with current technology, since the minimum mass necessary for deflection is more than three orders of magnitude above any current launching capabilities.

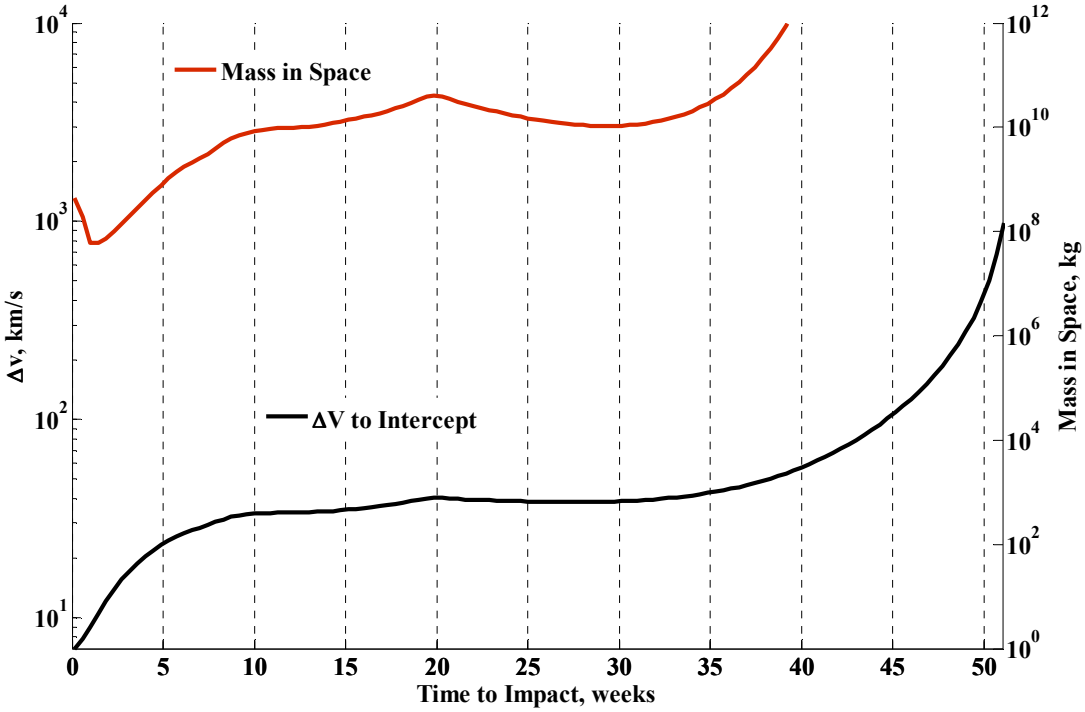

Fig. III-12 Minimum delta-velocity and mass in space for a nuclear interceptor if the comet is discovered one year prior to impact.

Finally and again without considering the year-limit warning time constraint, Fig. III-13 shows the Pareto front of the nuclear impactor for the *Comet S-T*. As we can see, given enough warning time, it could be possible to deflect a comet like the fictitious *Comet S-T*. It is therefore the constraint in warning time of a realistic Nearly-isotropic comet impact threat that poses the most challenging demands.

[10] A pork-chop plot is a graph that depicts the transfer delta-velocities in all possible combinations of launch date and time of flight. It is named after the characteristic pork-chop shaped contours displayed in the graph.

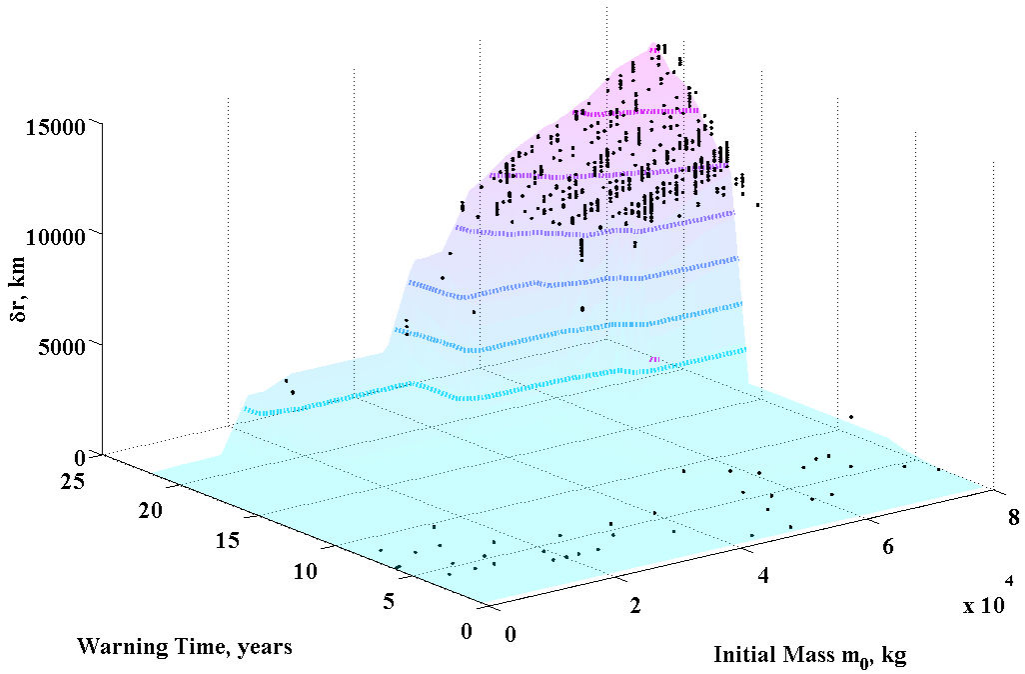

Fig. III-13 Pareto sets for the nuclear interceptor deviation method applied to asteroid *Comet S-T*.

Concluding, we can then say that Nearly-isotropic comets, and particularly long period ones, are definitely the most difficult objects to deflect, should this necessity arise. On a more positive note, *Stokes et al.* [10] showed, by reviewing several authors' estimates, that the approximate comparative value of the threat posed by cometary objects is around 1% the threat posed by Near Earth Asteroids.

III.3. Chapter Summary

This chapter used the six deflection methods modelled in Chapter II to create thousands of preliminary mission design through an agent-based search approach. We then compare these missions scenarios using two methods. We used deviation isolines to show the part of the studied domain on warning time and mass into space where each deflection method could successfully deflect the different asteroidal test cases (i.e., Fig. III-2, Fig. III-4 and Fig. III-6). We then proposed a second comparison procedure based on the concept of dominance (i.e., Table III-3 to Table III-11). Using this original method the comparison is not subject to any particular ideal or fictitious situation in which the deflection method is applied. We also introduce the analysis of the technology readiness of each deflection method and, adding time margins for technology development, perform a third comparison taking into account technological issues (i.e., Table III-14, Table III-15 and Table III-16).

The cometary impact threat is also analysed using *Comet S-T* as test case. This time, the study of the deflection and a preliminary analysis of the transfer leg are performed separately. The results show that, despite the fact that impulsive deflection manoeuvres have a good efficiency on comets and that the delta-velocity of its interception transfer is much less demanding than a rendezvous, requirement for a low thrust methodology, the one-year warning time constraint poses an apparently insuperable obstacle for the feasibility of the hazard mitigation of such a threat.

Chapter IV

On the Consequences of a Fragmentation Due to a NEO Mitigation Strategy

Along previous chapters we have attempted to classify, evaluate and compare a group of deflection techniques in terms of deflection efficiency, other similar studies with different efficiency definitions can be found in the literature[42],[53],[89],[90],[70], but very little has been done on the analysis of a possible fragmentation of the threatening object[50]. This chapter aims to fill this void by assessing the viability of a single-impulsive deflection of an Earth threatening object and examining the possible consequences of a catastrophic fragmentation outcome. In particular, the chapter considers the minimum level of energy (collisional energy) required to deviate an asteroid by a distance that ensures a successful deflection, taking also into account the hyperbolic trajectory that the asteroid will follow when approaching the Minimum Orbit Interception Distance (MOID) from the Earth. The collisional energy is then compared with the predicted specific energy required to completely fracture the asteroid and, as will be shown, for some warning times the collision energy required for an impulsive deviation technique can rise well above the theoretical catastrophic fragmentation limit. As a consequence the asteroid can fragment in an unpredictable number of pieces having different mass and velocity. The velocity associated with each piece of the asteroid uniquely determines its future trajectory.

The chapter will consider two possible cases: the fragmentation being the desired outcome of the deviation strategy or the undesired product of a mitigation mission. In the latter case we will analyse the evolution of the cloud of fragments and the probability that the bigger pieces in the cloud have to impact the Earth. In fact, if the initial relative velocity yielded to the larger pieces is not high enough, the gravity attraction of the largest fragment does not allow for a complete disgregation of the cloud of fragments, and an important fraction of the mass re-accumulates forming a rubble-pile asteroid. As a

consequence of the uncertainties in magnitude and direction of the orbital velocity of this new rubble pile object, the potential risk to Earth is increased with respect the risk expected after the mitigation attempt. We will also show how the potential risk to Earth can be reduced by providing enough velocity dispersion to the fragments or by fragmenting the asteroid to sizes under a threshold at which they do not pose any danger to the Earth surface.

IV.1. Fragmentation of Asteroids

In order to assess the likelihood of a fragmentation outcome from an impulsive mitigation technique, the asteroid resistance to fragmentation needs first to be estimated. The critical specific energy Q^* is defined as the energy per unit of mass necessary to *barely catastrophically disrupt* an asteroid; an asteroid is *barely catastrophically disrupted* when the mass of the largest fragment of the asteroid is half the mass of the original asteroid, or in other words, the remaining mass of the original asteroid is half the initial mass. If f_r is the fragmentation ratio, defined as:

$$f_r = \frac{m_{\max}}{M_a} \tag{4.1}$$

where m_{max} is the mass of the largest fragment and M_a the initial mass of the asteroid, then a catastrophic fragmentation is defined as a fragmentation where $f_r < 0.5$.

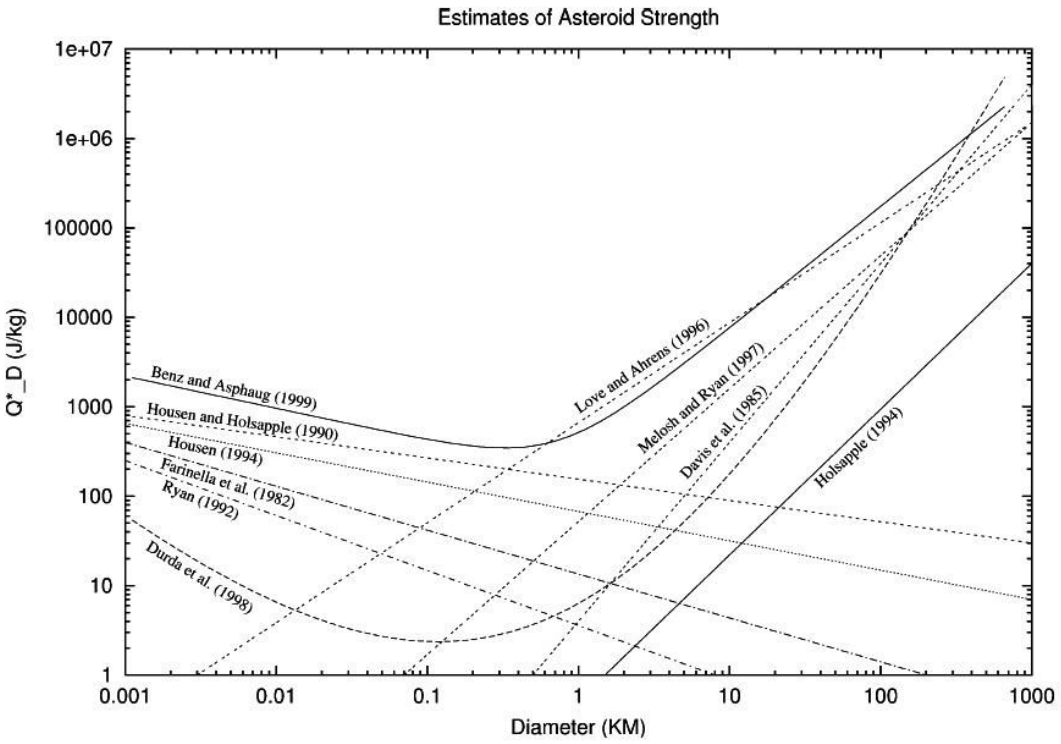

Fig. IV-1 Estimates by different authors of critical specific energy Q^* to *barely catastrophically disrupt* (i.e., f_r=0.5) an asteroid.

Fig. IV-1 shows several estimates of the critical specific energy Q^* from various authors, which were collected and published by *O'Brien & Greenberg*[91]. Estimates on asteroid strength shown in Fig. IV-1 are based on power-law parameterizations with two different gradients; one slope for small objects, which rely on their material strength to avoid break-up, and another slope for large objects, where gravity dominates material strength through self-compression and gravitational re-accumulation. This chapter addresses the issue of fragmentation of small to medium size asteroids. These are celestial objects ranging from 40 m to 1 km in diameter and constitute the main bulk of the impact threat. Asteroids smaller than 40 m in diameter are expected to dissipate at a high altitude in the Earth atmosphere[19] , thus nothing smaller than 40 m will be included in the following analysis. On the other hand, the survey of objects with a diameter larger than 1 km is believed to be almost complete, therefore only the remaining small not discovered asteroids pose a threat[10].

The uncertainty associated to the description of the fragmentation process is clear if one looks at the different scaling laws from Fig. IV-1. Furthermore, the exact value of Q^* depends on a number of factors, such as the composition and structure of the asteroid or the velocity and the size of the impactor. For the sake of analysis, in this chapter, a

complete and exact description of the fragmentation process is not required and an approximate estimate of the value of the critical specific energy Q^* is sufficient.

The work of *Ryan & Melosh*[92] and *Holsapple*[93] provided the necessary tools to understand and approximate the qualitative limits of the critical specific energy Q^* for the range of studied asteroids. Fig. IV-2 shows the critical specific energy Q^* for asteroids ranging from 40 m to 1 km diameter, computed by using the scaling laws provided by the aforementioned authors. *Ryan & Melosh*[92] provide a scaling law for three different material strengths (basalt, strong mortar and week mortar) that also considers the velocity of the impactor and impacted object diameter. Fig. IV-2 shows then two different impact velocities for *Ryan & Melosh*'s scaling laws; 10 km/s and 50 km/s, which account for an example of a prograde orbit impactor and an example of a retrograde one, respectively. On the other hand, *Holsapple*'s[93] scaling law only considers a general representative material strength, and so, the only varying parameter is the diameter of targeted object.

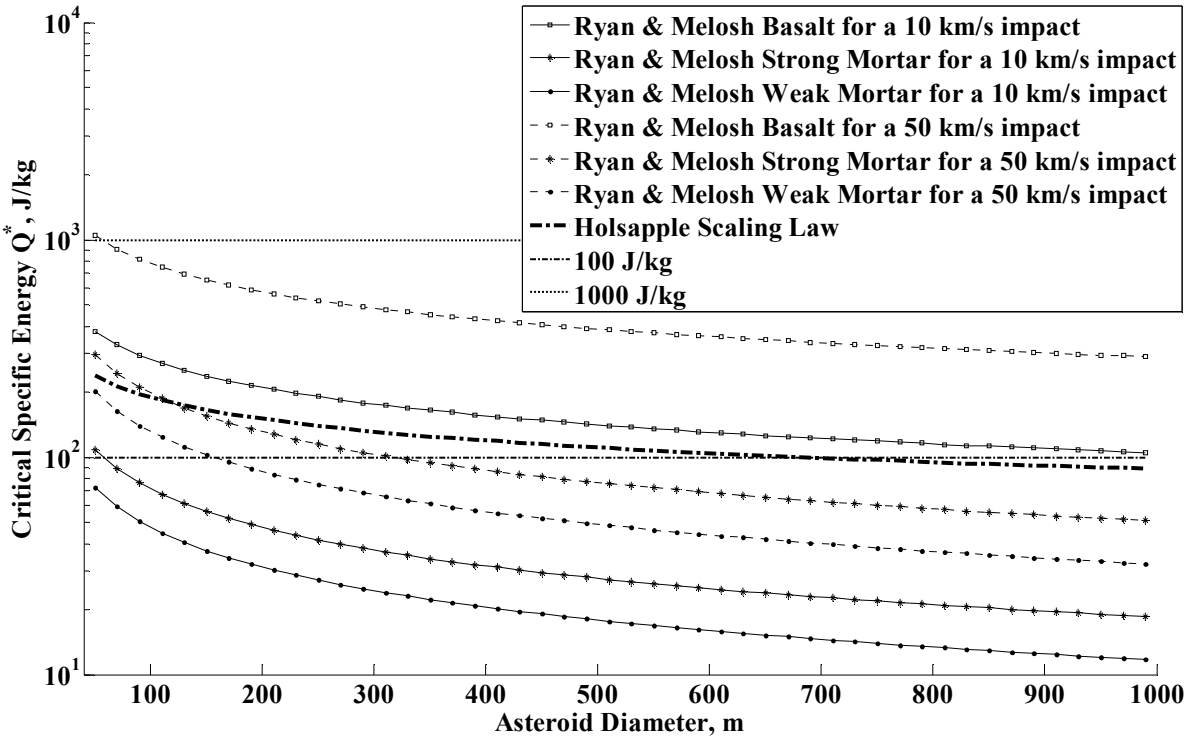

Fig. IV-2 Critical Specific Energy Q^* for *barely catastrophically disrupting* asteroids from 40 m to 1 km in diameter, calculated using *Ryan & Melosh*[92] and *Holsapple*[93].

In light of the results shown in Fig. IV-2, two general qualitative limits were drawn: one at 1000 J/kg and a second at 100 J/kg. The upper fragmentation limit at 1000 J/kg is above any of the specific energies Q^* expected from the scaling laws in Fig. IV-2, including those of basalt strength from *Ryan & Melosh*[92]. In some cases, this upper limit

is more than one order of magnitude above the predicted Q^*. Hence, for the studied range of diameters, the limit at 1000 J/kg is considered here as a fated catastrophic fragmentation. On the other hand, the lower fragmentation limit at 100 J/kg is at the same energy level of most of the critical energies Q^* predicted by Fig. IV-2, and more importantly, the 100 J/kg limit is, in general, above the four predicted Q* using *Ryan & Melosh*[92]'s mortar strengths. If asteroids have the tensile strength of "rubble piles", as the rotational state of small asteroids seems to indicate[36], the scaling laws for mortar tensile strength from Fig. IV-2 may be a good approximation. Hence, the 100 J/kg limit may be considered as a reasonable fragmentation limit according the results of *Ryan & Melosh*[92] and *Holsapple*[93] scaling laws.

IV.2. NEO Deflection Requirements

In order to compute the minimum deflection required to deviate a threatening asteroid, we will need to define the minimum distance that an asteroid needs to be shifted in order to miss the Earth. Since the threatening asteroid will follow a hyperbolic approach at the proximity of the Earth, the minimum distance of one Earth radius $R_\oplus$ will need to be corrected in order to account for the gravitational pull of the Earth in its final approach. This correcting factor is:

$$\varepsilon = \frac{r_a}{r_p} = \sqrt{1 + \frac{2\mu_e}{r_p v_\infty^2}} \tag{4.2}$$

where r_a is the minimum distance between the hyperbola asymptote and the Earth, i.e., focus[11] of the hyperbola, r_p is the perigee distance, which is fixed to $R_\oplus$ (minimum distance to avoid collision without considering the atmosphere altitude), μ_e is the gravitational constant of the Earth and v_∞ the hyperbolic excess velocity. Note that the correcting factor only depends on the hyperbolic excess velocity of the threatening object.

As will be seen later, the analysis carried out in this chapter is very sensitive to the orbital parameters of the asteroid. Table IV-1 summarizes the different orbital elements of the four test cases that are used here to provide a better insight to the analysis. Together with the six Keplerian elements, the epoch of elements, the t_{MOID} or time of the minimum interception distance that is used as the virtual impact, the hypebolic factor ε, the impact

[11] The minimum distance between the focus and the asymptote of a hyperbolic orbit is equal to minus the semiminor axis b of the hyperbola, $r_a = -b$.

velocity and the mass of each test case are also shown in the table. A circular orbit was also added to the test cases in order to provide a more manageable example of the orbital dynamics of the dispersion of fragments, since this type of orbit has as the main advantage that the dispersion of fragments will not depend on the point along an orbit at which the break-up occurred.

Table IV-1 Summary of the orbital characteristics of the four cases analysed during the chapter.

	Apophis	*Shiva*$_3$	*Apollyon*$_3$	*Circular*
a [AU]	0.922	0.875	1.706	1.000
e	0.191	0.313	0.518	0
i [deg]	3.331	7.828	10.70	0
Ω [deg]	204.5	259.9	266.8	0
ω [deg]	126.4	50.65	121.2	0
M [deg]	222.3	97.21	18.09	0
Epoch [MJD]	53800.5	62481.0	62488.0	62488.0
t_{MOID} [MJD]	62240.3	62182.1	62488.0	62500.0
ε	2.16	1.52	1.29	22.50
v_{impact} [km/s]	12.62	14.85	17.78	11.19
M_a [kg]	$2.7\text{x}10^{10}$	$5.0\text{x}10^{10}$	$5.0\text{x}10^{10}$	$5.0\text{x}10^{10}$

It can be noted, in Table IV-1, that the *Circular* case has a very large hyperbolic factor compared to the other cases; this is due to the resemblance of the *Circular* orbit to the Earth orbit. The more an orbit resembles the Earth orbit, the lower the relative velocity at the encounter will be and, clearly, this makes the asteroid more susceptible to be affected by the Earth gravity, since it will spend more time in close encounter. For example, a relative velocity of 0 km/s has an infinite hyperbolic factor and a minimum impact velocity of 11.18km/s, which is the theoretical parabolic escape velocity. The opposite is also true; the more an orbit differs from the Earth orbit, the higher its relative velocity at encounter and the lower the hyperbolic factor. In fact, without considering the *Circular* case, *Apollyon*$_3$ is carrying the highest amount of kinetic energy, but it is *Apophis* that is the most prone to "fall" into Earth, due to its larger hyperbolic factor.

IV.2.1. Minimum Change of Velocity

Once the minimum distance to avoid collision is set, the minimum change of velocity to provide a safe deflection can be calculated. Fig. IV-3 presents the necessary change of

velocity within an interval of time spanning 20 years before the hypothetical impact at time t_{MOID} to deviate the four test cases. The minimum change of velocity required to deviate an object by a given distance from its initial orbit is computed by means of the proximal motion equations expressed as a function of the variation of the orbital elements. The variation of the orbital elements was then computed with Gauss' planetary equations. A complete description of the methodology is presented in the Appendices, Section A.1.

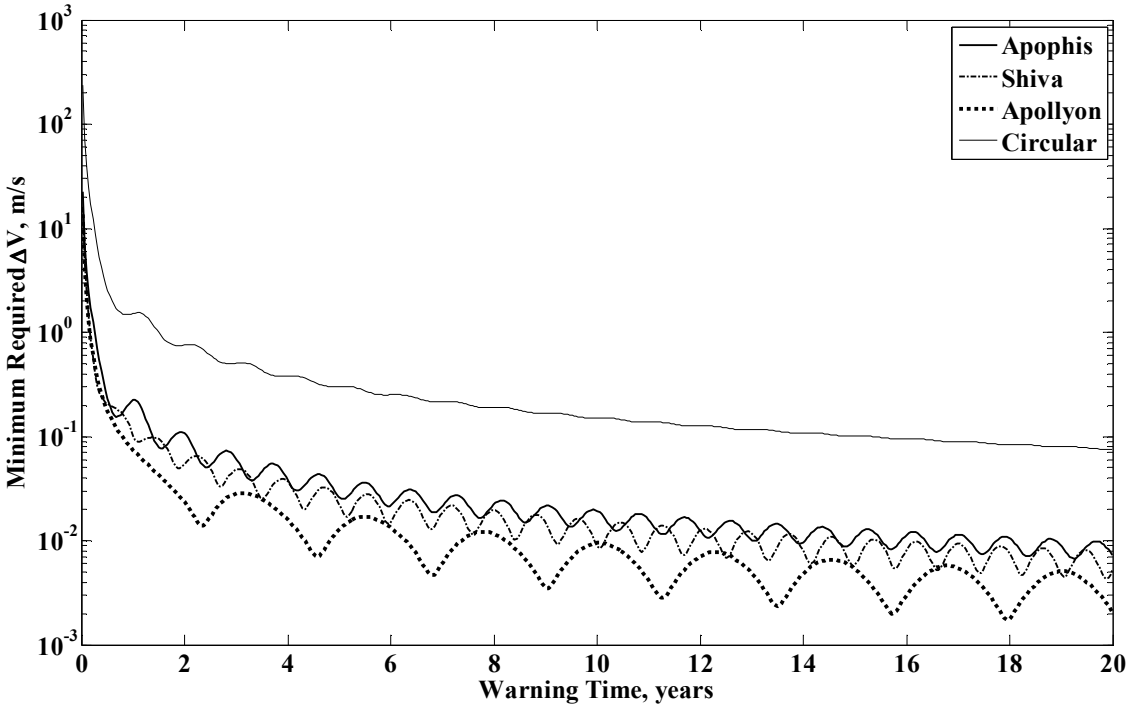

Fig. IV-3 Minimum required Δv for a $\varepsilon \cdot R_{\oplus}$ deflection.

The minimum required Δv in Fig. IV-3 were computed using the hyperbolic factor ε of each particular case. The *Circular* case, although an unrealistic orbit for an asteroid[10], is a good example to show that although objects with high eccentricity and large semimajor axis will have very high impact velocities (e.g. Apollo asteroids or comets), objects with low excess velocities v_{∞} will have slightly lower impact energies, but the required change of velocity to deflect them would be considerably higher. Another distinctive feature of Fig. IV-3 is the oscillatory behaviour of the minimum required Δv. This sinusoidal evolution repeats with the orbital period of the asteroid and its amplitude is a function of the orbital variations of the velocity. Each minimum occurs at the point where the asteroid is moving at its highest speed, thus its perihelion, and so, it is more vulnerable to changes in its orbital period.

IV.2.2. Kinetic Impactor & Nuclear Interceptor

Any of the mitigation techniques seen in Chapter II could be capable of providing the necessary change of velocity to ensure that a threatening object misses the Earth, but only impulsive mitigation actions can provide quasi-instantaneously specific energies of the order of the Critical Energy Q^* from Fig. IV-2. Hence, deflection strategies such as kinetic impactor and nuclear interceptor could trigger a catastrophic outcome as a result of a deviation attempt. The remaining of this section will briefly remind the main features of these two mitigations strategies, for more comprehensive description refer back to Chapter II or to *J.P.Sanchez et al*[70].

The Kinetic Impactor is the simplest concept for asteroid hazard mitigation: the asteroid's linear momentum is modified by ramming a mass into it. The impact is modelled as an inelastic collision resulting into a change in the velocity of the asteroid multiplied by a momentum enhancement factor[47]. This enhancement is due to the blast of material expelled during the impact, although if the asteroid undergoes a fragmentation process after the impact, the enhancement factor should be considered 1, since all the material is included in the fragmentation process. Accordingly, the variation of the velocity of the asteroid $\Delta\mathbf{v}_a$ due to the impact is given by:

$$\Delta\mathbf{v}_a = \beta \frac{m_{s/c}}{\left(M_a + m_{s/c}\right)} \Delta\mathbf{v}_{s/c} \tag{4.3}$$

where β is the momentum enhancement factor, $m_{s/c}$ is the mass of the kinetic impactor, M_a is the mass of the asteroid and $\Delta\mathbf{v}_{s/c}$ is the relative velocity of the spacecraft with respect to the asteroid at the time when the mitigation attempt takes place.

Knowing the minimum change of velocity required for a deflection (see Fig. IV-3), Eq.(4.3) can be used to compute the Specific Kinetic Energy (SKE) that an asteroid would have to absorb from a kinetic impactor mission attempting to modify its trajectory:

$$SKE = \frac{1}{2} \frac{m_{s/c} \Delta v_{s/c}{}^2}{M_a} = \frac{1}{2} \frac{\left(M_a + m_{s/c}\right)^2}{\beta^2 \cdot M_a \cdot m_{s/c}} \Delta v_a^2 \tag{4.4}$$

Fig. IV-4 presents an example of the Specific Kinetic Energy (SKE) as a function of warning time that a kinetic impactor should apply to the asteroid in order to provide the $\Delta\mathbf{v}_a$ required in Fig. IV-3. The impactor mass $m_{s/c}$, for this example, was set to 5,000 kg and the impact velocity $\Delta\mathbf{v}_{s/c}$ was calculated with an enhancement factor β equal to 2,

which, as discussed in Chapter II, is a conservative value for this parameter. Note also that, for a given a delta-velocity $\Delta\mathbf{v}_a$, the SKE will vary with the kinetic impactor mass $m_{s/c}$, thus, an example with higher impact mass will provide a lower value of SKE. The two aforementioned fragmentation limits of 1000 J/kg and 100 J/kg are also superposed on the figure. In general terms, the SKE needed for very short warning times (<2 years) is clearly above the fragmentation limits, only for very long warning times (> 10 years) the energy required for a kinetic deflection begins to move below the fragmentation limits.

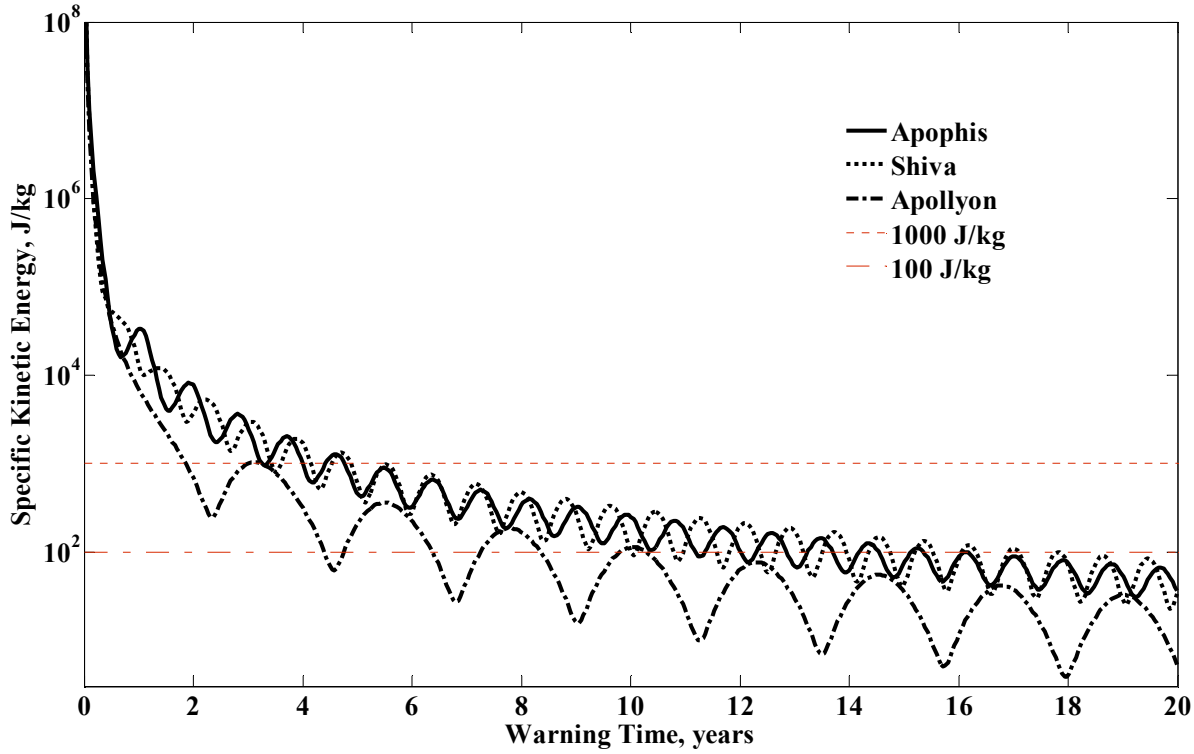

Fig. IV-4 Minimum SKE required for a deflection mission with 5,000 kg of impact mass as a function of warning time.

It should also be noted that a kinetic impactor may require unrealistic impact velocities $\Delta\mathbf{v}_{s/c}$ to provide very large SKE. For example, in order for a kinetic impactor to deliver collisional energies greater than 1000 J/kg it would need an impact mass of more than 50 tons and relative velocity larger than 50 km/s. Considering retrograde trajectories, impact velocities of at least 60 km/s are possible[56] even without using advanced propulsion concepts[57]. Therefore, assuming impact velocities close to 50 km/s only a few tons of impact mass would be required to provide a collisional energy in the order of 100 J/kg.

The Nuclear Interceptor strategy considers a spacecraft carrying a nuclear warhead and intercepting the asteroid. The model used in this study, fully described in Section 2

from Chapter II, is based on a stand-off configuration over a spherical asteroid, i.e., the nuclear device detonates at a given distance from the asteroid surface. The energy released during a nuclear explosion is carried mainly by X-rays, neutrons and gamma radiation that are absorbed by the asteroid surface. This sudden irradiation of the asteroid, which causes material ablation and a large and sudden increase of the surface temperature, would induce a stress wave that while propagating through the asteroid could trigger not only the surface material ablation that was intended to obtain a change of velocity, but also the fragmentation of the whole body. The Specific absorbed Nuclear Energy (SNE) is defined here as the portion of the energy released that is radiated over the asteroid divided by the mass of the asteroid:

$$SNE = \frac{E_t \cdot S}{M_a} \tag{4.5}$$

where E_t is the total energy released by the nuclear device and S is the fraction of the area of the shock wave that intersects the asteroid (Eq.(2.2)).

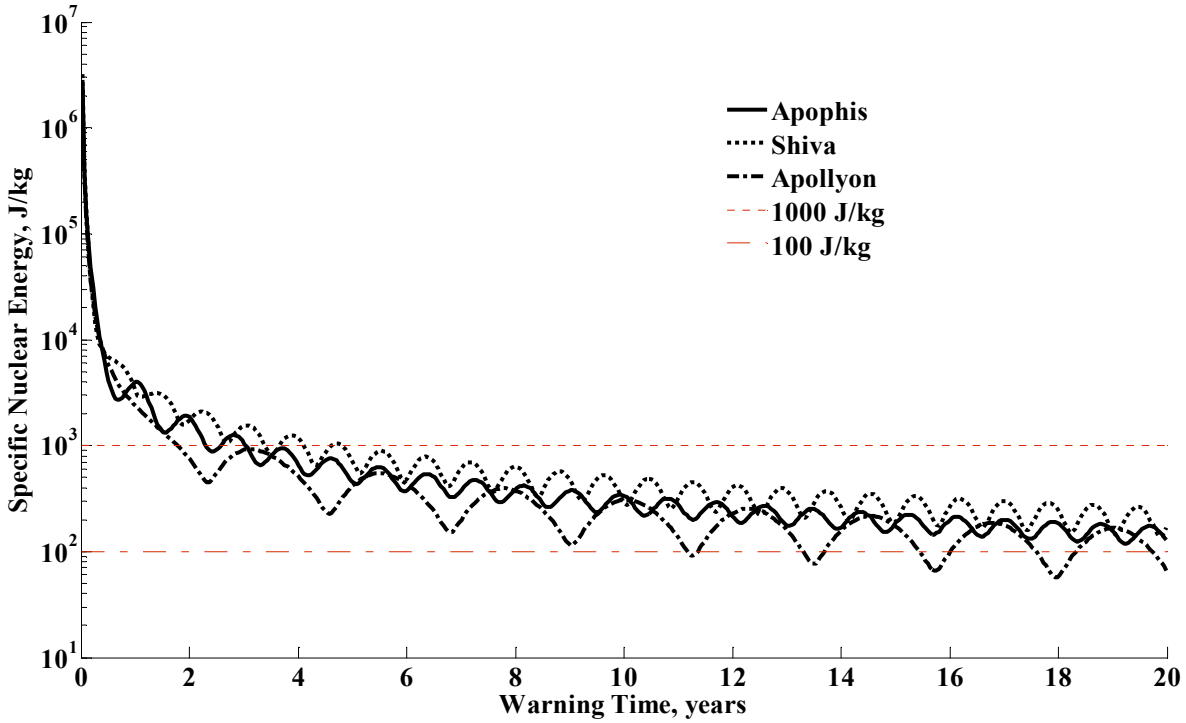

Fig. IV-5 Specific absorbed Nuclear Energy (SNE) provided for a nuclear interceptor (see Section II.1) attempting to deflect a threatening asteroid by delta-velocity as specified in Fig. IV-3.

The two suggested limits (1000 J/kg and 100 J/kg) must be taken cautiously when assessing the likelihood of fragmentation triggered by a nuclear interceptor. Since these two limits were estimated from hypervelocity impact studies[94], the actual fragmentation

energies for an asteroid being deflected by a nuclear device may be different, because of the different physical interaction. However, in this work it was considered that the shock wave caused by an impact and the thermal stress wave generated by the nuclear explosion are analogous, and therefore the associated fragmentation energies are expected to have similar orders of magnitude. It is also interesting to note that the SNE remains at higher levels of specific energy for long warning times, compared with the SKE. This is a consequence of the fact that at low levels of energies, an increasing percentage of the nuclear energy delivered is used to heat the asteroid up, without ablating material, there is therefore no change in linear momentum and the nuclear impactor becomes less efficient in terms of energy. Despite this loss of efficiency, the dry mass required for an equivalent deflection using a kinetic impactor will still be several orders of magnitude higher.

IV.3. Statistical Model of a Fragmented Asteroid

From the energetic requirements of a hazard mitigation mission, we can conclude that the possibility of an undesired break-up of an asteroid during a deflection attempt cannot be ignored. The consequences of an undesired fragmentation can be evaluated by studying the evolution of the cloud of fragments generated during the break-up process. The quantity, size and velocity of the pieces spawned by the fragmentation process needs then to be assessed. Building a deterministic dynamical model of the fragmentation and dispersion process is out of the scope of this work, instead the following section proposes a statistical model of the initial distribution of the fragments with associated positions and velocities and a methodology to calculate the probability to find the fragments in particular positions in space at different times.

IV.3.1. Fragmented Asteroid Dispersion

The position and velocity of every piece of a fragmented asteroid can be described as a stochastic process, even if the dynamical system is deterministic, since the initial conditions of the system are not known and can only be assessed through a probability density function. In particular, considering a scalar function describing the probability density of a dynamic system such as $\rho(\mathbf{X}(t)) = \rho(\mathbf{x}, \mathbf{v}; t)$, where $\rho(\mathbf{x}, \mathbf{v}; t)$ is the probability of a fragment to have position $\mathbf{x}$ and velocity $\mathbf{v}$ at a time t. The probability density function $\rho(\mathbf{X}(t))$ relates to an initial probability density function $\rho(\mathbf{X}(0))$ through the equation:

$$\rho(\mathbf{X}(t)) = \int_{\Gamma} \delta\left(\mathbf{X}(t) - \phi^t(\mathbf{X}(0))\right)\rho(\mathbf{X}(0))\, d\Xi(0) \tag{4.6}$$

where $\phi^t(\mathbf{X}(0))$ denotes the *flux* of the system, or evolution of the state $\mathbf{X}(0) = [\mathbf{x}(0), \mathbf{v}(0)]^T$ over a time-span t so that $\phi^t(\mathbf{X}(0))$ is equal to $[\mathbf{x}(t), \mathbf{v}(t)]^T$, $\delta(\mathbf{y})$ is a multi-dimensional Dirac-delta, which represents the product of the one-dimensional Dirac-delta functions, that will allow a probability $\rho(\mathbf{X}(0))$ to be added to the total probability of $\rho(\mathbf{X}(t))$, only if the initial state vector $\mathbf{X}(0)$ can effectively evolve to $\mathbf{X}(t)$, and finally, $d\Xi(0)$ refers to the product of the one-dimensional differential components of the vector $\mathbf{X}(0)$, i.e., $dx \cdot dy \cdot dz \cdot dv_x \cdot dv_y \cdot dv_z$, and defines the volume of an infinitesimal portion of the phase space Γ, which is the feasible phase space in which the system evolves.

If we introduce the new variable $\mathbf{z} = \phi^t(\mathbf{X}(0))$ and the associated Jacobian determinant as $|\mathbf{J}| = \left|\frac{\partial \phi^t(\mathbf{X}(0))}{\partial \mathbf{X}(0)}\right|$, we can substitute the differential $d\Xi(0)$ with $d\zeta / \|\mathbf{J}\|$ in Eq.(4.6), where $d\zeta$ is the product of the one-dimensional differentials components of the vector $\mathbf{z}$ and $\|\mathbf{J}\|$ is the absolute value of the Jacobian determinant. This allows us to integrate Eq.(4.6) using the feasible phase space at time t instead of the initial phase space, resulting in the following integration:

$$\rho(\mathbf{X}(t)) = \int_{\Gamma} \delta\left(\mathbf{X}(t) - \mathbf{z}\right)\rho\left(\phi^{-t}(\mathbf{z}); 0\right)\frac{d\zeta}{\|\mathbf{J}\|} \tag{4.7}$$

Using the definition of a Dirac-delta function[12], Eq.(4.7) resolves to:

$$\rho(\mathbf{X}(t)) = \rho(\mathbf{x}, \mathbf{v}; t) = \frac{1}{\|\mathbf{J}\|}\rho(\phi^{-t}(\mathbf{x}, \mathbf{v}); 0) \tag{4.8}$$

Invariance of the volume element of the phase space

Eq.(4.8) tells us that the probability of a particular fragment having position $\mathbf{x}$ and velocity $\mathbf{v}$ at a time t is the same probability of having the initial conditions that can make the fragment dynamically evolve to the particular state $\mathbf{X}(t)$ and then scaled by the absolute value of the Jacobian determinant $\|\mathbf{J}\|$. The Jacobian determinant $\|\mathbf{J}\|$ defines the evolution of the volume of the phase space from the initial time of the break-up to a given time t.

[12] $\int_{-\infty}^{\infty} \delta(x-a)\varphi(x)dx = \varphi(a)$

Hamiltonian system dynamics will be used in the remainder of this section to prove that $\|\mathbf{J}\| = 1$.

Considering a Hamiltonian $H(\mathbf{q},\mathbf{p})$, where $\mathbf{q}$ is a 3-D vector of generalized coordinates and $\mathbf{p}$ is a 3-D vector of generalized momenta, the dynamical system will evolve as $\mathbf{Q}(t) = (\mathbf{q}(t),\mathbf{p}(t)) = \phi^t(\mathbf{Q}(0))$, where the flux $\phi^t(\mathbf{q},\mathbf{p})$ is defined by Hamilton equations as:

$$\begin{aligned} \dot{q}_i &= \frac{\partial H(\mathbf{q},\mathbf{p})}{\partial p_i} \\ \dot{p}_i &= -\frac{\partial H(\mathbf{q},\mathbf{p})}{\partial q_i} \end{aligned} \tag{4.9}$$

Eq.(4.9) can be written in a more compact form using matrix nomenclature:

$$\dot{\mathbf{Q}}(t) = \mathbf{A} \cdot \frac{\partial H(\mathbf{q},\mathbf{p})}{\partial \mathbf{Q}(t)} \tag{4.10}$$

where $\mathbf{A}$ is an asymmetric square matrix for a 6-D state vector $\mathbf{Q}(t) = (\mathbf{q}(t),\mathbf{p}(t))$ defined as follows:

$$\mathbf{A} = \begin{pmatrix} \mathbf{0} & \mathbf{I} \\ \mathbf{-I} & \mathbf{0} \end{pmatrix}$$

where $\mathbf{I}$ is a 3×3 unit matrix and $\mathbf{0}$ is a 3×3 null matrix.

The partial derivative of $\mathbf{Q}(t)$ with respect to time t can be written using the chain rule as:

$$\dot{\mathbf{Q}}(t) = \frac{\partial \mathbf{Q}(t)}{\partial \mathbf{Q}(0)} \cdot \frac{\partial \mathbf{Q}(0)}{\partial t} = \mathbf{J} \cdot \frac{\partial \mathbf{Q}(0)}{\partial t} \tag{4.11}$$

where $\partial\mathbf{Q}(t)/\partial\mathbf{Q}(0)$ is a Jacobian matrix $\mathbf{J}$ of partial derivatives, thus Eq.(4.11) can be rewritten, using the Hamilton equations matrix nomenclature introduced in Eq.(4.10), as:

$$\dot{\mathbf{Q}}(t) = \mathbf{J} \cdot \mathbf{A} \cdot \frac{\partial H(\mathbf{q},\mathbf{p})}{\partial \mathbf{Q}(0)} \tag{4.12}$$

We can now write the last element in the right side of Eq.(4.12) as:

$$\frac{\partial H(\mathbf{q},\mathbf{p})}{\partial \mathbf{Q}(0)} = \left(\frac{\partial H(\mathbf{q},\mathbf{p})}{\partial \mathbf{Q}(t)}^T \cdot \frac{\partial \mathbf{Q}(t)}{\partial \mathbf{Q}(0)} \right)^T = \mathbf{J}^T \frac{\partial H(\mathbf{q},\mathbf{p})}{\partial \mathbf{Q}(t)} \tag{4.13}$$

where $\mathbf{J}^T$ is the transpose Jacobian Matrix $\mathbf{J} = \left(\frac{\partial \phi^t(\mathbf{Q}(0))}{\partial \mathbf{Q}(0)} \right)$. Eq.(4.12) and Eq.(4.13) can now be set together as:

$$\dot{\mathbf{Q}}(t) = \mathbf{J} \cdot \mathbf{A} \cdot \mathbf{J}^T \cdot \frac{\partial H(\mathbf{q},\mathbf{p})}{\partial \mathbf{Q}(t)} \tag{4.14}$$

Since Eq.(4.14) must be equal to the Eq.(4.10), we can conclude that $\mathbf{J} \cdot \mathbf{A} \cdot \mathbf{J}^T = \mathbf{A}$. Taking the determinant, we have $|\mathbf{J}|^2 |\mathbf{A}| = |\mathbf{A}|$ and we can therefore conclude that $|\mathbf{J}| = \left| \frac{\partial \phi^t(\mathbf{Q}(0))}{\partial \mathbf{Q}(0)} \right|$ must be 1 for Hamiltonian systems. This also demonstrates that the Jacobian determinant in Eq.(4.8) is 1 since the *flux* $\phi^t(\mathbf{X}(0))$ that defines our system is a two body problem dynamics, which is also a Hamiltonian system (i.e., the forces in the system are velocity invariant).

Transition Matrix

Eq.(4.6) can finally be expressed as:

$$\rho\left(\mathbf{X}(t)\right) = \rho(\phi^{-t}(\mathbf{x},\mathbf{v});0) \tag{4.15}$$

Hence, to compute the probability of having a fragment with a state vector $\mathbf{X}(t)$ it is necessary to calculate the forefather of $\mathbf{X}(t)$ at break-up. A state transition matrix $\mathbf{\Phi}(t,t_0)$ such as:

$$\mathbf{\Phi}(t,t_0) = \begin{bmatrix} \frac{\partial \mathbf{x}(t)}{\partial \mathbf{x}(t_0)} & \frac{\partial \mathbf{x}(t)}{\partial \mathbf{v}(t_0)} \\ \frac{\partial \mathbf{v}(t)}{\partial \mathbf{x}(t_0)} & \frac{\partial \mathbf{v}(t)}{\partial \mathbf{v}(t_0)} \end{bmatrix} \tag{4.16}$$

will provide this direct mapping from an initial state vector $\mathbf{X}(t_0)$ to the final state vector $\mathbf{X}(t)$ necessary to calculate Eq.(4.15).

$$\begin{pmatrix} \mathbf{x}(t) \\ \mathbf{v}(t) \end{pmatrix} = \mathbf{\Phi}(t,t_0) \begin{pmatrix} \mathbf{x}(t_0) \\ \mathbf{v}(t_0) \end{pmatrix} \tag{4.17}$$

Since we are interested in studying the dispersion of a cloud of particles, we can work in relative coordinates to study the differences in position and velocity with respect to the unperturbed orbit of the asteroid prior to fragmentation. Eq.(4.17) can be simplified by assuming that all the fragmented particles depart from the centre of mass of the asteroid (i.e., the relative initial position $\Delta\mathbf{x}(t_0)$ is 0), and by computing only the relative final position $\Delta\mathbf{x}(t)$:

$$\Delta\mathbf{x}(t) = \left[\frac{\partial\Delta\mathbf{x}(t)}{\partial\Delta\mathbf{v}(t_0)}\right]\Delta\mathbf{v}(t_0) \tag{4.18}$$

This simplifies the problem considerably, since only the 3×3 relative transition matrix $\partial\Delta\mathbf{x}(t)/\partial\Delta\mathbf{v}(t_0)$ is required. The matrix $\partial\Delta\mathbf{x}(t)/\partial\Delta\mathbf{v}(t_0)$ used in this work is described in Section A.2.4, and can also be found in *Vasile & Colombo*[95], or, for a more extensive explanation, refer to *Schaub & Junkins*[96]. The transition matrix used is given by the product of the linear proximal motion equations and the Gauss' planetary equations. This calculation provides a linear approximation of the nonlinear two body dynamics, but if the dispersive velocity is small compared to the nominal velocity of the unfragmented asteroid, it is an acceptable approximation[95].

Probability to find a particle in a particular position

Since we are interested in the probability of finding a fragment in a certain position in space at a particular time *t*, the probability function $\rho(\mathbf{x},\mathbf{v};t)$ will need to be integrated over all the feasible space of velocities:

$$P(\mathbf{x};t) = \int_{\Gamma}\rho(\mathbf{x},\mathbf{v};t)d\upsilon(t) = \int_{\Gamma}\rho(\phi^{-t}(\mathbf{x},\mathbf{v});0)d\upsilon(t) \tag{4.19}$$

where $d\upsilon(t)$ is the product of the one-dimensional differentials components of the velocity, $dv_x \cdot dv_y \cdot dv_z$.

Since the probability density function $\rho(\mathbf{x},\mathbf{v};0)$ is the probability to have a fragment in a position $\mathbf{x}(0)$ with velocity $\mathbf{v}(0)$ and having already assumed that the dispersion of fragments initiates from the centre of mass of the unfragmented asteroid, we can express $\rho(\mathbf{x},\mathbf{v};0)$ as the product of two separate probability density functions:

$$\rho(\mathbf{x},\mathbf{v};0) = \delta(\mathbf{x}(0)-\mathbf{r_0})\cdot G(\mathbf{v}(0)) \tag{4.20}$$

where $\delta(\mathbf{x}(0)-\mathbf{r_0})$ is the probability of a particular fragment to have position $\mathbf{x}(0)-\mathbf{r_0}$, $\mathbf{r}_0$ is the position of the centre of mass of the unfragmented asteroid at $t=0$ and $G(\mathbf{v}(0))$ is the probability that the same fragment has velocity $\mathbf{v}(0)$. Now, Eq.(4.19) can be rewritten using Eq.(4.20) as:

$$P(\mathbf{x};t)=\int_{\Gamma}\delta(\phi^{-t}(\mathbf{x},\mathbf{v})_{\mathbf{r}}-\mathbf{r_0})\cdot G(\phi^{-t}(\mathbf{x},\mathbf{v})_{\mathbf{v}})d\upsilon(t) \tag{4.21}$$

where $\phi^{-t}(\mathbf{x},\mathbf{v})_{\mathbf{r}}$ and $\phi^{-t}(\mathbf{x},\mathbf{v})_{\mathbf{v}}$ are, respectively, the components of the position and velocity of the *flux* $\phi^{-t}(\mathbf{x},\mathbf{v})$. Now, similarly to what was done with Eq.(4.6), the element of volume of the space of velocities $d\upsilon(t)$ can be related to the element $d\xi(0)=dx\cdot dy\cdot dz$ through their Jacobian:

$$d\upsilon(t)=\left\|\frac{\partial\mathbf{v}(t)}{\partial\mathbf{x}(0)}\right\|d\xi(0) \tag{4.22}$$

allowing us to solve the integral in Eq.(4.19) as:

$$P(\mathbf{x};t)=\left\|\frac{\partial\mathbf{v}(t)}{\partial\mathbf{x}(0)}\right\|G((\phi^{-t}(\mathbf{x},\mathbf{v}_*)_{\mathbf{v}}) \tag{4.23}$$

where $\mathbf{v}_*$ is the solution of the equation:

$$\phi^{-t}(\mathbf{x},\mathbf{v}_*)_{\mathbf{r}}=\mathbf{r_0} \tag{4.24}$$

so that $\delta(\phi^{-t}(\mathbf{x},\mathbf{v})_{\mathbf{r}}-\mathbf{r_0})$ is 1. Besides, the absolute value of the Jacobian in Eq.(4.23) relates to the transition matrix $\partial\Delta\mathbf{x}(t)/\partial\Delta\mathbf{v}(t_0)$ in Eq.(4.18) as follows:

$$\left\|\frac{\partial\mathbf{v}(t)}{\partial\mathbf{x}(0)}\right\|=\frac{1}{\left\|\frac{\partial\mathbf{x}(0)}{\partial\mathbf{v}(t)}\right\|}=\frac{1}{\left\|\frac{\partial\Delta\mathbf{x}(t)}{\partial\Delta\mathbf{v}(t_0)}\right\|} \tag{4.25}$$

Finally, the probability to find a piece of asteroid in a particular position relative to the unperturbed orbit at a given time after a fragmentation is given by:

$$P(\Delta\mathbf{x};t)=\frac{1}{\left\|\frac{\partial\Delta\mathbf{x}(t_0)}{\partial\Delta\mathbf{v}(t)}\right\|}G\left(\left[\frac{\partial\Delta\mathbf{x}(t)}{\partial\Delta\mathbf{v}(t_0)}\right]^{-1}\Delta\mathbf{x}(t)\right) \tag{4.26}$$

IV.3.2. Velocity Dispersion Model

The probability density function defined in Eq.(4.20) depends on two terms, a Dirac delta such as $\delta(\mathbf{x}(0)-\mathbf{r_0})$ for the position, which is equivalent to one Dirac delta function for each one of the components of the vector $\mathbf{x}(0)$, and a function $G(\mathbf{v}(0))$ that describes the dispersion of the values of the initial velocity $\mathbf{v}(0)$. For the latter purpose, we will use three Gaussian distributions; each Gaussian distribution will describe the velocity dispersion in one direction of the cartesian $\hat{t}-\hat{n}-\hat{h}$ reference frame or the tangential, normal and out-of-plane direction:

$$G\left(v_t(0),v_n(0),v_h(0)\right)=\frac{1}{\sigma_t\sqrt{2\pi}}e^{\frac{-\left(v_t-\mu_t\right)^2}{2{\sigma_t}^2}}\cdot\frac{1}{\sigma_n\sqrt{2\pi}}e^{\frac{-\left(v_n-\mu_n\right)^2}{2{\sigma_n}^2}}\cdot\frac{1}{\sigma_h\sqrt{2\pi}}e^{\frac{-\left(v_h-\mu_h\right)^2}{2{\sigma_h}^2}} \qquad (4.27)$$

Six parameters will be needed in order to define the dispersion of velocities: three mean velocities $\boldsymbol{\mu}=[\mu_t \quad \mu_n \quad \mu_h]$, and three standard deviations $\boldsymbol{\sigma}=[\sigma_t \quad \sigma_n \quad \sigma_h]$.

Assuming a kinetic impactor scenario, we can hypothesize that an infinitesimal instant after the impact, but before the fragmentation takes place, the system asteroid-spacecraft forms a single object, which moves according to the law of conservation of linear momentum. In fact, after the kinetic impactor mission triggers a catastrophic fragmentation, it is reasonable to think that the system asteroid-spacecraft would preserve the total linear momentum. Hence, given the SKE of a particular collision, Eq.(4.4) will provide the change of velocity of the centre of mass of the system only by considering the momentum enhancement factor β equal to 1. It also seems sensible to think of the mean vector $\boldsymbol{\mu}=[\mu_t \quad \mu_n \quad \mu_h]$ as the change of velocity of the centre of mass, since the highest probability to find a fragment should be at the centre of mass of the system. As a result, the norm of the mean of the dispersion should be:

$$\left|\boldsymbol{\mu}\right|=\left|\Delta\mathbf{v}_\mathbf{a}\right|=\frac{\sqrt{2M_a m_{s/c}SKE}}{\left(M_a+m_{s/c}\right)} \qquad (4.28)$$

The direction of $\left|\boldsymbol{\mu}\right|$ is defined by the direction of the impact relative velocity $\Delta\mathbf{v}_{s/c}$. Since the trajectory of a kinetic impactor should be designed to achieve the maximum possible deviation, $\left|\boldsymbol{\mu}\right|$ should be directed along the tangential direction (see Section A.2.5 in the Appendices). Accordingly, given the SKE of the collision, the mean velocity dispersion vector can be taken as:

$$\boldsymbol{\mu} = \begin{bmatrix} \dfrac{\sqrt{2M_a m_{s/c} SKE}}{\left(M_a + m_{s/c}\right)} & 0 & 0 \end{bmatrix} \tag{4.29}$$

Just as it is sensible to think that after a dish has shattered on the floor, the smallest fragments are generally found the furthest, one would expect that the smaller the fragments of the asteroid are, the larger their velocity dispersion $\boldsymbol{\sigma} = [\sigma_t \quad \sigma_n \quad \sigma_h]$ will be. The mass of the fragment must therefore have an influence on the dispersion of velocities. Let us assume that a fragment with mass m_i has a velocity Δv_i defined by an inelastic collision such that[13]:

$$m_i \Delta v_i \approx m_{s/c} \Delta v_{SKE \cdot m_i} \tag{4.30}$$

where $\Delta v_{SKE \cdot m_i}$ is a collisional velocity such that the fragment m_i takes with it its share of collisional energy SKE, that is:

$$\Delta v_{SKE \cdot m_i} = \sqrt{\frac{2 \cdot SKE \cdot m_i}{m_{s/c}}} \tag{4.31}$$

Clearly, $\Delta v_{SKE \cdot m_i}$ is only a mathematical entity that helps us to develop the theory here. The real impact occurs between the unfragmented asteroid with mass M_a and the spacecraft with mass $m_{s/c}$ at a relative velocity of:

$$\Delta v_{s/c} = \sqrt{\left(2 \cdot SKE \cdot M_a\right) / m_{s/c}} \tag{4.32}$$

Writing Eq.(4.31) as a function of the *real* impact velocity $\Delta v_{s/c}$ of the spacecraft leads us to:

$$\Delta v_{SKE \cdot m_i} = \sqrt{\frac{m_i}{M_a}} \cdot \Delta v_{s/c} \,. \tag{4.33}$$

Using the virtual inelastic collision Eq.(4.30) and Eq.(4.33), we can write Δv_i as:

$$\Delta v_i = \frac{m_{s/c}}{m_i} \sqrt{\frac{m_i}{M_a}} \cdot \Delta v_{s/c} \tag{4.34}$$

[13] In the following, and only to simplify the equations, it is considered that $m_{s/c}$ is always orders of magnitude smaller than both M_a and m_i, thus $M_a + m_{s/c} \approx M_a$ and $m_i + m_{s/c} \approx m_i$

As was said before, the centre of mass of the cloud of fragments is likely to follow the law of conservation of linear momentum (i.e., $M_a \Delta v_a \approx m_{s/c} \Delta v_{s/c}$), hence Eq.(4.34) finally settles down to the following expression:

$$\Delta v_i = \sqrt{\frac{M_a}{m_i}} \cdot \Delta v_a \tag{4.35}$$

Note that Eq.(4.35) is only a step away from:

$$\frac{1}{2} m \Delta v^x = constant \tag{4.36}$$

when x is equal to 2. Hence, we are assuming a homogenous distribution of the translational kinetic energy among all the fragments, or equipartition of translational kinetic energy. Several experimental works have intended to adjust a similar relation (i.e., Eq.(4.36)) to their fragment size and velocity experimental data: *Gault et al.*[97] found an exponent of 2.25 for his cratering experiments, while *Davis & Ryan*[94] found exponents between 1.92 and 1.41 on their fragmentation experiments. An equipartition effect was also suggested by *Wiesel*[98] while studying the explosion of objects such as spacecraft in Earth orbit.

Recalling the definition of standard deviation, $\sigma = \sqrt{\langle \mathbf{\Delta v}^2 \rangle - \langle \mathbf{\Delta v} \rangle^2}$, and assuming that $\langle \mathbf{\Delta v} \rangle$ is equal to zero for a homogeneous spherical dispersion from the centre of mass of the cloud of fragments, we can compute the norm of the standard deviation of velocity $\sigma(m_i)$ using Eq.(4.35) as:

$$\sigma(m_i) = \sqrt{\frac{M_a}{m_i}} \cdot \sigma_0 \tag{4.37}$$

where σ_0 is defined as:

$$\sigma_0 = \frac{\Delta v_a}{k} \tag{4.38}$$

with k a constant value. The constant k is 1 if we consider the velocity of the fragment with mass m_i as described above, i.e., Eq.(4.35).

In fact, one could think of k as the efficiency of transmission of the collisional energy. If part of the collisional energy is lost in processes such as melting or breaking, one could expect k to be larger than 1. On the other hand, k could also be smaller than 1 for

fragments coming from areas in the asteroid where there was a higher reservoir of collisional energy, e.g., close to the impact site. Therefore, it would be sensible to expect that small fragments may have k equal to 1 or smaller, since small fragments must come from areas with higher reservoir of collisional energy so that this energy was able to break the material to smaller sizes. Large fragments may have instead k larger than 1 from opposite reasons. Using experimental data published by *Davis & Ryan*[94], one can fit their experiments with available velocity dispersion data to find an average value of k (see Appendix A.4). Doing so, k results to be 1.4, thus:

$$\sigma_0 = \frac{\Delta v_a}{1.4} \tag{4.39}$$

To finish, the norm of standard deviation of velocity is $\sigma(m_i)$ as in Eq.(4.37), and since we assume an homogeneous spherical dispersion on the initial velocities at the break-up point, we can write the vector of the standard deviation as assuming three equal 1-dimensional values:

$$\boldsymbol{\sigma} = \left[\frac{1}{\sqrt{3}} \sqrt{\frac{M_a}{m_i}} \cdot \sigma_0 \quad \frac{1}{\sqrt{3}} \sqrt{\frac{M_a}{m_i}} \cdot \sigma_0 \quad \frac{1}{\sqrt{3}} \sqrt{\frac{M_a}{m_i}} \cdot \sigma_0 \right] \tag{4.40}$$

IV.4. On the Nature of the Cloud of Fragments

Once the feasibleness of the fragmentation scenario has been highlighted and the statistical model has been described, the following sections will give some insight into the evolution and dispersion of the fragments. While Section IV.1 supported for a lower limit of the critical fragmentation energy only of 100 J/kg, Fig. IV-4 and Fig. IV-5 in Section IV.2 showed that the minimum required specific energy to deflect an asteroid, which depends on the warning time available for the deflection, is very often above this lower critical limit. We also saw that, for short warning times (< 4 years), the critical fragmentation energy can also go above the upper limit of 1000 J/kg. Along the following section an intermediate level of energy at 500 J/kg will be used to evaluate the statistical model introduced in the previous section. Some insight into the statistical composition of the cloud of fragments in terms of quantity and size of its fragments will also be given and, finally, we will also assess the influence of the gravitational force on the disgregation and dispersion of the fragmented asteroid.

IV.4.1. Time Evolution of the Cloud of Fragments

The following figures, Fig. IV-6 to Fig. IV-8, show the evolution of the probability density function of a fragmentation occurring after providing 500 J/kg of collisional energy to a $5x10^{10}$kg *Circular* asteroid (see Table IV-1). A successful deflection attempt, with a collisional energy of 500 J/kg, would have provided an approximate change of velocity of $\Delta v_a = 0.02\, m/s$, using an impactor mass $m_{s/c}$ of 18,500 kg. If a *barely catastrophic fragmentation* occurs, according to the model developed in this chapter, the largest fragment (i.e., $2.5x10^{10}$kg) would have a mean velocity of $\boldsymbol{\mu} = [0.02 \quad 0 \quad 0] m/s$ (Eq.(4.29)) and a standard deviation of $\boldsymbol{\sigma} = [0.012 \quad 0.012 \quad 0.012] m/s$ (Eq.(4.40)).The following images show the evolution, during the first complete orbit after the break-up, of the volume enclosing 97% probability to find the large $2.5x10^{10}$kg-fragment. The images are taken every 30 degrees difference in true anomaly during the first half of the orbit and 45 degrees during the second half, which corresponds approximately to a time step of 30 and 45 days respectively.

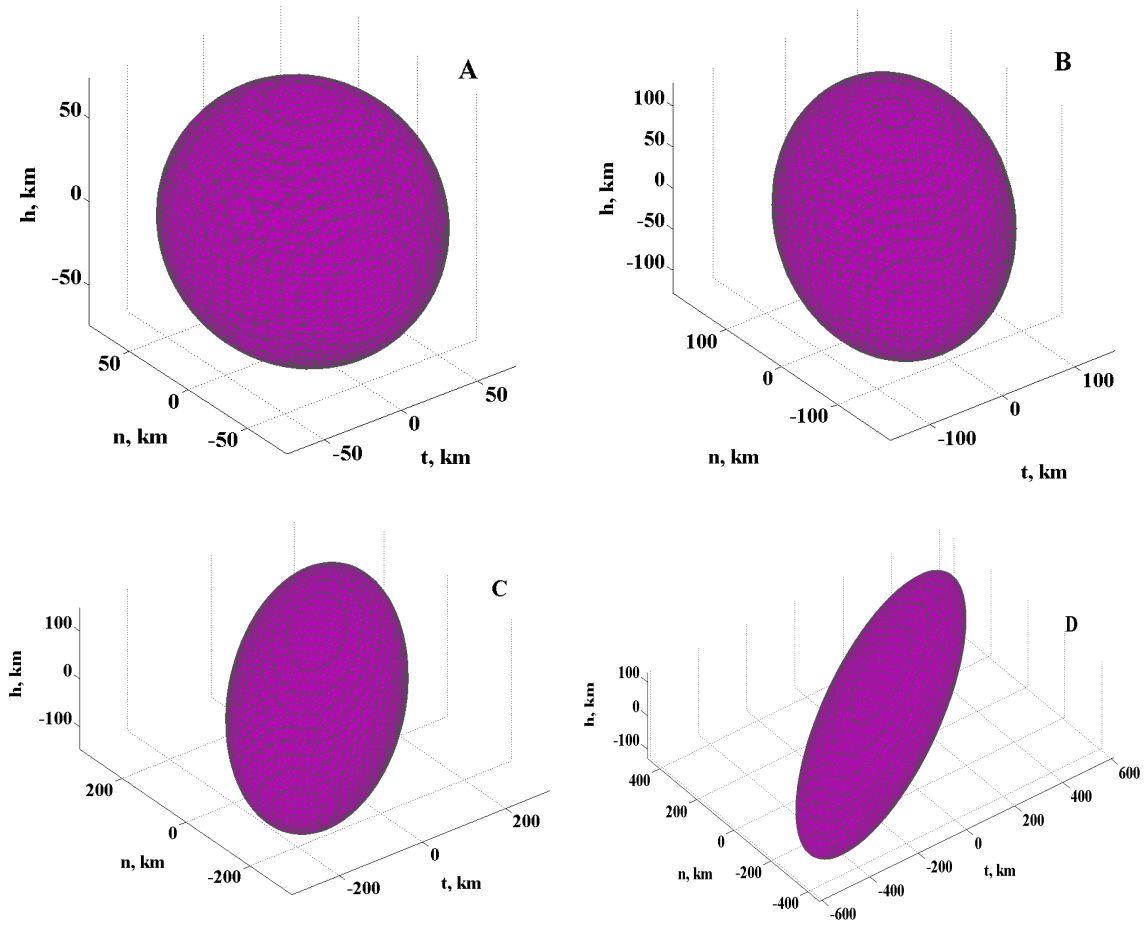

Fig. IV-6 Volume enclosing 97% probability to find the largest fragment of a fragmentation with f_r=0.5 for a *Circular* asteroid. The initial distribution of velocities is modelled with $\boldsymbol{\mu} = [0.02 \quad 0 \quad 0] m/s$ and $\boldsymbol{\sigma} = [0.012 \quad 0.012 \quad 0.012] m/s$. The difference between the true anomaly at the break-up point and at each image is: A) 30^0, B) 60^0, C) 90^0 and D) 120^0.

Note that the growth and re-shaping of the volume plotted along Fig. IV-6 to Fig. IV-8 is only the consequence of the dispersion of velocities, which in the example here is $\boldsymbol{\sigma} = [0.012 \quad 0.012 \quad 0.012] m/s$. The centre of the ellipsoidal shaped cloud is a position along the orbit perturbed by the mean velocity $\boldsymbol{\mu} = [0.02 \quad 0 \quad 0] m/s$, thus the centre of mass of all the fragments. The origin of the coordinate frame of the figures is the centre of the ellipsoid and orientation of the frame is given by the cartesian $\hat{t} - \hat{n} - \hat{h}$ or tangential, normal and out-of-plane frame of the initial unperturbed orbit.

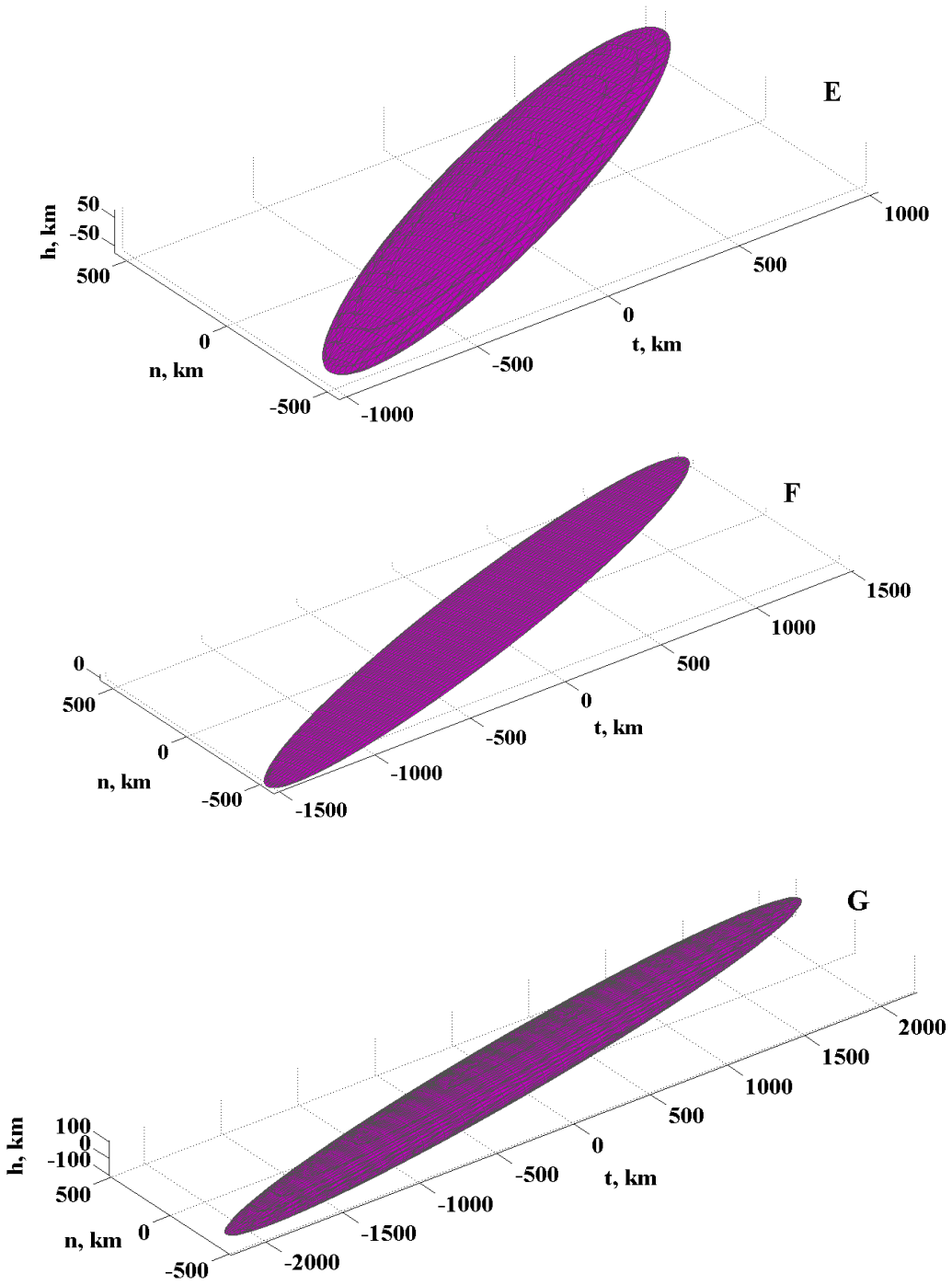

Fig. IV-7 Volume enclosing 97% probability to find the largest fragment of a fragmentation with f_r=0.5 for a *Circular* asteroid. The initial distribution of velocities is modelled with $\mu = [0.02 \quad 0 \quad 0] m/s$ and $\sigma = [0.012 \quad 0.012 \quad 0.012] m/s$. The difference between the true anomaly at the break-up point and at each image is: E) 150^0, F) 180^0 and G) 225^0.

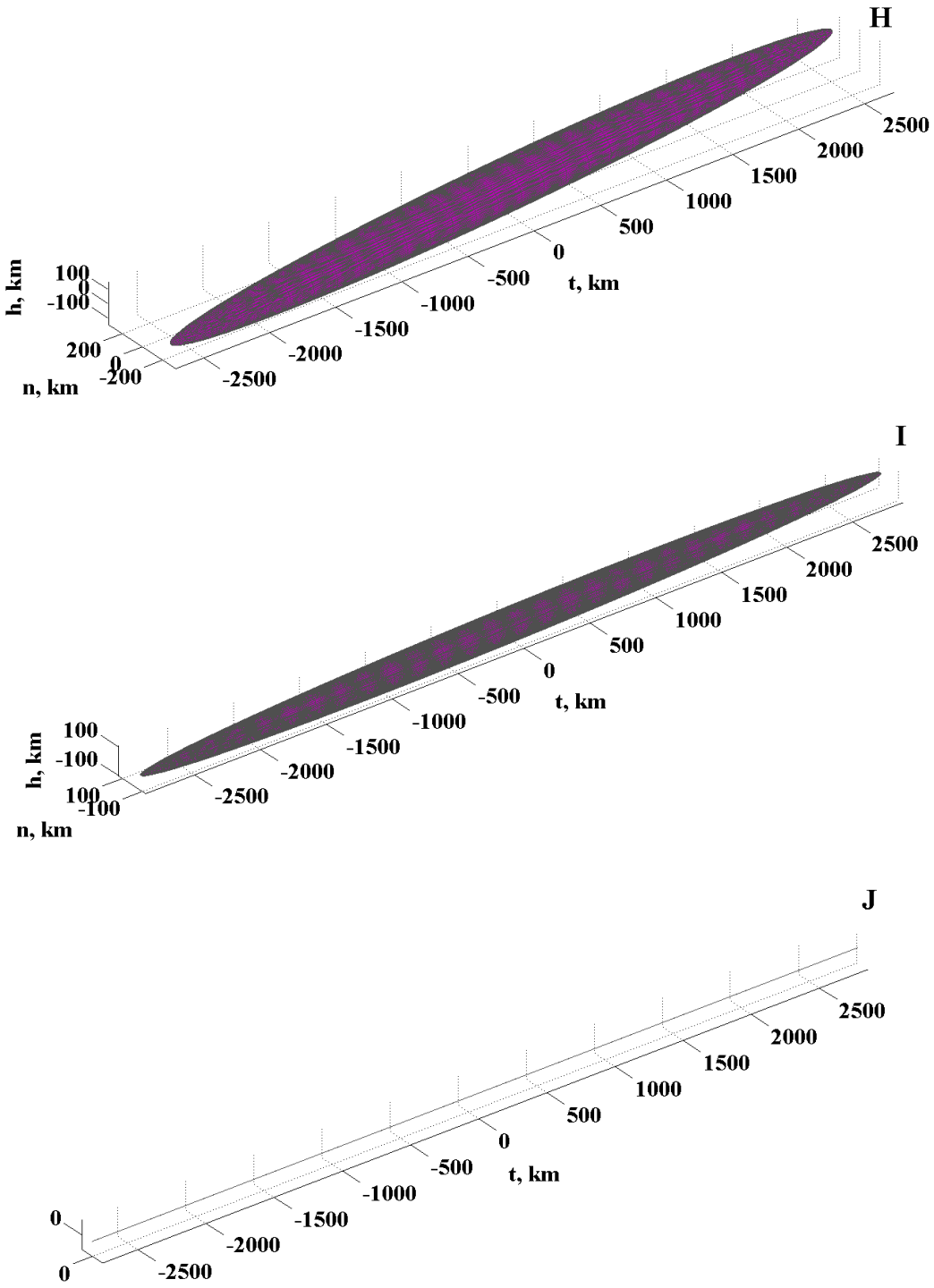

Fig. IV-8 Volume enclosing 97% probability to find the largest fragment of a fragmentation with f_r=0.5 for a *Circular* asteroid. The initial distribution of velocities is modelled with $\boldsymbol{\mu} = [0.02 \quad 0 \quad 0] m/s$ and $\boldsymbol{\sigma} = [0.012 \quad 0.012 \quad 0.012] m/s$. The difference between the true anomaly at the break-up point and at each image is: H) 270^0, I) 315^0 and J) 360^0. Note that in figure J the volume is almost a line in space, thus the largest fragment has a 97% probability to be located at some point in the line.

Let us suppose, for the moment, that the gravity interaction among the different fragments is negligible. Doing so, the same calculation can be extended to any fragment size, which would only modify the standard deviation **σ** by a factor $\sqrt{M_a/m_i}$, where m_i is the mass of a given size of fragments. The factor $\sqrt{M_a/m_i}$ would increase the dispersion of elements with a decreasing m_i, thus the equivalent volumes enclosing a given probability will grow when analysing smaller sizes. For fragment sizes with m_i a few orders of magnitude smaller than $f_r \cdot M_a$ the number of pieces is already expected to be of a few tens, thus the volumes represented from Fig. IV-6 to Fig. IV-8 can be also interpreted as the physical shape of the cloud of fragments, at least for those fragment sizes that have abundant elements, since the probability density function describes the regions where, statistically at least, there is a higher concentration of fragments.

The most prominent feature that stands out from the images above is the ellipsoidal shape of the volume enclosing a particular probability, or cloud of particles. In order to better understand the dynamics of the dispersive cloud of particles, we can try to understand the evolution of the four salient features of the elliptical cloud. These four features are: the semimajor axis *a*, the semiminor axis *b*, the dispersion along the *h* axis or out-of-plane and the angle α between the semimajor axis *a* and the tangential direction axis *t*, as shown in Fig. IV-9.

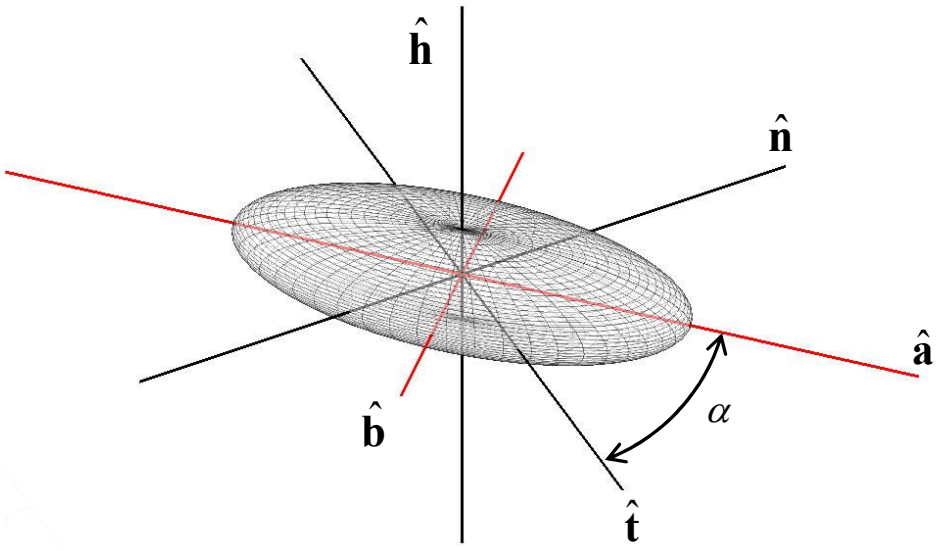

Fig. IV-9 Schematic of the 4 features describing the shape and attitude of the ellipsoidal shaped cloud of fragments.

Fig. IV-10 summarizes the evolution of the four aforementioned features that describe the volume enclosing 97% probability to find the largest fragment of a *barely catastrophic fragmentation* with $\boldsymbol{\sigma} = [0.012 \quad 0.012 \quad 0.012] m/s$. The figure also extends the time-span to complete a two years propagation from the break-up point. It is important to note that the evolution of the shape of the cloud is essentially driven by the dynamics of the system, which were defined by the proximal motion equations that were used to construct the transition matrix in Eq.(4.18). Therefore, studying the motion of a single perturbed particle using proximal motion dynamics will prove very useful to help us to understand the transformation with time of the probability density function and its four salient features (i.e., *a*, *b*, α and *h*).

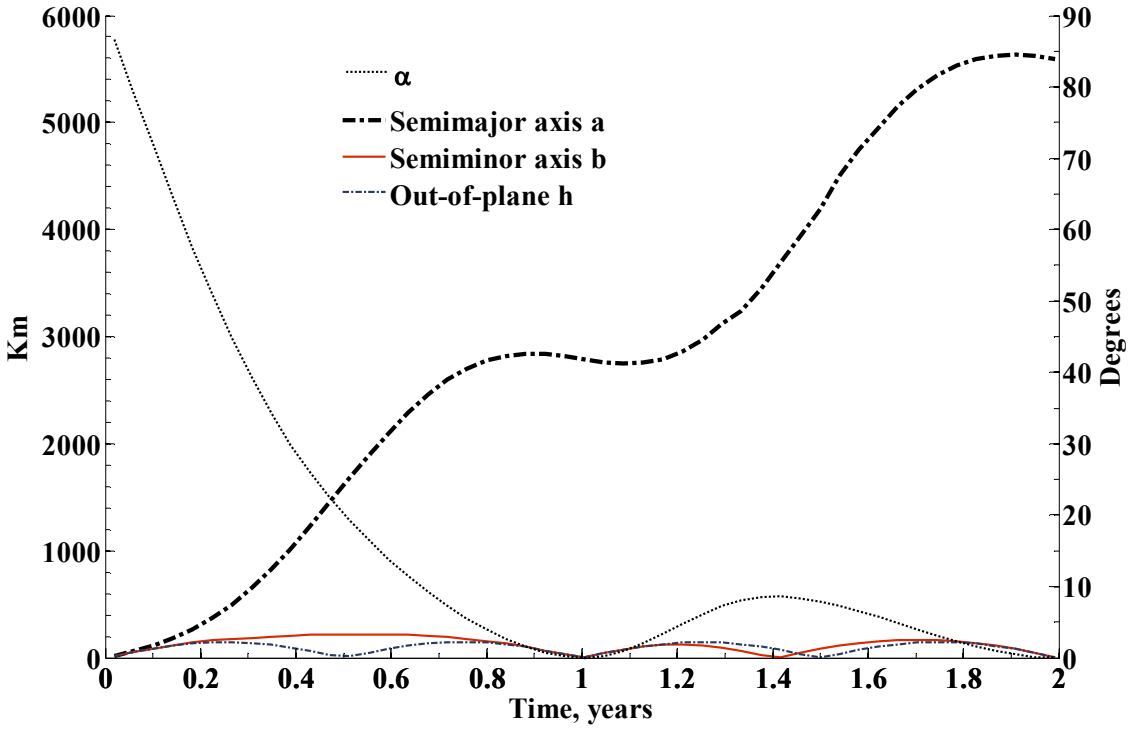

Fig. IV-10 Two years evolution of the four features defining the ellipsoidal cloud enclosing 97% probability to find the single 2.5x10^{10}kg fragment.

Fig. IV-11 shows three relative motion trajectories that a particle would travel along if perturbed in 0.012 m/s in tangential direction $\hat{t}$ (black line), normal direction $\hat{n}$ (blue line) and in out-of-plane direction $\hat{h}$ (red line), these trajectories represent two complete orbits drift after the perturbation from its initial circular orbit. Also note that the delta-velocity of 0.012 m/s is the same as each one of the components of the standard deviation $\boldsymbol{\sigma}$ of the example used above. The motion of a particular fragment in the dispersive cloud will follow a particular combination of the three trajectories described in Fig. IV-11,

depending on the components of its initial relative velocity $\left[\Delta v_{\hat{t}} \quad \Delta v_{\hat{n}} \quad \Delta v_{\hat{h}}\right]$. A few of the most important characteristics of the evolution described in Fig. IV-10 can now be more easily understood by looking at Fig. IV-11.

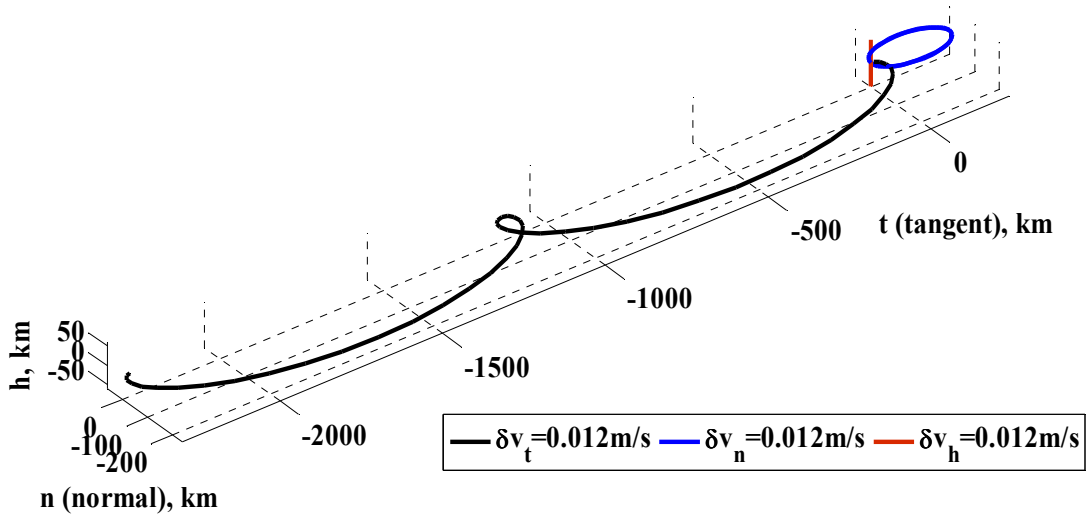

Fig. IV-11 Relative motion trajectories. An asteroid fragment perturbed in 0.012 m/s from its initial circular orbit would follow one of the three trajectories on the figure if the perturbation was entirely in tangent direction $\hat{t}$ (black line), normal direction $\hat{n}$ (blue line) or in out-of-plane direction $\hat{h}$ (red line).

Probably, the most important characteristic of the dispersion of the cloud of fragments is the evolution of the semimajor axis of the ellipsoidal shape. This evolution is a direct consequence of the fact that a velocity perturbation in the tangential direction, i.e., in the direction of the orbital velocity, is the only perturbative component that provides an unbounded drift from the initial relative position. While delta-velocities in the normal or the out-of-plane directions mostly change the direction of the orbital velocity, but do not substantially modify its magnitude, delta-velocities in the tangential direction only change the magnitude of the orbital velocity. If a fragment is provided only with relative velocities in the normal and out-of-plane direction, the fragment will perform a relative orbit around the unperturbed position, while if the fragment has tangential velocity, its orbital period will be modified and, as a consequence, will drift away from the unperturbed initial position. The perturbance in tangential direction therefore defines the semimajor axis a after a very short period of time (i.e., at the very beginning of the dispersion the three components have equal magnitudes of deviation).

Both the semimajor axis a of a volume enclosing a given probability and the angle α, or angle between the semimajor axis a and the tangential direction $\hat{t}$, are then defined

by the tangential component of the initial relative velocity of the particles of the cloud, and thus, its behaviour can be readily understood by looking at the black line ($\Delta v_{\hat{t}}$ perturbation) in Fig. IV-11. For example, in Fig. IV-10, we see that the angle α undergoes a change from 90 to 0 degrees during the first orbit and then has decreasing rebounds over 0 degrees in subsequent orbits, which can be explained by the evolution of a vector from the origin of the coordinate frame of Fig. IV-11 to a position moving along the black line. The angle of this vector with the tangent direction will behave exactly like the angle α. The fact that the semimajor axis *a* seems to take a break in its growth at each multiple of the orbital period is also seen in the behaviour of the black line in Fig. IV-11. This is a consequence of the fact that drifting in the positive tangential direction is achieved through shortening the period of the perturbed fragment, which translates into a negative delta-velocity in the tangential direction. When the perturbed fragments reaches close to the point along the orbit where it was perturbed, the unperturbed position has therefore more velocity and for an instant seems to catch up with the perturbed object.

The semiminor axis *b* and out-of-plane deviation *h* are defined by the perturbation in the normal direction and in the out-of-plane direction respectively, and will therefore remain enclosed between very small boundaries. The out of plane deviation *h* will become zero twice per orbit, both at the ascending node and the descending node of the perturbed orbit, while the semiminor axis *b* has only one zero during the first orbit and two zeros thereafter. The zeros of the semiminor axis *b* occur when the deviation spawned by the delta-velocities with tangential and normal directions are aligned (i.e., have the same direction), consequently at those times all the particles of the cloud form a line in the $\hat{t}-\hat{n}$ plane (see image J in Fig. IV-8).

To summarize, the help of the proximal motion trajectories (Fig. IV-11) makes Fig. IV-10 much more understandable and general trends for the four features can be inferred for further propagations; the angle α will follow a damped-like oscillatory motion with decreasing amplitude in its rebounds, the semimajor axis will keep growing at the same rate and the out-of-plane *h* deviation and the semiminor axis b will remain bounded under the same limit, giving to the ellipsoidal shape a more overstretched look as the time passes.

Finally, Fig. IV-12 shows the evolution of the probability $P(\mathbf{x};t)$ at the centre of the dispersive cloud. As predicted by the discussion above, the probability drops several orders of magnitude during the first half of the orbit and then has periodical peaks due to the bounded components of the motion, namely normal and out-of-plane components, that

repeat, in general, every half a period. At the end of each complete orbit both deflections collapse to zero, hence a maximum in probability density occurs at the centre of the ellipsoid. At the half of each orbit the deflection in the out-of-plane collapses again to zero, thus the density also increases at each half an orbit. Moreover, another peak appears at 1.41 years after the break-up and repeats at 2.45 and 3.46 years, this third peak is due to the collapse of the semiminor *b* axis, which as time passes moves closer to the half an orbit point due to the smaller oscillations of the angle α.

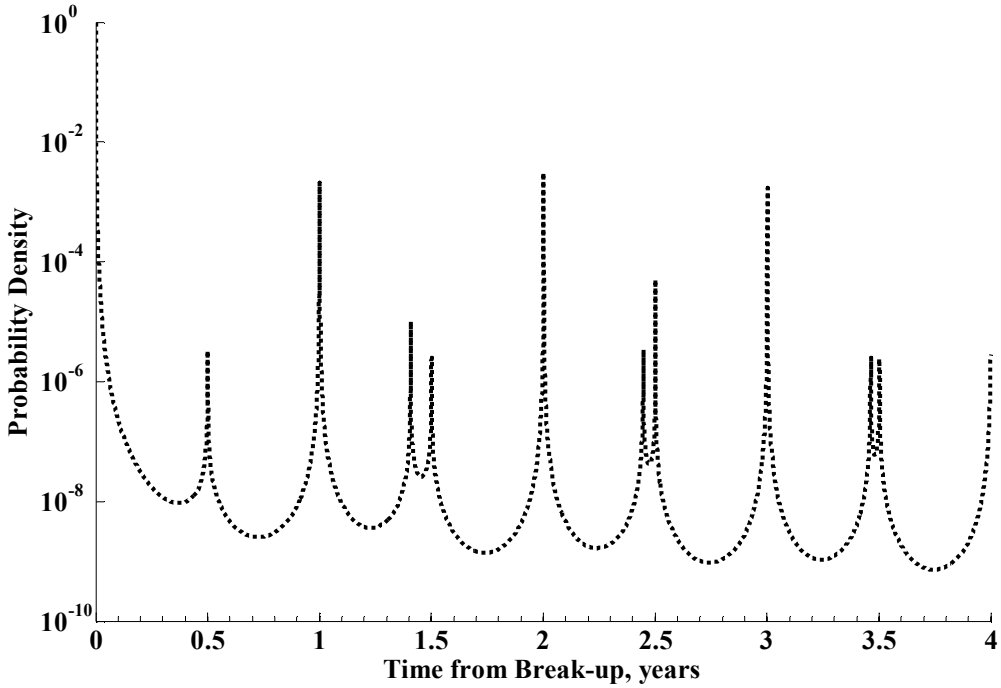

Fig. IV-12 Evolution of the probability density $P(\mathbf{x};t)$ in the centre of the dispersive cloud for a *Circular* case, fragment mass of 2.5x10^{10}kg and $\boldsymbol{\sigma} = [0.012 \quad 0.012 \quad 0.012]\, m/s$. Note that the Circular case has exactly 1 year orbital period.

IV.4.2. Fragment Size Distribution

It is out of the scope of this thesis to describe the physics of the fragmentation of a brittle solid, such as an asteroid, and a simple statistical distribution of fragments will serve better to our purposes. The aim here is only to discern the intrinsic risks of an impulsive asteroid hazard mitigation strategy. This purpose can be achieved by estimating the approximate number of fragments within a given range of mass. With this, we will also be able to perform a preliminary analysis of the gravitational interaction among the different components of the cloud.

Early works in collisional fragmentation have used accumulative power law distribution to model fragment size distribution[99]. Two- or three- segments power laws have been found to fit much better to experimental data[94],[100], particularly when the fragmentation data comprises sizes many orders of magnitude smaller than the original size. However, for the analysis carried out here, we will use only one segment accumulative power law distribution such as:

$$N(>m) = Cm^{-b} \tag{4.41}$$

since this is already an acceptable approximation for a qualitative analysis inside a range of 3 orders of magnitude of the fragment mass. Eq.(4.41) provides the number of fragments above a given mass *m*, therefore if m_{max} is the mass of the largest fragment, $N(\geq m_{\max})$ must be 1, and thus the constant C must be:

$$C = m_{\max}{}^{b} \tag{4.42}$$

Now, If we integrate the mass over all fragment sizes, the total mass must be equal to the unfragmented asteroid mass M_a:

$$M_a = \int_1^{\infty} m \cdot dN(>m) = \left[\frac{bC}{(1-b)}\right] m_{\max}{}^{1-b} \tag{4.43}$$

Using Eq.(4.42) in Eq.(4.43), the exponent *b* becomes a function only of the ratio between the largest fragment mass m_{max} and the total mass of the asteroid M_a:

$$b = \left(1 + \frac{m_{\max}}{M_a}\right)^{-1} \tag{4.44}$$

where the fraction $m_{\max}/M_a$ is the *fragmentation ratio* f_r.

Fig. IV-13 shows the number of fragments that a one-segment power law distribution such as Eq.(4.41) predicts for three different catastrophic fragmentations of *Apophis* test case: $f_r = 0.5$ (blue bars), $f_r = 0.25$ (green bars) and $f_r = 0.1$ (red bars). Only the range of fragments that can pose threat to Earth are shown in the figure, thus from m_{max} to, roughly, the mass of a 40m diameter rocky object. The number of fragments are counted inside equally wide and equispaced boxes, the width of the plotted bar is only chosen for clarity.

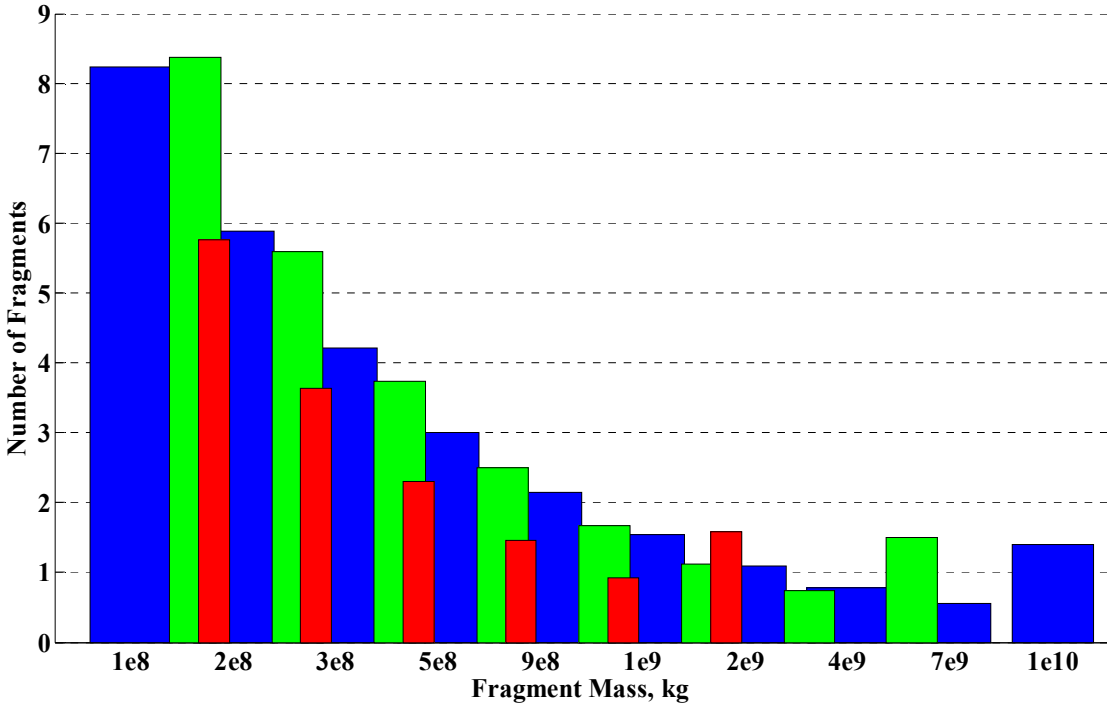

Fig. IV-13 Approximated number of pieces expected to be found in a fragmentation cloud of an asteroid with 2.7x10^{10}kg of mass resulting from disruptions with f_r=0.5 (blue bars), f_r=0.25 (green bars) and f_r=0.1 (red bars). The largest fragment, i.e., surviving mass of the asteroid, is counted in the initial bin of the histogram for each level of disruption.

It is interesting to note that the higher the level of disruption the lesser the number of dangerous fragments. In fact, the total mass of the dangerous fragments is 85%, 63% or 30% the mass of the unshattered asteroid for fragmentation ratios f_r of 0.5, 0.25 and 0.1 respectively, thus, a priori, the higher the level of fragmentation the lesser the risk for the Earth. By definition a fragmentation equal to the critical specific energy Q^* triggers a *barely catastrophic fragmentation*, $f_r = 0.5$, yet if the energy provided by an impulsive mitigation mission differs from this, a different level of disruption should be expected. In fact, the fragmentation ratio f_r in *Benz & Asphaug*[101] simulations adjusted very well to a simple linear function of the ratio between the specific energy applied and the critical specific energy Q^*, at least for a range between 0.5 to 2 times Q^*. Although *Benz & Asphaug*[101]'s results cannot be extrapolated to this work since their simulations considered impact velocities only up to 5 km/s, they emphasise that for specific energies just a few times larger than Q^*, the fragmentation ratio could decrease even more than one order of magnitude. In all the remaining analysis, we will consider three different fragmentation ratios ($f_r = 0.5$, $f_r = 0.25$ and $f_r = 0.1$) in order to represent different possible break-up scenarios.

IV.4.3. Gravity Re-accumulation

Both, unshattered asteroids used in this chapter and the largest fragment resultant from their catastrophic fragmentation, have very weak gravitational attraction due to their small mass. Despite this, their gravity will still be the principal source of gravitational force inside a sphere centred on these bodies and smaller than one kilometre in radius. Although this is a very small volume of interplanetary space, the gravitational interaction among the different fragments, during the initial moments after the break-up, may play a very important role on the nature of the dispersive cloud of fragments. It may well happen that some of the fragments, most probably the larger ones, are provided with very little relative velocity with respect to the largest fragments of the cloud, and so, they may spend too much time in very close proximity to the most massive pieces of the cloud. Those fragments will not disperse as the dispersion model foresees, but rather, will re-accumulate into rubble piles or become orbiting satellites of a larger fragment.

Considering the coarse statistical description of the model, it is deemed that a full treatment of the gravity perturbation on each fragment due to the gravitational attraction of all the other fragments is not necessary at this stage, nevertheless the total re-accumulated mass needs to be determined. Hence, as a first approximation, we will compute the percentage of mass (or number of fragments) that are able to escape from the vicinity of the largest and most massive fragment, avoiding being either re-accumulated or becoming an orbiting satellite. The final census of fragments and the mass of the largest one will be then updated. Eventually, the number of fragments that manage to escape the largest mass' gravity well will evolve using the afore-used statistical description of the problem.

If the *escape velocity* of a fragment f_i is computed as:

$$v_{esc} = \sqrt{\frac{2Gm_{\max}}{r_i}} \tag{4.45}$$

where G is the Newtonian constant of gravitation and r_i is the minimum distance between the centres of two spherical volumes with mass $m_{\max}$ and m_i and density ρ 2600 kg/m^3 (see asteroid's data in Chapter I), the percentage of fragments f_i avoiding being captured by the gravity pull of the largest fragment $f_{\max}$ can be calculated by computing the probability of those fragments to have a relative velocity with respect to the largest fragment $f_{\max}$ higher than the escape velocity in Eq.(4.45). Thus, the probability that a

fragment f_i escapes from the gravity of $f_{\max}$ should be computed by integrating the following expression:

$$P(\Delta v > v_{esc}) = \int_{-\infty}^{\infty}\int_{-\infty}^{\infty}\int_{-\infty}^{\infty}\int_{-\infty}^{\infty}\int_{-\infty}^{\infty}\int_{-\infty}^{\infty} \mathrm{F}(\mathbf{v}_{f_i}(0), \mathbf{v}_{\max}(0)) \cdot d\upsilon_{f_i}(0) d\upsilon_{\max}(0) \quad (4.46)$$

where $d\upsilon_{f_i}(0) = dv_{tf_i} dv_{nf_i} dv_{hf_i}$, $d\upsilon_{\max}(0) = dv_{t_{\max}} dv_{n_{\max}} dv_{h_{\max}}$ and the function F is:

$$\mathrm{F}(\mathbf{v}_{f_i}(0), \mathbf{v}_{\max}(0)) =$$
$$\begin{cases} G\left(v_{tf_i}(0), v_{nf_i}(0), v_{hf_i}(0)\right) \cdot G\left(v_{t\max}(0), v_{n\max}(0), v_{h\max}(0)\right), & \left|\mathbf{v}_{f_i}(0) - \mathbf{v}_{\max}(0)\right| > v_{esc} \\ 0, \quad \text{otherwise} \end{cases} \quad (4.47)$$

Integral Eq.(4.46) is computationally very expensive, thus a method to reduce the computational time (which was of the order of several days) without impairing the result of the integration was needed. Using the law of cosines, we can relate the modulus of the relative velocity $\mathbf{v}_{f_i}(0) - \mathbf{v}_{\max}(0)$ to the norm of the velocity $\mathbf{v}_{f_i}(0)$ and $\mathbf{v}_{\max}(0)$ as:

$$\left|\mathbf{v}_{f_i}(0) - \mathbf{v}_{\max}(0)\right|^2 = \left|\mathbf{v}_{f_i}(0)\right|^2 + \left|\mathbf{v}_{\max}(0)\right|^2 - 2 \cdot \left|\mathbf{v}_{f_i}(0)\right| \cdot \left|\mathbf{v}_{\max}(0)\right| \cdot \cos(\alpha) \quad (4.48)$$

where α is the angle between the two vectors $\mathbf{v}_{f_i}(0)$ and $\mathbf{v}_{\max}(0)$. Since the velocity distribution accounts for three equally distributed cartesian components, that is, equal mean and standard deviation for all components, angle α has a homogeneous probability to have a value between 0 a 360 degrees. Then, by averaging $\cos(\alpha)$ in Eq.(4.48) between 0 and 360 degrees, resulting in $\langle \cos(\alpha) \rangle = 0$, we obtain an average modulus of the relative velocity as:

$$\left|\mathbf{v}_{f_i}(0) - \mathbf{v}_{\max}(0)\right|^2 = \left|\mathbf{v}_{f_i}(0)\right|^2 + \left|\mathbf{v}_{\max}(0)\right|^2 \quad (4.49)$$

Using Eq.(4.49), the integral Eq.(4.46) can be reduced to a double integral if we use the norms of the vectors $\mathbf{v}_{f_i}(0)$ and $\mathbf{v}_{\max}(0)$ instead of the six cartesian components:

$$P(\Delta v > v_{esc}) = \int_{-\infty}^{\infty}\int_{-\infty}^{\infty} l\left(v_{f_i}(0), v_{\max}(0)\right) \cdot dv_{f_i}(0) dv_{\max}(0) \quad (4.50)$$

where function l becomes:

$$l\left(v_{f_i}(0), v_{\max}(0)\right) =$$

$$\begin{cases} \dfrac{1}{\sigma_{f_i}\sqrt{2\pi}} e^{\frac{-v_{f_i}^{\,2}}{2\sigma_{f_i}^{\,2}}} \cdot \dfrac{1}{\sigma_{\max}\sqrt{2\pi}} e^{\frac{-v_{\max}^{\,2}}{2\sigma_{\max}^{\,2}}}, & \sqrt{\left|\mathbf{v}_{f_i}(0)\right|^2 + \left|\mathbf{v}_{\max}(0)\right|^2} > v_{esc} \\ 0, \quad \text{otherwise} \end{cases} \tag{4.51}$$

$$\text{with } \sigma_{f_i} = \sqrt{\frac{M_a}{m_i}} \cdot \sigma_0 ; \sigma_{\max} = \sqrt{\frac{M_a}{m_{\max}}} \cdot \sigma_0$$

Expression Eq.(4.51) does not include the mean of the distribution, since both fragments have, by definition, the same mean velocity.

Fig. IV-14 and Fig. IV-15 show the results of the integral Eq.(4.50) on the fragmentation of the asteroids *Apophis*, *Shiva*$_3$ and *Apollyon*$_3$. Integral Eq.(4.50) is a function uniquely determined by the mass of the asteroid, energy used for the break up and fragmentation ratio, thus, since they have the same mass, the results for *Shiva*$_3$ and *Apollyon*$_3$ are equivalent (Fig. IV-15). An interesting conclusion highlighted by the two figures concerns rubble pile asteroids; 100 J/kg of impact energy may be the minimum energy required to fragment an asteroid, only if the asteroid happens to have a rubble-pile structure, if the fragmentation occurs at this level of energy, the velocities provided to the different spawned fragments would certainly not be enough to completely disperse the asteroid, which, most likely, would become a rubble pile asteroid again, losing only a small fraction of its mass during the process of break-up and subsequent re-aggregation.

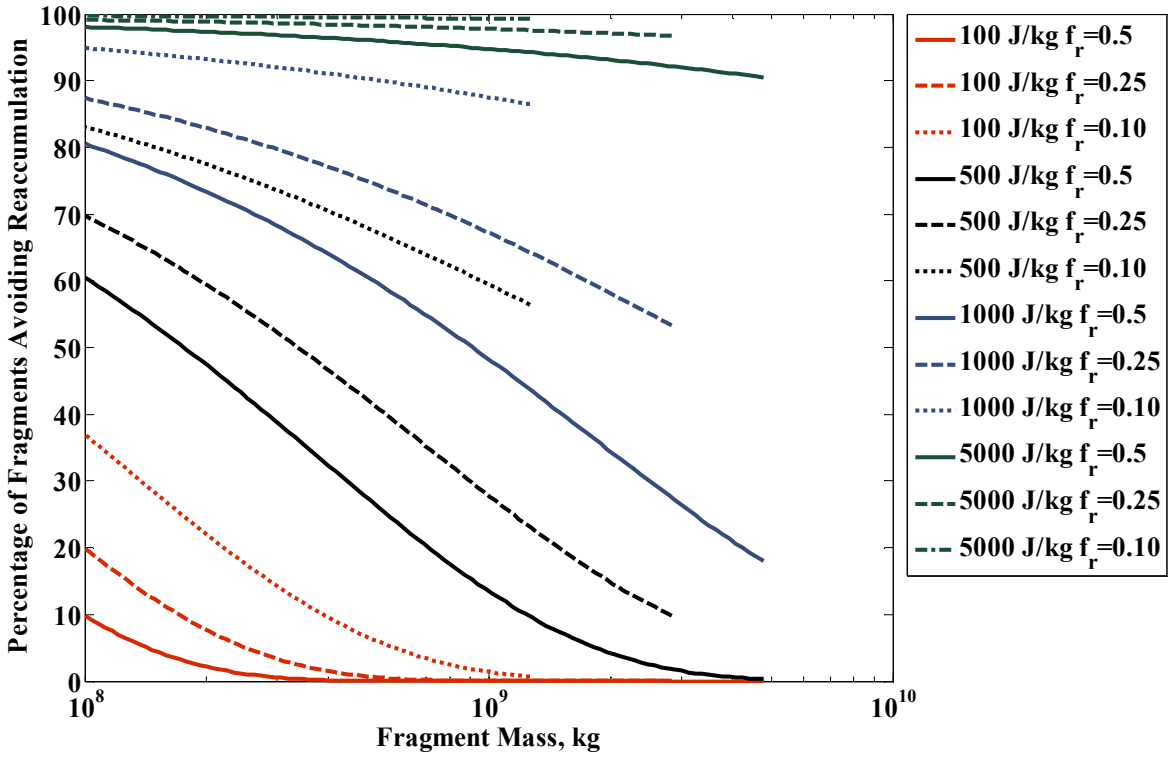

Fig. IV-14 Percentage of fragments escaping the gravitational field of the largest fragment and avoiding being re-aggregated into the largest remaining mass of *Apophis*. The figure shows break-ups at four different levels of energy and three different levels of fragmentation for each level of energy.

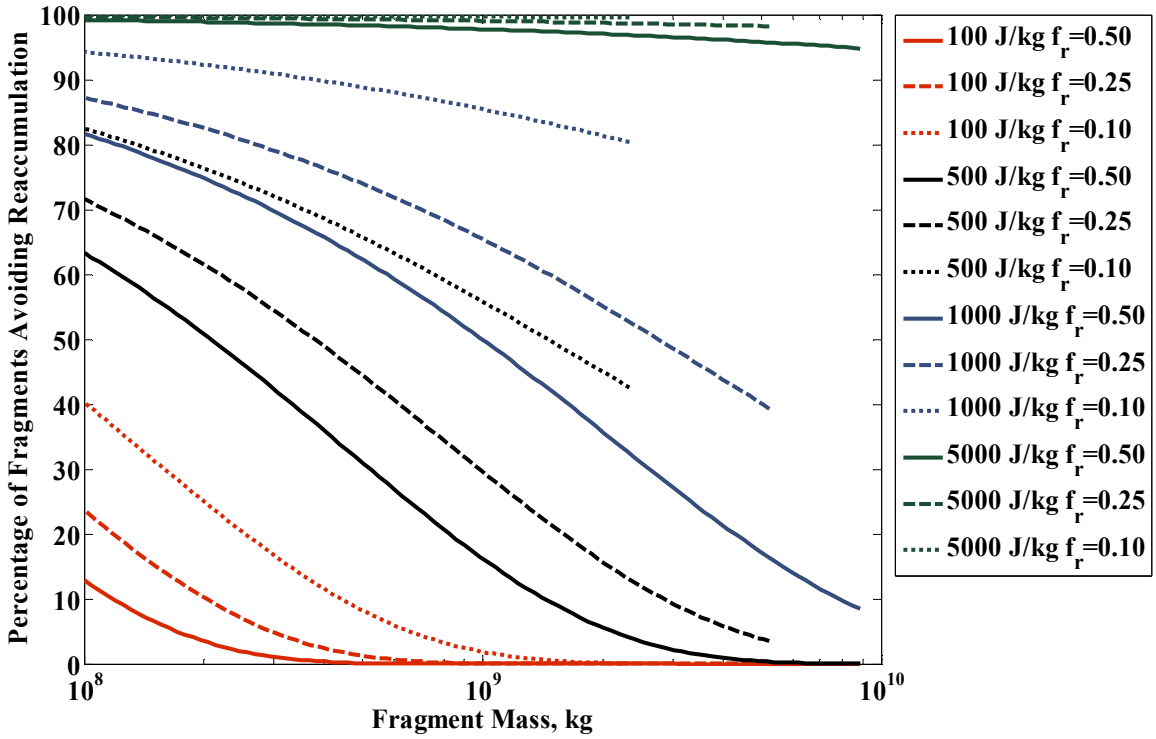

Fig. IV-15 Percentage of fragments escaping the gravitational field of the largest fragment for *Shiva₃* and *Apollyon₃*. The figure shows break-ups at four different levels of energy and three different levels of fragmentation for each level of energy.

IV.5. Consequences of a Fragmentation

If the impact of each asteroid test case is assumed to occur at the MOID point for each test case listed in Table IV-1, the impact likelihood can be calculated by integrating over the volume inside a sphere centred at the asteroid's MOID point with radius equal to the Earth capture volume $dV(r)$:

$$L = \int_{V(r=0)}^{V(r=\varepsilon \cdot R_{\oplus})} P(\mathbf{x};(t_{MOID} - t_0)) \cdot dV(r) \qquad (4.52)$$

Note that the capture volume is approximated by the Earth radius corrected with the hyperbolic factor ε, to account for the final gravitational focusing of the Earth.

From Eq.(4.52) we can see that the total impact likelihood for a particular fragment size and test case is only a function of the time of the closest approach t_{MOID}, the time at which the break up occurred (the difference between these two times is here referred to as the warning time) and the specific collisional energy used to break up the asteroid. Fig. IV-16 shows the evolution along warning time of the impact likelihood of the largest fragment from a *barely catastrophic fragmentation* emanating from the hypothetical break-

up of each test case presented in Table IV-1. In this first example, the hyperbolic factor ε particular to each test is not yet taken into account and a 2.16 value, i.e., *Apophis* hyperbolic factor, is instead used for all the four orbits. Using the same factor ε for all the test cases avoids adding third body effects (i.e., Earth final hyperbolic approach) to the problem of the dispersion of fragments, which, at this point, eases the analysis on the evolution and dispersion of the cloud of fragments.

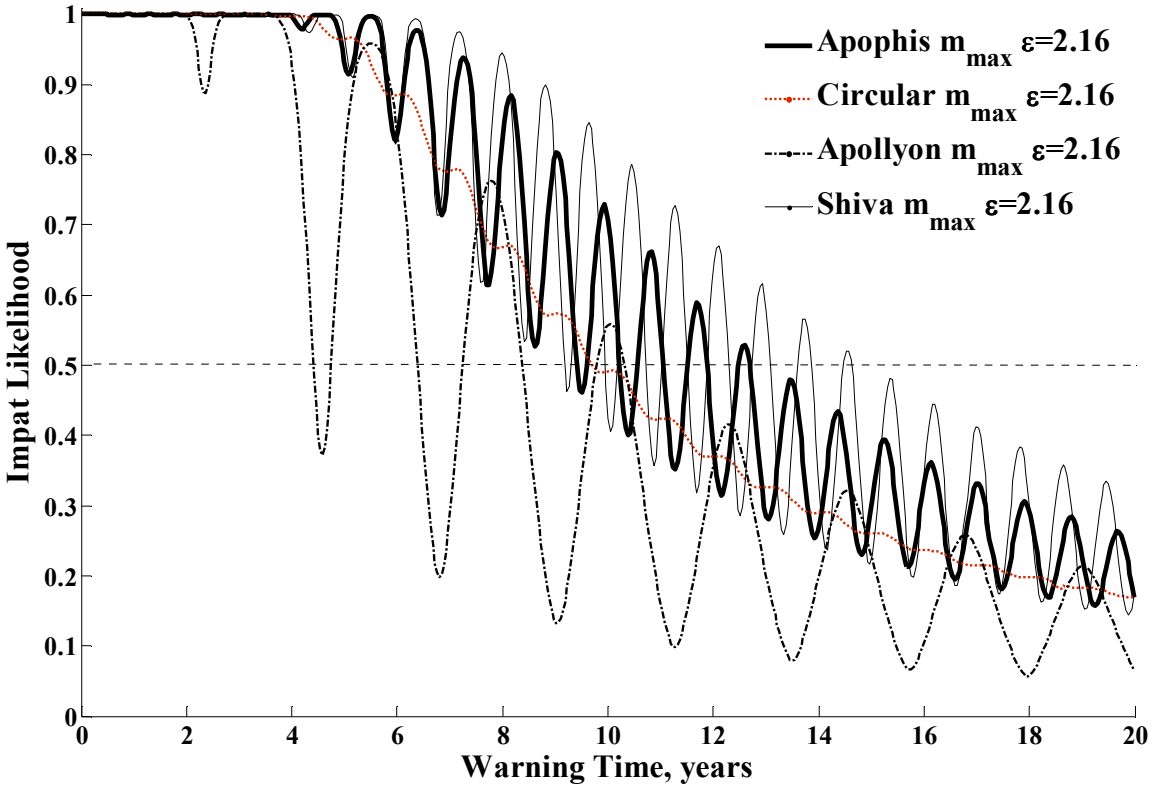

Fig. IV-16 Impact likelihood for all the four test cases from Table IV-1 as a function of warning time or time span between break-up and impact. The fragmentation is spawned by 500 J/kg of collisional energy causing a dispersion of the largest fragment $m_{\max}$ with $\boldsymbol{\mu} = [0.014 \quad 0 \quad 0] m/s$ and $\boldsymbol{\sigma} = [0.008 \quad 0.008 \quad 0.008] m/s$ for all the four test cases. The hyperbolic factor ε is fixed to 2.16 for all the four cases.

The collisional energy or SKE of the impact likelihood plotted in Fig. IV-16 was set at 500 J/kg. Such a collisional energy causes a change of velocity of the centre of mass of the system (i.e., cloud of particles) of $[0.014 \quad 0 \quad 0] m/s$ and a standard deviation of the velocity of the largest fragment resulting from the break-up of $[0.008 \quad 0.008 \quad 0.008] m/s$, which is almost 60% the δv of the centre of mass. An important difference with respect to the results in Section IV.4 is the fact that in Fig. IV-16 the break up of the asteroid moves backwards in time in order to have an increase in warning time, while the hypothetical impact time t_{MOID} is kept fixed. A consequence of this is that the break up occurs at

different orbital positions of the unperturbed orbit of asteroid, and the periodic variations of the impact likelihood that can be observed are primarily due to this change in orbital position of the break up point.

One of the figure's most outstanding features is the large variation of the impact likelihood within one orbital period. This variation increases with the eccentricity of each test case, hence the *Circular* case is the asteroid with minimum variation of the impact likelihood, while *Apollyon* is the case with the largest. For the latter the difference between the maximum and minimum impact probability within the same orbit reaches a maximum of 70%. Another distinctive feature of the evolution of the curves in Fig. IV-16 is the timing of each minimum, occurring at the perihelion position of each asteroid orbit. Both features are direct consequences of the variation of semimajor axis of the initial orbit δa, which is the only variation of Keplerian elements that allows for an unbounded relative orbit of the fragments. The first Gauss planetary equation states:

$$\delta a = \frac{2a^2 v}{\mu} \delta v_t \tag{4.53}$$

which, for a fixed δv_t, will be maximum at perihelion, since the orbital velocity v will also be highest. At the same time, the orbital variation of the velocity v is larger the higher the eccentricity of the asteroid, hence the orbital variation of the impact likelihood is also larger the higher the eccentricity.

The instantaneous change of velocity required to deflect each one of the asteroids in Fig. IV-16 a distance equal to $2.16 \times R_{\oplus}$ can be computed using the same procedure explained in Section IV.2.1. The minimum required delta-velocities can then be mapped to the correspondent impact probability of each asteroid at the same warning time. Fig. IV-17 shows this mapping of the results on Fig. IV-16 and several interesting conclusions can be drawn from it. All the asteroids reach 50% chance of impact when the minimum required δv for a $2.16 \times R_{\oplus}$ deflection is 0.014 m/s; note that this is the same δv that our fragmentation provided to the centre of mass of the fragmented cloud. At warning times such that the required δv for a $2.16 \times R_{\oplus}$ deviation is 0.014 m/s the centre of mass of the fragmented asteroid is moving just outside of the integrated volume, thus, if the length or semimajor axis of the cloud of fragments is not larger than the diameter of the integrated volume, half of the cloud should still remain inside the integrated volume. The impact likelihood should therefore be 50% (note that the cloud is aligned with the radii of the integrated sphere, since the centre of it is the position at t_{MOID} of the unperturbed and

unfragmented asteroid and is also included inside the cloud). In general, the conclusion from Fig. IV-17 is that the impact likelihood can be almost perfectly mapped into a simple one-dimensional Gaussian distribution of the delta-velocity in the tangential direction δv_t, thus, for example, the impact probability reaches ~98 % at the time that the δv required for a $2.16\times R_\oplus$ deviation is 0.030 m/s, using a simple Gaussian distribution, tangential velocities larger than $\langle \delta v_t \rangle + 2\sigma_t$ would be reached by 2.28%, thus driving the impact likelihood to ~98 %.

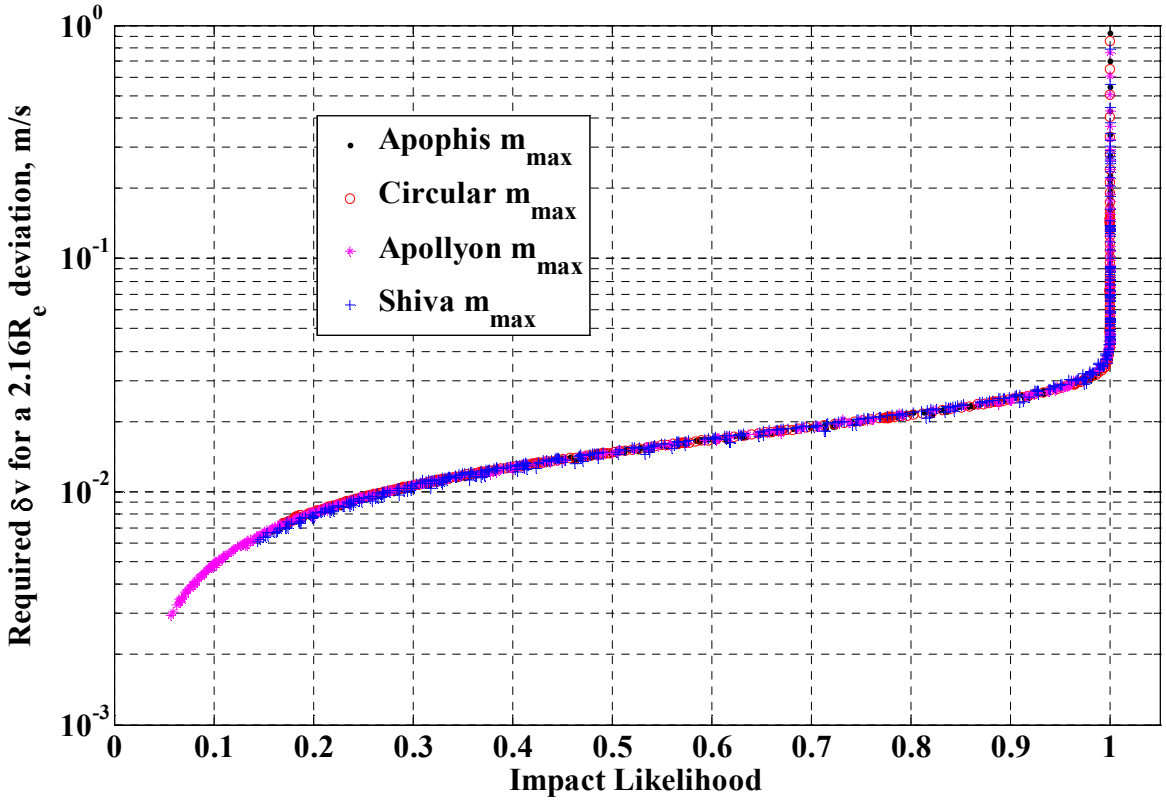

Fig. IV-17 Impact likelihood mapping into minimum required δv to achieve a deflection equal to $2.16\times R_\oplus$.

IV.5.1. Average Predicted Fragments and Impacts: SKE=500 J/kg

This section presents the impact likelihood and the average number of expected impacts for three different *catastrophic fragmentations*, $f_r \le 0.5$, triggered with a 500 J/kg kinetic impactor mission at some point during the last 20 years of collision course of *Apophis*, *Shiva*$_3$ and *Apollyon*$_3$. In the example used here, The 500 J/kg of collisional energy accounts for a kinetic impactor with a mass of 10,000 kg to deflect *Apophis* or 18,520 kg for the larger cases of *Shiva*$_3$ and *Apollyon*$_3$. As a consequence, the impact velocity necessary to provide the required collisional energy is 52 km/s. Such a deflection

mission would provide a change of the velocity of the unfragmented asteroid (or centre of mass of the fragmented case) of $\Delta \mathbf{v}_a \sim \left[0.019 \quad 0 \quad 0\right] m/s$.

Only a discrete number of size samples were computed due to the large computational cost of the impact likelihood integration (i.e., Eq.(4.52)), in particular, six different fragment masses were studied for each given case; five general masses for all the small fragments, 10^{10}kg, $5x10^9$kg, 10^9kg, $5x10^8$kg and 10^8kg plus a varying mass accounting for the largest fragment of each fragmentation case. As defined by Eq.(4.1), for the three fragmentations ratios, f_r equal to 0.5, 0.25 and 0.1, the largest *Apophis*' fragment should contain a mass of $1.35x10^{10}$kg , $6.75x10^9$kg or $2.7x10^9$kg respectively, while for *Shiva*$_3$ and *Apollyon*$_3$ the largest fragment mass should be $2.5x10^{10}$kg, $1.25x10^{10}$kg or $5x10^9$kg for the same fragmentation ratios. Considering the re-aggregation of mass and the fragment size distribution previously described in this Chapter, together with a collisional energy at 500 J/kg, the largest fragments of three test cases will instead be $2.1x10^{10}$kg, $1.35x10^{10}$kg and $4.46x10^9$kg for *Apophis* or $4.08x10^{10}$kg, $2.72x10^{10}$kg and $9.68x10^9$kg for the other two larger asteroids. As we can see, the effect of the gravity is considerable, re-aggregating enough mass to yield an effective fragmentation ratio between 0.82 and 0.17, instead of ranging from 0.50 to 0.10. Table IV-2 summarizes the number of dangerous fragments considering a power law distribution such as Eq.(4.41) and the re-aggregation as in Section IV.4.3.

Table IV-2 Fragment groups used for the computation of impact likelihood and average number of impacts for catastrophic fragmentation with f_r equal to 0.5, 0.25 and 0.1. Note that the smallest mass is $8x10^7$kg, since the lower limit is set by the lower diameter limit of 40m. N is the number of average fragments rounded to the closest integer number.

	N *Apophis*			N *Shiva*$_3$ & *Apollyon*$_3$			Representative Mass
f_r=	*0.50*	*0.25*	*0.10*	*0.50*	*0.25*	*0.10*	
$5x10^{10}\,kg > m > 1.5x10^{10}\,kg$	1	1	0	1	1	0	$2.5x10^{10}\,kg$
$1.5x10^{10}\,kg \geq m > 7x10^{9}\,kg$	0	0	1	0	0	1	$1x10^{10}\,kg$
$7x10^{9}\,kg \geq m > 2x10^{9}\,kg$	0	0	0	0	0	1	$5x10^{9}\,kg$
$2x10^{9}\,kg \geq m > 7x10^{8}\,kg$	1	1	1	1	2	2	$1x10^{9}\,kg$
$7x10^{8}\,kg \geq m > 2x10^{8}\,kg$	3	5	5	5	8	8	$5x10^{8}\,kg$
$2x10^{8}\,kg \geq m > 8x10^{7}\,kg$	8	11	11	12	19	18	$1x10^{8}\,kg$

As described in Section IV.3.2, all the fragments, no matter their mass, will have the same mean velocity, thus fulfilling the law of conservation of momentum, while the

dispersion of velocity from the centre of mass of the system is driven by Eq.(4.37), thus is a function of the mass of the fragment. When calculating the impact likelihood of the largest fragment, it is considered that its velocity dispersion corresponds to the dispersion of the fragment with mass equal to $f_r \cdot M_a$, so the mass of the largest fragment prior to re-aggregation process. This assumption considers that the re-aggregation process does not substantially modify the statistical description of the velocity of the largest fragment. In fact, if the velocity of the largest fragment is modified, it will tend to be accelerated, changing only marginally its direction; this is due to the fact that the largest fragment has more probability to interact with fragments with low relative velocities, moving slightly faster, since it is statistically the slowest fragment, and moving in the same direction (or similar). The perturbation caused by all the re-aggregating fragments will then tend to be low and in the same direction.

The impact likelihood of the remaining fragments is then computed by approximating the dispersion of velocity $\boldsymbol{\sigma}$ of each fragment to the dispersion of velocity $\boldsymbol{\sigma}$ of the closest of the calculated representative masses in Table IV-2. Note that by doing so we have considered that the statistical description of the fragments that avoided being re-aggregated remains unchanged. This implicitly slows down the velocity of the escaped fragments, since those had a relative velocity higher than the dispersion of velocity calculated by Eq.(4.40). In fact, the excess mean dispersion $\boldsymbol{\sigma}$ of the escaped fragments, i.e., average velocity relative to the centre of mass of the system outside the sphere of influence of the largest fragment, differs from the results calculated by Eq.(4.40) by less than 20%. On top of that, the gravitational perturbation to each particular fragment will vary depending on its actual dispersion of velocity, and for the quickest moving fragments the error is negligible, since they are barely affected by the gravity of the largest fragment. Since another approximation is also done by assuming that the mass of each fragment is equal to the closest representative mass in Table IV-2, calculating the dispersion of velocities $\boldsymbol{\sigma}$ directly from Eq.(4.40), thus without gravitational perturbations, is considered to be an acceptable approximation, given the level of accuracy seek in this work.

Finally, the integrated Earth capture volume of each asteroid is corrected, now, with the corresponding hyperbolic factor ε (see Table IV-13 in Chapter I), to account for the different Earth gravitational effect to each asteroid orbit. Therefore *Apophis*'s likelihood integration is a sphere of $2.16 \times R_{\oplus}$, *Shiva*'s sphere is $1.52 \times R_{\oplus}$ and *Apollyon*'s is $1.29 \times R_{\oplus}$.

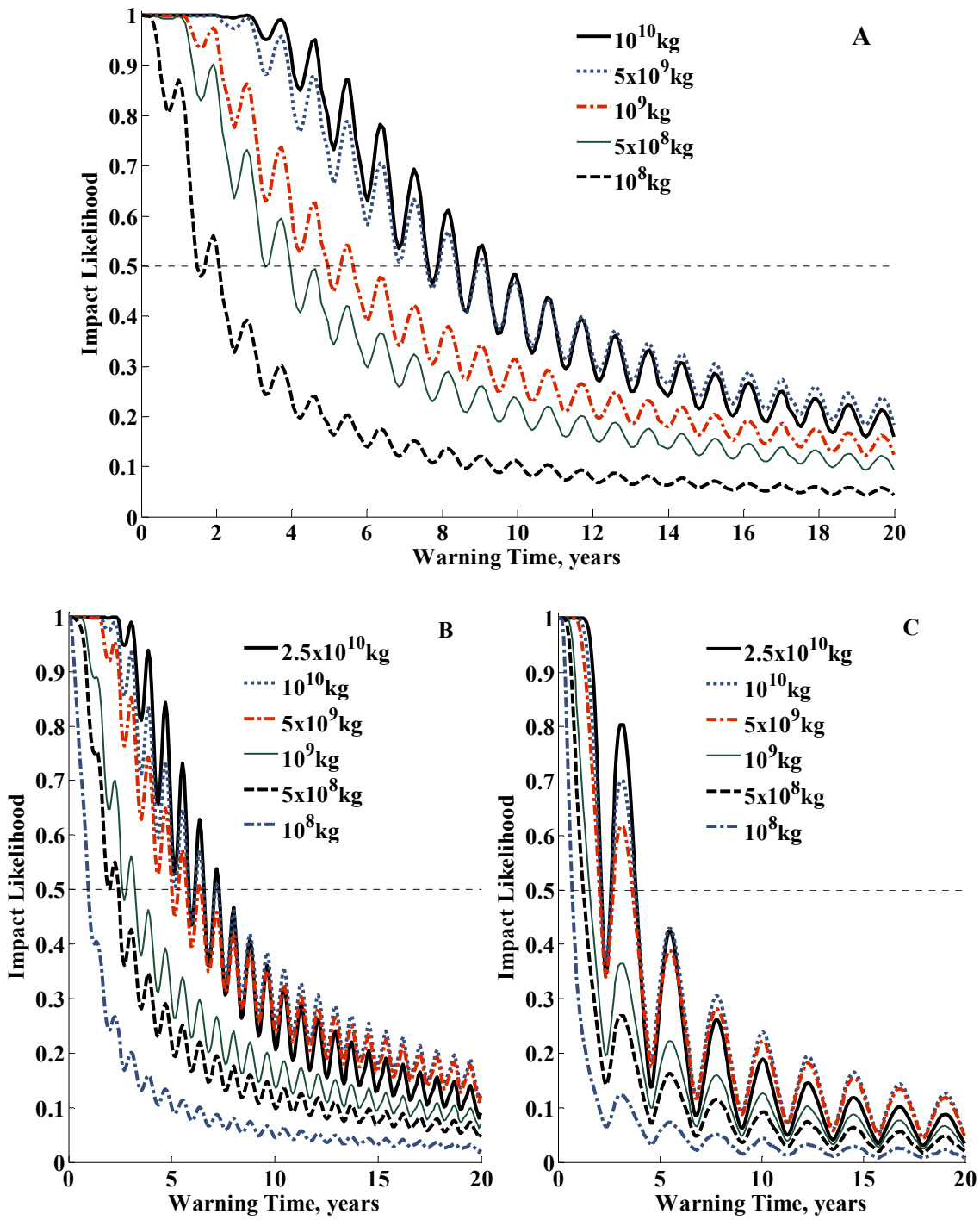

Fig. IV-18 Evolution of the impact likelihood for different fragment sizes along warning times ranging from 0 to 20 years: A) *Apophis* B) *Shiva*$_3$ C) *Apollyon*$_3$. The simulations accounts for an SKE of 500 J/kg providing $\Delta v_a \sim \left[0.019 \quad 0 \quad 0\right] m/s$ to the centre of mass of the fragmentation.

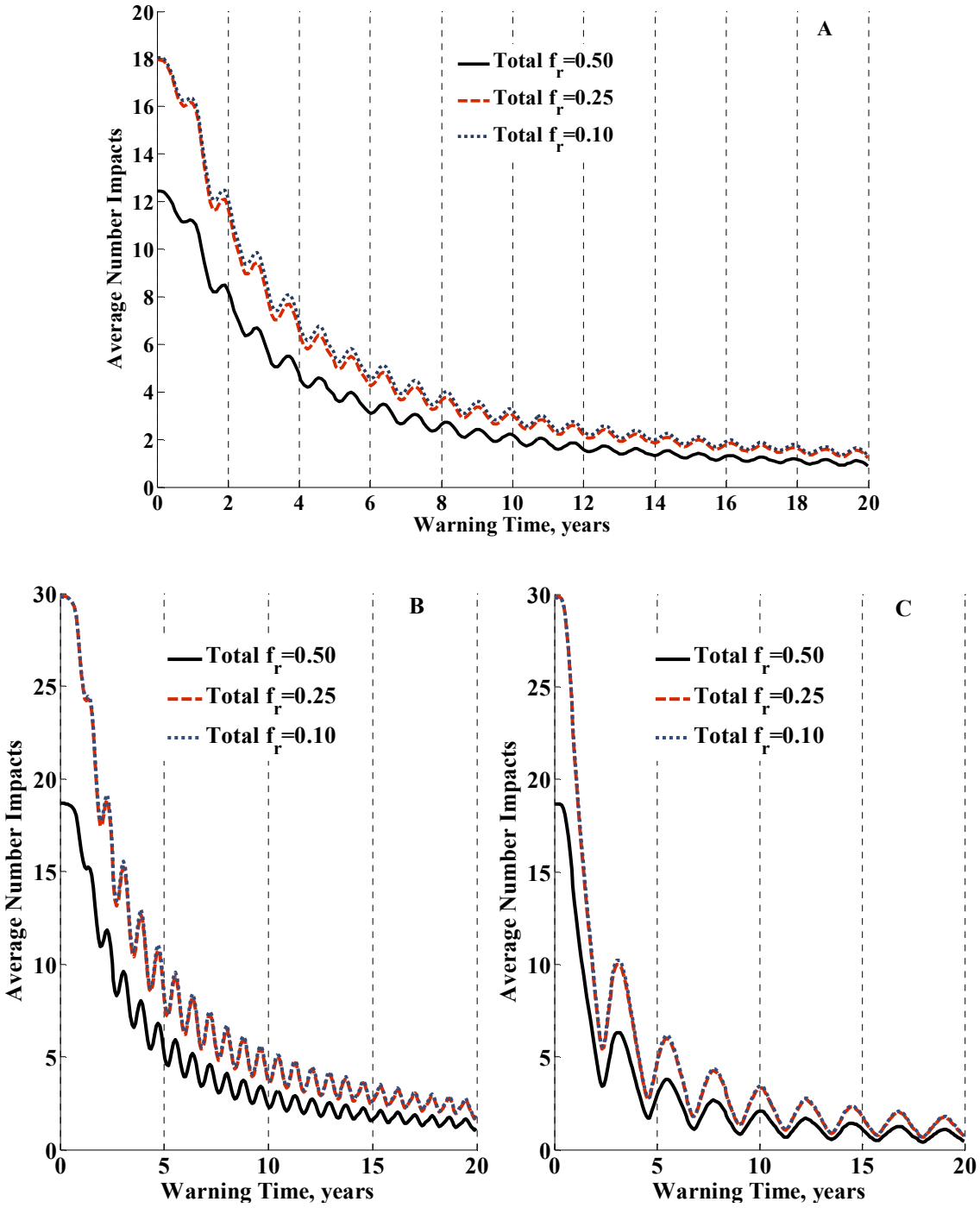

Fig. IV-19 Average number of impacts for three different fragmentation ratios as a function of the warning time: A) *Apophis* B) *Shiva*$_3$ C) *Apollyon*$_3$. The simulations accounts for an SKE of 500 J/kg providing $\Delta v_a \sim [0.019 \quad 0 \quad 0] m/s$ to the centre of mass of the fragmentation.

Fig. IV-18 shows the evolution over warning time of the impact likelihood for the three test cases and different fragment sizes. Fig. IV-19 shows the average number of impacts, thus including the complete census of fragment, for the three different levels of fragmentation. As was expected, the smaller a fragment is, the quicker its impact

likelihood begins to drop, which is due to the higher velocity dispersion of the smaller fragments. At a certain point, this trend changes for all fragment sizes with dispersion of velocity smaller than their mean velocity, since the centre of the ellipsoid of uncertainty moves out of the integrated volume and then the smaller the ellipsoid is the lower will be the impact likelihood. Despite that, in general, the impact likelihood decreases with a decreasing mass, the number of expected impacts grows with a decaying mass and, as seen in Fig. IV-19, even if the break-up occurred 20 years in advance a few impacts should still be expected.

IV.5.2. Expected Damage

As shown for *Apophis*, *Shiva* and *Apollyon* in Fig. IV-19, if the outcome of an attempt of asteroid deflection is the break-up of the threatening object, several impacts of small fragments could be expected even if the fragmentation or break-up occurred 20 years prior to the forecasted impact. Nevertheless, the number of expected impacts is not a good figure to evaluate the risk that these small objects pose to Earth. The work of *Hills & Goda*[19] and *Chesley & Ward*[102] will be used to assess the damage that these smaller fragments can cause and, finally, the damage will be compared with the initial damage that the unshattered object would have caused.

Clearly, an asteroid or fragment threatening to impact the Earth would have 2/3 chances to fall into the water and only 1/3 to fall into land. A small land impact tends to be much more localized than a sea impact, since water can transmit the impact energy over very large distances on two-dimensional waves. Adding to the efficient energy propagation, the high coastal density population makes water impacts a major element of the impact hazard.

The next three tables (Table IV-3 to Table IV-5) show the expected damage for both the unshattered objects and each one of the fragment sizes analysed earlier. Land damage is assessed using *Hills & Goda*[19]'s calculations; for all fragments size, the radius of destruction is taken from the worse case between soft and hard stone for a 20km/s impact. Water damage, instead, is evaluated using data accounting also for 20km/s water impacts found in *Stokes et al*[10]., which were computed using the assessment on damage generated by tsunamis from *Chesley & Ward*[102]. Since the impact velocity of the three test cases analysed here differs from 20km/s (see Table IV-1), the predicted areas were scaled by the collisional energy fraction to the power of 2/3, which is believed to be the way that explosive devastation area scales with the energy[2].

Table IV-3 Expected damaged area for *Apophis*. Table summarizes the damage for the unshattered object and its fragments, including the aggregated largest fragments for break-ups with f_r at 0.50, 0.25 and 0.10.

Mass	Diameter	Land Damage Area [km^2]	Water Damage Area [km^2]	Weighted Damage Area [km^2]
$2.7x10^{10}$kg	270m	~5,920	~56,940	~39,930
$2.1x10^{10}$kg$^{fr=0.50}$	250m	~5,253	~44,340	~31,311
$1.35x10^{10}$kg$^{fr=0.25}$	215m	~4,429	~30,000	~21,477
$4.46x10^{9}$kg$^{fr=0.10}$	149m	~2,988	~7,719	~6,142
$1x10^{9}$kg	90m	~2,080	~240	~860
$5x10^{8}$kg	71m	~750	~40	~280
$1x10^{8}$kg	42m	~40	~0	~10

Table IV-4 Expected damaged area for *Shiva*. Table summarizes the damage for the unshattered object and its fragments, including the aggregated largest fragments for break-ups with f_r at 0.50, 0.25 and 0.10.

Mass	Diameter	Land Damage Area [km^2]	Water Damage Area [km^2]	Weighted Damage Area [km^2]
$5x10^{10}$kg	332m	~11,260	~110,770	~77,600
$4.1x10^{10}$kg$^{fr=0.50}$	311m	~9,959	~93,650	~65,632
$2.7x10^{10}$kg$^{fr=0.25}$	271m	~7,390	~71,110	~49,867
$9,68x10^{9}$kg$^{fr=0.10}$	192m	~4,990	~29,020	~21,011
$5x10^{9}$kg	154m	~3,910	~12,200	~9,440
$1x10^{9}$kg	90m	~2,590	~300	~1,070
$5x10^{8}$kg	71m	~930	~50	~350
$1x10^{8}$kg	42m	~50	~0	~20

Table IV-5 Expected damaged area for *Apollyon*. Table summarizes the damage for the unshattered object and its fragments, including the aggregated largest fragments for break-ups with f_r at 0.50, 0.25 and 0.10.

Mass	Diameter	Land Damage Area [km^2]	Water Damage Area [km^2]	Weighted Damage Area [km^2]
5x10^{10}kg	332m	~14,310	~140,830	~98,660
4.1x10^{10}kg$^{fr=0.50}$	311m	~12,200	~119,070	~83,443
2.7x10^{10}kg$^{fr=0.25}$	271m	~9,390	~90,400	~63,400
9,68x10^{9}kg$^{fr=0.10}$	192m	~6,350	~36,890	~26,713
5x10^{9}kg	154m	~4,970	~15,510	~12,000
1x10^{9}kg	90m	~3,290	~390	~1,350
5x10^{8}kg	71m	~1,180	~70	~440
1x10^{8}kg	42m	~70	~0	~20

Hills & Goda[19] estimated that asteroidal bolides larger than a few tens of meters in diameter are already able to cause damage to the Earth surface, although only due to the sudden blast produced in the final moments of the dissipation of the bolide when crossing the Earth atmosphere. This will not leave long lasting scars on the surface, but only cause an atmospheric explosion like the one occurred in Tunguska (Siberia) in 1908[18]. On the other hand, bolides above 150-200m in diameter[19],[20] reach the Earth surface producing cratering events and, if falling into the sea, dangerous tsunamis[102]. Note from the tables above, the sudden reduction in *water damaged area* below the 150m diameter. This is due to the low efficiency of air blasts in transmitting their energy to the ocean surface in order to initiate a tsunami.

We also considered a *weighted* damage ratio. The weighted damage ratio considers the mean damage of a statistical distribution of land and sea impacts. One could think that although for small fragments the number of impacts is high enough to make the weighted damage a good approximation, for the largest fragments and especially for the unfragmented asteroid the approximation can drive to misleading results, since a single fragment would not cause a *weighted* damage, but one of the two options, i.e., either land or water impact.

Let us suppose that a fragmentation spawning several big fragments (i.e., >5x10^{9}kg) occurs. This kind of fragmentation outcome would be a very rare occurrence when the break-ups is triggered by only 500 J/kg of SKE, but may happen more often for higher

collisional energies. If several large fragments are then spawned by the break-up of an asteroid, the most worrying scenario would occur if the unshattered object was meant to have a land impact, but because of the failed attempt to mitigate the threat, at least 1 of the large fragments falls into the sea. This scenario would yield more damage to Earth than previous unfragmented scenario and, considering each fragment as statistically independent, would occur with little less than 33% probability (if having several large objects).On the other hand, if the unshattered object is meant to hit the sea, only the very infrequently occurring scenario of several large objects, which manage not to become re-aggregated, and all of them falling into the water could possibly increase the damage caused by the tsunami produced by the single unshattered object. To sum up, there is only a little more than 33% probability to increase the damage by fragmentation of the original asteroid, if both the unshattered object and all its fragments fall onto Earth. Highlighting the latter result, the statistical *weighted* damage is used in the rest of the analysis of consequences of a fragmentation.

Fig. IV-20 shows the evolution with time of the three different damages produced by a barely catastrophic fragmentation, i.e., f_r=0.50, of *Apophis*. As shown in the figure, despite an increasing number of fragments, the damaged area drops with a decreasing fragment mass, being the largest fragment clearly the most dangerous of all, although even the smallest fragments, 10^8kg, may still cause considerable damage.

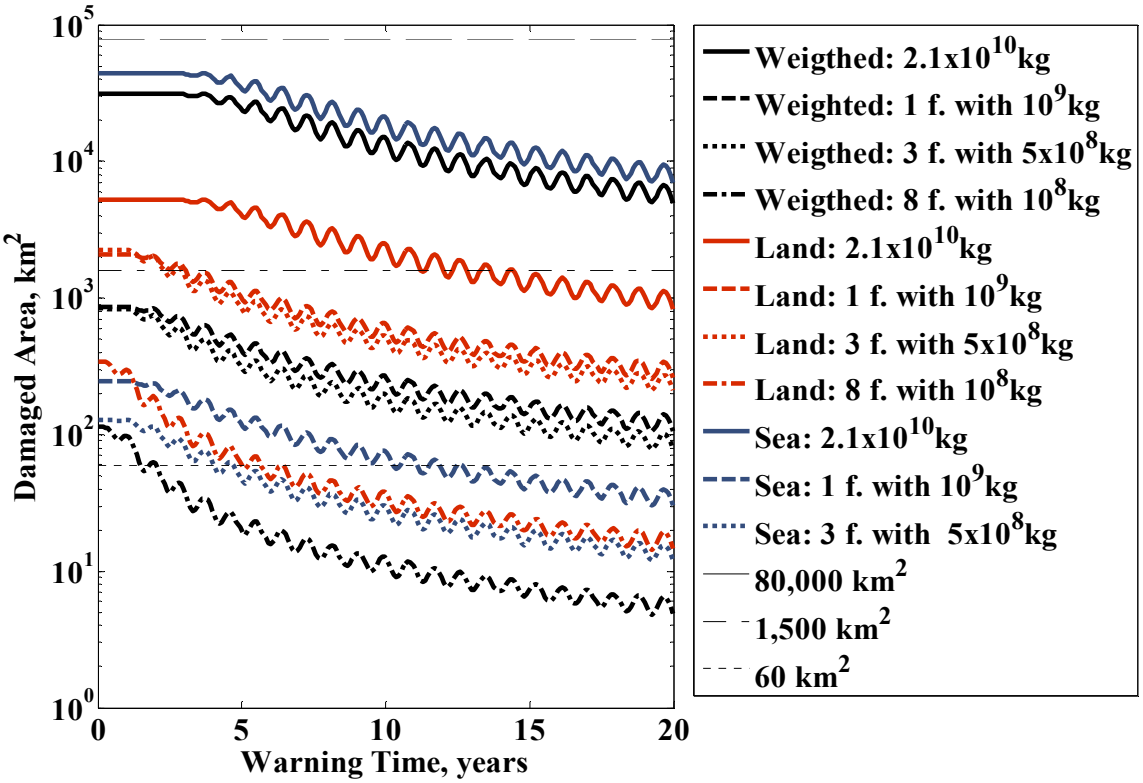

Fig. IV-20 Damage evolution of a barely catastrophic fragmentation of *Apophis* for land impacts, sea impacts and weighted damage. For comparison, the three straight lines represent the area of Scotland (~80,000km^2), the area of London (~1,500km^2) and the area of Manhattan (~60km^2).

Fig. IV-21 compares the expected damage of the unshattered *Apophis* with the potential damage of all fragments from the three different catastrophic fragmentation levels. The damage of the fragmented case is computed by adding the predicted weighted damage of each fragment size, thus multiplying the areas in Table IV-3 by the number of expected impacts of each fragment size previously calculated and shown in Fig. IV-19. The statistical damaged area shown in Fig. IV-21 is scaled by the weighted damage of the unfragmented *Apophis*, ~40,000 km^2. The fragmentation represented in Fig. IV-21 was triggered by a kinetic impactor with a $m_{s/c}$ of 10,000 kg providing 500 J/kg of SKE. If *Apophis* does not shatter under such a collisional energy the asteroid could be deflected with a velocity of $\boldsymbol{\mu} \sim [0.019m/s \quad 0 \quad 0]$, assuming an enhancement factor β of only 1.

As seen in Fig. IV-21, the unshattered *Apophis* completely misses the Earth 12 years after its orbit was altered by 0.019m/s, while within 6 to 12 years of warning time, *Apophis* misses the Earth only if the deflection occurs at several optimal orbital positions. The damage ratio of the unshattered object (blue line) was computed not only by applying a delta-velocity $\delta\mathbf{v} \sim [0.019m/s \quad 0 \quad 0]$ to *Apophis*, but also adding a small error to account for

sensible uncertainties during the mitigation mission. A standard deviation σ_0 of 1/6th the delta-velocity is chosen as a generic error for all the unfragmented computations. This standard deviation states that, after taking into account the uncertainties of the model, the ultimate value of the delta-velocity has a 99.7% of probability to be within 50% the value predicted by the model, thus:

$$3\sigma_0 = \frac{\Delta v_a}{2} \tag{4.54}$$

Without this hypothetical error in the kinetic impactor performance, the damage ratio (blue line) would simply resemble a step function.

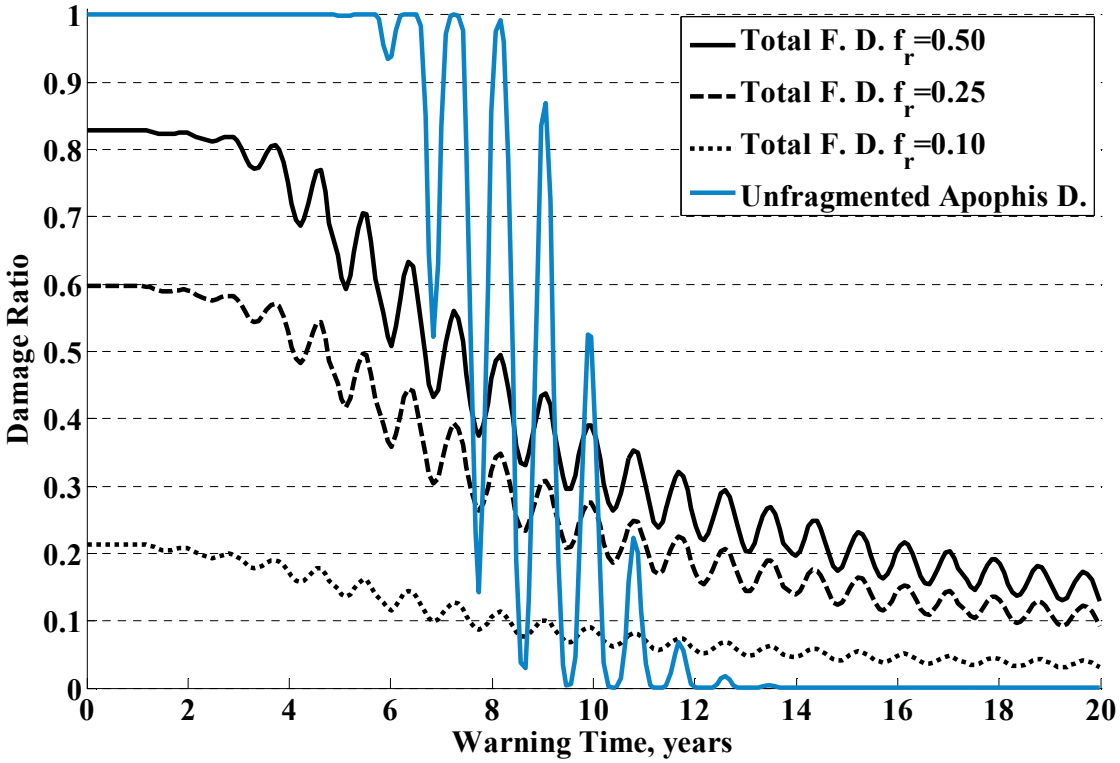

Fig. IV-21 Damage ratios of *Apophis*: fragmented case f_r=0.50 (black solid line), f_r=0.25 (black dashed line), f_r=0.10 (black dotted line) and unshattered case (blue line) with a tree sigma equal to 50% in the delta-velocity.

Finally, Fig. IV-22 completes the comparison on the consequences of a fragmentation for *Shiva*$_3$ and *Apollyon*$_3$ cases and a SKE of 500 J/kg. The unshattered damage for these two objects is also calculated using the same generic error described above. Fig. IV-21 and Fig. IV-22 highlight several interesting features on the consequences of a catastrophic fragmentation; if a fragmentation occurs, the maximum damage, i.e., the damage that would be caused by all fragments impacting the Earth, is smaller than that of the unshattered object, and keeps decreasing with a decreasing fragmentation ratio. There is

however an exception to this: as we can see by using the data available from Table IV-3 to Table IV-5, several land impacts will easily cause more harm that the unshattered land damage, while the opposite occurs for sea impacts.

An interesting feature for long warning times (> 10 years) in Fig. IV-21 and Fig. IV-22 is the higher damage ratio of all the fragmented scenarios opposed to the zero damage of the unshattered case. We should notice from Fig. IV-20 that, at this SKE level, the damage is driven by the largest fragment: on the one hand, since the potential damage of the largest fragment is smaller than the unshattered object, the risk should be reduced, although on the other hand, the orbital uncertainty associated to the fragmentation greatly enhances the risk. Notice from Fig. IV-3 that the delta-velocities required to deflect the collisional course of a threatening object vary very little for long warning times, being the uncertainties associated to the fragmentation much larger.

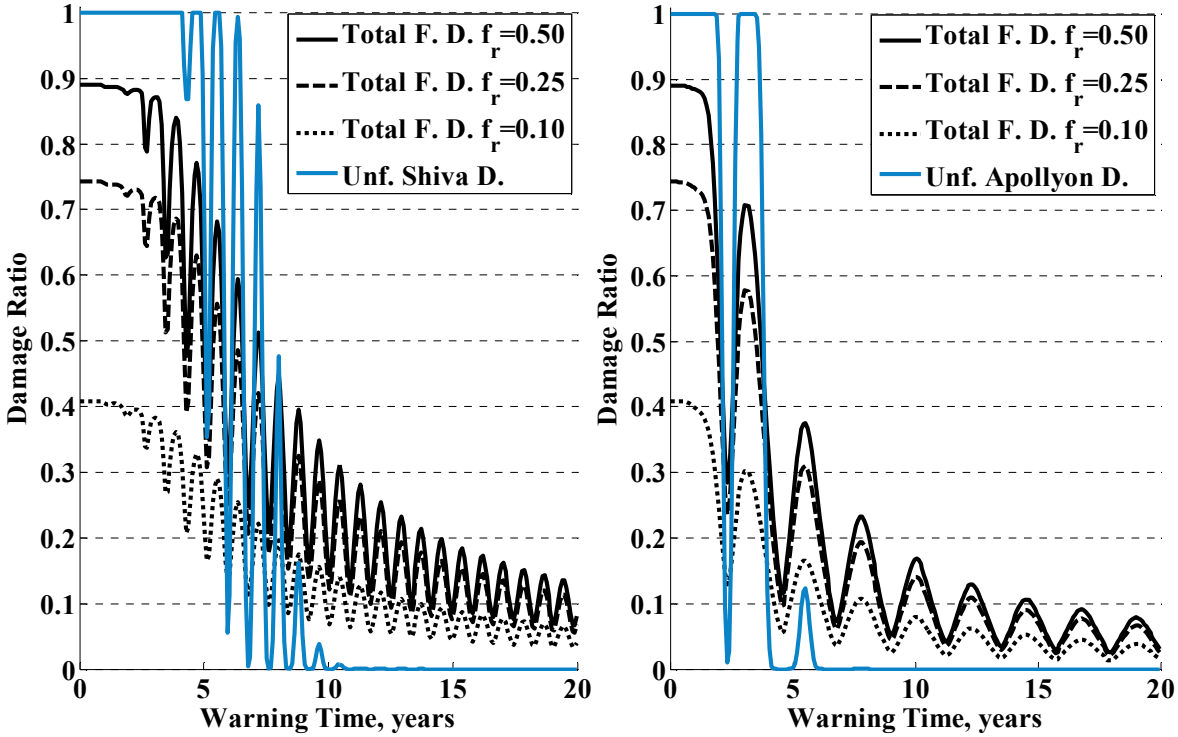

Fig. IV-22 Damage ratios of *Shiva*$_3$ and *Apollyon*$_3$: fragmented case f_r=0.50 (black solid line), f_r=0.25 (black dashed line), f_r=0.10 (black dotted line) and unshattered case (blue line) with a tree sigma equal to 50% in the delta-velocity.

IV.5.3. Other Scenarios Analysed

In terms of the break-up and dispersion model described in this chapter, the following points should be highlighted:

- For a fixed impactor mass $m_{s/c}$, the delta-velocity provided to the centre of mass of the asteroid is only a function of the collisional energy or *SKE* used during the mitigation attempt.
- The dispersion of the cloud of fragments of a given size is only a function of the delta-velocity provided to the centre of mass.
- The potential damage that a fragmented asteroid could cause to Earth is, therefore, a function only of two variables; the delta-velocity provided to the centre of mass of the asteroid, which depends only on the *SKE*, and the fragmentation ratio of the break-up.
- A *barely catastrophic fragmentation*, i.e., f_r equal to 0.5, only occurs if *SKE*(or *SNE*) is equal to Q^*, otherwise if *SKE*(or *SNE*) is larger than Q^* the fragmentation ratio f_r will be smaller.
- The critical specific energy Q^* is uncertain; possibly close to 100 J/kg for "rubble piles" and still below 1000 J/kg even for strong monolithic asteroids.

Up to this point, the chapter has only analyzed the consequences of a 500 J/kg impact triggering three different levels of fragmentation and, given the aforementioned statements about the model, a few more possible scenarios should also be assessed. The following scenarios are here presented; a *barely catastrophic fragmentation* triggered by a very low level of collisional energy (100 J/kg), different level of *catastrophic fragmentation* triggered by the upper limit of collisional energy (1000 J/kg) and, finally, a highly *catastrophic fragmentation* achieved with an energy much higher than the upper fragmentation limit to account for the possibility of a hazard mitigation mission attempting to destroy and disperse the impact threat as oppose to deviate it. Table IV-6 summarises all the different scenarios computed for the analysis carried out in this chapter.

Table IV-6 Summary of the fragmentation scenarios simulated in the chapter. K.I. refers to the use of the kinetic impact model, while N.I. refers to the nuclear interceptor model.

	100 J/kg	500 J/kg	1000 J/kg	5000 J/kg
Apophis	K.I. $\Delta\mathbf{v}_a \sim [0.006 \quad 0 \quad 0] m/s$ $m_{s/c} = 5{,}000 kg$ $\Delta\mathbf{v}_{s/c} \sim [33 \quad 0 \quad 0] km/s$	K.I. $\Delta\mathbf{v}_a \sim [0.019 \quad 0 \quad 0] m/s$ $m_{s/c} = 10{,}000 kg$ $\Delta\mathbf{v}_{s/c} \sim [52 \quad 0 \quad 0] km/s$	K.I. $\Delta\mathbf{v}_a \sim [0.038 \quad 0 \quad 0] m/s$ $m_{s/c} = 20{,}000 kg$ $\Delta\mathbf{v}_{s/c} \sim [52 \quad 0 \quad 0] km/s$	N.I. $\Delta\mathbf{v}_a \sim [0.161 \quad 0 \quad 0] m/s$ $m_{s/c} = 550 kg$
$Shiva_3$	K.I. $\Delta\mathbf{v}_a \sim [0.006 \quad 0 \quad 0] m/s$ $m_{s/c} = 9{,}260 kg$ $\Delta\mathbf{v}_{s/c} \sim [33 \quad 0 \quad 0] km/s$	K.I. $\Delta\mathbf{v}_a \sim [0.019 \quad 0 \quad 0] m/s$ $m_{s/c} = 18{,}520 kg$ $\Delta\mathbf{v}_{s/c} \sim [52 \quad 0 \quad 0] km/s$	K.I. $\Delta\mathbf{v}_a \sim [0.038 \quad 0 \quad 0] m/s$ $m_{s/c} = 37{,}040 kg$ $\Delta\mathbf{v}_{s/c} \sim [52 \quad 0 \quad 0] km/s$	N.I. $\Delta\mathbf{v}_a \sim [0.165 \quad 0 \quad 0] m/s$ $m_{s/c} = 1{,}020 kg$
$Apollyon_3$	K.I. $\Delta\mathbf{v}_a \sim [0.006 \quad 0 \quad 0] m/s$ $m_{s/c} = 9{,}260 kg$ $\Delta\mathbf{v}_{s/c} \sim [33 \quad 0 \quad 0] km/s$	K.I. $\Delta\mathbf{v}_a \sim [0.019 \quad 0 \quad 0] m/s$ $m_{s/c} = 18{,}520 kg$ $\Delta\mathbf{v}_{s/c} \sim [52 \quad 0 \quad 0] km/s$	K.I. $\Delta\mathbf{v}_a \sim [0.038 \quad 0 \quad 0] m/s$ $m_{s/c} = 37{,}040 kg$ $\Delta\mathbf{v}_{s/c} \sim [52 \quad 0 \quad 0] km/s$	N.I. $\Delta\mathbf{v}_a \sim [0.165 \quad 0 \quad 0] m/s$ $m_{s/c} = 1{,}020 kg$

Barely catastrophic fragmentation with 100 J/kg

A SKE of 100 J/kg provides very little velocity to the threatening object as can be seen in Fig. IV-23, where the impulse provided to the three unshattered object is barely able to deflect *Apollyon*$_3$ (blue lines). On the other hand, if the asteroid shatters, the fragments will have very little velocity and most of the mass will re-accumulate. As described in Table IV-7, less than 10% of the mass is predicted to escape the re-accumulation process, thus the potential risk of damage comes almost entirely from the large re-accumulated fragment. There is a small initial reduction on the damage caused by the fragmented cases, caused by the mass loss, since all the small fragments that do manage to escape the gravitational re-accumulation are, in fact, too small to reach the Earth surface and cause any noticeable damage. We can notice however a higher damage on the fragmented case for long warning times in the *Apollyon*$_3$'s figure, which is caused by the increased uncertainty on the motion of the new "rubble pile" asteroid. The same trend will be also observed in *Apophis* and *Shiva*$_3$ figures if the warning time was extended.

Table IV-7 Approximate fragment census for a barely catastrophic fragmentation triggered with 100 J/kg.

Representative Mass	N *Apophis* f_r=0.50	N *Shiva*$_3$ & Apollyon$_3$ f_r=0.50
Largest Fragment	$2.45x10^{10}\,kg$	$4.6x10^{10}\,kg$
$1x10^{10}\,kg$	0	0
$5x10^{9}\,kg$	0	0
$1x10^{9}\,kg$	0	0
$5x10^{8}\,kg$	0	0
$1x10^{8}\,kg$	1	2

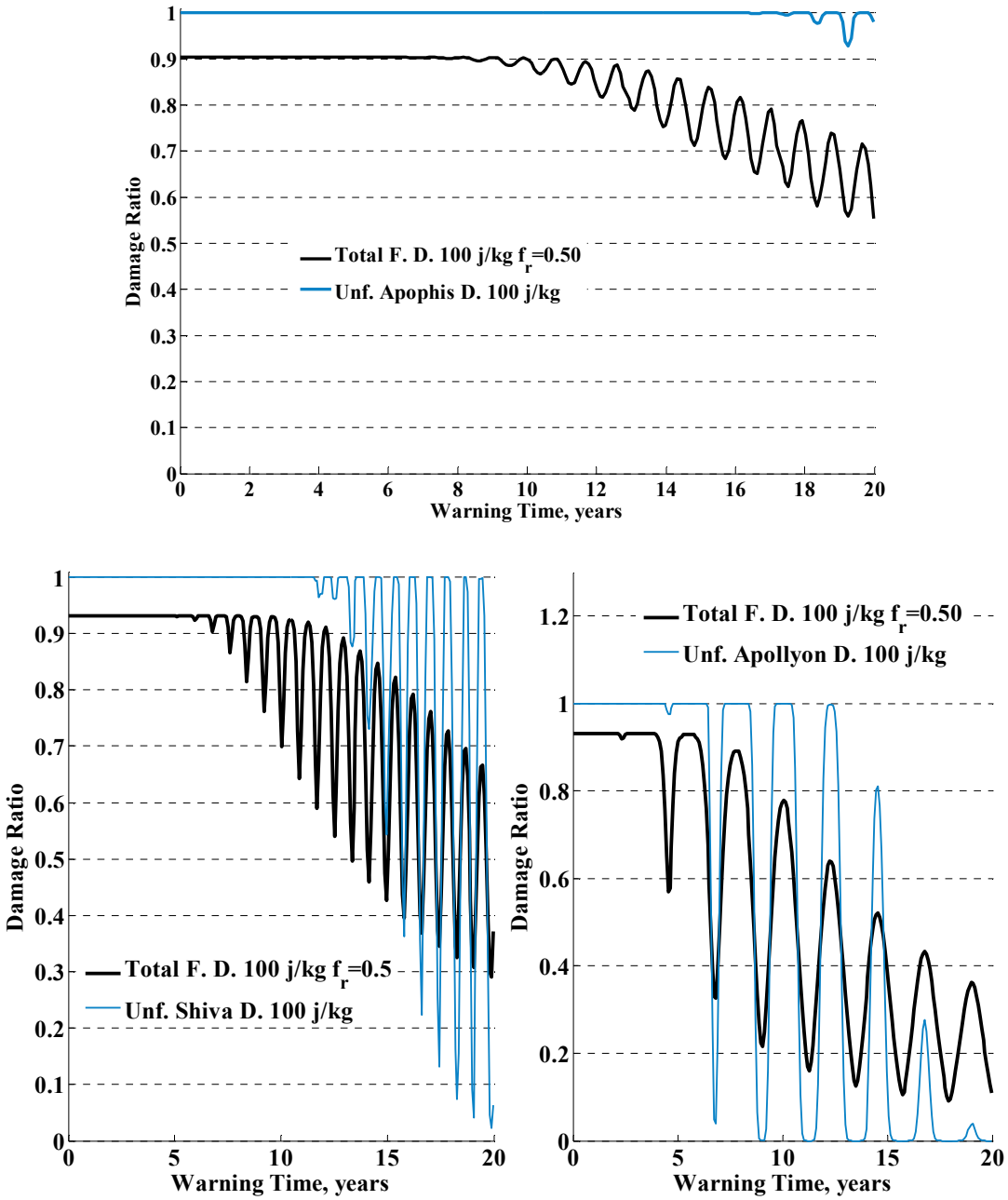

Fig. IV-23 Damage ratios of *Apophis*, *Shiva* and *Apollyon* for a 100 J/kg break-up: fragmented case (black line) and unshattered case (blue line) with a tree sigma equal to 50% in the delta-velocity.

Catastrophic fragmentations with 1000 J/kg

If energies of around 1000 J/kg are provided, most of the mass escapes re-accumulation, thus increasing the population of fragments for all sizes. At this energy, several large and dangerous fragments should be expected. The potential risk decreases with increasing warning time and reaches levels that are approximately half of those achieved through a deflection with 500 J/kg. Perhaps the most important drawback of this energy level is the fact that a secondary attempt of deflection will have to deal not only with one dangerous fragment but with 3 to 6 dangerous fragments. On top of that, at this level of collisional energy and by the results on fragmentation energies from Fig. IV-2, it seems clear that the most probable outcome of an impulsive mitigation attempt would be a catastrophic fragmentation as described in Table IV-8.

Table IV-8 Approximate fragment census for three catastrophic fragmentations triggered with 1000 J/kg.

Representative Mass	N *Apophis*			N *Shiva*$_3$ & *Apollyon*$_3$		
f_r=	*0.50*	*0.25*	*0.10*	*0.50*	*0.25*	*0.10*
Largest Fragment [kg]	$1.75x10^{10}$	$9.15x10^{9}$	$2.93x10^{9}$	$3.5x10^{10}$	$1.93x10^{10}$	$6.06x10^{9}$
$5x10^{9}\,kg$	1	1	1	1	1	1
$1x10^{9}\,kg$	2	2	2	3	4	3
$5x10^{8}\,kg$	6	7	6	8	12	10
$1x10^{8}\,kg$	11	15	12	16	24	21

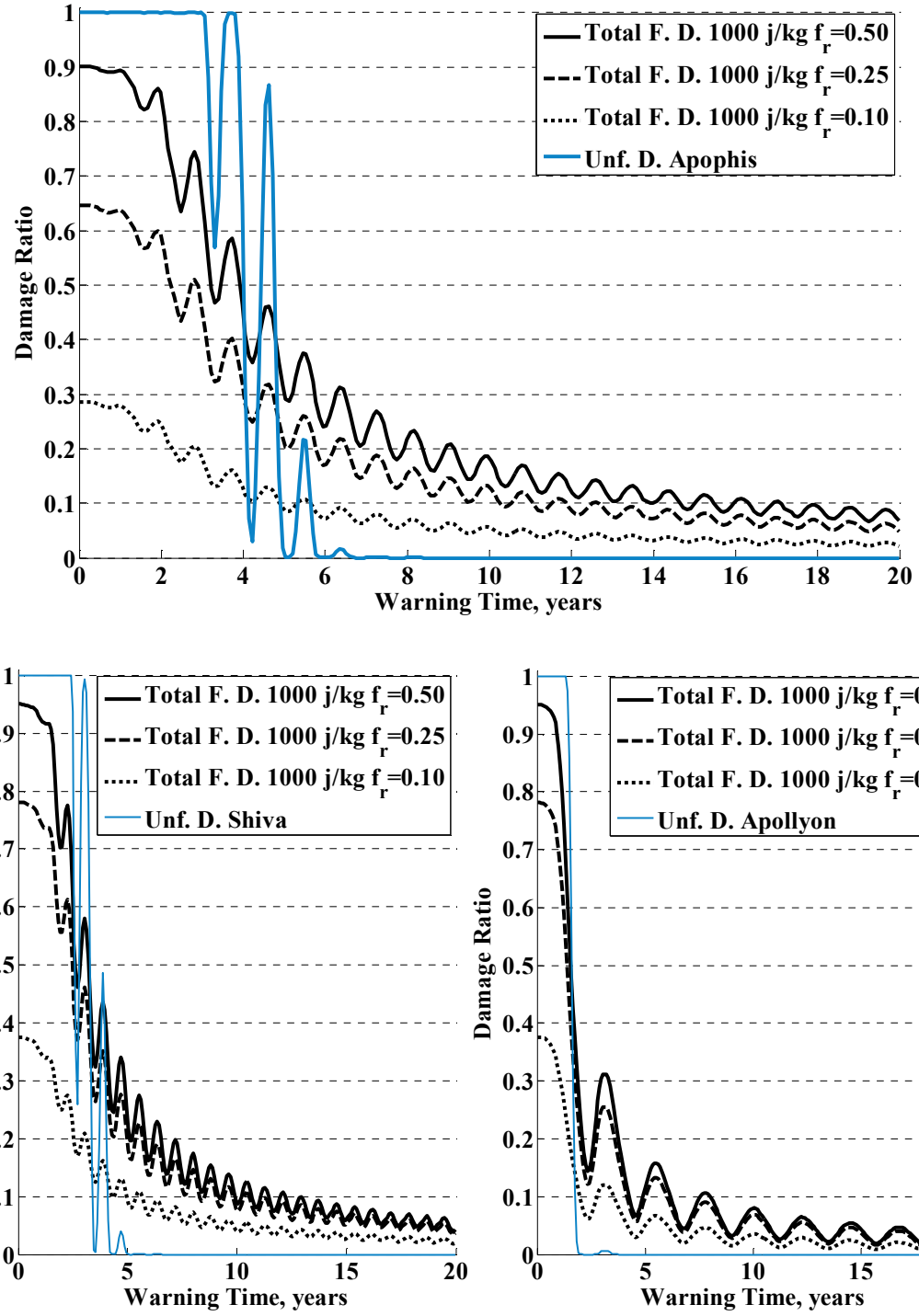

Fig. IV-24 Damage ratios of *Apophis*, *Shiva* and *Apollyon* for a 1000 J/kg break-up: fragmented cases (black lines) and unshattered cases (blue lines) with a tree sigma equal to 50% in the delta-velocity.

Highly catastrophic fragmentations with 5000 J/kg

With a five-fold increase of the upper fragmentation limit considered in this work, the fragmentation should be expected to be *highly catastrophic*. The fragmentation level is clearly unknown, although, as seen by the fragmentations with f_r=0.25 and f_r=0.10, a very high dispersion should be expected, achieving very low risk for long warning times, which in some cases can be deemed negligible. However, although the unfragmented case seems highly improbable to exist at this level of energy, we should notice that the unfragmented option still represent a safe option to achieve zero potential risk only after very short period.

Table IV-9 Approximate fragment census for two highly catastrophic fragmentations triggered with 5000 J/kg.

Representative Mass	N *Apophis*		N *Shiva*$_3$ & Apollyon$_3$	
	f_r=0.25	f_r=0.10	f_r=0.25	f_r=0.10
Largest Fragment	$5.7x10^9\,kg$	$2.29x10^9\,kg$	$1.1x10^{10}\,kg$	$4.37x10^9\,kg$
$1x10^{10}\,kg$	0	0	1	0
$5x10^9\,kg$	1	1	2	1
$1x10^9\,kg$	4	2	6	4
$5x10^8\,kg$	9	6	15	11
$1x10^8\,kg$	17	13	28	23

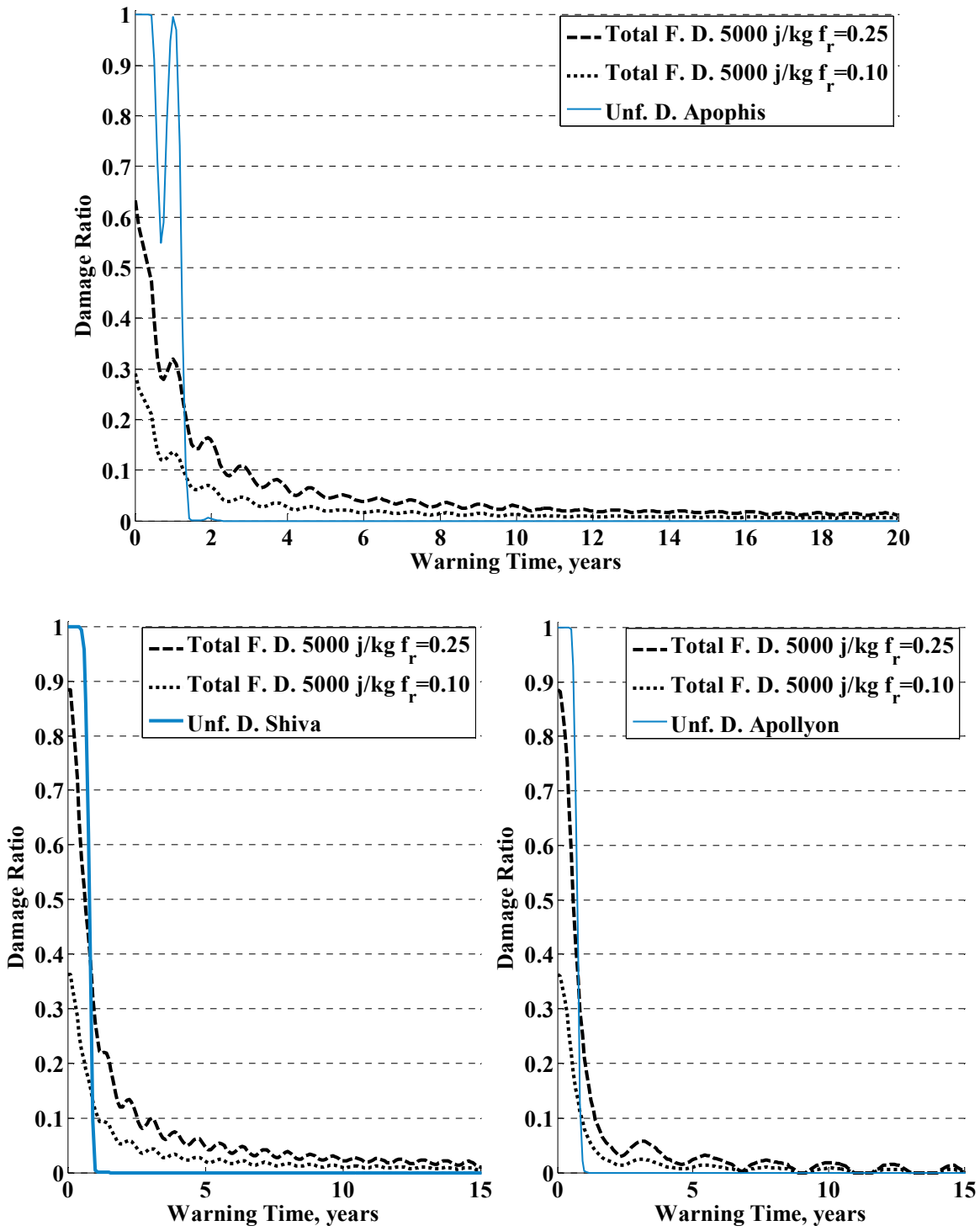

Fig. IV-25 Damage ratios of *Apophis*, *Shiva* and *Apollyon* for a 5000 J/kg break-up: fragmented cases (black lines) and unshattered cases (blue lines) with a tree sigma equal to 50% in the delta-velocity.

IV.6. Chapter Summary

The work described in this chapter examined the risk of fragmentation that impulsive asteroid deflection missions, such as the kinetic impactor or the nuclear interceptor, can cause when attempting to deflect an asteroid in a single impulsive manoeuvre. The levels of collisional energy required to break-up an asteroid were first estimated and, then, a fragmentation and dispersion model was introduced. The model was then used to analyse the evolution of fragments for up to 20 years after the break-up of the asteroid. Using the Earth impact probability of five different fragment sizes together with the approximate area that could be destroyed by each one fragments analysed, the consequences of a fragmentation were estimated for several illustrative examples.

The energies required for a single impulsive deflection manoeuvre, i.e., those of a kinetic impactor (Fig. IV-4) or a nuclear interceptor (Fig. IV-5), are dangerously close to the energies required to catastrophically disrupt an asteroid (Fig. IV-2). Even for relatively large warning times, more than 10 years prior to the collision, the risk of fragmentation seems still considerable. We should also bear in mind that even if, instead of a single manoeuvre, several smaller impulses are given to the asteroid, in order to avoid surpassing the catastrophic fragmentation level, the material strength of the asteroid will decrease at each small impact, and the risk of fragmentation will not disappear, even if it may be reduced.

If an undesired fragmentation of the threatening object occurs, it may result in a substantial increase of risk to Earth. Considering that an undesired fragmentation may occur when applying collisional energies ranging from 100 J/kg to 1000 J/kg, we can distinguish three different trends in Fig. IV-21, Fig. IV-22, Fig. IV-23 and Fig. IV-24. Initially, the potential damage caused by the fragmented asteroids is lower than the unshattered object. This occurs not because some fragments miss the Earth, but as a result of the fragments that are two small to yield any noticeable damage at the surface of the Earth. Clearly, the maximum fragmented damage is strongly related with the fragmentation ratio f_r resultant from a particular break-up. Secondly, we observe that at the moment when the unfragmented scenario begins to transit from a potential damage ratio of 1 to 0, i.e., time at which the deflection mission was intending to fulfil the deflection requirements, all the fragmented scenarios still retain a potential damage ratio that is considerably high, going approximately from 0.5 to 0.15, depending on fragmentation ratio and exact warning time. We can therefore conclude that an undesired fragmentation outcome would represent

a failure on the deflection mission, where, if no further deflection attempt is performed, the potential damage to Earth would remain still considerably high at the predicted collision time. Finally, for very long warning times, the fragments disperse enough so that the damage becomes negligible. The time required to reach this point depends on the collisional energy used in the deflection attempt, although for energies between 100 J/kg to 1000 J/kg the required warning time to reach negligible damage is longer than 20 years.

Applying collisional energies much higher than 1000 J/kg will result on highly catastrophic fragmentation. This kind of fragmentation may be used to fragment and disperse an asteroid to such a level that the potential damage becomes almost negligible (Fig. IV-25). This may be achieved for long warning times (>10 years), although serious questions should be arisen about the optimality of such an option if enough warning time is available that both kinetic impulses lower than the fragmentation limit and low thrust deflection techniques are also efficient options.

Chapter V

Conclusions

This thesis is the culmination of a three-year research study on the deflection of asteroids. Specifically, the research was conducted on asteroid deflection techniques, analysis of possible mission scenarios and asteroid fragmentation and its consequences. The author hopes that the results presented in the previous chapters will contribute to the understanding of the problem and help to identify possible solutions. The following sections summarize the main research outcomes and proposed further lines of work.

V.1. Summary of the Research Results

Chapter I set the boundaries of the problem at hand. We saw that most of the future impact risk may come from small asteroids, having less than a few hundred meters in diameter. We presented three asteroidal test cases; *Apophis*, *Shiva* and *Apollyon*, whose orbital characteristics are the result of statistical analysis of currently surveyed population, and together with a varying asteroidal mass of four orders of magnitude, presents a meaningful set of realistic scenarios encompassing not only asteroid size, thus impact frequency, but also orbital characteristics. We also analysed the magnitude of the minimum deflection required to deviate an object from an Earth-impact trajectory, and saw that we need to take into account not only the physical volume of the Earth, but also the gravitational focusing of our planet.

Chapter II presented six different methods that could be use to change the collisional course of a threatening object, two impulsive strategies, i.e., nuclear interceptor and kinetic impactor, one multi-impulsive, mass driver, and three low acceleration methods, i.e., low thrust propulsion, solar collector and gravity tug.

Without considering political and security issues related to the use of nuclear devices, the nuclear stand off explosion proved to have very good deflection capabilities. The reliability of the stand off configuration to uncertainties, on both asteroid characteristics such as composition and shape, and nuclear device performances, was also analysed (see

appendices for the latter). The optimal detonation distance was also investigated and found to be dependant on the yield of the nuclear device and density and size of the asteroid.

The velocity at impact was shown to be a paramount feature for the efficiency of the kinetic impactor. If impact speeds of around 50 km/s are attained, asteroids up to few hundred meters in diameter can be successfully deflected by impactors smaller than 3,000 kg. This kind of hypervelocity impact could be achieved through retrograde orbits.

With the analysis of spacecraft propulsion model (also referred as low thrust method), we saw that it is not necessary to modify the asteroid rotational state in order to deflect it and that, despite the obliquity of the asteroid, using a multi-engine approach is possible to achieve at least 30% efficiency on the push without having to perform very complex operations to de-spin or precess the asteroid. We also saw that limiting the thrusting operations to the first half of the total available pushing time could achieve better deflections than thrusting all the available time. Finally, we showed that the spacecraft propulsion/low thrust approach can deviate asteroids below 150 meters in diameter with only a few thousand kilograms of dry mass plus propellant for deflection operations. Asteroids below 150 meters diameter have an accumulative impact probability of 0.3% in the next 20 years.

The mass driver concept was also showed to be a successfully performing deflection technique. This concept was capable of deflecting all the asteroidal test cases with less than 10,000 kg of dry mass. Clearly, the efficiency of this method is the result of using in-situ material to provide a change in the linear momentum of the asteroid, although the technology requirements for this kind of deflection method is surely much more demanding than for other techniques, with the exception perhaps of the solar collector.

Among all the techniques analysed, the solar collector is the deflection concept that is the most affected by the orbital characteristics of the targeted asteroid. The concentration ratio of the collector implies a distance threshold from the Sun at which the solar collector does not focus enough energy to sublimate surface material, and is therefore not able to produce thrust. The concentration ratio used throughout the thesis was 2500, which corresponds to a threshold of approximately 2.5 AU (there are other factors that contribute to this distance, such as the rotational state of the asteroid). Despite this, solar collectors of less than 20 meters diameter could successfully deflect the three virtual asteroids at the upper end of the warning time (~ 20 years), with dry masses not higher than 1000 kg.

Finally, the gravity tug also showed a certain capability to deflect small asteroids, although somewhat smaller than the rest. It may be surmised however that a technology like the gravity tug could be easily used to deflect asteroids from passing through impact keyholes (see resonant returns, Section I.3.2). The gravity tug also showed better performance than the low thrust for deflection manoeuvres longer than 135 years, although this duration of the pushing manoeuvre is unrealistically long for both options.

In Chapter III, a comprehensive comparison among the different strategies was presented. The methodology used consisted in; firstly, computing thousands of preliminary mission designs for each combination of deflection method and asteroidal test case, which included transfer leg and deflection operations, and secondly, comparing all those solutions by means of deflection isolines and dominance tables. Solar collector and nuclear interceptor resulted to be the two most efficient methods. The solar collector concept showed better results for Aten-like asteroids, while the nuclear interceptor seems more efficient in Apollo asteroids. The modest kinetic impactor concept performs surprisingly well for all test cases studied, competing at the same level or above other more complex deflection methodologies such as low thrust propulsion technique or gravitational tug. It should be noted that the impact trajectories for this approach computed in Chapter III were the result of a Lambert's arc, and thus, the efficiency of the kinetic impact would therefore be increased by studying more complex trajectories. The technology level of each deflection strategy was also discussed in Chapter III and a further comparison was presented, which took into account the approximate time that a deflection technology would need before becoming usable. Following this additional constraint, the kinetic impactor performed very well, as should be expected since similar missions have already flown successfully. The solar mirror was shown to be a competitive technology despite being, together with the mass driver, the technique needing the most technological development. For cometary hazard, it was shown that, among the objects studied, Nearly-isotropic comets are the most difficult objects to deflect from an impacting trajectory. The reason of this difficulty is the intrinsic short warning time that a realistic impact scenario of this type of object would face, most likely in the order of only a few months.

In most of the work presented in this thesis, an asteroid is considered as a monolithic unbreakable object, Chapter IV however showed that the risk of triggering a catastrophic fragmentation while attempting a single-impulsive mitigation, such as nuclear interceptor or kinetic impactor, is indeed very high. Analysing both the statistical size distribution of fragments spawned by the impulsive mitigation and the dispersion of material based on an

original velocity dispersion model, also presented in Chapter IV, shows that a fragmentation outcome generally results in an increased threat for the Earth than its unfragmented counterpart. This increased potential damage is inherent to the uncertainty in the velocity magnitude and direction of the largest fragments of the break-up. For short warning times and high fragmentation levels, i.e., impact energies above the critical catastrophic fragmentation level, the fragmentation outcome obtained reduced potential damage. This is due to the fact that the higher the level of fragmentation is the larger the number of spawned fragments with size below the limit threshold at which a fragment is not able to penetrate deep enough in the atmosphere to pose any risk to the Earth surface will be. We also saw that for low critical specific energies the velocity dispersion of the different fragments is rather low, and as a consequence a substantial fraction of the asteroid mass would gravitationally re-accumulate into a new single object. This is an interesting result that indicates that at the level of energy that a rubble pile asteroid is thought to fragment, more than 90% of the mass will re-accumulate again, forming another rubble pile asteroid with almost the same mass. This is a very coherent result, which points out the consistency of the models developed to study the consequences of an asteroidal fragmentation.

V.1.1. Conclusions

In the light of current surveys on NEO population, we must avoid to use Apophis as the only yardstick with which to measure how good a given deflection method is. An Apophis-size impact is thought to occur every 25,000 years approximately and, in fact, the current impact probability of Apophis itself does not exceed this background impact probability. It is therefore much more plausible that the first ever deflection carried out by mankind will be on much smaller objects, for example, those having impact frequencies around 1,000 years, also known as Tunguska-class. It is also reasonable to think that the orbital characteristics of a future impact-threatening object will not differ by much from those analysed in this thesis.

Considering therefore objects below 150 meters diameter as possible threatening objects, many possible methods could become successful candidates for their deflection. Among them, the kinetic impactor is probably the most obvious choice since it does not require any further technological development and, as shown previously, objects of this size could be easily deflected with impactors equal in size to currently flying interplanetary spacecrafts (e.g. ESA's 1578-kg Rosetta spacecraft could successfully deflect a 75m-diam

Aten object using a simple prograde trajectory if at least 10 years warning time are available). Future technology trends and research interest could finally draw the decision makers towards one of the different technologies investigated. Considering objects with a few hundred meters diameter, only a limited number of technologies could be plausible candidates; nuclear interceptor, mass driver and solar collector. Although the solar collector and mass driver concepts present nowadays clear technology issues, these may change in future, since both technologies could become an interesting investment for future space utilization, such as space mining or solar energy enhancement. On the other hand, the use of nuclear warheads in space may pose serious political and moral issues and as many may agree, the proliferation of nuclear warheads in space could potentially pose a higher risk than the possible benefit. Finally, considering the impact threat posed by Nearly-isotropic comets, the most serious problem that we would face is its intrinsic short warning time, which makes even attempts with impulsive methods such as kinetic impactor and nuclear interceptor highly difficult challenges.

Another important issue that we discussed here is asteroid fragmentation due to impulsive deflections. Fragmentation may occur when attempting to deflect an asteroid, especially if the impulsive deflection is applied to an asteroid with less than 10 years warning time. If a fragmentation is the undesired outcome of a deflection attempt, the uncertainties of the resultant cloud of fragments will intrinsically pose a threat to Earth, only reducing by half the potential damage to Earth of the asteroid at the predicted impact time. As an alternative option, an asteroid could be highly disrupted and dispersed with the sole purpose of reducing the potential damage to Earth to negligible terms. Although this alternative could be used as a final backup option, serious doubts about the efficiency of the option should be raised. In order to make the total destruction of the asteroid viable enough warning time needs to be provided, and thus, the same threatening scenario could be resolved using low thrust deflections methods. On the other hand, further study should be provided to assess the threat that the fragments could cause in future Earth encounter.

V.2. Further Research

Several issues were identified as possible lines for continuity of the work presented along the thesis:

- We have considered the optimal deflection direction uniquely as the direction that maximizes the asteroid-Earth distance at a given time. Future work on

impact hazard mitigation should expand the study on the optimality of a deflection in order to account for the stability of the new deflected orbit, and ensure that near-term perturbations would not provide any further chances of Earth impact in the following decades or centuries. Also, the issue of the resonant return impact should be studied and optimal deviation strategies for resonant returns should also be assessed.

- Trajectory design was limited here to either a Lambert's arc impulsive trajectory or a direct low-thrust spiral. A straightforward improvement of the study developed here should include deep space manoeuvres in the calculation of the impulsive transfer legs. Further improvements could account for multiple fly-by trajectories, both using low thrust and chemical transfers.

- Several could be the working lines in order to further develop the analysis on the consequences of an asteroid fragmentation. Some examples are; assessing a qualitative probability of fragmentation for multi-impulsive manoeuvres, improving the gravitational interaction model between the different fragments and the link between this and the statistical description of the escaped fragments or adding other perturbative forces to the analysis, such as Yarkovsky effect or solar pressure.

Finally, many other related studies could follow the research developed in this thesis, some potential candidates are; solar collector sample return mission or asteroid capture trajectories. The solar collector is probably the most interesting deflection method among the studied techniques. Alternative space application of this technology could be investigated in order to prompt the technological development of this concept. For example, the feasibility of asteroidal sample return missions using ablation of material as collecting system could be investigated. Although this may now seem science fiction, shepherding the asteroidal and cometary population for several purposes such as avoiding any threat to Earth, taking advantage of its natural resources or simply building small space outpost on them may become an alternative in the years to come. In this context, planetary capture of asteroids should be investigated. Using low stability orbits this possibility may be exploited at a reasonably low energetic cost.

VI.

Appendices

A.1. Deflection Formulas

Throughout this thesis, the distance that a deflected asteroid achieves at the Earth encounter has been calculated either by simply referring to the proximal motion equations and Gauss' variational equations or by referring to the work of *Vasile* & *Colombo*[95]. This section will extend the explanation of the procedure used to calculate the deflection and, more importantly, the optimal direction of the deflection impulse. Some insight into the accuracy of the methodology will also be given.

A.1.1. Gauss' Variational Equations

Let us assume that a given deflection model provides the asteroid with a $\delta\mathbf{v}$ vector of impulsive change of velocities at a time t_0. Expressing this $\delta\mathbf{v}$ vector in a Cartesian rotating frame $\left\{\hat{i}_t \quad \hat{i}_n \quad \hat{i}_h\right\}$, where $\hat{i}_t$ is the direction along the orbit velocity vector, $\hat{i}_h$ is parallel to the orbital momentum vector, thus the out-of-plane direction, and $\hat{i}_n$ completes the right-hand coordinates system, we can express the variation of the orbital elements of the asteroid at the time t_0 (i.e., when the impulsive change occurs) with the following system of equations:

$$
\begin{aligned}
\delta a &= \frac{2a^2 v_0}{\mu}\delta v_t \\
\delta e &= \frac{1}{v_0}\left[2\left(e+\cos f_0\right)\delta v_t - \frac{r}{a}\sin f_0 \delta v_n\right] \\
\delta i &= \frac{r_0\cos\theta_0}{h}\delta v_h \\
\delta\Omega &= \frac{r_0\sin\theta_0}{h\sin i}\delta v_h \\
\delta\omega &= \frac{1}{ev_0}\left[2\sin f_0\delta v_t + \left(2e+\frac{r_0}{a}\cos f_0\right)\delta v_n\right] - \frac{r_0\sin\theta_0\cos i}{h\sin i}\delta v_h \\
\delta M &= -\frac{b}{eav_0}\left[2\left(1+\frac{e^2 r_0}{p}\right)\sin f_0\delta v_t + \frac{r_0}{a}\cos f_0\delta v_n\right]
\end{aligned}
\tag{6.1}
$$

where $\{a \;\; e \;\; i \;\; \Omega \;\; \omega \;\; M\}$ are the keplerian elements, v is the orbital velocity of the asteroid, μ is the gravitational constant, f is the true anomaly, r is the distance to the Sun or norm of the position, θ is the argument of latitude (i.e., $\omega + f$) and p is the semilatus rectum. All the parameters in Eq.(6.1) are obviously referred to the nominal unperturbed orbit of the asteroid at time t_0. Eq.(6.1) are known as Gauss' Variational equations.

If instead of an impulsive mitigation action, a continuous gentle push is provided by one of the low thrust models (i.e., low thrust propulsion, solar collector or gravity tug) the variational equations Eq.(6.1) will take the following form:

$$
\begin{aligned}
\frac{da}{dt} &= \frac{2a^2 v}{\mu}a_t \\
\frac{de}{dt} &= \frac{1}{v}\left[2\left(e+\cos f\right)a_t - \frac{r}{a}\sin f a_n\right] \\
\frac{di}{dt} &= \frac{r\cos\theta}{h}a_h \\
\frac{d\Omega}{dt} &= \frac{r\sin\theta}{h\sin i}a_h \\
\frac{d\omega}{dt} &= \frac{1}{ev}\left[2\sin f a_t + \left(2e+\frac{r}{a}\cos f\right)a_n\right] - \frac{r\sin\theta\cos i}{h\sin i}a_h \\
\frac{dM}{dt} &= n - \frac{b}{eav}\left[2\left(1+\frac{e^2 r}{p}\right)\sin f a_t + \frac{r}{a}\cos f a_n\right]
\end{aligned}
\tag{6.2}
$$

where n is the mean angular motion of the orbit, and integrating Eq.(6.2) the total variation of the keplerian elements will be obtained.

A.1.2. Proximal Motion Equations

A very convenient way of describing the *deflected* orbit of the asteroid is by using a relative orbit description. Assuming a two body problem with no disturbance, the six variations of the orbital elements $\{\delta a \quad \delta e \quad \delta i \quad \delta\Omega \quad \delta\omega \quad \delta M_{end}\}$, where δM_{end} indicates the variation in mean anomaly at a given time t_{end}, remain invariant with time, and thus, knowing the initial orbital elements and the variations of the perturbed orbit, the position of the perturbed asteroid can be computed at any time by solving Kepler's equation. Note that δM_{end} accounts for the change in mean anomaly with respect to the unperturbed orbit at the time t_0, thus time at which either the impulsive manoeuvre was applied or the low thrust acceleration began. δM_{end} is therefore expressed as:

$$\delta M_{end} = \delta M + \delta n\left(t_{end} - t_0\right) \text{ (Impulsive manoeuvre)} \tag{6.3}$$

$$\delta M_{end} = \left[n_f \left(t_{end} - t_f\right) + \Delta M_{t_f - t_0} \right] - n_0 \left(t_{end} - t_0\right) \text{ (Low thrust push)} \tag{6.4}$$

where, in Eq.(6.3), $\delta n = \sqrt{\mu/a^3} - \sqrt{\mu/\left(a+\delta a\right)^3}$ and, in Eq.(6.4), the subscript f refers to time when the low thrust pushing manoeuvre is stopped, and the asteroid is then coasting from t_{f} to t_{end}. This methodology is considered convenient simply because five of the six relative orbital elements are constant with time, unlike when using the relative Cartesian elements of the two orbits. This orbital description eases the interpretation of the shape of the relative orbits.

Since the change in the orbital elements $\{a \quad e \quad i \quad \Omega \quad \omega \quad M\}$ of the initial unperturbed orbit is small, we can express the position of the *deflected* asteroid relative to the *virtual* position of the unperturbed asteroid by using the linear mapping provided by proximal motion equations[96]:

$$\begin{aligned}
\delta s_r &\approx \frac{r}{a}\delta a + \frac{ae\sin f}{\eta}\delta M_{end} - a\cos f\,\delta e \\
\delta s_\theta &\approx \frac{r}{\eta^3}\left(1+e\cos f\right)^2 \delta M_{end} + r\delta\omega + \frac{r\sin f}{\eta^2}\left(2+e\cos f\right)\delta e + r\cos i\,\delta\Omega \\
\delta s_h &\approx r\left(\sin\theta\,\delta i - \cos\theta\sin i\,\delta\Omega\right)
\end{aligned} \tag{6.5}$$

where δs_r, δs_θ. and δs_h are the displacements in the Hill's reference frame, i.e., radial, transversal and perpendicular to the orbit plane directions respectively, and $\eta = \sqrt{1-e^2}$.

A.1.3. Accuracy of the Proximal Motion

The following five figures (Fig. A-1 to Fig. A-5) show the deflection error and relative error for *Shiva* and *Apollyon* cases and the relative error for the cometary example *Comet S-T*. The error was computed by comparing the resulting deflection triggered by a change of velocity $\begin{bmatrix}\delta v_t & 0 & 0\end{bmatrix}$ and computed using both the method described above (i.e., combining Gauss'equations and linearized proximal motion) and a propagation of the two orbits, the unperturbed and the perturbed by the change of velocity. In light of the results shown in the figures, the proximal motion and Gauss equation method provides a very efficient way to compute the deflection of an asteroid for all the range of delta-velocities and warning times that have been used throughout this thesis. On the other hand, as shown in Fig. A-5, when computing the deflection of bodies with orbital elements similar to those of comet S-T, the method should only be used for long warning times (> 6 years) and very low delta-velocities (<0.01 m/s).

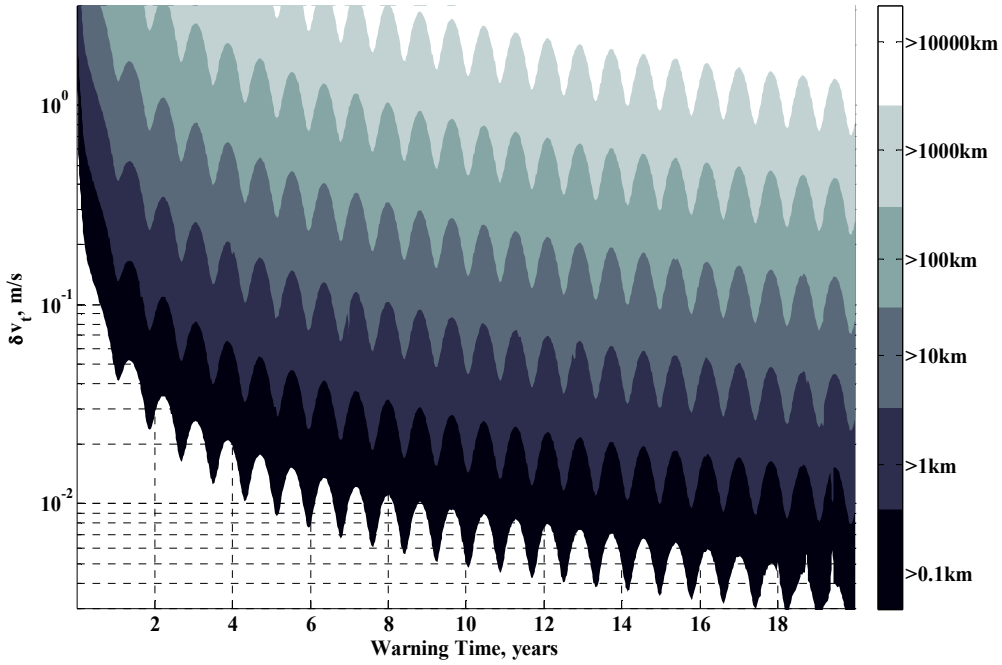

Fig. A-1 Deflection error as a function of Warning Time and δv_t applied to *Shiva*.

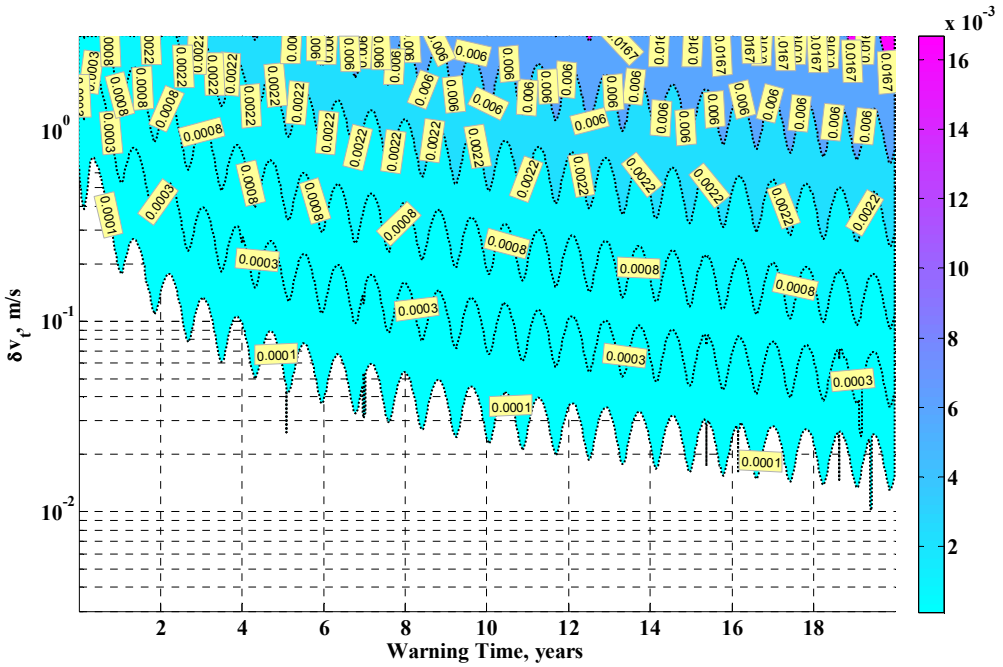

Fig. A-2 Deflection relative error as a function of Warning Time and δv_t applied to *Shiva*.

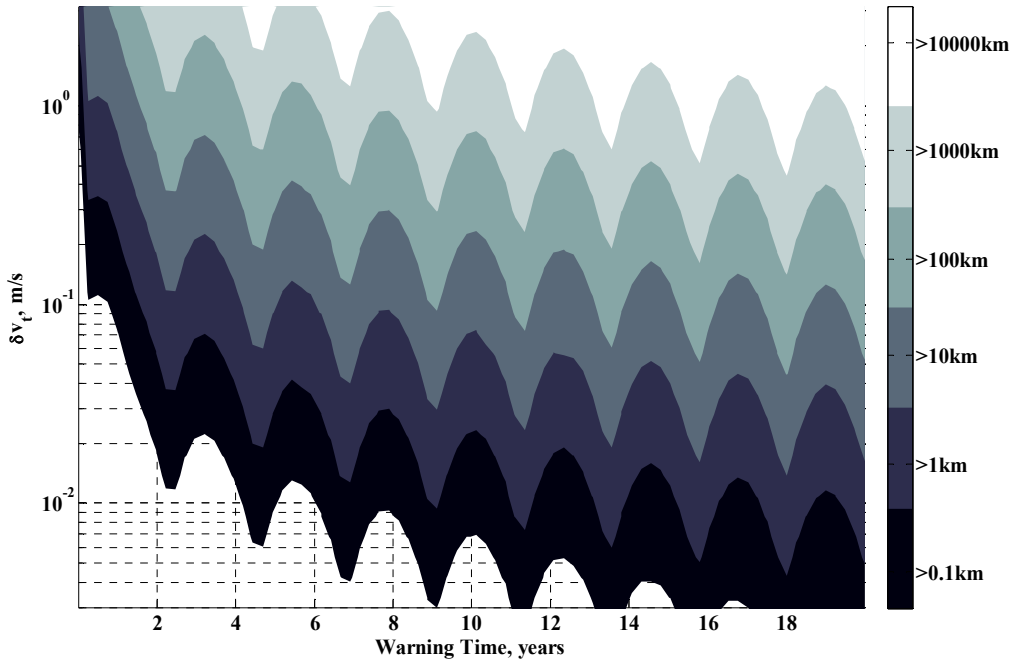

Fig. A-3 Deflection error as a function of Warning Time and δv_t applied to *Apollyon*.

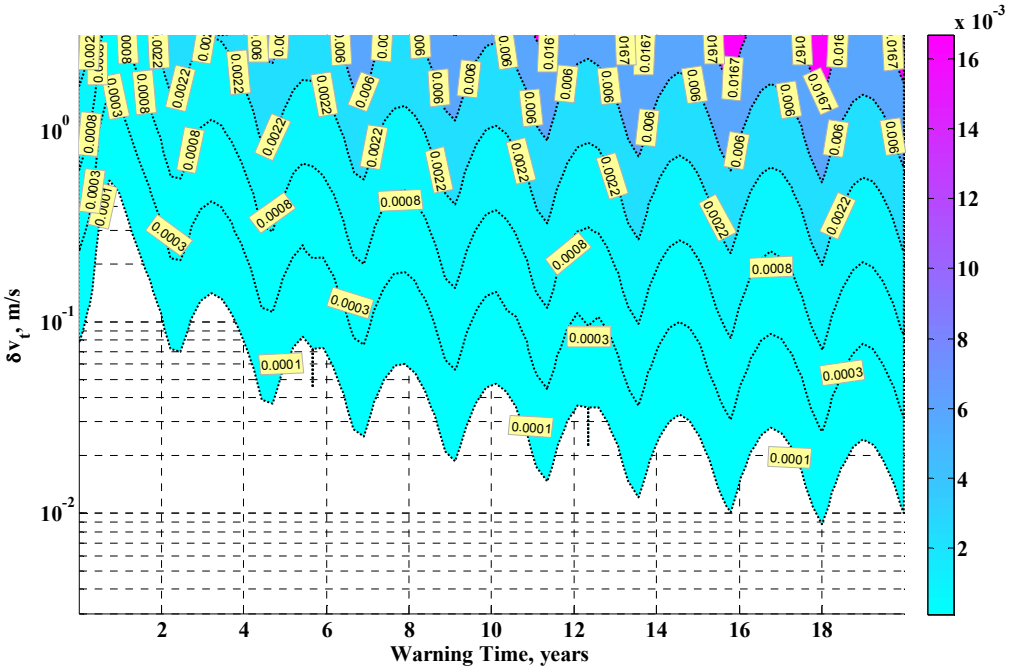

Fig. A-4 Deflection relative error as a function of Warning Time and δv_t applied to *Apollyon*.

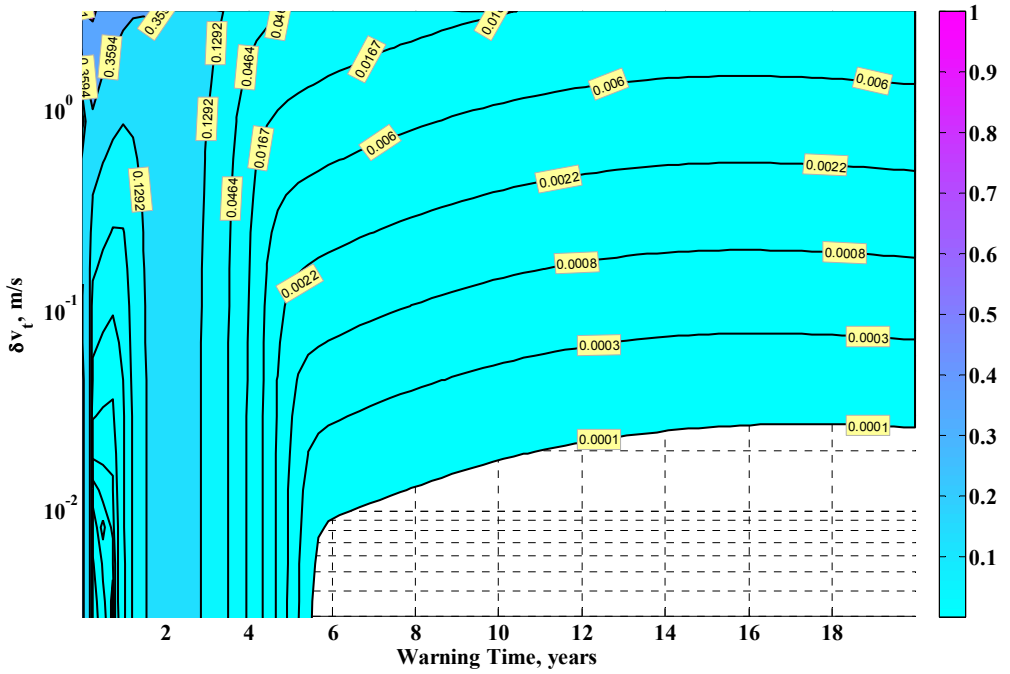

Fig. A-5 Deflection relative error as a function of Warning Time and δv_t applied to *Comet S-T*.

A.1.4. State Transition Matrix

Combining Eq.(6.1) and Eq.(6.5) it is possible to assemble a state transition matrix that provides us a direct mapping for a given time t between the initial $\delta\mathbf{v}$ and relative position vector $\delta\mathbf{r}$ of the new perturbed position with respect the "virtual" unperturbed position.

$$\delta\mathbf{r}(t) = \left[\frac{\partial\delta\mathbf{r}(t)}{\partial\delta\mathbf{v}(t_0)}\right]\delta\mathbf{v}(t_0) \tag{6.6}$$

The matrix $\left[\partial\delta\mathbf{r}(t)/\partial\delta\mathbf{v}(t_0)\right]$ is formed by two matrices, one containing the proximal motion equations (**A**) and a second containing the Gauss'equation (**G**).

$$\left[\frac{\partial\delta\mathbf{r}(t)}{\partial\delta\mathbf{v}(t_0)}\right] = \mathbf{A}^T\cdot\mathbf{G}_0$$

$$\mathbf{A}^T = \begin{bmatrix} \frac{r}{a} - \frac{3}{2}\frac{e\sin\theta}{\eta}\frac{\sqrt{\mu}}{a^{\frac{3}{2}}}\Delta t & -\frac{3}{2}\frac{r}{\eta^3}\left(1+e\cos\theta\right)^2\frac{\sqrt{\mu}}{a^{\frac{5}{2}}}\Delta t & 0 \\ -a\cos\theta & \frac{r\sin\theta}{\eta^2}\left(2+e\cos\theta\right) & 0 \\ 0 & 0 & r\sin\theta^* \\ 0 & r\cos i & -r\cos\theta^*\sin i \\ 0 & r & 0 \\ \frac{ae\sin\theta}{\eta} & \frac{r}{\eta^3}\left(1+e\cos\theta\right)^2 & 0 \end{bmatrix} \tag{6.7}$$

$$\mathbf{G}_0 = \begin{bmatrix} \frac{2a^2}{h}e\sin\theta_0 & \frac{2a^2}{h}\frac{p}{r_0} & 0 \\ \frac{p\sin\theta_0}{h} & \frac{\left(p+r_0\right)\cos\theta_0 + r_0 e}{h} & 0 \\ 0 & 0 & \frac{r_0\cos\theta_0}{h\sin i} \\ 0 & 0 & \frac{r_0\sin\theta_0^*}{h\sin i} \\ -\frac{p\cos\theta_0}{he} & \frac{\left(p+r_0\right)\sin\theta_0}{he} & -\frac{r_0\sin\theta_0^*\cos i}{h\sin i} \\ \frac{b}{ahe}\left(p\cos\theta_0 - 2r_0 e\right) & -\frac{b}{ahe}\left(p+r_0\right)\sin\theta_0 & 0 \end{bmatrix}$$

where the term $-\frac{3}{2}\left(\sqrt{\mu}\Big/a^{\frac{5}{2}}\right)\delta a$ in the first row of matrix $\mathbf{A}^T$ makes implicit the dependence on δa of δM_{end}.

A.1.5. Optimal Deflection Direction

Now that the transition matrix is defined, we can use Eq.(6.6) to study the optimal direction to deflect a threatening asteroid. As suggested by Conway[103], in order to maximize the vector $\delta\mathbf{r}(t)$ given an impulse $\delta\mathbf{v}(t_0)$, the associated quadratic form $\left[\partial\delta\mathbf{r}(t)/\partial\delta\mathbf{v}(t_0)\right]^{\mathrm{T}}\left[\partial\delta\mathbf{r}(t)/\partial\delta\mathbf{v}(t_0)\right]$ has to be maximized by choosing an impulse vector $\delta\mathbf{v}(t_0)$ parallel to the eigenvector $\mathbf{v}$ associated to the maximum eigenvalue of $\left[\partial\delta\mathbf{r}(t)/\partial\delta\mathbf{v}(t_0)\right]^{\mathrm{T}}\left[\partial\delta\mathbf{r}(t)/\partial\delta\mathbf{v}(t_0)\right]$. Fig. A-6 shows the deflection achieved as a function of warning time for an impulsive deflection of *Shiva*. Four different directions of impulse are applied; one along each direction of the *t-n-h* Cartesian reference and one along the optimal direction as proposed by Conway's approach. Fig. A-6 shows how, in general, the optimal deflection direction matches perfectly that of the tangential direction. Only for very short warning times (less than half a year) the optimal direction is achieved through a combination of the three *t-n-h* Cartesian directions.

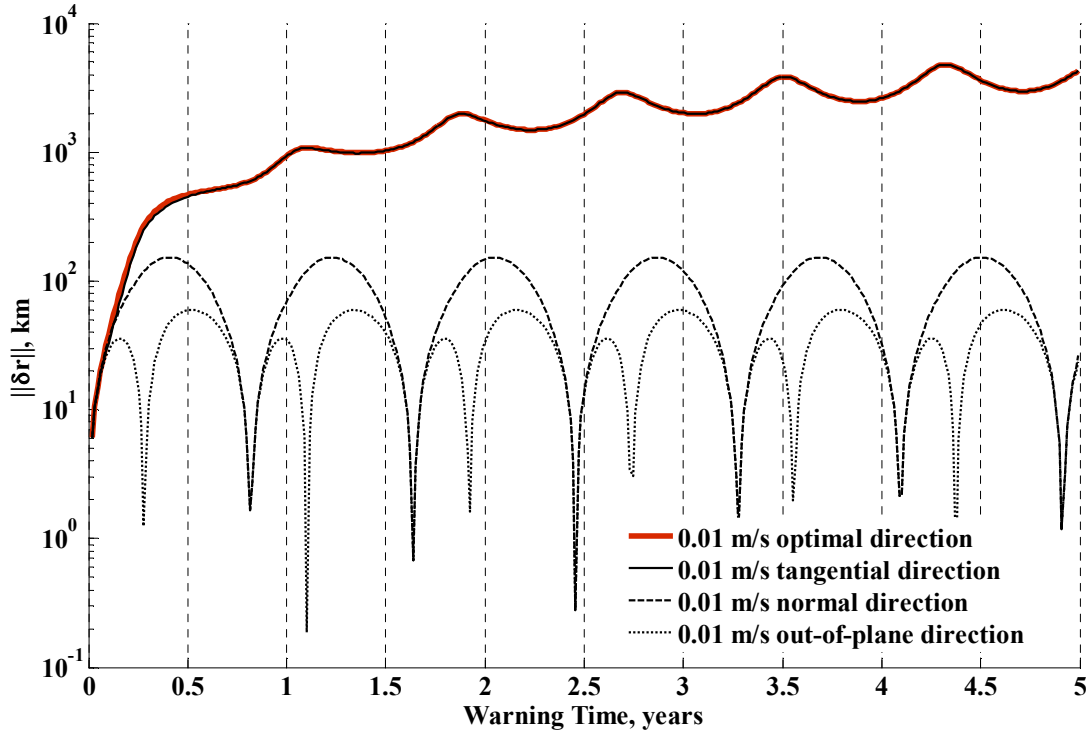

Fig. A-6 Deviation achieved on *Shiva* with $||\delta v||$=0.01 m/s.

A.2. Nuclear Interceptor Appendices

A.2.1. Further Derivations

The inclusion of the elevation angle ε in the Eq.(2.13) is critical, since without it the mass ablated would have been substantially overestimated. The integration, Eq.(2.13), echoes the calculation of the volume of a parallelipede, thus, as seen in Fig. A-7, area of the base *dA* multiplied by height *Z*.

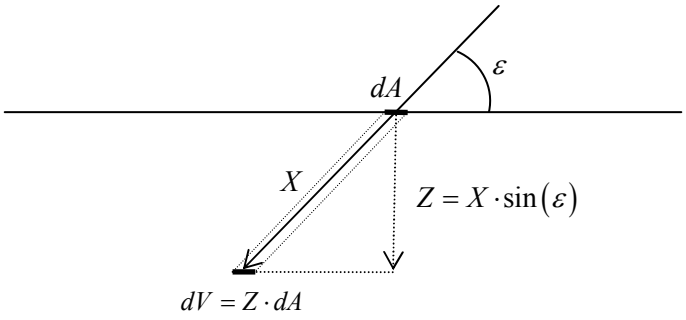

Fig. A-7 Schematic of the geometry behind the integration in Eq.(2.13) .

The integration of Eq.(2.13) was solved analytically, shortening the computation of the model. This is an important issue when the model needs to be calculated several hundred thousand times, as was the case during the multi-criteria optimization. What follows is the analytical solution of Eq. (2.13):

$$P_A = \int_0^{Z_{\max}\cdot\sin\varepsilon} \rho_a \sqrt{2\left(\mu_o E_A(0) e^{-\rho_a \mu_0 \frac{z}{\sin\varepsilon}} - E_v\right)}\, dz \tag{6.8}$$

Eq.(6.8) can be rewritten in a more practical manner by collecting constant parameters:

$$P_A = \sqrt{2}\cdot\rho_a \int_0^{Z_{\max}\cdot\sin(\varepsilon)} \left(ae^{-Cz} - b\right)^{1/2} dz \tag{6.9}$$

$$\text{with } a = \mu_{en}\frac{f_{radiation}\cdot E_t}{4\pi\left[h(\lambda)\right]^2}; b = E_v; C = \frac{\rho_a \mu_o}{\sin(\varepsilon)}$$

The following change of variable eases the integration of Eq.(6.9):

$$e^{-Cz} = x \rightarrow -Ce^{-Cz}dz = dx \rightarrow -Cxdz = dx \rightarrow dz = -\frac{dx}{Cx} \tag{6.10}$$

and so Eq.(6.9) becomes:

$$P_A = \frac{-\sqrt{2}\cdot\rho_a}{C}\int_{e^{-C0}}^{e^{-CZ_{\max}\cdot\sin(\varepsilon)}} \frac{(ax-b)^{1/2}}{x}dx\,, \tag{6.11}$$

$$\text{with } a=\mu_{en}\frac{f_{radiation}\cdot E_t}{4\pi\left[h(\lambda)\right]^2}; b=E_v; C=\frac{\rho_a\mu_o}{\sin(\varepsilon)}.$$

after substituting the change of variables of Eq.(6.10) into Eq.(6.9). The integration in Eq.(6.11) can be more readily solved using the following expression:

$$\begin{aligned}\int\frac{\sqrt{ax+b}}{x}dx &= 2\sqrt{ax+b}+b\cdot\int\frac{dx}{x\sqrt{ax+b}}\\ \int\frac{dx}{x\sqrt{ax+b}} &= \frac{2}{\sqrt{-b}}\tan^{-1}\left(\sqrt{\frac{ax+b}{-b}}\right)\end{aligned} \tag{6.12}$$

The solution of which can be found in mathematical tables[104]. The final analytical expression yields:

$$P_A = \frac{-\sqrt{8}\cdot\rho_a}{C}\left[\sqrt{ae^{-CZ_{\max}\cdot\sin(\varepsilon)}-b}-\sqrt{b}\cdot\tan^{-1}\left(\sqrt{\frac{ae^{-CZ_{\max}\cdot\sin(\varepsilon)}-b}{b}}\right)-\sqrt{a-b}+\sqrt{b}\cdot\tan\left(\sqrt{\frac{a-b}{b}}\right)\right] \tag{6.13}$$

$$\text{with } a=\mu_{en}\frac{f_{radiation}\cdot E_t}{4\pi\left[h(\lambda)\right]^2}; b=E_v; C=\frac{\rho_a\mu_o}{\sin(\varepsilon)}$$

Expression Eq.(6.13) can be now integrated over the entire radiated surface using the equation of the surface of a spherical cap $S=2\pi R_a b$ (see Fig. II-2). Thus the differential of surface area becomes $dS=2\pi R_a^2\cdot\sin(\lambda)d\lambda$, allowing the integration of the linear momentum per unit area P_A only integrating over the asteroid central angle λ.

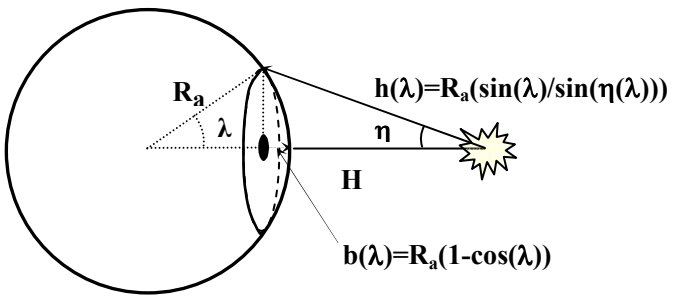

Fig. A-8 Surface integration using the spherical cap surface $S_{cap} = 2\pi R_a b$. This reduces the surface integration to a one variable integration.

The final expression takes the following form:

$$P = \sqrt{8}\pi R_a^2 \rho_a \int_0^{\lambda_{\max}} (\Pi)\sin\lambda d\lambda$$

$$\Pi = \left(\frac{-2}{C} \left[\sqrt{ae^{-CZ_{\max}\cdot\sin(\varepsilon(\lambda))} - b} - \sqrt{b}\cdot\tan^{-1}\left(\sqrt{\frac{ae^{-CZ_{\max}\cdot\sin(\varepsilon(\lambda))} - b}{b}} \right) - \sqrt{a-b} + \sqrt{b}\cdot\tan\left(\sqrt{\frac{a-b}{b}} \right) \right] \right)$$

$$a = \mu_{en} \frac{f_{radiation}\cdot E_t}{4\pi\left[h(\lambda)\right]^2}$$

$$b = E_v$$

$$c = \frac{\rho_a \mu_o}{\sin(\varepsilon(\lambda))}$$

$$h = R_a \cdot \left(\frac{\sin(\lambda)}{\sin(\eta)} \right)$$

$$\eta = \tan^{-1}\left(\frac{\sin(\rho)\sin(\lambda)}{1-\sin(\rho)\cos(\lambda)} \right)$$

$$\rho = \sin^{-1}\left(\frac{R_a}{R_a + H} \right)$$

$$\varepsilon = 90^o - \eta - \lambda \qquad (6.14)$$

Eq.(6.14) was implemented in Matlab in order to be solved numerically.

A.2.2. Model Uncertainties in Composition and Radiative Energy

As expressed in Section II.1.2, the main sources of uncertainty in the model are both the opacity μ_o and the absorption μ_{en}. The values of these two constants depend on the radiation type, the wavelength or energy and the composition of the asteroid surface. Table A-1 summarises the main sources of error for opacity μ_o and absorption μ_{en} and the approximate influence in percentage on the nominal value used in Table A-1. Fig. A-9 shows a comparison between the change of velocity computed by the model using nominal values for opacity μ_o and absorption μ_{en} or using one of the two uncertainty types; maximum variation by error in the radiation wavelength or maximum variation by error in asteroid composition. The example shown is based on a 600-kg fusion device and detonating it at a varying altitudes.

Table A-1 Approximate maximum error committed by the assumptions in composition and radiation wavelength.

Radiation Type	Uncertainty type	Approximate variation	Notes
Neutron Radiation	Wavelength	0.2%	In a fission reaction, neutron radiation of 14 Mev is 100 times more frequent than any other[54].
Neutron Radiation	Composition	25%	Considering composition of enstatite chondrites instead of forsterite[45] .
X-Ray	Wavelength	100%	X-ray radiation at 100 Kev instead of radiation at 10Kev, which would be equivalent to black body radiation from a source at 10^8K instead of 10^7K.
X-Ray	Composition	400%	Considering an enstatite chondrite without volatile materials.
Gamma-Ray	Wavelength	50%	Considering one order of magnitude switch in the wavelength
Gamma-Ray	Composition	15%	Considering an enstatite chondrite without volatile materials.

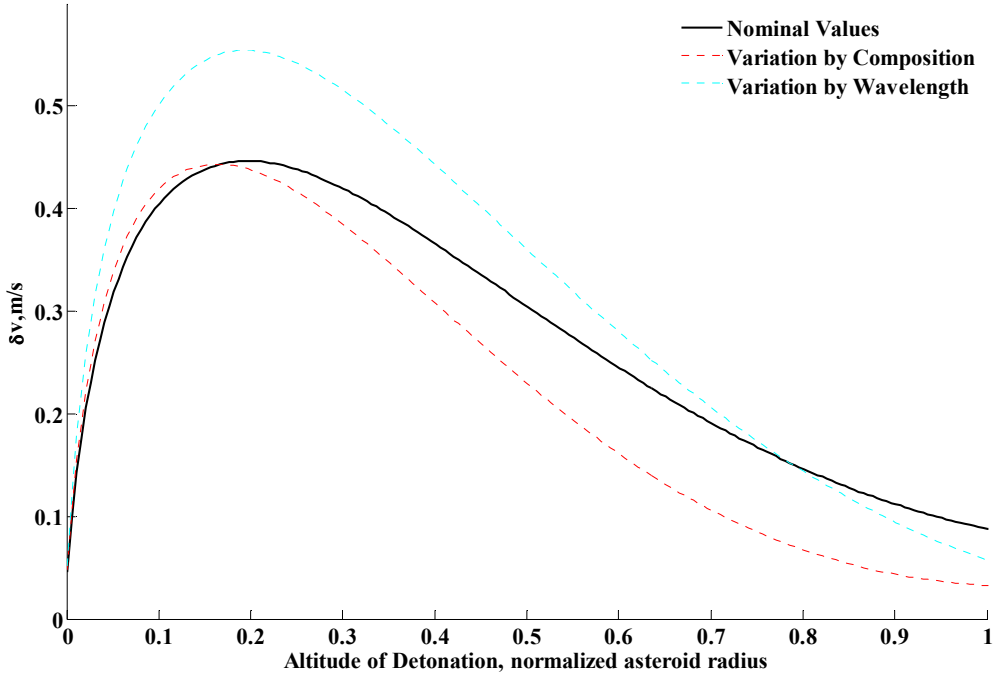

Fig. A-9 Total achieved change of velocity of asteroid Apophis; with the nominal values of opacity and absorption (black solid line), with the maximum change by variation of composition (red dotted line) and with the maximum variation on radiation wavelength (blue dotted line).

A.2.3. Model Uncertainties with Asteroid Shape

As a final consideration on the nuclear interceptor model elaborated in this thesis, it should be remembered that the total momentum change is dependent on both the area radiated by the nuclear device and the elevation angle. The radiated area and the elevation angles are also dependent on the shape of the asteroid and the model assumed spherical shape. If the asteroid is not spherical but is an elongated body with the same mass, the worst case scenario would be when the explosion occurs over the side of the asteroid with the smallest cross section area. In order to evaluate the loss of efficiency in the worst case scenario, the ratio between the total Δv for an elongated asteroid and the total Δv for a spherical asteroid with equal mass was computed. Fig. A-10 shows the Δv-ratio as a function of the elongation. Considering the typical measured elongation of known asteroids the maximum expected value is 2.5 for asteroid Geographos[14], which corresponds only to an 18% reduction in the performance of the nuclear interceptor.

[14]http://echo.jpl.nasa.gov/~lance/nea_elongations.html

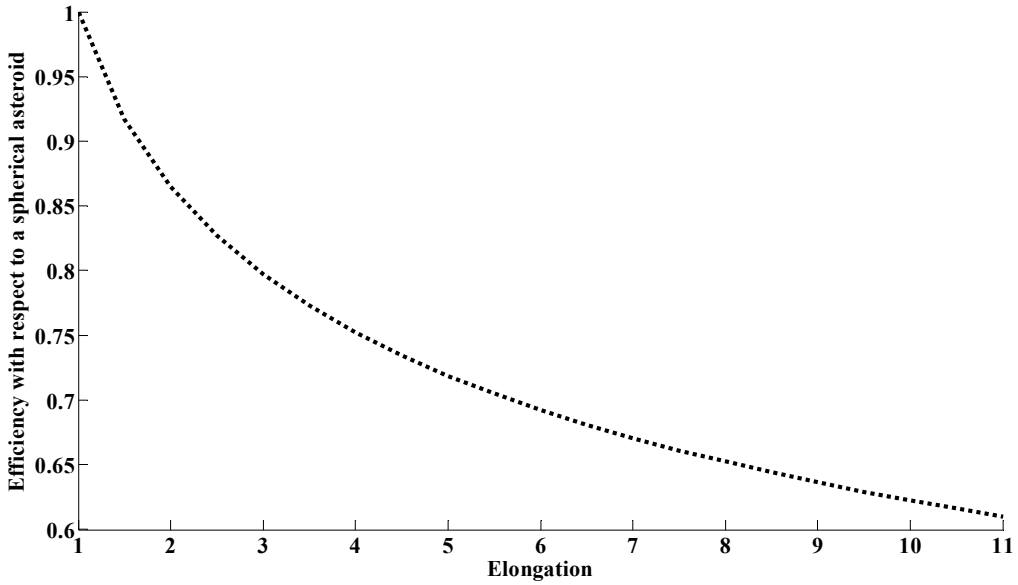

Fig. A-10 Efficiency of the nuclear deflection for an elongated body. Nuclear detonation occurs over the side with the minimum cross-sectional area.

A.3. Solar Collector Appendices

A.3.1. Expelled Mass Integration

The mass flow rate of the system described in Section II.5.3 is:

$$\frac{dm_{exp}}{dt} = \frac{1}{E_v}\left(P_{solar} - Q_{rad} - Q_{cond}\right) \tag{6.15}$$

where $dm_{\exp}/dt$ is the mass flow per unit area, E_v is the enthalpy of sublimation, which is 5.03 kJ/g (Wang[49]) considering forsterite (i.e. Mg_2SiO_4) as the main component of the asteroids, P_{solar} is the power density at the illuminated spot on the surface of the asteroid and, finally, Q_{rad} and Q_{cond} are the radiation and conduction loss respectively.

Eq.(6.15) needs to be integrated over the entire illuminated surface in order to obtain the total mass flow out-coming from the asteroid:

$$(\dot{m}_{exp})_{total} = \int_{x_{in}}^{x_{out}} \int_{y_{\min}}^{y_{\max}} \frac{dm_{exp}}{dt} \cdot dx \cdot dy \tag{6.16}$$

The axis $\hat{x}$ and $\hat{y}$ are, respectively, perpendicular and parallel to the rotational axis of the asteroid, so that the axis $\hat{x}$ is along the direction of the movement of the surface under the illuminated spot. This definition allows us to relate the horizontal surface position x and the illumination (or exposure) time through the rotational velocity, v_{rot}, such that $x = v_{rot} \cdot t$

and thus $dx = v_{rot} \cdot dt$. Therefore, the integral in Eq.(6.16) can be rewritten in terms of the exposure time *t* (as described in Eq.(2.36) in Chapter II):

$$(\dot{m}_{exp})_{total} = 2v_{rot} \int_0^{y_{max}} \int_{t_{in}}^{t_{out}} \frac{1}{E_v}\left(P_{in} - Q_{rad} - Q_{cond}\right) dt\, dy \tag{6.17}$$

where the limits of the integration t_{in} and t_{out} are the times at which the asteroid surface moves inside and outside the illuminated spot respectively and the integration from y_{min} to y_{max} is symmetric and goes from the centre of the illuminated spot to distance y_{max} from the centre such that $v_{rot} t_{in} = \sqrt{D^2 - 4y_{max}}$, thus assuring that there is sublimation.

The integral in Eq.(6.17) can be rewritten now as:

$$(\dot{m}_{exp})_{total} = 2v_{rot} \int_0^{y_{max}} \int_{t_{in}}^{t_{out}} \left(A - B\sqrt{\frac{1}{t}}\right) dt\, dy \tag{6.18}$$

where $A \equiv \frac{1}{E_v}\left(P_{solar} - Q_{rad}\right)$ and $B \equiv \frac{T_{subl} - T_0}{E_v}\sqrt{\frac{c\kappa\rho_a}{\pi}}$. If *t* is defined as 0 when the rotating asteroid surface moves inside the illuminated spot, then t_{in} is the time at which the sublimation starts, being equal to $t_{in} = \left(B/A\right)^2$, so that $P_{in} - Q_{rad} - Q_{cond} = 0$, and t_{out} is the time at which the surface moves out of the illuminated spot, which for a surface moving at a velocity v_{rot} , is $\sqrt{D^2 - 4y^2}/v_{rot}$.

The integration of the exposure time yields:

$$(\dot{m}_{exp})_{total} = 2v_{rot} \int_0^{y_{max}} \left(A \cdot \left(\frac{\sqrt{D^2 - 4y^2}}{v_{rot}} - t_{in} \right) - 2B \cdot \left(\frac{\left(D^2 - 4y^2\right)^{1/4}}{\sqrt{v_{rot}}} - \sqrt{t_{in}} \right) \right) \cdot dy \tag{6.19}$$

Eq.(6.19) is split in four different smaller integrals, some of which can be readily solved as follow:

$$\begin{aligned}
(\dot{m}_{exp})_{total} &= A_{\dot{m}_{exp}} + B_{\dot{m}_{exp}} + C_{\dot{m}_{exp}} + D_{\dot{m}_{exp}} \\
A_{\dot{m}_{exp}} &= 2A \int_0^{y_{max}} \sqrt{D^2 - 4y^2} \cdot dy \\
B_{\dot{m}_{exp}} &= 2v_{rot} A \int_0^{y_{max}} t_{in} \cdot dy = -2v_{rot} A y_{max} \\
C_{\dot{m}_{exp}} &= -4B\sqrt{v_{rot}} \int_0^{y_{max}} \left(D^2 - 4y^2\right)^{1/4} dy \\
D_{\dot{m}_{exp}} &= 4Bv_{rot}\sqrt{t_{in}}\, y_{max}
\end{aligned} \tag{6.20}$$

Finally, in the integrations $A_{\dot{m}_{exp}}$ and $C_{\dot{m}_{exp}}$, $2y$ can be substituted by $D\cos\theta$, becoming:

$$A_{\dot{m}_{exp}} = -AD^2 \int_{\pi/2}^{\arccos(2y_{\max}/D)} \sin^2\theta d\theta = \frac{AD^2}{2}\left[\frac{1}{2}\sin(2\theta_{\max}) - \theta_{\max} + \pi\right]$$
$$C_{\dot{m}_{exp}} = 2B\sqrt{v_{rot}D^3} \int_{\pi/2}^{\arccos(2y_{\max}/D)} \sqrt{\sin^3\theta}\, d\theta \tag{6.21}$$

The integration $C_{\dot{m}_{exp}}$ can be solved analytically using elliptic integrals or numerically.

A.4. Appendices on the Consequences of Asteroid Fragmentation

A.4.1. Expelled Mass Integration

Davis & Ryan[94] provided the data of a set of 30 experiments on the fragmentation of cement mortar targets that can be used to test the velocity dispersion model and the validity of some of the assumptions described along Section IV.3. Table A-2 shows some valuable data of those 30 experiments, while for the complete a description of each experiment refer to *Davis & Ryan*[94] using the shot number found in the table.

Table A-2 30 experiments from *Davis & Ryan*[94].

Shot number	Target mass [g]	Projectile mass [g]	Impact Speed [m/s]	Fragmentation Ratio f_r	SKE [J/kg]
820302	1346	1.05	1330	0.4	689.95
820303	1385	1.05	1770	0.056	1187.56
820304	1354	0.38	1990	0.6	555.70
820306	1318	0.38	2240	0.25	723.33
820308	1279	0.29	1960	0.78	435.52
850841	1085	0.29	1010	0.32	136.33
850842	1116	0.29	1600	0.31	332.62
850843	1085	0.29	750	0.33	75.17
850844	1056	0.29	2250	0.33	695.13
850845	1333	8.1	180	0.91	98.44
850846	1375	66.65	130	0.48	409.59
850847	1354	66.65	90	0.46	199.36
850850	1393	66.65	50	0.52	59.81
851204	1375	0.29	2190	0.42	505.77
851205	1382	0.29	1750	0.79	321.32
851206	1347	0.29	1340	0.98	193.29
851207	1304	0.29	1470	0.97	240.28
851208	1322	0.29	1580	0.68	273.81
851209	1269	0.29	950	0.99	103.12
851213	1407	8.1	290	0.96	242.08
851214	1336	28.2	250	0.54	659.62
851215	1107	0.29	440	0.96	25.36
860414	1318	0.38	1510	0.972	328.69
860415	1370	0.38	1690	0.928	396.10
860416	1323	0.38	1690	0.963	410.17
860417	1325	0.38	2150	0.826	662.85
860418	1313	0.38	2070	0.86	620.05

860419	1316	0.38	2230	0.84	717.97
860420	1326	0.38	2040	0.492	596.31
860503	1317	0.38	3140	0.111	1422.42

Having assumed, in Chapter IV, a relation such as:

$$\frac{1}{2}m\Delta V^2 = cte\,, \tag{6.22}$$

for all fragments oncoming from the same break-up, we can define the constant value of Eq.(6.22) as:

$$\frac{1}{2}m_i\Delta V_i^2 = \frac{1}{2}M_a\Delta V_a{}^2\,. \tag{6.23}$$

Recalling now the definition of standard deviation, $\sigma = \sqrt{\langle \mathbf{\Delta v}^2 \rangle - \langle \mathbf{\Delta v} \rangle^2}$, and considering $\langle \mathbf{\Delta v} \rangle$ equal zero since we assume homogeneous spherical dispersion from the centre of mass of the system or cloud of fragments, we can rewrite Eq.(6.23) as:

$$\frac{1}{2}m_i\sigma_i^2 = \frac{1}{2}M_a\sigma_0{}^2\,, \tag{6.24}$$

which leads us back to the Eq.(4.37) from Chapter IV, where σ_0 is defined as :

$$\sigma_0 = \frac{\Delta V_a}{k}\,, \tag{6.25}$$

where *k* is a constant that, as discussed in Chapter IV, will be 1 only if there is a perfect spreading and sharing of collisional energy and no loss through processes such as melting or breaking. We will use the data from the 30 experiments of *Davis & Ryan*[94] to assess an approximate value for *k*. Table A-3 shows *Davis & Ryan*'s fragment speed measurements for the 30 experiments in Table A-2. From Table A-3, columns 1,2, 3 and 5 are data provided in *Davis & Ryan*[94], while columns 4,6,7 and 8 were worked out to test the validity of the model. Column 8 shows the constant *k* that provides a perfect match between our model and mean velocity of fragments measured in the experiments.

Table A-3 30 experiments from *Davis & Ryan*[94]. Column 2 is the number of ejecta fragments which the experiment successfully measured its 2D velocity. Column 3 is the percentage of ejecta encompassed by the fragments recovered, note that this is only the ejecta percentage, which corresponds to the mass remaining after subtracting the mass of the largest fragments. Column 4 is the average mass of each one of the fragments, thus is an arithmetic average of the ejecta mass recovered divided by the number of fragments. Column 5 is the average speed of the fragments provided by *Davis & Ryan*[94].

Column 6 is the predicted ΔV_a of the target + projectile. Column 7 is the dispersion of velocity calculated with Eq.(4.35) of chapter IV of the fragments with the mass correspondent to the mass in column 4, note that this considering an *k* in Eq.(6.25) equal 1. Column 8 is the *k* of Eq.(6.25) that would make the data in column 5 to perfectly fit in our model, note that to calculate *k* the 2D speed needs to be corrected to 3D.

Shot number	Number of Fragments	% of Ejecta Mass	Fragment Average Mass [g]	Mean 2D Speed [m/s]	ΔV_a [m/s]	$\sqrt{\frac{M_a}{m}}\Delta V_a$ [m/s]	*k*
820302	8	45	45.4	4.8	1.038	5.648	1.06
820303	9	18	26.1	12.5	1.342	9.766	0.67
820304	6	13	11.7	4.3	0.558	5.999	1.21
820306	8	10	12.4	4.2	0.646	6.670	1.39
820308	7	49	19.7	4.4	0.444	3.581	0.70
850841	8	44	40.6	1.3	0.270	1.396	0.96
850842	6	42	53.9	1.7	0.416	1.892	1.01
850843	4	86	156.3	0.9	0.200	0.528	0.53
850844	7	32	32.3	1.4	0.618	3.531	2.44
850845	4	23	6.9	3.5	1.094	15.205	4.04
850846	6	25	29.8	9.2	6.301	42.810	4.65
850847	11	19	12.6	11.6	4.430	45.872	3.76
850850	8	30	25.1	6.1	2.392	17.831	2.79
851204	9	88	78.0	3.2	0.462	1.940	0.53
851205	7	46	19.1	3	0.367	3.126	0.90
851206	5	33	1.8	5.4	0.288	7.941	1.23
851207	6	37	2.4	4.6	0.327	7.601	1.39
851208	9	88	41.4	3.1	0.347	1.959	0.54
851209	5	40	1.0	17.2	0.217	7.676	0.37
851213	10	96	5.4	3.8	1.670	26.942	6.85
851214	8	30	23.0	9.8	5.277	40.178	4.04
851215	7	16	1.0	1.9	0.115	3.812	1.68
860414	12	43	1.3	5.8	0.435	13.744	2.00
860415	8	21	2.6	4.9	0.469	10.782	1.88
860416	7	42	2.9	7.2	0.485	10.302	1.21
860417	8	20	5.8	6.3	0.617	9.349	1.27
860418	10	25	4.6	5.6	0.599	10.126	1.55
860419	15	30	4.2	4.5	0.644	11.383	2.20
860420	13	57	29.5	3.1	0.585	3.917	1.12
860503	19	36	22.2	8.5	0.906	6.981	0.70

The following procedure has been followed to compute the constant *k* from Table A-3 using *Davis & Ryan*'s[94] experiments: assuming homogeneous spherical dispersion, the experimental 2D mean velocity was converted to 1D velocity by simply dividing it with $\sqrt{2}$ factor, then the 3D experimental velocity is calculated by approximating it to:

$$\Delta v_{\exp_i} = \sqrt{\left(\overline{v}_{1D} - \Delta v_a\right)^2 + 2 \cdot \overline{v}_{1D}{}^2}\ , \tag{6.26}$$

using Eq.(4.30) from Chapter IV, the theoretical Δv_i for an fragment mass equal to the average mass of the fragments in the experiment (i.e., Table A-3 column 4) is calculated, and finally the fraction $\Delta v_i / \Delta v_{\exp_i}$ gives us the constant *k* (i.e., Table A-3 column 8).

Fig. A-11 shows each one of the calculated *k* plotted against the mass fraction of each experiment mean fragment size. As can be seen in Table A-3, the constant *k* ranges from 0.37 to 6.85. Since the lower limit of *k* is 0, an histogram of $\log_{10}(k)$ will provide us better insight to the distribution of the values of this constant. Fig. A-12 shows the $\log_{10}(k)$ histogram and points out a distribution of values around a mean of 1.4.

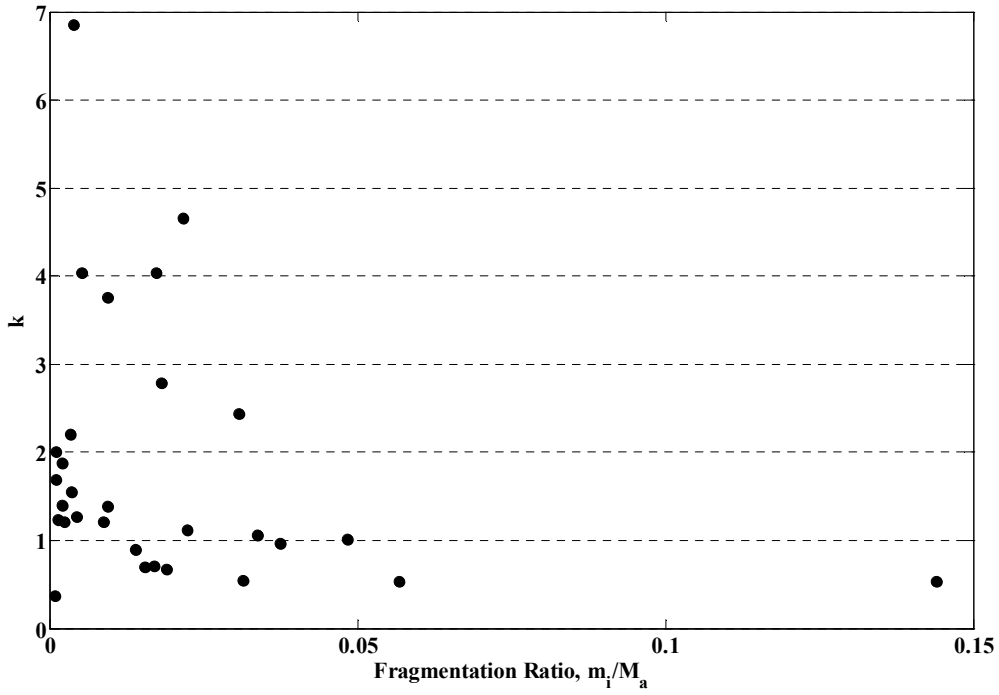

Fig. A-11 Calculated *k* for each one of the experiments in Table A-3.

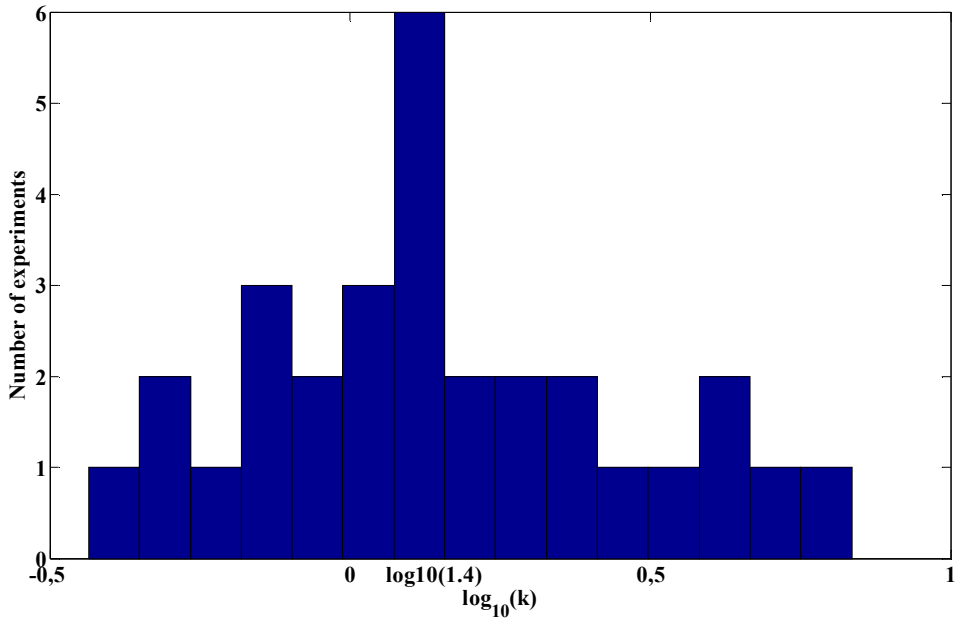

Fig. A-12 Histogram of constant *k* calculated in column 8 of Table A-3.

The work developed in this section only aimed to test the model developed in Section IV.3.2 and at the same time obtaining an approximate and realistic qualitative value of *k*. I believe that this was achieved through the analysis of data provided by *Davis & Ryan*[94], despite it lacks of some important information such as the proportion of small fragments from the ejecta recovered or the methodology in calculating the 2D mean velocity.

A.5. Bibliography

[1] "Planetary Defense: Eliminating the Giggle Factor", 2008: http://www.airpower.maxwell.af.mil/airchronicles/cc/france2.html [last viewed on 24 November 2008]

[2] C. R.Chapman and D. Morrison, "Impacts on the Earth by asteroids and comets: assessing the hazard", *Nature*, Vol. 367, Jan. 1994, pp. 33-40.

[3] L.W. Alvarez, W. Alvarez, F. Asaro and H. V. Michel, "Extraterrestrial Cause for the Cretaceous-Tertiary Extinction", *Science*, Vol. 208, No. 4448, Jun. 1980, pp. 1095-1108.

[4] "Earth Impact Database", 2008: http://www.unb.ca/passc/ImpactDatabase/images/odessa.htm [last viewed on 24 November 2008].

[5] F.Watson, *Between the Planets*, The Blakiston Company, Philadelphia, 1941, pp. 222.

[6] E. J. Öpik, "On the Catastrophic Effect of Collisions with Celestial Bodies," *Irish Astronomical Journal*, Vol. 5, No. 36, 1958.

[7] R. B. Baldwin, *The Face of the Moon*, University of Chicago Press, Chicago, 1949, pp. 239.

[8] MIT students, *Project Icarus*, The MIT Press, Cambridge, MA, 1968.

[9] H. Atkinson, C. Tickell, and D. Williams, "Report of the Task Force on Potencially Hazardous Near Earth Objects", British National Space Center, London, Sept. 2000.

[10] G. H. Stokes, D. K. Yeomans, W. F. Bottke, D. Jewitt, S. R. Chesley, T. S. Kelso, J. B. Evans, R. S. McMillan, R. E. Gold, T. B. Spahr, A. W. Harris and S.P. Worden, "Study to Determine the Feasibility of Extending the Search for Near-Earth Objects to Smaller Limiting Diameters", NASA, Near-Earth Object Science Definition Team, 22 Aug. 2003.

[11] D. J. Tholen, "Asteroid Taxonomy from Cluster Analysis of Photometry", University of Arizona, Doctoral Thesis.

[12] S. R. Chesley, P. W. Chodas, A. Milani and D. K. Yeomans, "Quantifying the Risk Posed by Potential Earth Impacts", *Icarus*, Vol. 159, No. 2, Jan 2002, pp. 423-432. DOI:10.1006/icar.2002.6910

[13] J. Crovisier, "Cometary diversity and cometary families", Proceedings of the XVIIIemes Rencontres de Blois, *Planetary Science: Challenges and Discoveries*, Blois, France, 28th May 2006. 2007.arXiv:astro-ph/0703785v1

[14] E. M. Drobyshevski, "Stardust Findings Favor not only the Planetary Origin of Comets but the Underlying Close-binary Cosmology of the Solar System as well", *Icarus*, Vol. 197, No. 1, Mar 2008, pp. 203-210. DOI:10.1016/j.icarus.2008.03.025

[15] H. A. Ishii, J. P. Bradley, Z. R. Dai, M. Chi, A. T. Kearsley, M. J. Burchell, N. D. Browning, and F. Molster, "Comparison of Comet 81P/Wild 2 Dust with Interplanetary Dust from Comets", *Science*, Vol. 319, Jan 2008, pp. 447-450. DOI:10.1126/science.1150683

[16] J. M. Sunshine, O. Groussin, P. H. Schultz, M. F. A'Hearn, L. M. Feaga, T. L. Farnham, and K. P. Klaasen, "The Distribution of Water Ice in the Interior of Comet Tempel 1", *Icarus*, Vol. 190, No. 2, May 2007, pp. 284-294. DOI:10.1016/j.icarus.2007.04.024

[17] E. M. Shoemaker, R. S. Wolfe and C. S. Shoemaker, "Asteroid and Comet Flux in the Neighborhood of the Earth", *In Lunar and Planetary Institute*, Special Paper 247, 1988, pp. 155-170.

[18] D. Steel, "Tunguska at 100," *Nature*, Vol. 453, Jun 2008, pp. 1157-1159. DOI:10.1038/4531157a

[19] J. G. Hills and M. P. Goda, "The Fragmentation of Small Asteroids in the Atmosphere", *The Astronomical Journal*, Vol. 105, No. 3, Mar 1993, pp. 1114-1144. DOI:10.1086/116499

[20] P. A. Bland and N. A. Artemieva, "Efficient Disruption of Small Asteroids by Earth's Atmosphere", *Nature*, Vol. 424, Jul 2003, pp. 288-291. DOI:10.1038/nature01757

[21] O. B. Toon, K. Zahnle, D. Morrison, R. P. Turco and C. Covey, "Environmental Perturbations Caused by The Impact of Asteroids and Comets", *Reviews of Geophysics*, Vol. 35, No. 1, Feb 1997, pp. 41-78.

[22] "NEODys, Near Earth Objects Dynamic Site", 2008: http://newton.dm.unipi.it/cgi-bin/neodys/neoibo [last viewed on 25 November 2008].

[23] "Near Earth Objects Program," 2008: http://neo.jpl.nasa.gov/ [last viewed on 25 November 2008].

[24] R. P. Binzel, "The Torino Impact Hazard Scale", *Planetary and Space Science*, Vol. 48, No. 4, Jan 2000, pp. 297-303. DOI:10.1016/S0032-0633(00)00006-4

[25] "Large Synoptic Survey Telescope", 2008: http://www.lsst.org/lsst_home.shtml [last viewed on 25 November 2008].

[26] "Panoramic Survey Telescope & Rapid Response System", 2008: http://pan-starrs.ifa.hawaii.edu/public/ [last viewed on 25 November 2008].

[27] S. R. Chesley and T. B. Spahr, "Earth Impactors: Orbital Characteristics and Warning Times", *Mitigation of Hazardous Comets and Asteroids* Cambridge University Press, 2003.

[28] P. W. Chodas and J. D. Giorgini, "Impact Warning Times for Near Earth Asteroids", Proceedings of ACM 2008, *Asteroids, Comets and Meteors*, Baltimore, Maryland, USA, 2008.

[29] G. B. Valsecchi, A. Milani, G. F. Gronchi and S. R. Chesley, "Resonant Returns to Close Approaches: Analytical Theory", *Astronomy and Astrophysics*, Vol. 408, No. 3, 2003, pp. 1179-1196. DOI:10.1051/0004-6361:20031039

[30] P. W. Chodas, *Bulletin of the American Astronomic Society*, Vol. 33, 1999, pp. 1117.

[31] S. R. Chesley, "Potential Impact Detection for Near-Earth Asteroids: the Case of 99942 Apophis (2004 MN_4)", Proceedings IAU Symposium, *Asteroids, Comets and Meteors*, 7-8-2005, Vol. 229, International Astronomical Union, 2005. DOI:10.1017/S1743921305006769

[32] J. G. Giorgini, L. A. M. Benner, S. J. Ostro, M. C. Nolan and M. W. Busch, "Predicting the Earth Encounters of (99942) Apophis," *Icarus*, Vol. 193, No. 1, Jan 2008, pp. 1-19. DOI:10.1016/j.icarus.2007.09.012

[33] M. Delbo, A. Cellino and E. F. Tedesco, "Albedo and Size Determination of Potentially Hazardous Asteroids:(99942) Apophis", *Icarus*, Vol. 188, No. 1, May 2007, pp. 266-269. DOI:10.1016/j.icarus.2006.12.024

[34] D. J. Scheeres, L. A. M. Benner, S. J. Ostro, A. Rossi, F. Marzari, and P. Washabaugh, "Abrupt Alteration of Asteroid 2004MN4's Spin State During its 2029 Earth Flyby", *Icarus*, Vol. 178, No. 1, Nov 2005, pp. 281-283. DOI:10.1016/j.icarus.2005.06.002

[35] M. R. Rampino and B. M. Haggerty, "The "Shiva Hypothesis": Impacts, Mass Extinctions, and the Galaxy", *Earth, Moon, and Planets*, Vol. 71, No. 3, Dec 1995, pp. 441-460. DOI:10.1007/BF00117548

[36] A. W. Harris, "The Rotation Rates of Very Small Asteroids: Evidence for 'Rubble Pile' Structure", *Lunar and Planetary Science*, Vol. 27, Mar 1996, pp. 493.

[37] A. W. Harris, "The H-G Asteroid Magnitude System: Mean Slope Parameters," *Lunar and Planetary Science*, Vol. 20, Mar 1989, pp. 375-376.

[38] E. M. Shoemaker, "Collision of Asteroids and Comets with the Earth: Physical and Human Consequences", *NASA Workshop*, Snowmass, Colorado, USA, 13th July 1981, 1981.

[39] D. J. Scheeres and R. L. Schweickart, "The Mechanics of Moving Asteroids", 2004 Planetary Defense Conference: Protecting Earth from Asteroids, *Planetary Defense Conference*, 23rd Feb 2004, American Institute of Aeronautics and Astronautics, Orange County, California 2004. AIAA 2004-1446

[40] E. T. Lu and S. G. Love, "Gravitational Tractor for Towing Asteroids", *Nature*, Vol. 438, Nov 2005, pp. 177-178. DOI:10.1038/438177a

[41] J. N. Spitale, "Asteroid Hazard Mitigation using the Yarkovsky Effect", *Science*, Vol. 296, No. 5565, Apr. 2002, pp. 77. DOI:10.1126/science.1069577

[42] H. J. Melosh, I. V. Nemchinov and Y. I. Zetzer, "Non-nuclear Strategies for Deflecting Comets and Asteroids", *Hazard Due to Comets and Asteroids*, edited by T.Gehrels University of Arizona, Tucson, 1994, pp. 1110-1131.

[43] J. Olds, A. Charania, M. Graham, and J. Wallace, "The League of Extraordinary Machines: A rapid and Scalable Approach to Planetary defense Against Asteroid Impactors", Call for Proposals CP-02-02, Version 1, NASA Institute for Advanced Concepts (NIAC), 30 Apr. 2004.

[44] C. Sagan, *Pale Blue Dot: A Vision of the Human Future in Space*, Random House, Toronto, 1994.

[45] P. Hammerling and J. L. Remo, "NEO Interaction with Nuclear Radiation", *Acta Astronautica*, Vol. 36, No. 6, Sep 1995, pp. 337-346. DOI:10.1016/0094-5765(95)00111-5

[46] S. Glasstone, *The Effects of Nuclear Weapons*, U.S. Atomic Energy Commission, Washington, D.C., 1962.

[47] W. J. Tedeschi, J. L. Remo, J. F. Schulze and R. P. Young, "Experimental Hypervelocity Impact Effects on Simulated Planetesimal Materials", *International Journal of Impact Engineering*, Vol. 17, No. 4-6, 1995, pp. 837-848. DOI:10.1016/0734-743X(95)99904-6

[48] J. H. Hubbell and S. M. Seltzer, "Tables of X-Ray Mass Attenuation Coefficients and Mass Energy-Absorption Coefficients," 1996: http://physics.nist.gov/PhysRefData/XrayMassCoef/cover.html [last viewed on 25 November 2008]

[49] J. Wang, A. M. Davis, R. N. Clayton and A. Hashimoto, "Evaporation of Single Crystal Forsterite:Evaporation Kinetics, Magnesium Isotope Fractionation, and Implications of Mass-dependent Isotopic Fractional of a Diffusion-Controled Reservoir", *Geochimica et Cosmochimica Acta*, Vol. 63, No. 6, Jul 1999, pp. 953-966. DOI:10.1016/S0016-7037(98)00286-5

[50] T. J. Ahrens and A. W. Harris, "Deflection and Fragmentation of Near-Earth Asteroids", *Nature*, Vol. 360, Dec 1992, pp. 429-433. DOI:10.1038/360429a0

[51] J. R. Wertz and W. J. Larson, *Space Mission Analysis and Design*, third edition, Microcosm Press 2003, pp. 703.

[52] P. L. Smith, M. J. Barrera, E. T. Campbell, K. A. Fedman, G. E. Peterson and G. N. Smit, "Deflecting a Near Earth Object with Today's Space Technology", *Planetary Defense Conference*, 23rd Feb 2004, American Institute of Aeronautics and Astronautics, Orange County, California 2004. AIAA 2004-1447

[53] J. L. Remo, "Energy Requirements and Payload Masses for Near-Earth Objects Hazard Mitigation", *Acta Astronautica*, Vol. 47, No. 1, Jul. 2000, pp. 35-50. DOI:10.1016/S0094-5765(00)00008-4

[54] C. Sublette, "The Nuclear Weapon Archive," 1994: http://nuclearweaponarchive.org/ [last viewed on 25 November 2008]

[55] K. A. Holsapple, "The Scaling of Impact Processes in Planetary Science", *Annual Review of Earth and Planetary Science*, Vol. 21, May 1993, pp. 333-373. DOI:10.1146/annurev.ea.21.050193.002001

[56] C. McInnes, "Deflection of Near-Earth Asteroids by kinetics Energy Impacts from Retrograde Orbits", *Planetary and Space Science*, Vol. 52, No. 7, Jun 2004, pp. 587-590. DOI: 10.1016/j.pss.2003.12.010

[57] A. E. Petropoulos, T. D. Kowalkowski, M. A. Vavrina, D. W. Parcher, P. A. Finlayson, G. J. Whiffen and J. A. Sims, "1stACT global trajectory optimisation competition: Results found at the Jet Propulsion Laboratory", *Acta Astronautica*, Vol. 61, No. 9, Nov 2007, pp. 806-815. DOI: 10.1016/j.actaastro.2007.03.013

[58] D. J. Scheeres, "Close Proximity Operations for Implementing Mitigation Strategies", 2004 Planetary Defense Conference: Protecting Earth from Asteroids, *Planetary Defense Conference*, California, 23 Feb. 2004, Orange County, California 2004. AIAA 2004-1445

[59] P. Lehmann, B. Reck, J. Behrens and M. D. Vo, "Acceleration of a Suborbital Payload Using an Electromagnetic Railgun", *IEEE Transactions on Magnetics*, Vol. 43, No. 1, Jan 2007, pp. 480-485. DOI:10.1109/TMAG.2006.887666

[60] M. Anttila and T. Ylikorpi, "Defining the Technical Requirements for Subsurface Mars Driller", *Sixth International Conference on Mars*, Pasadena, California., 20 July 2003, Paper 3020.

[61] Y. Liu, B. Weinberg and C. Mavroidis, "Mechanical Design and Modelling of a Robotic Planetary Drilling System", IDETC/CIE 2005, *ASME 2006 International*

Design Engineering Technical Conferences & Computers and Information in Engineering Conference, DETC2006-99699, Philadelphia, Pennsylvania, USA, 2006.

[62] M. Thomas, "Inflatable Space Structures", *IEEE Potentials Magazine*, Vol. 11, No. 4, Dec. 1992, pp. 29-32. DOI:10.1109/45.207143

[63] J. M. Hedgepeth and R. K. Miller, "Structural concepts for large solar concentrators", *Acta Astronautica*, Vol. 17, No. 1, Jan. 1988, pp. 79-89. DOI:10.1016/0094-5765(88)90131-2

[64] J. L. Remo, "Classifying and modelling NEO material properties and interactions", *Hazards due to Comets and Asteroids*, 1st Edition, The University of Arizona Press, Tucson, 1994, pp. 551-596.

[65] C. Maddock, J. P. Sanchez, M. Vasile and G. Radice, "Comparison of Single and Multi-Spacecraft Configurations for NEA Deflection by Solar Sublimation", *New Trends in Astrodynamics and Applications III*, Vol. 886, Feb 2007, pp. 303-316. DOI:10.1063/1.2710064

[66] M. Vasile, "A Multimirror Solution for the Deflection of Dangerous NEOs", *Journal of Communications in Nonlinear Science and Numerical Simulation*, in press, July 2008.

[67] C. McInnes, "Near Earth Object Orbit Modification Using Gravitational Coupling", *Journal of Guidance, Control and Dynamics*, Vol. 30, No. 3, Jun. 2007, pp. 870-873. DOI:10.2514/1.25864

[68] S. B. Broschart and D. J. Scheeres, "Control of Hovering Spacecraft Near Small Bodies: Application to Asteroid 25143 Itokawa", *Journal of Guidance, Control and Dynamics*, Vol. 28, No. 2, Mar. 2005, pp. 343-354. DOI:10.2514/1.3890

[69] J. Kawaguchi, A. Fujiwara and T. Uesugi, "Hayabusa—Its technology and science accomplishment summary and Hayabusa-2," *Acta Astronautica*, Vol. 62, No. 10-11, Apr. 2008, pp. 639-647. DOI:10.1016/j.actaastro.2008.01.028

[70] J. P. Sanchez, C. Colombo, M. Vasile and G. Radice, "Multi-criteria Comparison among Several Mitigation Strategies for Dangerous Near Earth Objects", *Journal of Guidance, Control and Dynamics*, Vol. 32, No. 1, Jan. 2009, pp. 121-142. DOI:10.2514/1.36774

[71] D. Massonnet and B. Mayssignac, "A Captured Asteroid: Our David's Stone for Shielding Earth and Providing the Cheapest Extraterrestrial Material", *Acta Astronautica*, Vol. 59, No. 1-5, Apr. 2006, pp. 77-83. DOI:10.1016/j.actaastro.2006.02.030

[72] M. Vasile, "Robust Mission Design Through Evidence Theory and Multiagent Collaborative Search", *Annals of the New York Academy of Sciences*, Vol. 1065, Dec. 2005, pp. 152-173. DOI:10.1196/annals.1370.024

[73] M. Vasile, "A Hybrid Multi-Agent Collaborative Search Applied to the Solution of Space Mission Design Problems", Proceedings of the GO 2005, *Global Optimization Workshop*, San Jose, Almeria, Spain, 18th Sep. 2005, University of Almeria, pp. 247-252.

[74] G. B. Valsecchi, "Close Encounters and Collisions of Near-Earth Asteroids with the Earth," *Comptes Rendus Physique*, Vol. 6, No. 3, Apr. 2005, pp. 337-344. DOI:10.1016/j.crhy.2004.12.014

[75] P. De Pascale and M. Vasile, "Preliminary Design of Low-Thrust Multiple Gravity Assist Trajectories", *Journal of Spacecraft and Rockets*, Vol. 43, No. 5, Sep. 2006, pp. 1065-1076. DOI:10.2514/1.19646

[76] J. C. Mankins, "Approaches to Strategic Research and Technology (R&T) Analysis and Road Mapping", *Acta Astronautica*, Vol. 51, No. 1-9, Jul. 2002, pp. 3-21. DOI:10.1016/S0094-5765(02)00083-8

[77] D. J. Moorhouse, "Detailed Definitions and Guidance for Application of Technology Readiness Levels", *Journal of Aircraft*, Vol. 39, No. 1, Sep. 2002, pp. 190-192.

[78] M. Gulgielmi, "TRL and Development Time", personal communication, 2008.

[79] "Discovery is NEAR", 2002: http://near.jhuapl.edu/ [last viewed on 13 December 2008].

[80] P. Ferri and G. Schwehm, "Rosetta: ESA's Comet Chaser Already Making its Mark", *ESA bulletin*, Vol.123, 15 Aug. 2005, pp. 62-66.

[81] J. Blacic, D. Dreesen and T. Mockler, "Report on Conceptual System Analysis of Drilling Systems for 200-m-Depth Penetration and Sampling of the Martian Subsurface", Los Alamos National Laboratory, Technical Report LAUR00-4742, Oct. 2000.

[82] B. Basso, P. Bartlett, S. Gorevan, T. Kennedy, G. Paulsen, J. Wilson and L. Yachbes, "Surface Anchoring and Deflection Concepts for Earth-crossing Comets and Asteroids", *Workshop on Spacecraft Reconnaissance of Asteroid and Comet Interiors*, Santa Cruz, California, 5th Oct. 2006, Paper 3032, pp. 16-17.

[83] D. Carrier, "Apollo 15 Drilling Problems", 2003: http://history.nasa.gov/alsj/a15/a15carrier.html [last viewed on 13 December 2008].

[84] J. Olds, A. Charania and M. G. Schaffer, "Multiple Mass Drivers as an Option for Asteroid Deflection Missions", *AIAA Planetary Defense Conference*, Washington, D. C., 5th Apr. 2007, AIAA Paper 2007 S3-7.

[85] M. A. Vorontsov, V. V. Kolosov and A. Kohnle, "Adaptive Laser Beam Projection on an Extended Target: Phase- and Field-conjugate Precompensation", *Journal of the Optical Society of America*, Vol. 24, No. 7, Jul 2007, pp. 1975-1993. DOI:10.1364/JOSAA.24.001975

[86] R. Angel, J. Burge, K. Hege, M. Kenworthy and N. Woolf, "Stretched Membrane with Electrostatic Curvature (SMEC): A New Technology for Ultra-lightweight Space Telescopes", Proceedings SPIE 4013, *UV, optical, and IR space telescopes and instruments*, Munich, 29th Apr. 2000, 4013, Society of Photo-Optical Instrumentation Engineers, Bellingham, WA, pp. 699-705.

[87] "Composite ultra-light weight active mirror for space applications", U.S. Patent 7064885, 4th Oct. 2005.

[88] "A New Deployable Thin-film, Ultralight Mirror for Future Space Telescopes and Surveillance Satellites", *Current Science*, Vol. 79, No. 1, Jul. 2000, pp. 12-13.

[89] V. V. Ivashkin and V. V. Smirnov, "An Analysis of Some Methods of Asteroid Hazard Mitigation for the Earth", *Planetary and Space Science*, Vol. 43, No. 6, Nov. 1994, pp. 821-825.

[90] "Near-Earth Objects Survey and Deflection Analysis of Alternatives", National Aeronautics and Space Administration, Report to the Congress, NASA Authorization Act of 2005 (Public Law No. 109-155), Mar. 2007.

[91] D. P. O'Brien and R. Greenberg, "Steady-state size distributions for collisional populations: analytical solution with size-dependent strength", *Icarus*, Vol. 164, No. 2, Apr. 2003, pp. 334-345. DOI:10.1016/S0019-1035(03)00145-3

[92] E. V. Ryan and H. J. Melosh, "Impact Fragmentation: From the Laboratory to Asteroids", *Icarus*, Vol. 133, No. 1, Apr. 1998, pp. 1-24. DOI:10.1006/icar.1998.5915

[93] K. A. Holsapple, "Catastrophic disruptions and cratering of solar system bodies: a review and new results", *Planetary and Space Science*, Vol. 42, No. 12, May 1994, pp. 1067-1078. DOI:10.1016/0032-0633(94)90007-8

[94] D. R. Davis and E. V. Ryan, "On Collisional Disruption: Experimental Results and Scaling Laws", *Icarus*, Vol. 83, No. 1, Jan. 1990, pp. 156-182. DOI:10.1016/0019-1035(90)90012-X

[95] M. Vasile and C. Colombo, "Optimal Impact Strategies for Asteroid Deflection", *Journal of Guidance, Control and Dynamics*, Vol. 31, No. 4, Jul. 2008, pp. 858-872. DOI:10.2514/1.33432

[96] H. Schaub and J. L. Junkins, *Analytical mechanics of space systems*, 1st Edition, AIAA Education Series, American Institute of Aeronautics and Astronautics, Inc. 2003.

[97] D. E. Gault, E. M. Shoemaker and H. J. Moore, "Spray Ejected from the Lunar Surface by Meteoroid Impact," NASA, NASA Technical Note D-1767, 1963.

[98] W. Wiesel, "Fragmentation of Asteroids and Artificial Satellites in Orbit", *Icarus*, Vol. 34, No. 1, Apr. 1978, pp. 99-116. DOI:10.1016/0019-1035(78)90130-6

[99] R. Greenberg, J. F. Wacker, W. K. Hartmann and C. R. Chapman, "Planetesimal to Planets: Numerical Simulations of Collisional Evolution", *Icarus*, Vol. 35, No. 1, Jul. 1978, pp. 1-26. DOI:10.1016/0019-1035(78)90057-X

[100] H. Mizutani, Y. Takagi and S. I. Kawakami, "New Scaling Laws on Impact Fragmentation", *Icarus*, Vol. 87, No. 2, Oct. 1990, pp. 307-326. DOI:10.1016/0019-1035(90)90136-W

[101] W. Benz and E. Asphaug, "Catastrophic Disruptions Revised", *Icarus*, Vol. 142, No. 1, Nov. 1999, pp. 5-20. DOI:10.1006/icar.1999.6204

[102] S. R. Chesley and S. N. Ward, "A Quantitative Assessment of the Human and Economic Hazard from Impact-generated Tsunami", *Natural Hazards*, Vol. 38, No. 3, Jul. 2006, pp. 355-374. DOI:10.1007/s11069-005-1921-y

[103] B. A. Conway, "Near-Optimal Defection of Earth-Approaching Asteroids", *Journal of Guidance, Control and Dynamics*, Vol. 24, No. 5, 2001, pp. 1035-1037.

[104] M. R. Spiegel and L. Abellanas, *Fórmulas y Tablas de Matemática Aplicada*, McGraw-Hill 1988, pp. 213.